



HAL
open science

Thin film modeling of crystal growth and dissolution in confinement

Luca Gagliardi

► **To cite this version:**

Luca Gagliardi. Thin film modeling of crystal growth and dissolution in confinement. Geophysics [physics.geo-ph]. Université de Lyon, 2018. English. NNT : 2018LYSE1211 . tel-02044046

HAL Id: tel-02044046

<https://theses.hal.science/tel-02044046>

Submitted on 21 Feb 2019

HAL is a multi-disciplinary open access archive for the deposit and dissemination of scientific research documents, whether they are published or not. The documents may come from teaching and research institutions in France or abroad, or from public or private research centers.

L'archive ouverte pluridisciplinaire **HAL**, est destinée au dépôt et à la diffusion de documents scientifiques de niveau recherche, publiés ou non, émanant des établissements d'enseignement et de recherche français ou étrangers, des laboratoires publics ou privés.



N° d'ordre NNT : 2018LYSE1211

THÈSE DE DOCTORAT DE L'UNIVERSITÉ DE LYON

opérée au sein de
l'Université Claude Bernard Lyon 1

École Doctorale ED 52
Physique et Astrophysique de Lyon

Spécialité de doctorat : Physique

Soutenue publiquement le 6 Novembre 2018, par :

Luca Gagliardi

Modèle de film mince pour la croissance et la dissolution de cristaux confinées

Sous la direction de Olivier Pierre-Louis

Devant le jury composé de :

Colombani Jean, Professor, Université Lyon 1

Président(e)

Cuerno Rodolfo, Professeur, Universidad Carlos III de Madrid

Rapporteur

Plapp Mathis, Directeur de Recherche, Ecole Polytechnique

Rapporteur

Renard Francois, Professeur, University of Oslo

Rapporteur

Shahidzadeh Noushine, Professeur Associé, University of Amsterdam

Examinatrice

Dysthe Dag Kristian, Professeur, University of Oslo

Examineur

Pierre-Louis Olivier, Directeur de Recherche, Université Lyon 1

Directeur de thèse

*A Diodato Gagliardi,
mio nonno.*

Ces travaux de thèse ont pour objet l'étude de la croissance et de la dissolution de cristaux confinés à travers le développement et l'application d'un modèle continu.

La croissance et la dissolution confinées des cristaux sont couramment observées dans les environnements naturels: les exemples vont de la géologie et la biominéralisation, aux matériaux de construction. En particulier, nous nous concentrons sur trois phénomènes: la dissolution sous contrainte, la formation de cavités sur la face confinée d'un cristal en croissance sur un substrat, et la force de cristallisation.

La dissolution sous contrainte est la dissolution induite par une charge extérieure sur un ensemble de grains en solution et le compactage qui en résulte. Ceci est un problème classique en géologie, lié par exemple à l'évolution des bassins et des roches sédimentaires, et à la formation de stylolites (plans de discontinuité irréguliers entre deux unités rocheuses).

La formation de cavités et de rebords sur la surface confinée de cristaux en croissance est un phénomène observé depuis plus d'un siècle, mais encore mal compris.

La force de cristallisation est la force exercée par un cristal contraint contre les parois de pores ou de failles d'un matériel hôte. Ce phénomène est d'une grande importance pour comprendre les mécanismes d'érosion dans les roches naturelles, les bâtiments ou le patrimoine historique.

Des mesures précises dans de tels systèmes sont difficiles et les résultats expérimentaux montrent souvent des différences importantes entre eux. D'autres difficultés d'interprétation sont liées aux lois heuristiques souvent employées pour décrire les données expérimentales ou le recours systématique à la thermodynamique d'équilibre pour décrire des phénomènes qui sont intrinsèquement dynamiques. En général, il émerge le besoin de concevoir des modèles hors-équilibre pour démêler le nombre de questions débattues.

Lors de la croissance et de la dissolution sous contrainte, un film mince de solution, permettant le transport de masse, est souvent présent entre le cristal et le substrat. Cependant, les approches théoriques existantes n'incluent pas des ingrédients importants tel que la pression de disjonction et l'hydrodynamique.

Afin de construire un modèle qui inclut de manière cohérente ces ingrédients physiques, nous nous concentrons sur la dynamique au sein des contacts lubrifiés. Nous développons un modèle continu de couche mince prenant en compte la diffusion, la cinétique de surface, l'hydrodynamique, la tension de surface et les interactions avec le substrat (pression de disjonction). Le modèle est dérivé à partir de la limite de petites pentes à l'aide d'un développement asymptotique standard qui exploite la minceur du film. Certaines approximations supplémentaires sont effectuées, par exemple en considérant un cristal rigide, des densités égales entre le liquide et le cristal, la limite diluée dans la solution, et uniquement des déplacements verticaux.

Le modèle est ensuite appliqué aux différents problèmes susmentionnés. Dans un premier temps, nous étudions la dissolution induite par une charge externe. Nous nous concentrons sur le rôle des interactions entre cristal et substrat sur la dynamique de dissolution pour un contact unique. On considère que le contact est une arête symétrique (1D) ou axisymétrique (2D).

Nous nous intéressons au cas où la cinétique de surface est rapide par rapport à la diffusion dans la région du contact. Nous trouvons que la forme fonctionnelle de la pression de disjonction – finie ou divergente au contact – est cruciale pour déterminer les vitesses de dissolution et les morphologies stationnaires. Une interaction singulière en loi de puissance conduit par exemple à des profils aplatis et à un taux de dissolution qui augmente indéfiniment avec la charge en loi de puissance. Ces lois de puissances sont caractérisées par des exposants qui dépendent de la valeur de la viscosité. Nous identifions deux régimes. Un premier régime, à forte viscosité, où la charge externe est équilibrée par la dissipation visqueuse dans le film. Un second régime, à faible viscosité, où la charge est équilibrée par la pression de disjonction. Étonnamment, pour des charges externes importantes, une interaction exponentielle finie conduit à un profil stationnaire de forme pointue et dont la vitesse de dissolution est indépendante de la charge appliquée. Malgré la pression de disjonction finie, il n'est pas possible d'observer un cristal qui touche le substrat à une charge finie dans un état stationnaire. Cela est dû au couplage entre la dissipation visqueuse et la tension superficielle. Celle-ci, en régularisant la pointe, implique que le liquide soit évacué moins efficacement.

Deuxièmement, nous considérons un cristal en croissance à proximité d'un mur plat. Nous supposons un contact axisymétrique. Dans un premier temps, nous considérons la croissance dans un régime dominé par la diffusion (cinétique de surface rapide). Nous constatons qu'une cavité apparaît sur la surface cristalline confinée. Nous obtenons un diagramme de morphologie hors-équilibre décrivant la formation de la cavité qui dépend d'un taux de croissance critique. Ce résultat est en accord avec les observations expérimentales effectuées par Felix Kohler et Dag Kristian Dysthe à l'Université d'Oslo. En traversant la ligne de transition, la cavité apparaît en manière continue si l'interaction avec le substrat est purement répulsive. Par ailleurs, nous observons que lorsque la séparation avec le substrat est nanométrique, dû à l'effet d'une attraction van der Waals avec le substrat, la transition apparaît en manière discontinue et avec hystérésis. De plus, dans ce cas, les effets hydrodynamiques peuvent entraver la formation de la cavité. Nous montrons qu'au-dessus d'une viscosité critique ou au-dessous d'une épaisseur de film critique, aucune cavité ne peut se former. Nous considérons ensuite, des dynamiques de croissance dominées par la cinétique de surface et non par la diffusion. En particulier, le diagramme de morphologie peut être généralisé pour inclure les effets d'une cinétique de surface lente. Par ailleurs, l'inclusion de la cinétique de surface dans la description du phénomène permet, sous certaines restrictions, de décrire la forme globale d'un cristal en croissance sur un substrat après, par exemple, sédimentation ou nucléation hétérogène.

Enfin, nous abordons la question de la force de cristallisation exercée par un cristal en croissance entre deux parois planes. Nous considérons un cristal entre deux contacts parallèles dans une géométrie axisymétrique. Premièrement, nous considérons le cristal à l'équilibre. Nous montrons l'importance de la définition de la surface de contact pour déterminer la pression d'équilibre. Par exemple, avec une définition spécifique du rayon de contact à l'équilibre et pour une pression de disjonction répulsive, le modèle implique une pression d'équilibre identique à l'expression thermodynamique standard d'un cristal macroscopique. En particulier, notre résultat ne montre aucune dépendance vis-à-vis de la taille du contact. Cependant, lorsqu'on considère une interaction attractive, avec une définition alternative du rayon de contact, des corrections pour les cristaux de taille finie apparaissent. Ces corrections dépendent de l'angle de contact. Nous traitons ensuite le problème hors équilibre, en laissant le cristal croître sous l'effet d'une sursaturation fixée en dehors de la région de contact. Nous observons que pendant la croissance, la ligne triple peut subir une transition cinétique qui comporte la formation d'un film macroscopique. La transition dépend uniquement du rapport entre la constante de diffusion, et le produit de la constante cinétique de surface et de la distance entre les murs. Avant la transition, la pression de cristallisation hors équilibre est proche de la valeur d'équilibre obtenue à la même sursaturation. Par contre, au-delà de la transition la force de cristallisation diminue jusqu'à s'annuler.



N ° d'ordre NNT : 2018LYSE1211

Thesis submitted to
UNIVERSITÉ DE LYON
Université Claude Bernard Lyon 1

for the degree of **Philosophia Doctor**

Department of Physics

Presented by :
Luca Gagliardi
November 6th, 2018

Thin film modeling of crystal growth and dissolution in confinement

Under the supervision of Olivier Pierre-Louis

Before the following jury members:

Colombani Jean, Professor, Université Lyon 1

Président(e)

Cuerno Rodolfo, Professor, Universidad Carlos III de Madrid

Reviewer

Plapp Mathis, Senior Researcher CNRS, Ecole Polytechnique

Reviewer

Renard Francois, Professor, University of Oslo

Reviewer

Shahidzadeh Noushine, Associate Professor, University of Amsterdam

Examiner

Dysthe Dag Kristian, Professor, University of Oslo

Examiner

Pierre-Louis Olivier, Senior Researcher CNRS, Université Lyon 1

PhD supervisor

The subject of this thesis is the modeling of crystal growth and dissolution in confinement. The project is at the crossroad between hydrodynamics, surface physics, non-equilibrium statistical physics, and geophysics. The type of modeling we explored and more generally a large portion of the field of surface and interface physics belongs to the family, in the statistical physics community, known as non-linear physics: a field to which I was not familiar with before starting the PhD. My background was indeed more oriented on statistical mechanics and theoretical chemistry with a strong focus on computational methods (e.g. molecular dynamics, Monte Carlo, quantum physics methods). I had just a few elementary notions in surface physics, hydrodynamics and crystal growth.

Working on this project with Olivier I had the chance to familiarize and learn a suite of techniques and approaches which are at the frontier between theoretical physics and applied mathematics. It was a great chance to take part in developing a model from scratch, leaving ample space for reflection and physical intuition a taste which I think the three years spent in Olivier's group helped me to sharpen and appreciate. I alternated all along the PhD, phases of development of numerical methods – involving also purely computer science related questions (e.g. parallelization techniques) – to a meticulous analytical study (and on this I owe a lot to Olivier's help and scientific sensibility) of asymptotic and quasistatic limits of the model which were systematically compared to or inspired by the numerical work.

Beyond the one to one relationship with my supervisor and with the scientific environment in Lyon, I had the honor to be a part of the first generation of students of the large European Horizon2020 project called NanoHeal. This project, fixing some long-term and broad objectives, had the great merit to bring together people from different backgrounds and build a very stimulant interdisciplinary network of universities and industrial partners.

It is within this network that I had the chance to meet Felix Kohler and Dag Kristian Dysthe from the University of Oslo. The collaboration with them and the visiting period I had in Oslo were of great importance to mature part of the results which are discussed in this thesis.

Acknowledgments

I am first of all grateful to the NanoHeal project not only for providing funding for this work but mostly for the amazing people involved, whose professional and informal interactions I truly enjoyed. A special mention goes naturally to Felix Kohler and Dag Kristian Dysthe and the geophysics department of the University of Oslo. I express a special gratitude to Olivier Pierre-Louis for its indulgence, patience, and cleverness: It was a true honor to learn from you. I am also very thankful to jury members who made the effort to evaluate the manuscript and showed a sincere interest in this research overall.

To my grandparents, Antonella, Martial, and Odette. A very special thought to my grandfather Diodato, as both a scientist and my grandpa, you were the most attentive of the path I have undertaken. I owe you the rigor and thoroughness I tried to put in this work. You are a model of wisdom to me, I dedicate this thesis first of all to you with my deepest affection. To my parents Evelyne and Francesco, I thank you for your vicinity and your support which made all of this possible. A special thought goes also to my sister Juliette.

A dedicated thought to Carine, you closely supported me in these last years with patience and love.

I am also grateful to my other family members and friends who have supported me along the way. A particular thought goes to my flatmates of the first years spent in Lyon: Antoine, Geraldine, and Thibault. To my office colleagues and friends: first of all, Teresa who steadily accompanied me during these three years, Francesco and Antoine which alleviated the austerity of the lab, and then Francesca, Tanguy, and Pierre-Antoine. To each of the friends in Lyon outside from the lab. A special mention goes to Laura who saw it all, since the first days in Lyon at ENS. All of you are very special individuals for me who made Lyon and university a fun place.

To my life friends in Rome, a particular mention to Alessandro, Federico, Francesco (note here, given the homonymy, some economy of notations), Marco, Mimmo, and Valeria. To my friends scattered around the world: Alon, Juan, Ireth, Matteo, Francesc, and each of the others. In particular an affectionate thought to Elad. I'm glad after all these years we all still get along so well.

To my music friends at Marcel Frontale and ENM for the pleasant time spent together during the hard last year of thesis.

To my masters: Paolo Santilli, Alessandro Gwis, and Sara Bonella. You all were at a certain point a model to follow and imitate.

To music and jazz, my catharsis.

List of symbols		17
1 Introduction		19
1.1 Crystal growth and dissolution from solution		21
1.1.1 Roughening transition		21
1.1.2 Equilibrium shapes of crystals		22
1.1.3 Growth and dissolution kinetics		24
1.1.4 Growth shape		26
1.1.5 Effect of flows		28
1.2 Thin films		29
1.2.1 Lubrication and bearing		29
1.2.2 Disjoining forces between surfaces in liquid		30
1.2.3 Transport properties		32
1.3 Confined growth and dissolution in geology		35
1.3.1 Pressure solution		35
1.3.2 Crystallization force		37
1.4 Models of confined growth and dissolution		38
1.4.1 Nano-scale: molecular dynamics simulations		38
1.4.2 Meso-scale: Kinetic Monte Carlo models		39
1.4.3 Macro-scale: continuum modeling		39
1.5 Summary and objectives of this study		42
2 The Model		43
2.1 Introduction		43
2.2 General derivation		44
2.3 Contact region		46
2.3.1 Lubrication limit in the contact region		47
2.4 Simplifications and geometries		49
2.4.1 Symmetric ridge		50
2.4.2 Axisymmetric contact		50
2.4.3 Chemical potential		51
2.5 Summary of relations for slow surface kinetics		51
2.6 Summary of relations for fast surface kinetics		52
2.7 Numerical scheme and boundary conditions		52
2.7.1 Boundary conditions for a fixed simulation box		53
2.7.2 Boundary conditions for an expanding simulation box		53
2.8 Summary		55

3	Pressure Solution	57
3.1	Introduction	57
3.2	Simulation details	58
3.2.1	Interaction potentials	59
3.2.2	Normalization	59
3.2.3	Simulations parameters	60
3.3	Results	60
3.3.1	Singular repulsion: power law case	62
3.3.2	Finite repulsion: exponential case	66
3.4	Discussion	71
3.4.1	Orders of Magnitude	71
3.4.2	Comparison with existing literature	72
3.4.3	Quasi-static approximation	74
3.4.4	Limitations of the model	76
3.5	Summary	77
4	Confined Growth and cavity formation	79
4.1	Introduction	79
4.1.1	Summary of model equations	80
4.2	Morphology diagram and comparison to UiO experiment	81
4.2.1	Experimental setup and preliminary observations	81
4.2.2	Simulation details	82
4.2.3	Non-equilibrium morphology diagram	84
4.2.4	Determination of transition line and contact size in simulations	85
4.2.5	Determination of the transition in experiments	86
4.2.6	Results and comparison	87
4.3	Effect of nano-confinement	88
4.3.1	Simulation details	89
4.3.2	Discontinuous transition	91
4.3.3	Non-equilibrium morphology diagram	92
4.3.4	Critical supersaturation and critical viscosity	93
4.4	Effect of surface kinetics	97
4.4.1	Generalized morphology diagram	97
4.4.2	Growth rate before the transition	98
4.4.3	Simulations details and results	99
4.5	Discussion	101
4.5.1	Comparison with existing literature	101
4.5.2	Shape of a crystal growing on a substrate	102
4.5.3	The heuristic constant alpha	103
4.5.4	Limitations of the model	104
4.6	Summary	105
5	Crystallization force	107
5.1	Introduction	107
5.2	Thermodynamic Equilibrium	108
5.2.1	Equilibrium pressure with an attractive interaction	109
5.2.2	Equilibrium pressure with a repulsive interaction	110
5.3	Simulation details	110
5.4	Equilibrium simulations and contact area determination	112
5.5	Out of equilibrium results	114
5.5.1	Criterion for detachment	116
5.6	Discussion	119
5.6.1	Limitations and perspectives	119
5.6.2	Comparison with existing literature	120

5.7 Summary	122
Conclusions and perspectives	123
Funding acknowledgement	125
List of publications	125
Appendices	126
A Model derivation	127
A.1 Global mass conservation	127
A.2 Crystal mass conservation	128
A.3 Energy changes	129
A.3.1 Global force balance	131
A.4 Planar currents	132
A.4.1 Total flow	132
A.4.2 Concentration current	133
A.5 Lubrication expansion	134
A.5.1 Liquid velocity	135
A.5.2 Concentration field	135
A.5.3 Force balance	136
A.5.4 Identities resulting from translational invariance of the free energy	137
A.6 Mean curvature in axysymmetric contact	138
B Numerical methods	141
B.1 Numerical scheme for fast surface kinetics	141
B.2 Numerical scheme for slow surface kinetics	143
B.3 Numerical scheme for lateral growth	144
B.4 Conserved quantities during numerical integration	145
B.4.1 Expanding (shrinking) box	146
C Derivations of analytical relations in pressure solution	147
C.1 Steady state in the absence of surface tension	147
C.1.1 Singular power law repulsion	147
C.1.2 Finite exponential repulsion	149
C.1.3 1D case	150
C.2 Surface tension contribution in finite repulsion	150
C.2.1 1D case	150
C.2.2 2D case	150
C.2.3 Numerical solution	151
C.3 Beyond the linearization of the Gibbs-Thomson relation	152
D Analytic relation for cavity appearance and supplementary material	153
D.1 Viscosity effects in confined growth	153
D.1.1 Viscosity effect on the growth rate	154
D.1.2 Viscosity effect on the critical supersaturation	155
D.2 Growth rate hysteresis in nano-confinement	155
D.3 Probe the kinetic constant via the morphology diagram?	156
E Crystallization force	159
E.1 Thermodynamic equilibrium	159
E.1.1 1D line tension	160
E.1.2 General relations	162
E.2 Equilibrium simulations: Relaxation dynamics	162
E.3 Macroscopic film width after the detachment	163

- β : In the Introduction, surface energy term with different definitions. In Chapter 4, critical growth velocity for cavity formation.
- Label b : Fields and observables evaluated at the boundary of the contact size (contact radius in 2D).
- Label bc : Fields and observables evaluated at the boundary of the integration domain (simulation box).
- $c(x, y, z, t)$: Concentration of crystal type molecules in the liquid. As a consequence of the lubrication limit no dependence on z , i.e. $c(x, y, z, t) \rightarrow c(x, y, t)$.
- c_0 : Solubility of the crystal.
- $c_{eq}(x, y, t)$: Local equilibrium concentration at the liquid-crystal interface. In the dilute limit $c_{eq} \approx \exp[\Delta\mu/(k_B T)]$.
- $\Delta\mu(x, y, t)$: Chemical potential (with respect to a reference state) at the liquid-crystal interface.
- d : Separation between two surfaces. In Chapter 5, half separation between two parallel substrates.
- D : Diffusion of crystal type molecules in the liquid.
- Da : Damköhler number.
- ε' : Viscous stress tensor.
- ε : Small parameter.
- η : Viscosity of the liquid.
- $F(t)$: Crystallization force along z (equivalent to F_{Cz} with $u_{Cz} = 0$).
- $F_{Cz}(t)$: External force acting on the crystal along z .
- $\gamma(x, y)$: Surface tension.
- $\tilde{\gamma}(x, y)$: Surface stiffness.
- γ_{tl} : Line tension.
- γ_{tl}^0 : Line tension neglecting excess volume.

- $h_s(x, y)$: Substrate position (immobile, $\partial_t h_s = 0$). In the applications of the model showed in this work the substrate is also assumed flat, $h_s(x, y) = h_s$.
- $h(x, y, t)$: Liquid-crystal interface position in Chapter 2. Careful, in Chapters 4 and 5, h is the typical crystal-substrate separation, $\zeta \sim \mathcal{O}(h)$.
- \mathbf{j} : Diffusion flux of crystal type molecules in the liquid.
- κ : Mean curvature of the crystal profile.
- l : Length scale of the crystal interface. Typically $l \gg h$ with h a typical scale for ζ (lubrication limit). In the introduction, average separation between surface steps.
- L in Chapters 4 and 5: Contact radius. In Chapters 2 and 3, total size of the integration domain in 1D.
- LC: Liquid-crystal interface.
- LS: Liquid-substrate interface.
- $\hat{\mathbf{n}}$: Normal to the LC interface (oriented towards the liquid).
- ν : Kinetic constant for surface kinetics.
- Ω : Molecular/atomic volume in the crystal.
- $p(x, y, z, t)$: Pressure in the liquid.
- $P(t)$: Crystallization pressure along z .
- R 2D axysymmetric, or L 1D ridge (only in Chapter 3): Total size of the system.
- ρ_C : Crystal density (constant).
- ρ_L : Liquid density (constant).
- $\sigma(x, y, t) = c(x, y, t)/c_0 - 1$: Supersaturation.
- σ_b : Supersaturation at the edge of the contact.
- σ_{bc} : Supersaturation at the boundary of the integration domain.
- T and k_B : Temperature and Boltzmann constant, respectively. The temperature is assumed constant and uniform in space.
- $\mathbf{u}_C(t)$: Crystal rigid body velocity. u_{Cz} : Component along z , equivalent to growth or dissolution velocity.
- $\mathbf{u}_L(x, y, z, t)$: Liquid velocity.
- $U(\zeta)$: Interaction between crystal and substrate. $-U'(\zeta)$: Disjoining force.
- $v_n(x, y, t)$: Interface velocity (oriented towards the liquid).
- $v_{Cz} = \hat{\mathbf{z}} \cdot (v_n - \mathbf{n} \cdot \mathbf{u}_C)$: Local growth/dissolution rate along z .
- $\zeta(x, y, t) = h_s(x, y) - h(x, y, t)$: Film width.
- ζ_{bc} : Film width at the boundary of the integration domain (constant).
- $\zeta_0 = \zeta(r = 0, x = 0)$: Width at the center of the crystal profile.
- ζ_0^{eq} : Width at the center of the equilibrium crystal profile.
- $\zeta_{eq}^\infty(x, y)$: Equilibrium profile of a macroscopic crystal far from the substrate.

Crystal growth is at the heart of several disciplines such as metallurgy, microelectronics, biomineralization, and geophysics. We focus here on the subfield of crystal growth from solution and specifically on the case where the crystal, constrained by the presence of a substrate or another crystal, loses its translational invariance. We wish to investigate the growth/dissolution dynamics within the contact between the crystal and a substrate in the cases where a liquid film is present between the crystal and the confining wall. Confinement then affects both the growth of the crystal and its motion: indeed, growth at the confined crystal faces is altered by the reduced diffusion-transport across the thin liquid film and by interactions with the substrate. In addition, due to these interactions and viscous dissipation in the liquid, work must be performed on the system whenever the crystal is displaced.

This introduction wishes to bring the reader from a general perspective on crystal growth to the specific questions addressed within this work. The first part introduces some basic concepts in crystal growth/dissolution. They will help to set the framework of this study and give also a historical perspective. The second part reviews some effects of the confinement of liquid films between inert walls as known in the literature. The third part bridges between the two previous ones introducing some practical instances of confined growth and dissolution in geological applications. This is the place where thin film hydrodynamics, diffusion, surface interactions, and crystal growth/dissolution kinetics couple. In this section, we also report on the current questions addressed in experiments on confined growth and dissolution. An experienced researcher on crystal growth and thin films or nanofluidics can start the reading from this section. The fourth part is a concise state of the art of the existing theoretical models of confined growth and



Figure 1.1: Snowflakes are examples of dendritic crystal growth. By Charles Schmitt [Wikipedia Commons]

dissolution at different scales.

Finally, supported by the prior discussion, we summarize the current challenges addressed within the thesis using *thin film models*.

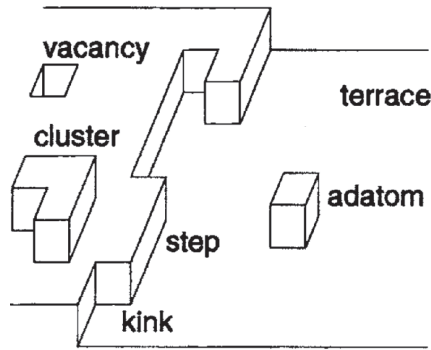


Figure 1.2: Schematic illustration of a surface structure with terraces bounded by a step with kinks. From [1].

1.1 Crystal growth and dissolution from solution

A basic introduction to the standard theory of crystal growth and dissolution is here provided. Microscopic features of a crystal surface, such as adatoms, terraces, steps, and kinks, are correlated with the macroscopic morphology and kinetics. Below the so-called roughening temperature, crystals are faceted and surface growth is controlled by screw dislocations or the 2D nucleation mechanism. Above the roughening temperature, crystals are rounded and growth is controlled by the abundant attachment sites which are present on the microscopically rough surfaces.

We introduce the important distinction between surface dominated as opposed to diffusion dominated kinetics, which is known to lead to very different behaviors with dendritic shapes and instabilities (Mullins-Sekerka instability) observed in the former and faceted or regular structures in the latter (Frank construction). In surface dominated growth, depending on the microscopic growth mechanism, different macroscopic laws are observed for the growth rate.

The fundamental microscopic elements at the crystal surface, which contribute to its kinetic behavior, are *terraces* separated by *steps* of atomic height. These steps themselves contains straight parts separated by *kinks*. On the terraces one can observe *adatoms* which are diffusive atoms which can be incorporated in the surface when meeting a step, and vacancies resulting from missing surface atoms.

As illustrated in the following, when a crystal is above the roughening temperature, the crystal surface contains many terraces and steps and many low energy sites are available for direct attachment of atoms. On the contrary, when surfaces are atomically flat i.e. in the presence of a facet, two-dimensional clusters on the surface or nucleus must form to provide low energy sites such as steps and kink positions before growth can proceed. This phenomenon is called two-dimensional nucleation. Alternatively, steps can also be produced by dislocations emerging at the surface, such as screw dislocations [1].

We proceed as follows. First, we discuss the roughening transition. Second, we illustrate the macroscopic equilibrium features of crystals in the absence or in the presence of a substrate. Third, we discuss growth and dissolution morphology and kinetics, and introduce the concept of surface dominated as opposed to diffusion dominated kinetics. Finally, we briefly review the effect of convective flows on free (unconstrained) crystal growth. Throughout the text, connections between macroscopic behaviors and subjacent microscopic features are made.

1.1.1 Roughening transition

The idea that there could be a “roughening” of the interface of a crystal in equilibrium with liquid or vapor at a particular temperature T_R was suggested by Burton, Cabrera and Frank [2]. Microscopically, above T_R the crystal surface is rough which means that many kink sites and steps

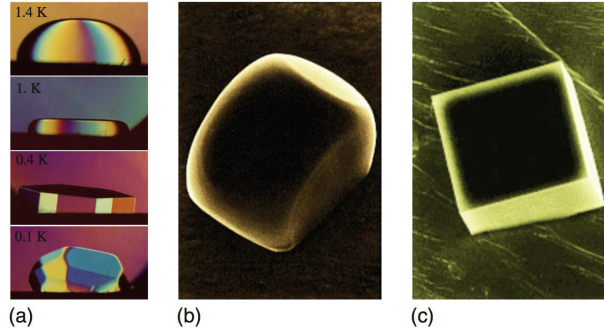


Figure 1.3: Roughening transition. (a) Faceting of He_4 crystal. From top to bottom the temperatures are 1.4, 1, 0.4 and 0.1 K. From Balibar et al. [9]. (b) and (c) NaCl crystal. From (b) to (c) the temperature is decreased leading to the appearance of a faceted shape with an atomically flat surface. From Heyraud and Métois [10]. Reprinted from Misbah et al. [4].

are present on the surface. Below T_R the crystal surface is flat and no thermally excited kinks are available. From a macroscopic point of view, crystals are faceted below T_R and smoothly rounded above T_R [3, 4] (see Fig. 1.3). This is why T_R is called roughening temperature or faceting temperature [1, 5, 6, 7, 8].

To characterize the roughening transition, let us consider a vicinal surface which is a surface misoriented by some small angle θ from a facet direction. The associated free energy projected on the facet orientation is

$$\gamma_s(\theta, T) = f_0(T) + \beta(T) \frac{|\tan \theta|}{h_0} + \mathcal{O}(\tan^2(\theta)) \quad (1.1)$$

with h_0 the step height and $l = h_0/\tan(\theta)$ their average separation. The first term is the free energy per area of the terrace, the second term, $\beta(T)$, is the free energy per length of step formation (edge free-energy). As temperature increases, $\beta(T)$ decreases due to increasing entropy associated with step-edge excitations (via the formation of kinks). Eventually $\beta(T)$ vanishes at T_R .

1.1.2 Equilibrium shapes of crystals

As illustrated in the previous section, the peculiarity of crystal interfaces with respect to liquids or amorphous solids is that the surface free energy γ is anisotropic because surface free energy reflects the underlying symmetry of the crystal lattice. At equilibrium, the crystal molecules will arrange in order to minimize this energy. This corresponds to minimizing the orientation-dependent surface free energy for a fixed volume. We here proceed to a brief review of basic notions in the analysis of macroscopic equilibrium crystal shapes.

The Wulff construction

The problem of the equilibrium crystal shape is habitually solved using the celebrated Wulff construction [11]. Wulff theorem has been proved by different authors [2, 12] and is a powerful tool to predict crystal shapes in absence of external fields such as gravity or interactions with a substrate. The Wulff construction is illustrated in Fig. 1.4. The prescription takes the following form: one begins with a polar plot of the surface free energy (γ -plot) as a function of an orientation angle (or the surface normal) and draws a perpendicular plane (or line in 2D) through the tip of each ray. The equilibrium shape is then formed by the interior envelope of these planes or lines. In 2D the geometrical construction corresponds to

$$r(\hat{\mathbf{h}}, T) = \min_{\theta} \left(\frac{\gamma(\theta, T)}{\hat{\mathbf{m}} \cdot \hat{\mathbf{h}}} \right), \quad (1.2)$$

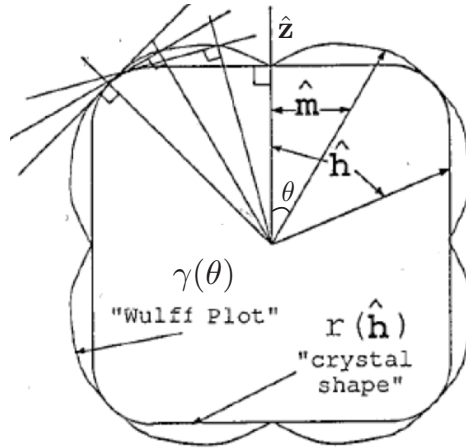


Figure 1.4: Schematic of the Wulff construction. The surface free energy per unit area $\gamma(\theta)$ is plotted in polar form. One draws a radius vector in each direction $\hat{\mathbf{m}}$ and constructs a perpendicular plane where this vector crosses the Wulff plot. The interior envelope of the family of “Wulff planes”, expressed by Eq. (1.2), is the crystal shape up to an overall scale factor. From Pimpinelli and Villain [6].

where $\hat{\mathbf{h}}$ is an arbitrary direction, $r(\hat{\mathbf{h}}, T)$ is a radial vector to the crystal surface, $\gamma(\theta, T)$ is the orientation-dependent surface free energy in the direction of the unit vector $\hat{\mathbf{m}}$ ($\cos \theta = \hat{\mathbf{m}} \cdot \hat{\mathbf{z}}$).

From Eq. (1.1) it can be seen [3] that above the roughening transition ($\beta = 0$ in Eq. (1.1)), the cusps in the γ -plot disappears and there are no facets in the Wulff construction.

Sharp Edges and facets

When the equilibrium crystal shape has a sharp edge or corner, the Wulff construction misses intermediate orientations [3, 6]. The accurate review from T.L. Einstein [3] presents in details issues connected with the Wulff theorem and the strategies developed in the literature to improve the Wulff construction.

Some continuum models, such as phase-field models, often make use of a regularization of the surface free energy when this presents sharp corners. A common strategy is to re-write the surface tensions $\gamma(\theta)$, with θ the angular orientation of the surface normal, as [13, 14]

$$\gamma(\theta) \approx \gamma_0(\theta) + \frac{\beta}{2} \kappa^2, \quad (1.3)$$

where $\gamma_0(\theta)$ is the physical surface tension, and β a parameter representing “corner energy”. This term is proportional to the square of the mean curvature κ , thus penalizes sharp corners. This is called the Willmore regularization in the mathematical literature. The constant β is a small parameter. In the limit $\beta \rightarrow 0$, $\gamma = \gamma_0$ represents the physical surface free-energy.

Another difficulty is that surface free-energy is not differentiable at the orientations corresponding to facets. Indeed as illustrated in Fig. 1.4 and Eq. (1.1), facet orientations are associated, for instance, to a cusp in the surface free-energy. This has important consequences on continuum models that are based on the differentiability of physical quantities. For example, the equilibrium shape Eq. (1.2) can be reformulated using the surface stiffness. In 2D, this leads to $\mu = \Omega_A \tilde{\gamma}$ where the chemical potential μ is a constant, Ω_A is the atomic area, and the stiffness is defined as $\tilde{\gamma}(\theta) = \gamma(\theta) + \gamma''(\theta)$ [1, 15]. Surface stiffness then becomes singular at faceted orientations.

Invoking for example finite size effects which usually prevent a true divergence of physical quantities, a simple ansatz is to assume a finite but large value of the stiffness at facets. Such an ansatz sometimes emerges as a consequence of some specific types of regularizations in continuum models to remove nonanalytic points associated with the presence of cusps. For example, some authors [16, 17] use a surface tension which, in the neighborhood of the facet orientation $\theta \rightarrow 0$,

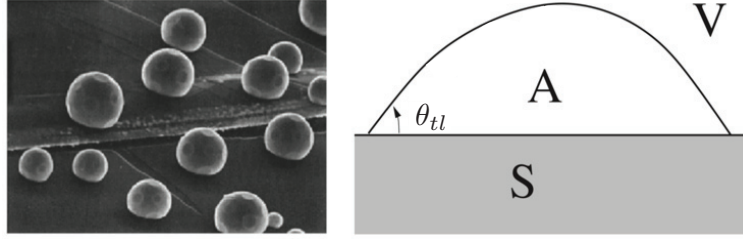


Figure 1.5: Left panel: Experimental image of Au/Graphite. Right panel, schematic of wetting. Reprinted from [15].

takes the form:

$$\gamma(\theta) \approx (\theta^2 + \epsilon)^{1/2}, \quad (1.4)$$

where ϵ is a small parameter. From the definition of stiffness, Eq. (1.4) implies a ratio between surface stiffness and surface tension at facet orientations $\tilde{\gamma}(0)/\gamma(0)$ of order $1/\epsilon$ representing a significant increase of the stiffness. This type of regularization has proven to compare well to other modeling approaches (e.g. step models) and experiments. We will show that our model needs, in some cases, to assume a similar increase in the surface stiffness to allow for good quantitative comparison to experiments (see Sections 4.2.2 and 4.5.4).

A more precise analysis of faceted crystals would require to consider the physics of atomic steps. However, this is beyond the scope of this thesis.

Presence of a substrate and solid wetting

When considering a crystal on a substrate, the new energetic contribution that has to be taken into account is the surface free energy of the crystal-substrate interface. In the absence of facets, the anisotropic Young contact angle condition describing solid wetting in 2D is [15]

$$\gamma_{SV} - \gamma_{SA} = \gamma(\theta_{tl}) \cos(\theta_{tl}) - \gamma'(\theta_{tl}) \sin(\theta_{tl}), \quad (1.5)$$

where, as illustrated in Fig. 1.5, γ_{SV} , γ_{SA} , and $\gamma_{AV} = \gamma$ represent the surface free energy per surface area (surface tension) between the different mediums: A is the crystal island, V is a liquid solution, and S the solid substrate. Assuming that the stiffness $\tilde{\gamma}(\theta) = \gamma(\theta) + \gamma''(\theta)$ is always positive, the condition of partial wetting ($0 < \theta_{tl} < \pi$) is given by

$$-2\gamma(0) < \gamma_{SV} - (\gamma_{SA} + \gamma(0)) < 0. \quad (1.6)$$

If crystal-substrate free energy is sufficiently small as compared to the liquid-substrate one, we thus observe (total) wetting and the crystal spreads on the substrate.

There exist Wulff-type constructions, such as the Kashew [18], Winterbottom, or Summertop ones [19], capable to describe crystal equilibrium in the presence of one or more substrates, and accounting for both wetting or partial wetting scenarios. However, these constructions are possible only for flat and homogeneous substrates. Non-flat substrates often lead to multi-stability (i.e. more than one locally stable shape) [15].

1.1.3 Growth and dissolution kinetics

Reaction kinetics

What follows assumes that a crystal is already present. Thus growth happens by the addition of material on a pre-existing surface. We do not discuss the problem of the nucleation of a seed crystal [20] which is beyond the scope of this study.

The kinetics of precipitation can be divided into the following sequence of steps [21, 22]:

1. Transport of material from the bulk to the surface: governed by diffusion and advection.

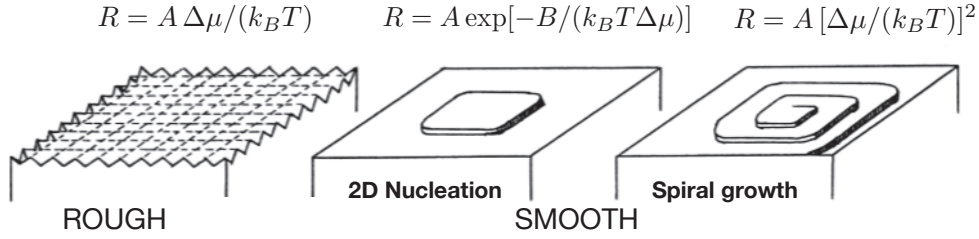


Figure 1.6: Interface structures and three types of growth mechanisms. R , growth rate; $\Delta\mu/k_B T$ driving force (chemical potential difference between solid and liquid phases); A , B , constants. First panel (from the left), growth from a rough surface. Second panel, 2D nucleation growth. Third panel, spiral growth. Readapted from Sunagawa [23].

2. Adsorption of solute to the surface.
3. Surface diffusion toward reactive sites.
4. Integration of the solute at the reactive sites (edges or kinks) by the formation of new bonds.

The reverse sequence would result in dissolution. In general, both the forward and backward sequences occur simultaneously, and the net mass balance leads to growth or dissolution. At equilibrium, the flux of atoms from any step to the next will be completely balanced by the reverse flux so that the net rate is zero. The first step is usually labelled as bulk transport. Processes 2-4, which themselves are an outline of several elementary steps, are called surface processes. What controls the kinetics of crystal growth and dissolution is the slowest among these processes. In this text, we will often refer to the first scenario as a diffusion driven/limited regime and to the second one as a surface/precipitation limited regime or slow surface kinetics.

In free growth, precipitation-limited phenomena are common. However in confinement, transport occurs through a liquid film facing the confined region and is therefore slower than in unconstrained space. As a consequence, diffusion is often the limiting kinetic step. This is a key issue extensively discussed at different places in this thesis report.

Surface controlled kinetics and growth rate laws

The reaction at the surface is driven by saturation ratio $S(t) = \text{IAP}(t)/K_{sp}$ with IAP the ionic activity product and K_{sp} the solubility product [22, 24]. In this thesis, since we assume the dilute limit in the solution, we work in terms of concentration rather than activities. This implies $\text{IAP}(t) \approx c(t)$ where c is the concentration, and $K_{sp} \approx c_0$ with c_0 the solubility. It follows that $S \approx \sigma + 1$, where

$$\sigma(t) = \frac{c(t) - c_0}{c_0} \quad (1.7)$$

is the (relative) supersaturation. The net growth or dissolution rate is often expressed as [21, 22]

$$R_{+,-} = k_{+,-} \sigma^n \approx k_{+,-} \left(\frac{\Delta\mu}{k_B T} \right)^n, \quad (1.8)$$

where R is the net rate (difference between forward and backward reaction rate) normalized by the reactive surface area, the labels $+$ and $-$ refer respectively to growth and dissolution, n is a fitting parameter, k is a kinetic constant, k_B the Boltzmann constant, T the temperature, and $\Delta\mu$ the chemical potential difference between the solid and the liquid solution. The last equality holds only close to equilibrium $c \approx c_{eq} = c_0 \exp(\Delta\mu/(k_B T))$ with c_{eq} the equilibrium concentration, and for small supersaturations, $\exp(\Delta\mu/(k_B T)) \approx 1 + \Delta\mu/(k_B T)$.

The parameter n can be related to the nature of the mechanism of growth and dissolution using models which assume different microscopic structures of the crystal surface. For example, linear response theory corresponds to a microscopically rough surface with $n = 1$, whereas $n \sim 2$

describes growth in presence of screw dislocations by spiral mechanism [21]. Finally, for defect-free facets, growth can be dominated by 2D nucleation of terraces. In this case the overall growth (dissolution) rate is $R \sim \exp(-\beta^2/\Delta\mu k_B T)$ [1, 23, 25] with β the step free energy per unit length. These different laws are summarized in Fig. 1.6. In this work, we will assume the simplest case, namely, the surface growth (dissolution) rate to be linear $n = 1$ with respect to the supersaturation. A more precise modelling should account for the details of the motion of atomic steps. However, as mentioned above, such an approach is beyond the scope of this thesis.

Crossover between diffusion and surface driven growth

Usually, as a rule of thumb, transport processes in the bulk are the limiting one (slowest) for high-solubility materials, while low-solubility materials will be dominated by surface processes. This can be seen with the following hand waving argument. Assuming linear kinetics, the surface growth rate is $R = k\sigma = \nu c_0\sigma$ where ν is a kinetic coefficient with the dimensions of a velocity. Then one has to compare the growth rate, R , to the bulk diffusion flux, $D\nabla c$. This leads to the ratio $(D/\nu)\nabla \ln \sigma$. Hence, the lengthscale of variation of the supersaturation σ , which are associated to the inverse of the gradient, must be compared to the physical lengthscale

$$l_0^f = \frac{D}{\nu}. \quad (1.9)$$

The label f is added to distinguish this length scale, associated to “free” (unconstrained) growth, with the one emerging from confined growth l_0 discussed ahead in this thesis (see for instance Section 2.6). The diffusion constant D at ambient temperature depends essentially on the size of the crystal molecules which in general does not vary of many orders of magnitude for different materials. On the contrary, ν can vary of several orders of magnitude and is usually higher for soluble materials than for less soluble ones (for instance $\nu \approx 10^{-3}\text{ms}^{-1}$ for the very soluble NaCl and $\nu \approx 10^{-5}\text{ms}^{-1}$ for the less soluble CaCO_3). Assuming that the length scale of gradients is fixed by the crystal size, from the above arguments it follows that growth of more soluble materials is more likely to be transport dominated and vice versa.

Finally, we expect that as temperature increases a surface limited reaction will change to a transport limited one. This is due to the fact that bulk diffusion and advection are weakly dependent on temperature, while chemical reactions at the surface exhibit an exponential Arrhenius dependence which would make them much faster at higher temperature [21].

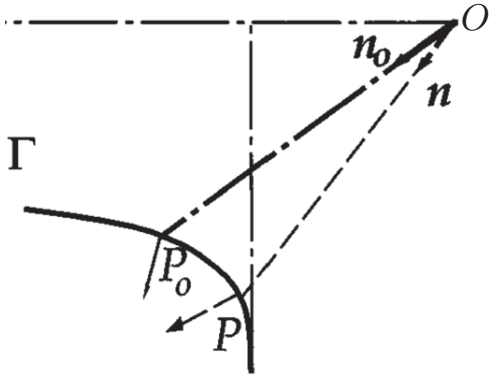
1.1.4 Growth shape

The non-equilibrium shapes emerging during crystal growth depend strongly on mass transport kinetics. We illustrate in the following two main regimes: one in which crystals asymptotically grow compact, and one characterized by morphological instabilities.

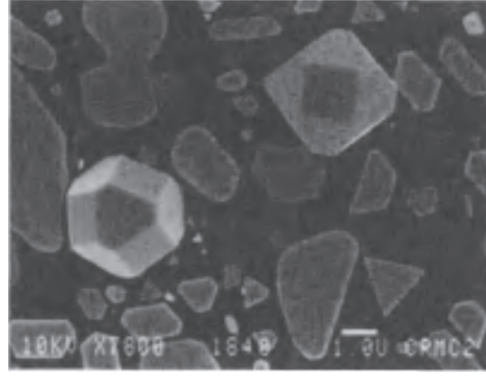
Kinetic limited growth: Frank construction

Frank’s model [6, 26] assumes surface-limited kinetics, where the growth velocity depends only on the local surface orientation. The asymptotic crystal shape within this model can be obtained from a construction similar to the Wulff one. Defining with v_n the normal velocity of a crystal surface, we assume $v_n = \hat{\mathbf{n}} \cdot \mathbf{v}_C(\hat{\mathbf{n}})$, where $\mathbf{v}_C(\hat{\mathbf{n}})$ is a function of the orientation of the surface. The statement of the theorem is the following. Consider the point P defined from an origin O by the relation $OP = \hat{\mathbf{n}}/v_C(\hat{\mathbf{n}})$, where $\hat{\mathbf{n}}$ is the normal to the crystal surface S . Then all points of the surface where the normal is $\hat{\mathbf{n}}$, move along a straight line parallel to the normal in P to the surface Γ spanned by P . The different objects defined in the theorem are represented in Fig. 1.7a.

It has been observed experimentally that crystal growth shapes are often characterized by more pronounced facets than the equilibrium shape (see Fig. 1.7b). Within the framework of Frank model, this can be explained by the very sharp minima usually found for $\mathbf{v}_C(\hat{\mathbf{n}})$ around slow growth orientations [6].



(a) Illustration of Frank's theorem as reported by Pimpinelli and Villain [6]. The vectors $\hat{\mathbf{n}}$ and $\hat{\mathbf{n}}_0$ are relative to two different surface orientations, Γ is the surface spanned by P defined by $OP = \hat{\mathbf{n}}/v_C(\hat{\mathbf{n}})$ where $v_C(\hat{\mathbf{n}})$ is the orientation dependent interface velocity of the crystal.



(b) Growth shapes of lead crystals near 120°C as reported by Heyraud and Métois [10]. Facets appear sharper than in equilibrium. Comparing the Wulff and Frank constructions, this suggests that the anisotropy of the kinetic coefficient is stronger than the anisotropy of surface tension.

However, two essential physical ingredients are absent from Frank's model: diffusion near the surface and surface tension effects. These two ingredients affect the local growth rate and can therefore lead to a breakdown of the validity of Frank's construction. In the case of growth, as illustrated in the following, diffusion near the surface is responsible for the appearance of instabilities.

Diffusion limited growth: the Mullins-Sekerka instability

The Mullins-Sekerka instability has been originally introduced in the context of growth from a melt of a solidification front advancing with velocity v into an undercooled melt [6, 27, 28]. However, since a parallelism can be drawn between thermal diffusion and diffusion induced by concentration gradients, the instability also applies to (diffusion driven) growth from solution.

Let us consider a 1D solidification front advancing with velocity v along z and a generic diffusion field u which can be governed by chemical potential (concentration) gradient or temperature gradient. The diffusion equation for the liquid facing the solid is

$$D\partial_x^2 u + v\partial_z u = \partial_t u. \quad (1.10)$$

Linear stability analysis considers solutions in the form of a small perturbation of the solid-liquid interface $z = \zeta$,

$$\zeta(x, t) = \hat{\zeta}_k e^{ikx + \omega_k t}, \quad (1.11)$$

where k is the wavenumber and ω is the angular frequency. In the stationary case $\partial_t u = 0$, assuming no coupling between temperature gradient and chemical potential (pure thermal driven or chemical driven system) and considering proper boundary conditions, one obtains a dispersion relation in the form [28]

$$\omega_k \approx kv - \beta k^3. \quad (1.12)$$

The parameter β is a constant proportional to the surface tension which has a stabilizing effect. Positive values of ω_k lead to a divergence with time of the corresponding amplitude. From the definition $k = 2\pi/\lambda$ where λ is the wavelength of the perturbation, Eq. (1.12) indicates that the instability appears at some finite wavelength corresponding to the maximum of ω_k . A sketch interpreting Mullins-Sekerka instability as a point effect is presented in Fig. 1.8.

This type of instability is at the origin of fascinating spontaneous pattern formation observed in nature such as dendrite growth (see Fig. 1.1) [28] or, for strongly anisotropic crystals, hopper growth [29].

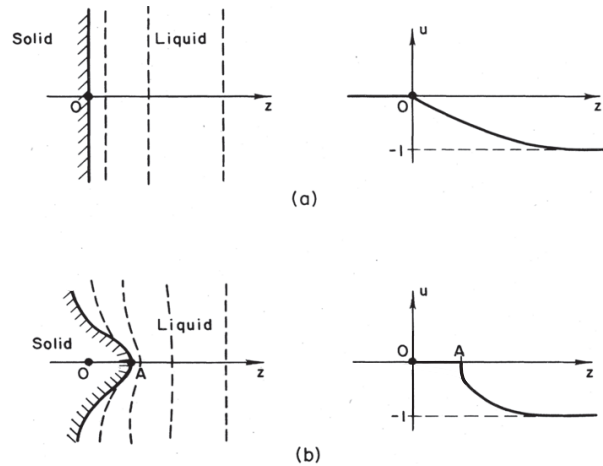


Figure 1.8: Schematic illustration of the Mullins-Sekerka instability as reported in [28]. The right panel represents the corresponding dimensionless diffusion field which can generally be concentration or temperature driven. Top panel: stable growth. Bottom panel: unstable growth (in the absence of surface tension). The point A steepens the diffusion field ahead of it resulting in a higher entering flux of particles and a consequent faster growth.

1.1.5 Effect of flows

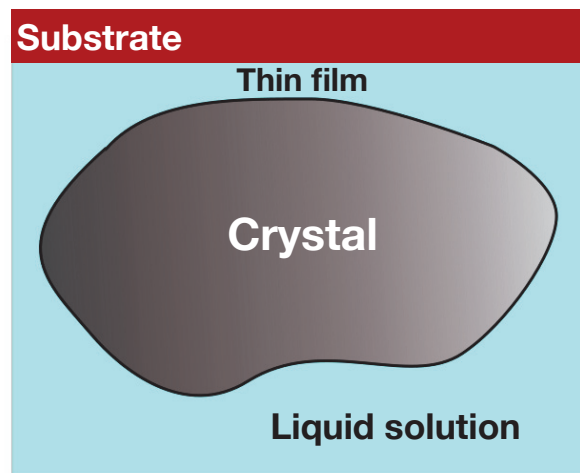
As a final point on the standard theory of free-growing crystals, it is important to mention the effects of flows. Flows can be due, for instance, to density changes, temperature differences in the solution (buoyancy-driven convection), or to external stirring. Even when these effects are neglected, liquid flow can be generated by crystal growth itself [30]. Let us consider a crystal growing with a flat interface. In the reference frame where the interface is immobile, the solid moves with growth velocity u_C . From the conservation of mass, the liquid velocity must move towards the interface due to crystal growth with a velocity $u_{Ln} = u_C n \rho_C / \rho_L$, where ρ_C and ρ_L are the density of the crystal and of the liquid solution, respectively [30] (see also Eq. (2.3)). This flow perpendicular to the interface will affect the growth rate [31] because it transports additional growth units to the interface via advection.

Another type of flow is the one parallel to the interface. In free growth, this is usually due to external stirring or external gradients and buoyancy effects. Parallel flow can be responsible for morphological instabilities such as the appearance of step bunches [32].

In general, when assessing the importance of the effects of flows over instabilities and local growth rate, one should consider a characteristic distance where transport due to hydrodynamic flows is comparable to diffusion transport. In free growth, this length scale is called the boundary layer thickness and is generally defined as the distance from the interface to a point where the flow velocity has essentially reached the free stream velocity. The specific definition of the boundary layer changes depending on the system considered and its precise calculation can be quite involved. In general, we expect mass transport due to liquid flow to be relevant at distances from the crystal interface larger than the diffusion boundary layer. A simple dimensional analysis allows for an estimation of this length scale $l_{BL} = D/u_L$. In confined growth problems, this distance is usually significantly larger than the typical scales emerging in the confined region (see for instance the discussion section of Chapter 4). This is why effects of hydrodynamic convection and stirring are usually discarded in most models of confined growth.

We will see in the next section that in lubricated contacts a flow parallel to the liquid-solid interface is induced by the rigid motion of the solid. However, we also show in Section 2.4 that in the lubrication expansion and in the dilute limit which will be used in this thesis, the consequences of advection of the concentration c by the flow are negligible. The only remaining effect of the flow will be in the global force balance on the crystal via viscous dissipation.

Figure 1.9: Sketch of a generic confined growing/dissolving crystal from solution.



1.2 Thin films

When crystals grow or dissolve in confinement (see Fig. 1.9) a thin liquid film can be present between the crystal and a confining wall. Hydrodynamics effects alone, i.e. without considering dynamical reshaping of the surfaces, lead to non-trivial laws associated with viscous forces when the distance between the crystal and the substrate is changed.

When film thickness becomes of the order of tens of nanometres surface-surface interactions will come into play. The most common interaction model between surfaces in a liquid is the DLVO theory which includes an electrostatic repulsion known as double layer repulsion. However, at shorter separations (below 3, 2nm) important deviations from the double-layer repulsion are observed. These effects, are usually associated with the so-called hydration forces.

Confinement-induced changes in the structure of the liquid at the nanoscale are also related to important effects on the transport properties (diffusion and viscosity) in the film.

In confined crystal growth or dissolution a thin liquid film of solution can be present allowing transport of solid units [33, 34, 35, 36]. In physics and biophysics thin films typically appear in the tribology of lubricated contacts such as bearings and animal joints, foam dynamics, nanoscale dewetting [15, 37, 38, 39] and nanofluidics [40]. They are rich physical objects described by highly nonlinear evolution equations leading to a variety of dynamical phenomena. A review of the type of equations and fascinating dynamics governing thin films was written by Oron et al. [41]. We will resort to similar approaches (lubrication limit) as those widely employed in thin films hydrodynamics to develop our model.

However, we here wish to focus on the physical properties of thin films between two surfaces in the absence of growth (dissolution). First, we discuss standard hydrodynamics of squeezed films. These films are known to have bearing properties strongly dependent on geometry and dimensionality. Second, the presence of liquid between mineral surfaces or salts induces electrostatic repulsion. When the thickness becomes of the order of tens of nanometers, this electrostatic force usually combines with van der Waals interactions. We therefore introduce some of the theories describing these interactions (disjoining pressures). Finally, we describe some of the phenomenology arising when the separation is reduced down to the nanoscale leading to effects both on the interactions between surfaces and on transport in the film.

1.2.1 Lubrication and bearing

Hydrodynamics of thin films has been studied for decades by the engineering and applied mathematics communities as a part of the field of research known as *tribology*. The development of

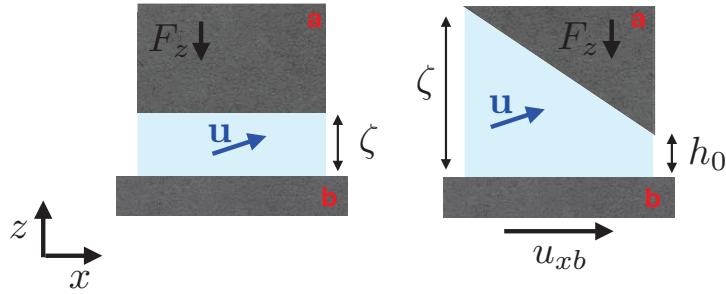


Figure 1.10: Sketch of a squeeze film bearing (left panel) and of an inclined slider bearing (right panel) projected on the $x - z$ plane. In the trust bearing case, the bottom plane slides with velocity u_{xb} .

this field was motivated by the need for gaining a better understanding of the mechanism of lubrication, friction, and wear of moving or stationary parts. In this context, the slenderness of the film can give alone (without considering interactions between surfaces) effective forces through viscous dissipation which resists to squeezing and suction of the liquid caused by the relative motion of the solids [42].

Without considering hydrostatic bearings, which are externally pressurized, hydrodynamic lubrication supports a normal load in two ways:

- i Squeeze film bearing: left panel of Fig. 1.10. The flow is induced only by the relative vertical motion of the surfaces.
- ii Slider bearing: right panel of Fig. 1.10. A stationary flow is also produced by sliding one surface.

The general differential equation governing the pressure distribution in fluid film lubrication is known as the Reynolds equation:

$$\nabla_{xy} \cdot \left(\frac{\rho_L \zeta^3}{12\eta} \nabla_{xy} p \right) = \nabla_{xy} \left[\frac{\rho_L \zeta (\mathbf{u}_{xya} + \mathbf{u}_{xyb})}{2} \right] + \partial_t (\rho_L \zeta), \quad (1.13)$$

where the labels a and b represent the two surfaces, xy refer to vector components on the plane of the bottom surface, \mathbf{u} is the liquid velocity with \mathbf{u}_{xya} and \mathbf{u}_{xyb} the in-plane velocity at the solids interface (no-slip condition), ζ is the distance between the surfaces, p is the pressure, ρ_L is the liquid density, and η the liquid viscosity.

In this type of problems, the shape of the surfaces has a fundamental role in determining the load as a function of the separation both in the squeeze film and slide bearing cases. A standard example are hydrodynamic squeeze bearing. For instance, in the case of a circular plate approaching a parallel plane (such as, considering the projection along the radius, the left panel of Fig. 1.10) the normal load is [42] $F_z \sim 1/\zeta^3$, i.e. no touching contact can be observed at a finite load. Similarly, in a fixed inclined slider bearing (represented in the right panel of Fig. 1.10) when considering flow in a single dimension (1D) the minimum separation decreases exponentially with the load [42], $h_0 \sim \exp(-F_z)$, but h_0 never vanishes, i.e. there is no touching contact. However, in the former, when the approaching surface has a parabolic contact, the divergence in the load reduces to $\sim 1/\zeta^{3/2}$, whilst in the latter, when including the flow in the transverse direction (2D problem), contact can be reached with a finite load.

In the context of this work two questions linked to lubrication in bearing surfaces are interesting for us: First, how is this picture changing when surfaces are dynamical objects such as dissolving or growing crystals, i.e. which can change shape in time; second, what happens when there is an interaction (*disjoining pressure*) between the surfaces.

1.2.2 Disjoining forces between surfaces in liquid

Thin films can be formed, maintained, and stabilized by surface-surface interactions acting at the nano-scale [35] (tens of nanometres separation [43]). These forces globally are referred to as

disjoining pressures.

The generic model to describe interactions between surfaces in water is the Derjaguin-Landau-Verwey-Overbeek (DLVO) continuum theory [44] which combines a (usually) repulsive electrostatic force and a (usually) attractive van der Waals force. This theory was first used to study colloidal interactions [45].

Charging of the surfaces in a liquid is due to ionization of surface groups or to adsorption of ions from the solution. The electrostatic repulsion originates from a diffuse atmosphere of counterions forming close to the charged surface. This rearrangement of charges is called the *electrical double layer*. The electric diffuse double layer has a characteristic thickness known as Debye length, λ_D . The repulsion arising from the electrical double layer for two planar surfaces and low surface potential is

$$E_{DL}(d) \approx \frac{2\sigma_q^2 \lambda_D}{\varepsilon} e^{-d/\lambda_D}, \quad (1.14)$$

where E is an energy per unit area, d the separation between the surfaces, σ_q the surface charge density (assumed equal on each surface) and ε the permittivity. The value of the Debye length is strongly dependent on electrolyte concentration and pH in the liquid solution and can range from a few to hundreds of nanometres [43].

Van der Waals interactions emerge from the combination of polarization induced interactions such as Debye-induction and Keesom-orientation forces, and London-dispersion forces. London dispersion forces are always present (even between neutral bodies). In the case of two surfaces facing one another van der Waals interaction energy (per surface area) assumes the form

$$E_W(d) = -\frac{A}{12\pi d^2}, \quad (1.15)$$

where A is the Hamaker constant. The Hamaker constant in a medium can be related to the susceptibility using Lifshitz theory and is usually of order $A \sim 10^{-20}$ J [43].

The sum of these two contributions, $E(d) = E_{DL}(d) + E_W(d)$, is the DLVO interaction potential which can assume a variety of forms: long-range repulsion, primary (adhesion force) and secondary minimum separated by an energy barrier, or purely attractive. The exact form depends strongly on the surface charge density and electrolyte concentration. This variety of behaviors is illustrated in Fig. 1.11a.

However, the DLVO theory is a nonspecific continuum theory that does not take into consideration the discrete molecular nature of the surfaces, solvent, or ions, and other factors that can become important at small distances.

SFA and AFM measurements and non-DLVO forces

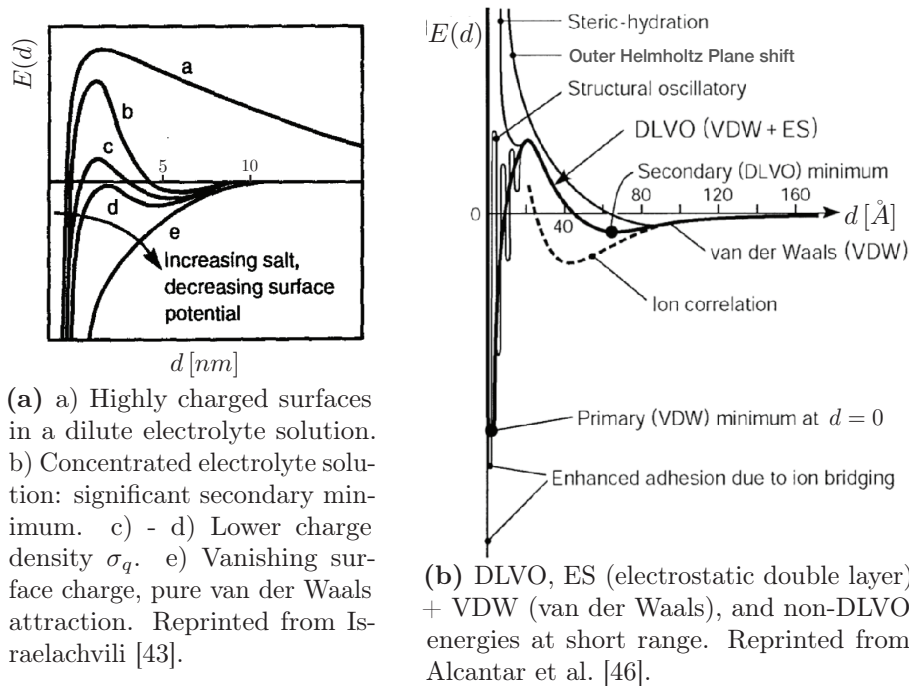
The DLVO theory performs well for dilute electrolyte solutions and smooth surfaces. However, significant deviation from DLVO can be observed at small separations (<3 nm) [43]. These additional non-DLVO forces have been found to depend on the specific nature of the surfaces, the solvent, the ions in the solvent, and the ions adsorbed on the surfaces and can be both repulsive or attractive [46, 47, 48, 49].

Different techniques can be used to probe experimentally interactions between surfaces. The most widely employed are Surface Force Apparatus (SFA) and Atomic Force Microscopy (AFM). SFA is an experimental technique which allows for direct measurement of force as a function of the distance between two surfaces with Angstrom resolution. This technique consists in approaching surfaces immersed in a liquid towards each other and measures forces using a spring connected to one of the surfaces [43, 46].

AFM is a technique based on the measure of the deflection of a cantilever connected to a tip raster scanning the surface of a solid. This device can be adapted to measure forces between surfaces substituting the tip with a colloidal probe [48, 49, 50].

Using SFA or AFM different authors reported significant deviations from DLVO at small surface separations. In particular short-range repulsive forces have been observed and associated with the presence of a structured layer of water molecules at the surface. The overlap of these

Figure 1.11: Left panel: Different forms that DLVO interaction potential can take depending on surface and separating liquid properties. Right panel: Non-DLVO disjoining forces.



hydrated layers gives rise to short-range repulsions which are commonly referred to as hydration forces. A detailed review of hydration forces and their possible origin was written by Valle-Delgado et al. [48]. Other deviations from DLVO include attractive ion-correlation and depletion effects, extensively discussed in the literature [46]. For illustrative purpose we show in Fig. 1.11b a summary of the type of behaviors that could be observed at small separations as reported in [46].

1.2.3 Transport properties

Modeling the forces induced by viscous dissipation (as discussed for instance in Section 1.2.1), the SFA technique has also been used to measure the viscosities of liquids in molecularly thin liquid films. From these experimental measurements, the viscosities of pure water and salt solutions were found to be essentially the same as in bulk, for films as thin as 20 \AA .

However, when the film thickness decreases further a higher effective viscosity is measured. The increase of the viscosity coefficient is found to be 20% to 60% higher than its bulk value and the effect is found to be maximal when the film thickness is comparable to the Debye length, λ_D [51, 52]. This higher apparent viscosity is in general associated to the movement of the diffuse ions in the electrical double layer. This results in a streaming current inducing flow of ions in the opposite direction as opposed to the main flow [51, 53]. This phenomenon is referred to as *electro-viscous* effect. The continuum description of the electro-viscous effect via electrokinetic models (coupling electrical double layer and fluid flow) has brought insight in nano-transport phenomena, allowing one to discuss the role of fluid properties [54] and irregular walls [55].

However, substantial quantitative discrepancies between experiments and theory are rather common, in particular for nanochannels [56]. Indeed, even though it is recognized that nanoconfinement affects transport coefficients, novel experimental observations [56] suggest better quantitative agreement with models based on local effects (near the charged substrates) of the electric field on the viscosity [57].

Similarly, the diffusion coefficient can be affected by confinement. Indeed, molecules and colloidal suspensions in micro and nano-channels [40, 58, 59] can exhibit effective diffusion coef-

ficients significantly smaller than their bulk values. This effect depends strongly on the charge, the ratio between the size of the molecule and channel size, and channel shape [60]. Also in this case, however, difficulties in experiments and in the theoretical description are encountered. For instance, a recent work suggests that the current theoretical approaches cannot account for the observed phenomenology since the drops in diffusivity of neutral and charged nano-confined molecules were found to be similar [59].

Overall, it is difficult to extract reliable numbers from the literature for confined liquids. We will, therefore, use bulk values for viscosity and diffusivity in our model, but keep in mind that these values could be affected by confinement in the discussion.

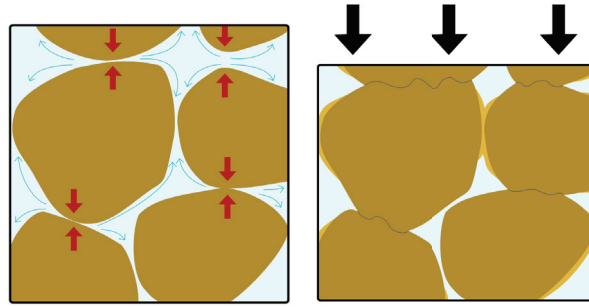


Figure 1.12: Schematic diagram of pressure solution in a clastic rock (rock formed by fragments of pre-existing minerals). Left panel: before compaction. Blue arrows indicate the flow of particles in solution. Red arrows indicate areas of maximum stress at grain contacts. Right panel: after compaction. In light colored areas new mineral growth leads to reduced pore space. By Woudloper [Public domain], from Wikimedia Commons.

1.3 Confined growth and dissolution in geology

Geology provides many natural instances of confined crystal growth and dissolution, where the coupling between the phenomena presented above – namely, growth and dissolution kinetics (mass transport and attachment), thin film hydrodynamics and disjoining pressure between surfaces – realize in practice. In particular, examples of confined growth and dissolution include respectively salt weathering (crystallization force) and rock diagenesis and compaction (pressure solution).

In this section, we focus on recent experimental results on pressure solution and on the force of crystallization. The picture emerging from experiments is that these phenomena are still not completely understood. Indeed the dispersion of the results and the interpretations are wide.

Crystal dissolution by the effect of an external load is commonly referred to as pressure solution. Pressure solution is considered a key aspect to describe the deformation and compaction of sediments and sedimentary rocks (see Fig. 1.12). It plays a determining role in diagenetic densification, porosity and permeability evolution in sedimentary basins [34, 61, 62, 63], and the development of stylolites (irregular planes of discontinuity between two rock units) [64, 65, 66, 67, 68].

Crystal growth in confinement is a ubiquitous phenomenon found in pores, faults, or gaps, of rocks and natural or artificial cement. In biomineralization - the process by which living organisms grow minerals - confinement also plays a key role to control the shape and phase of nano-crystals [69, 70, 71], and combines with the chemical environment [72] to govern microstructure formation in, e.g., bones or dentine. Constrained growth may cause large forces such as in salt weathering [73, 74, 75, 76], in the opening of veins in the Earth's crust [77, 78], or in frost heave [79, 80]. This is why this phenomenon is commonly referred to as crystallization force. Beyond its relevance for natural environments, motion produced by confined growth can be used in technological applications such as nanomotors [81].

During dissolution or growth in confinement, contacts play a major role. While growth and dissolution can occur at the free surface away from the contacts via bulk transport of growth units, growth in the contact regions requires mass transport along the interface between the crystals or between the crystals and a substrate (pore wall) [34]. The presence of a liquid film in the contact is, therefore, a key ingredient to allow for such mass transport during solution growth, as discussed extensively in the literature [33, 35, 36, 82].

1.3.1 Pressure solution

Pressure solution is a water-assisted dissolution process driven by stress-induced chemical potential gradients. This phenomenon is characterized by the three-step process of dissolution of solid

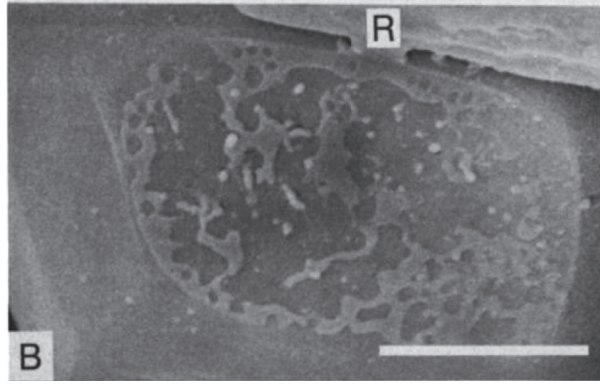


Figure 1.13: Ridge and plateau structure and isolated flat-bottomed pores on the exposed surface of a grain-to-grain contact. Reprinted from Cox and Paterson [83].

minerals at grain contacts, diffusion of solutes along the grain boundaries and reprecipitation at free surfaces [46, 61, 62, 82].

Most experimental studies have focused on the determination of the strain compaction rate in grain compaction experiments. Many authors fit the data according to power law relations between applied load and grain size and strain rate

$$\dot{s} \approx p^\alpha d^{-\beta}, \quad (1.16)$$

where \dot{s} is the strain rate, d is the grain diameter and p the external stress. The strain rate can be expressed as $\dot{s} \sim v_z/(R_c)$ with v_z the dissolution rate and $R_c \sim d$ the grain contact size representing a reference length [84]. Different authors report α ranging between 1 and 3 and β close to 1 or 3 [61, 63, 68, 84, 85]. According to a number of models, the values of these exponents could be traced back to the limiting rate process, with $\alpha = 1$ and $\beta = 3$ in diffusion limited scenarios and $\beta = 1$ with $\alpha \geq 1$ in the case of precipitation/dissolution limited rate (surface kinetics is the slowest process) [61, 62, 86].

However, the dispersion of the experimental results is important and different authors disagree on the interpretations. For instance, it is argued that geometrical considerations (aggregate structure/porosity) might lead to misinterpretation of the exponents [87]. Another important issue is the value of the effective diffusion constant in confined films which is assumed by some authors up to 5 orders of magnitude smaller than in bulk [82, 88] whereas recent studies do not support such large reduction [59, 89]. Furthermore, despite the widespread use of Eq. (1.16), as underlined by Croizé et al. [84], the dependence on the strain rate on stress is rather weak in most of the experiments. Globally the kinetics of the phenomenon remains poorly understood since the specific rate-controlling processes are not well known at the scale of the contact [61].

As far as contact morphologies are concerned, the problem appears more complex and less understood. The general observation is that complex contact morphologies – rough or labyrinthine contact regions – can be observed on the grain to grain contact surfaces after undergoing pressure solution [68, 83, 85] (see Fig. 1.13). In particular, the characteristic length scale of contact island on the crystal interface was found to increase during pressure solution with time to the power 1/3 [90]. Such complex morphological evolutions could have an effect on the measured strain rates. Interesting morphologies are also found at larger scales when looking at stylolites [64, 68] and have been correlated to the value of localized stress induced dissolution [65, 66]. Morphological instabilities of non-hydrostatically stressed surfaces can be due to the Asaro-Tiller-Grinfeld type instability. This instability is controlled by a competition between elastic strain relaxation that favor a roughening of the interface and a stabilizing force due to surface tension. Such stress-induced instabilities are a general problem encountered in various circumstances in physics and geophysics and have been investigated in different studies [67, 91, 92].

However, in this thesis, we do not discuss such type of morphological instabilities which involve elastic effects. Instead, we focus on the consequences of disjoining pressures, mass transport kinetics, and hydrodynamic flows at lubricated contact.

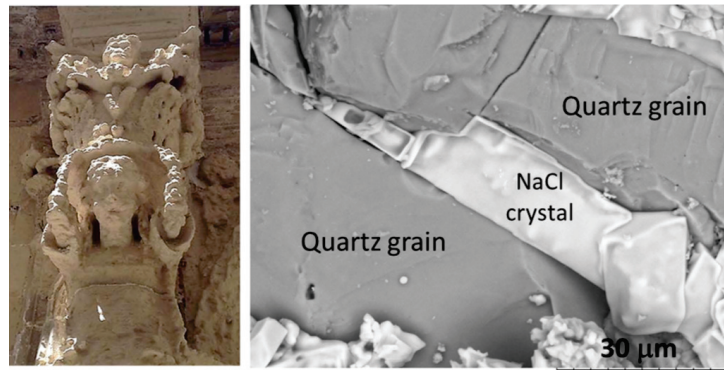


Figure 1.14: Left panel: Degradation of a historical stone sculpture (Lecce, Italy). Right panel: SEM image of a NaCl crystal (white) in the pore space of sandstone after evaporation of the salt solution. Reprinted from Désarnaud et al. [93].

1.3.2 Crystallization force

Salt crystals growing in confinement under supersaturated conditions exert a crystallization force against their host material, subjecting them to stresses (see Fig. 1.14). This phenomenon was first reported in 1853 by Lavalley [94]. Later, it was discussed in the seminal papers of Becker and Day [95, 96] and Taber [97] (see Fig. 1.15), and was quantified for the first time by Correns and Steinborn [98].

Recently, crystallization pressure has attracted renewed attention since it has been recognized as a major origin of the weathering (alteration and deterioration) of both natural and anthropogenic materials (buildings, tunnels, historical monuments) [73, 75, 99, 100]. Some theoretical models were able to correlate the normal stress exerted by a crystal growing within an idealized crack to the opening of the crack [101].

However, the *direct* measurement of the force exerted by a growing crystal in confinement is a challenge, as demonstrated by the small number of experimental results reported in the literature [76, 93, 98, 102].

Some recent laboratory measurements showed that crystallization forces can be very high (above 10^2 MPa) and can exceed the tensile strength of stone [76, 93]. The experimental setups are different but are all characterized by a crystal confined between two plates (like in the Correns or Becker experiments) [93, 102] or in a pore (nano-tube) [76]. One of the main difficulties of these experiments is that it is not always possible to reach high supersaturations due to heterogeneous nucleations on the surface [102]. Most studies have focused on how different salts could be more or less effective as damaging agents [76, 100]. Other authors have suggested to reformulate this question in terms of the dependence of double-layer repulsion strength on materials and liquid film properties [93].

A possible strategy which has been considered in order to decrease crystallization pressure is to use hydrophobic coatings. These prevent the formation of the liquid film between the pore wall and the growing crystal thus interrupting ions transport and precipitation [35, 93].

Another phenomenon relative to confined growth that was reported in Becker and Day [95] and Taber [97] experiments, is the formation of a rim on the confined surface of the growing crystal. The formation of the rim is an out of equilibrium effect which dynamically alters the contact area during confined growth, as recently observed with great detail using high-resolution microscopy [104, 105, 106]. An example of rim observation is shown in the right-hand side of Fig. 1.15. The details of the geometry of the rim are still not well understood and characterized and could have implications on the crystallization pressure.

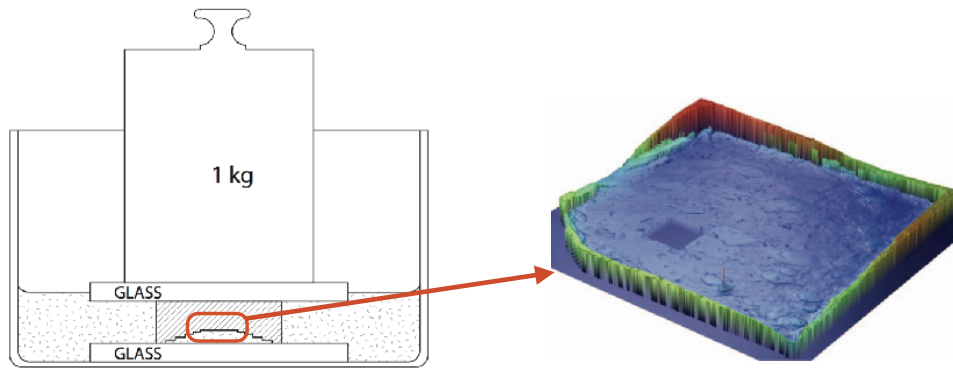


Figure 1.15: Left-hand side: simplified sketch of the setup of Becker and Day experiment [95, 96]. Right-hand side: an example of a rim on the confined interface of a NaClO_3 crystal measured after growth under 200g loading. The topography of the surface was obtained by white light interferometry. Figure realized combining images from [103].

1.4 Models of confined growth and dissolution

Whilst a fundamental understanding of the thermodynamics of crystallization in pores has been achieved [35, 89], the dynamical non-equilibrium processes behind pressure solution and crystallization force are still poorly explored.

Promising recent models able to overcome these challenges have been based on molecular dynamics simulations and kinetic Monte Carlo techniques. However, these approaches do not have access to the large temporal scales involved in geophysical problems or experiments.

Following the seminal model of Weyl [33], many continuum models have been proposed especially to describe compaction creep laws in pressure solution.

In general, a systematic limitation of the existing continuum models, both for pressure solution and crystallization force, is the absence of microscopic description of the interactions, hydrodynamics in the liquid film and effects of surface tension. A second limitation is that many approaches rely strongly on equilibrium thermodynamics.

We here review some of the existing modeling approaches used at different scales to address the problem of confined crystal growth and dissolution. We proceed in order of spatiotemporal resolution: From atomistic approaches (Molecular Dynamics) and mesoscale techniques (Kinetic Monte Carlo), to continuum models.

Particular emphasis is dedicated to continuum models treating the problems of pressure solution and crystallization force discussed in the previous section. We also discuss the Weyl model focusing on the properties of the rim at the confined surface of a growing crystal.

1.4.1 Nano-scale: molecular dynamics simulations

Even though it is well known that variations in the transport coefficient can be observed in narrow channels, precise quantitative assessment and understanding of the phenomenon are still not achieved in experiments. Indeed experiments become difficult when approaching liquid film thickness of the order of the nanoscale [40, 59]. Atomistic simulations constitute an important tool to compute effective parameters such as viscosity and diffusion constant in confinement. They also allow one to describe new phenomenology where continuum approaches break down [40, 107], for example when a reduced film thickness implies the reorganization of molecules in few layers [48].

For instance, molecular dynamics studies (MD) have investigated transport properties in liquid films down to a thickness of about 2\AA in smooth pores [108]. More recently, MD techniques were used to elucidate the mechanisms intervening in short-range interactions between surfaces in water [109, 110]. Another recent work revealed the sensitivity of water-mediated calcite

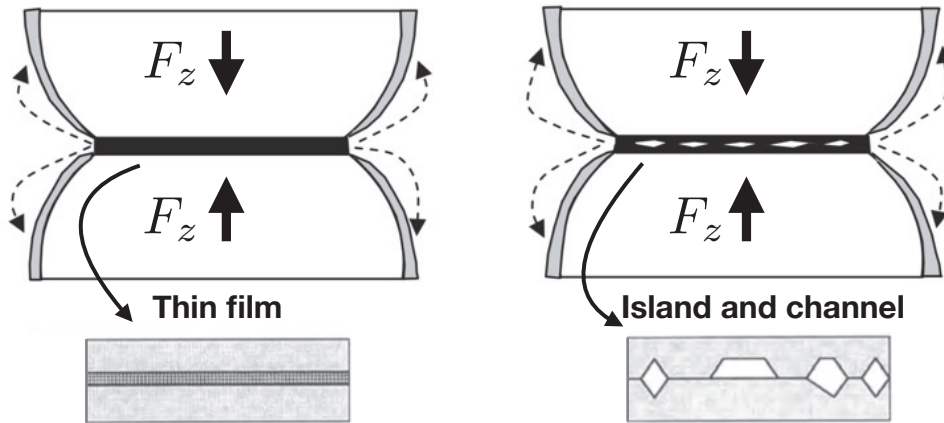


Figure 1.16: Models of intergranular pressure solution. Materials are dissolved at stressed grain contacts and transported via grain boundary. This boundary is a liquid film (“thin film” models) or a dynamic network of contacts and channel (“island and channel” models). Figure produced combining images from Zhang and Spiers [61] and de Meer and Spiers [62].

and aragonite surface interactions with respect to the topography of the surfaces at sub-nano confinement [111] and found important effects when these surfaces are shifted out of registry.

Molecular dynamics studies have been also used to directly address the problem of confined growth at reduced separations. Effects of confinement on crystallization were reported by Bresme and Cámara [112, 113]. These studies proved that crystallization can be induced by confinement itself (inducing significantly higher melting temperature). In addition, they showed that crystallization events cause forces on the pore walls.

1.4.2 Meso-scale: Kinetic Monte Carlo models

Kinetic Monte Carlo models (KMC) [114] have been developed extensively to describe surface morphology during growth and dissolution of free (non confined) crystal surfaces. They participated in achieving fundamental understanding of the roughening transition, kinetic roughening (dynamical non-equilibrium roughness produced by statistical fluctuations), morphological instabilities (such as mounds [115] and step meandering [116]), and effects of impurities (e.g. step bunching), as extensively discussed in the literature and in text books [1, 6, 8, 114, 117]. The development of KMC models is still an open field of research and recent works include for instance the detailed characterization of dissolution morphology and spatial distribution of reactive sites on the surface of different minerals [118, 119]. In the context of biophysics, a recent work used Monte Carlo techniques to address the effect of a confining membrane on the shape of a growing interface in 1D [120] revealing a rich phenomenology with smooth and rough interfaces and different scaling behavior depending on model parameters. However, as far as confined crystal dissolution and growth are concerned, Monte Carlo approaches are seldom used. We are only aware of the recent work from Høgberget et al. [121] which uses an SOS (solid-on-solid) KMC model which includes effective interactions between surface crystal molecules and a confining wall. This model is a very promising strategy to tackle confined growth/dissolution at the mesoscale and could give information on crystal growth morphology in confined geometries. However, some current limitations of this approach are that the system considered is 1D, that hydrodynamics in the film is not included and that the model does not account for the solute diffusion in the thin film. However, some of these questions are under current investigation at the University of Oslo [122].

1.4.3 Macro-scale: continuum modeling

Pressure solution creep models Most of the models proposed at the continuum scale were developed to describe pressure solution and grain compaction. If we exclude the possibility of

micro-cracks on the surface (grain-boundary model [123]), and grain boundary filled with clay platelets [62, 88], two main families of models of grain contact structures have been proposed: The thin film models and the island and channel models (see Fig. 1.16).

In the thin film models, the grain contacts are assumed to consist of a thin water film trapped inside contacts which cannot be squeezed out by the applied stress. The island and channel model assumes that both solid contacts and water channels are present within the grain boundary. In both models, water between the grain contacts is important to dissolve solid minerals and to transport material out of the contact areas [46, 61]. Both models derive very similar creep laws to describe the compaction problem [62, 63, 82, 87, 124]. These type of laws are in the form

$$\dot{s} \sim D_e \frac{p}{d^3}, \quad (1.17a)$$

$$\dot{s} \sim k \frac{p}{d}, \quad (1.17b)$$

where \dot{s} is the strain rate defined in Section 1.3.1, p the external pressure, d the grain size, D_e an effective diffusion constant (proportional to the film thickness in thin film models) and k is a precipitation/dissolution rate constant. The first equation is valid in the case of a diffusion limited process whilst the second is for a surface driven process.

Due to the slenderness of the film, most of the authors assume the diffusion limited scenario Eq. (1.17a). However, as suggested by different experiments [46, 63], in certain systems pressure solution could be limited by surface kinetics (Eq. (1.17b)).

While Eq. (1.17b) is linear in p , nonlinear dependencies with the applied stress are also proposed in the literature [62] for the surface limited process when assuming a nonlinear surface reaction kinetics (see Section 1.1.3). Other modeling approaches also consider the effect of plastic deformations on the creep laws. An important work in this regard is the model developed by Revil [89]. However, these models systematically lack microscopic physical ingredients such as viscosity, disjoining pressure, and surface tension.

An interesting approach has been recently proposed on the different but related problem of particle engulfment [125, 126], i.e. the inclusion or not of foreign particles in a solidification front. This model accounts self consistently for microscopic interactions, force balance, hydrodynamics, diffusion and heat transfer through a numerical finite-element method (FEM). In our opinion, this is a very promising modeling strategy that could be extended to the problem of pressure solution. However, a limitation of these studies is the important computational effort needed to solve the coupled 3D hydrodynamics and diffusion problem.

Crystallization force As first reported by Correns and Steinborn [98] for a macroscopic crystal in a dilute ideal solution the *equilibrium* crystallization pressure is given by

$$P_{eq} = \frac{k_B T}{\Omega} \ln(1 + \sigma), \quad (1.18)$$

where σ is the (equilibrium) supersaturation (Eq. (1.7)), Ω the molecular volume of crystal type molecules, k_B the Boltzmann constant, and T the temperature.

Relevant work on the thermodynamics of crystallization pressure has been performed in the literature and goes beyond Eq. (1.18) accounting for ionic number and non-ideal solutions (chemical activities) [127], the contribution of surface tension effects for microscopic crystals and coupling with pore geometry [35, 128], and pore deformation and size distribution [129].

It is often stated that the equilibrium theory sets the upper bound to the crystallization pressure in the limit that the disjoining pressure between surface and pore wall can sustain it [35, 93, 99]. However, it is not clear if and how the equilibrium expression Eq. (1.18) is applicable in out of equilibrium cases, where the supersaturation σ is not uniform in space.

Some recent works have brought advances in the understanding of the dynamical aspects of crystallization force (e.g. the role of surface kinetics in building up crystallization pressure [76, 130]). These approaches are based on the time evolution of the concentration field from precipitation kinetics, transport and mass conservation equations using FEM methods. However,

the resulting crystallization force is still calculated from the equilibrium formula [76, 131, 132]. Furthermore, these authors do not include a precise description of microscopic interactions with the pore wall nor surface tension effects or substrate inhomogeneities.

Weyl's model and rims Weyl's seminal model [33] is, to our knowledge, the only continuum model that includes both growth and dissolution considering the dynamics at a single contact (eventually relating it to the global creep problem). It can be included in the family of the thin film models but differs from the diffusional creep model usually used in pressure solution. Given its simplicity and elegance, Weyl's model could be considered the archetype of thin film models.

The model does not assume any thermodynamic equilibrium law and is based only on mass conservation augmented with the following assumptions: i) axisymmetric contact; ii) the concentration is a linear function of the stress across the film; iii) the thickness is constant (model A) or exponentially decreasing with stress (model B). With these assumptions, Weyl obtains dissolution rates (or creep laws) very similar to Eq. (1.17a). Furthermore, to the best of our knowledge, Weyl's model is the only theoretical model that can predict rims during confined growth as those first observed by Becker and Day [95] and Taber [97] and illustrated in Fig. 1.15. Assuming external stresses along z , according to the Weyl's model the rim or hollow center exists if the average pressure in the film is smaller than the equilibrium one

$$\bar{p} < p_{eq}, \quad (1.19)$$

where $\bar{p} = F/\pi R^2$ with F the applied load and R the radius of the crystal face. Furthermore, the width of the rim δ is linked to stress according to the expression

$$\frac{\delta}{R} = \sqrt{1 - 2\frac{\bar{p}}{p_{eq}}}. \quad (1.20)$$

However, a recent experimental work [104] contradicts this hypothesis and finds no correlation between rim size and stress. Instead, the authors propose a scenario where rim appearance depends on step density gradient coupled with concentration gradients oriented towards the center of the crystal (lower in the center) by confinement and/or Berg effect [133] (concentration higher at the corners of the crystal).

In general, one cannot expect Weyl's model to be quantitative given the heuristic nature of its derivation.

1.5 Summary and objectives of this study

We have shown that confined growth and dissolution of crystals is an interdisciplinary topic at the crossroads of independent fields of research such as thin film hydrodynamics, surface-surface interactions (disjoining pressures), nanofluidic phenomena and crystal growth kinetics. We discussed the geological phenomena of pressure solution (confined dissolution) and crystallization force (confined growth) and showed that their behavior differs significantly from standard unconstrained crystal growth and dissolution usually giving rise to faceted or dendritic crystals. Globally the experimental observations delineate a rich and complex picture which, however, due to the heuristic character of the interpretations and to experimental difficulties, still need further understanding. In particular, some of the questions which require better insights are:

- i The emerging morphologies in confined dissolution and growth.
- ii The observed dissolution and growth rates.
- iii How crystallization force builds up (role of disjoining pressures, supersaturation and growth kinetics); when and how the effective contact area changes during growth (rims formation); how crystallization pressure can be prevented in practice.

We have also reviewed some existing theoretical approaches. We found that a common limitation of the continuum approaches is the lack of description of microscopic interactions (disjoining pressure) and hydrodynamics in the liquid film. Disjoining pressure is assumed only as a mechanism to maintain the liquid film [46, 82] but is seldom correlated to the dynamical evolution of the thickness (except for some considerations in [89]). Hydrodynamics is never included. When the viscosity is considered it is only indirectly via the Stokes-Einstein relation to motivate an effective (higher) diffusion related to (or caused by) the electro-viscous effect [62, 63, 82, 89]. However, hydrodynamics in the liquid film could have important implications on pressure solution since it can make the process of evacuating the liquid out of the contact dynamically unfeasible (diverging time of approach). As far as pressure solution creep models are concerned, in our opinion, a second limitation is that surface tension effects are systematically neglected [61, 62, 89]. We will show that at high stresses surface energy can have important consequences on the contact morphology and asymptotic behaviors.

In regard to the problem of the force of crystallization, continuum out of equilibrium approaches are rare in the literature. Indeed, since the main aim of most authors has been to assess the maximum force of crystallization, equilibrium thermodynamics has been the dominant tool over alternative approaches. Furthermore, most of the research focused on refinements of the description of chemical processes – for instance to establish which are the most effective damaging materials (typically salts as sodium sulfate that can have hydrated metastable phases) [100] – but with a little accent on the general physical mechanism and dynamical aspects.

The study we present in this thesis is therefore motivated by the need for a consistent out of equilibrium description of confined growth and dissolution. Our objective is to develop a continuum model capable of describing the out of equilibrium growth and dissolution dynamics of a confined solid surface.

In the following, we build a continuum thin film model which accounts self-consistently (in the lubrication regime) for surface tension effects, for disjoining pressure, surface kinetics, diffusion, and hydrodynamic flow. For simplicity, a number of approximations will be made to analyze some of the main outcomes of the model. Motivated by the geological problems, we will provide quantitative discussions for mineral and salt crystals when possible.

We derive a three-dimensional continuum model for confined growth and dissolution which takes into account disjoining pressure effects, diffusion, surface kinetics, and hydrodynamics. A liquid film of solution separates an impermeable substrate from the crystal and is assumed to be thin as compared to the size of the contact. This disparity of length scales is used to reduce the dimensionality of the problem by means of the so-called lubrication expansion. Finally, evolution equations for the confined crystal interface are derived in some simplifying assumptions.

In particular, we discuss two different regimes: i) Fast or finite precipitation kinetics (diffusion limited regime); ii) Slow precipitation kinetics, where we include the possible competition between diffusion transport and surface kinetics. Both regimes result in a nonlinear and nonlocal partial differential equation for the evolution of the crystal interface. The contact region is assumed to be in contact with a macroscopic concentration bath. We discuss the boundary conditions used in the different class of problems and introduce a method for lateral growth of the contact. The equations will be applied in the following chapters to address three different problems: Dissolution induced by a load (pressure solution), growth on a substrate after sedimentation or heterogeneous nucleation of a seed crystal, and growth between two parallel substrates (crystallization force).

2.1 Introduction

In this chapter, we present a three-dimensional continuum model which takes into account dissolution or growth, disjoining pressure effects, diffusion, surface kinetics, and hydrodynamics. The

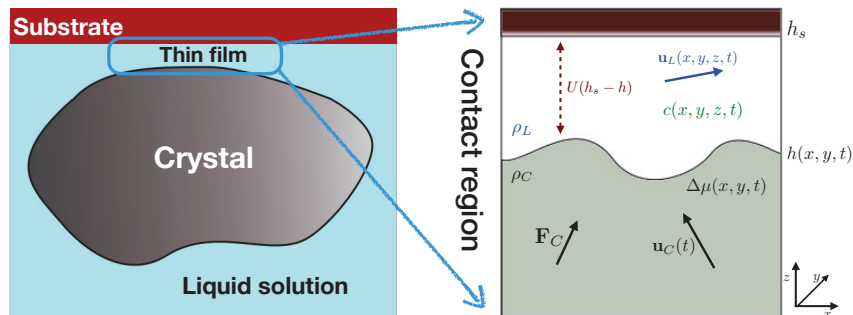


Figure 2.1: Sketch of an arbitrary shaped crystal and of the contact region with some variables and fields of the model. See text for notations.

key assumption that the film is thin in the contact region is formalized with the help of a multi-scale expansion defining the lubrication limit [41]. This limit, widely employed in engineering (trust bearing) [42, 134], physics (nanoscale dewetting) [15, 135, 136, 137] and biophysical models (membranes) [138, 139, 140], results in nonlinear and nonlocal thin film evolution equations for the profile of the crystal surface.

We initially proceed with the derivation of the evolution equations for the interface under relatively general conditions. Then we present some simplifying assumptions such as equal densities between the liquid and the solid, imposed symmetry (left-right symmetric ridge or axisymmetric contact), and the dilute limit which help to reduce the complexity of the model.

We then derive and present two sets of model equations. The first assumes a finite or fast surface kinetics, leading to a negligible contribution of attachment-detachment kinetics in lubrication expansion (diffusion is the slowest process). The second assuming slow attachment-detachment kinetics leads to slightly more complex equations accounting for scenarios where the time scales of diffusion and surface processes are comparable.

Finally, we discuss two alternative conditions at the boundary of the contact. The first assumes no lateral motion, the second allows for expansion or shrinking of the confined interface.

To facilitate the reading, many calculation details are omitted. For a more detailed understanding of the mathematical steps of the derivations, the reader should refer to Appendix A. Numerical methods are described in details in Appendix B.

2.2 General derivation

The system under study is represented in Fig. 2.1. For the sake of clarity, we designate the growing or dissolving solid by the name crystal. However, our model equally applies to amorphous phases, or to any other solid phases that can grow and dissolve from solution. We consider a crystal in a liquid medium, in the vicinity of a substrate, and subjected to an external force $\mathbf{F}_C(t)$ which will be sometimes denoted as the load. The crystal is assumed to be rigid, namely, we neglect the contribution of elastic deformations on the interface shape and chemical potential. We also assume a uniform and constant temperature T (isothermal conditions). For the sake of simplicity, we discard crystal rotations and consider only translations. The substrate at $z = h_s(x, y)$ is immobile i.e. $\partial_t h_s = 0$, and is impermeable. The Liquid Crystal interface (LC) at $z = h(x, y, t) < h_s(x, y)$ evolves with time. In the following we work in the reference frame where the substrate is immobile, $\mathbf{u}_S = 0$.

We assume an incompressible fluid

$$\nabla \cdot \mathbf{u}_L = 0, \quad (2.1)$$

where $\mathbf{u}_L(x, y, z, t)$ is the liquid velocity. Neglecting inertial effects (which are known to be negligible in the lubrication limit considered below see Appendix A.5.1 and [41, 141]), the liquid obeys the Stokes equation:

$$\eta \nabla^2 \mathbf{u}_L = -\nabla p, \quad (2.2)$$

where η is the viscosity, and $p(x, y, z, t)$ is the pressure. Global mass conservation at the LC interface (neglecting possible mass excess at the interface) reads [31] (see Appendix A.1)

$$\rho_L(\mathbf{u}_L \cdot \hat{\mathbf{n}} - v_n) = \rho_C(\mathbf{u}_C \cdot \hat{\mathbf{n}} - v_n), \quad (2.3)$$

where ρ_C is the constant crystal density, and ρ_L is the constant liquid density, \mathbf{u}_C is the translational velocity of the rigid crystal, $\hat{\mathbf{n}}$ is the normal to the LC interface and v_n is the normal velocity of the interface. Note that whenever a three-dimensional field such as \mathbf{u}_L appears in an equation evaluated at an interface, we consider implicitly the value of this field at this interface.

Finally, we assume no slip and no penetrability at the liquid-substrate (LS) interface

$$\mathbf{u}_L = \mathbf{0}, \quad (2.4)$$

and a no slip condition at the LC interface

$$\mathbf{u}_{L\parallel} = \mathbf{u}_{C\parallel}, \quad (2.5)$$

where the index \parallel indicates the projection of a vector on the plane tangent to the LC interface.

Local mass conservation of the solute (crystal ions or molecules in the fluid) reads in the liquid bulk

$$\partial_t c + \mathbf{u}_L \cdot \nabla c = -\nabla \cdot \mathbf{j}, \quad (2.6)$$

where \mathbf{j} is the diffusion flux. We assume that diffusion is governed by Fick's law

$$\mathbf{j} = -D(c)\nabla c. \quad (2.7)$$

As shown in Appendix A.2, the solute mass conservation at the LC interface imposes

$$\Omega^{-1}(v_n - \hat{\mathbf{n}} \cdot \mathbf{u}_C) = c(v_n - \hat{\mathbf{n}} \cdot \mathbf{u}_L) - \hat{\mathbf{n}} \cdot \mathbf{j}, \quad (2.8)$$

where Ω is the molecular volume in the crystal and we assumed no mass flux in the crystal bulk. The left-hand side of Eq. (2.8) is the mass of the molecules detached or absorbed in the crystal as a consequence of the movement of the LC interface. The first term in the right-hand side is the corresponding mass variations of crystal type molecules in the liquid. The second term accounts for the diffusion flux at the interface (in the liquid).

Assuming that the substrate is impermeable at the LS interface, we have

$$\mathbf{j} \cdot \hat{\mathbf{n}}_s = 0, \quad (2.9)$$

with $\hat{\mathbf{n}}_s$ the LS interface normal.

The crystallization/dissolution rate $v_n - \mathbf{n} \cdot \mathbf{u}_C$ is assumed to depend linearly on the departure from equilibrium

$$v_n - \mathbf{n} \cdot \mathbf{u}_C = \Omega\nu(c - c_{eq}), \quad (2.10)$$

where ν is a kinetic coefficient and $c_{eq}(x, y, t)$ the local equilibrium concentration. In the ideal limit, where the activity coefficient is equal to 1, we have

$$c_{eq} = c_0 e^{\Delta\mu/k_B T}, \quad (2.11)$$

where $\Delta\mu$ is the local chemical potential of the crystal at the interface and c_0 is the equilibrium concentration for an interface in an infinitely large crystal far from the substrate (solubility). The chemical potential at the LC interface reads [39, 142, 143]

$$\frac{\Delta\mu(x, y, t)}{\Omega} = \tilde{\gamma} : \kappa + W'(x, y, h) + \left(\frac{\rho_C}{\rho_L} - 1\right)(\varepsilon_{nn} + p_0), \quad (2.12)$$

where $\tilde{\gamma}(x, y)$ is the stiffness tensor, κ is the curvature tensor, $W' = \partial_h W(x, y, h)$ is the disjoining pressure and p_0 a reference pressure. The potential $W(x, y, h)$ depends on x and y to account for the possible spatial heterogeneities of the substrate height h_s , and of the substrate material properties. The liquid stress tensor is defined as $\varepsilon_{ij} = \varepsilon'_{ij} - \delta_{ij}p$ with $\varepsilon'_{ij} = \eta(\partial_j u_{Li} + \partial_i u_{Lj})$, and the index n indicates the normal direction. Equation (2.12) is similar to the usual Gibbs-Thomson effect which relates chemical potential and curvature. However, there are two extra terms. The first one accounts for the presence of a substrate via the interaction W' . The second one, proportional to the liquid-crystal density ratio, accounts for the energy cost associated with the volume change during the phase transformation [?]. One example where this latter term intervenes is when considering gravity. This is included adding $\rho g z$ in the pressure that enters in ε_{nn} which leads to the well-known contribution $(\rho_C - \rho_L)gh$ in the chemical potential [?].

Finally, since the crystal is a rigid body, the global force balance on the crystal reads

$$\mathbf{F}_C = \oint_{LC} dS [-\hat{\mathbf{n}} \cdot \varepsilon' + \hat{\mathbf{n}}(\tilde{\gamma} : \kappa + W')], \quad (2.13)$$

where the surface integral is performed along all the LC interface (since we discard crystal rotations, we do not consider the equilibrium of torques). This relation is derived in Appendix A.3.1.

The system of equations reported above describes the dissolution or growth dynamics of a rigid crystal interacting with an inert and impermeable substrate. In the following, we specialize the discussion to the contact region (see Fig. 2.1).

2.3 Contact region

In this section, we re-write mass conservation and force balance in a form which makes use of the geometry of the contact region. We assume that the LS and LC interfaces exhibit no overhang.

For any field $g(x, y, z)$ defined everywhere in the liquid, we consider the following integrated quantity along z

$$\langle g \rangle(x, y) = \int_{h(x, y)}^{h_s(x, y)} dz g(x, y, z). \quad (2.14)$$

As explicitly showed in Appendix A.4.1, using the incompressibility condition Eq. (2.1), the immobility of the substrate Eq. (2.4), and global mass conservation at the LC interface Eq. (2.3), we obtain a two-dimensional equation for liquid mass conservation

$$v_{Cz} \frac{\rho_C}{\rho_L} = -\nabla_{xy} \cdot \langle \mathbf{u}_{Lxy} \rangle - \partial_t (h_s - h), \quad (2.15)$$

where h_s has been inserted for convenience using the relation $\partial_t h_s = 0$. Here and in the following, vectors with the index xy indicate a two-dimensional vector in the x, y plane without the z component. In addition, we have used the geometric relations

$$\hat{\mathbf{n}} = \frac{(-\nabla_{xy} h, 1)}{[1 + (\nabla_{xy} h)^2]^{1/2}}, \quad (2.16)$$

$$v_n = \frac{\partial_t h}{[1 + (\nabla_{xy} h)^2]^{1/2}}, \quad (2.17)$$

and we have defined the crystallization-dissolution rate along z

$$v_{Cz} = \partial_t h - u_{Cz} + \mathbf{u}_{Cxy} \cdot \nabla_{xy} h. \quad (2.18)$$

Similarly (see Appendix A.4.2), using Eqs. (2.8) and (2.9), mass conservation for the solute concentration c can be re-written in a two-dimensional form

$$\frac{v_{Cz}}{\Omega} + \partial_t \langle c \rangle + \nabla_{xy} \cdot \langle \mathbf{u}_{Lxy} c \rangle = -\nabla_{xy} \cdot \langle \mathbf{j}_{xy} \rangle. \quad (2.19)$$

In order to write the force balance at the contact, we make use of three additional physical assumptions. First, we assume that the pressure outside the contact is approximately constant and equal to p^{ext} . Second, we assume that the interaction term vanishes, i.e. $W' \approx 0$, away from the contact. Third, we assume that viscous stresses ε' vanish outside the contact region. Then, force balance Eq. (2.13) is re-written as

$$\mathbf{F}_C = \iint_{\text{contact}} dS [\hat{\mathbf{n}}(p - p^{ext}) + W'(x, y, h) - \hat{\mathbf{n}} \cdot \varepsilon']. \quad (2.20)$$

This equation makes use of fact that the total force exerted by surface tension or by a constant external pressure on a crystal of arbitrary shape vanishes

$$\begin{aligned} \oint_{LC} dS \hat{\mathbf{n}}(\tilde{\gamma} : \kappa) &= 0. \\ \oint_{LC} dS \hat{\mathbf{n}} p^{ext} &= 0. \end{aligned} \quad (2.21)$$

These two identities are proved in Appendix A.5.4.

2.3.1 Lubrication limit in the contact region

Here, we show that the lubrication limit, based on the small slope approximation, allows one to express the quantities integrated along z in Eqs. (2.15), (2.19) and (2.20), thereby leading to closed-form equations for three quantities. The two first quantities are time and space-dependent fields: the pressure p and the thickness of the liquid film

$$\zeta(x, y, t) = h_s(x, y) - h(x, y, t). \quad (2.22)$$

The third quantity is the time-dependent crystal velocity \mathbf{u}_C .

The lubrication limit [141] makes use of a disparity of length scales: the lateral extent of the variations along the film is assumed to be large $x \sim \mathcal{O}(\epsilon^{-1})$ as compared to the film thickness $\zeta = (h_s - h) \sim \mathcal{O}(1)$ with $\epsilon \ll 1$. The mathematical procedure to derive these equations is well known [41, 141], we therefore only provide the main steps of the derivation. More details are given in Appendix A.5. Formally, we identify a small parameter $\epsilon = h_0/l$, where l is the typical extent of the contact region and h_0 is the typical gap between the crystal and the substrate. Spatial coordinates then scale with this small parameter as $x \sim y \sim \ell \sim h_0/\epsilon$, and $z \sim h_0$. Furthermore, assuming that the typical fluid velocity parallel to the substrate is $\mathbf{u}_{Lxy} \sim u_0$, we also consistently choose $u_{Lz} \sim \epsilon u_0$, pressure $p \sim \eta u_0/(\epsilon h_0)$, and time $t \sim h_0/\epsilon u_0$.

Conservation and transport laws

Substituting these scalings of physical variables in the model equations we obtain the lubrication expansion [41, 141]. To leading order in ϵ , Eq. (2.2) reduces to

$$\partial_z p = 0, \quad (2.23)$$

$$-\nabla_{xy} p + \eta \partial_z^2 \mathbf{u}_{Lxy} = 0. \quad (2.24)$$

The first equation indicates that the pressure does not depend on z , but only on x, y , and t . Solving the second equation using the boundary conditions Eqs. (2.4) and (2.5) results in a Poiseuille (parabolic) flow for \mathbf{u}_{xy} ,

$$\mathbf{u}_{Lxy} = -\frac{(h_s - z)(z - h)}{2\eta} \nabla_{xy} p + \frac{h_s - z}{\zeta} \mathbf{u}_{Cxy}. \quad (2.25)$$

Integrating over the film thickness, we obtain

$$\langle \mathbf{u}_{Lxy} \rangle = -\frac{\zeta^3}{12\eta} \nabla_{xy} p + \frac{\zeta}{2} \mathbf{u}_{Cxy}. \quad (2.26)$$

Combining Eqs. (2.15) and (2.26), we obtain

$$\boxed{v_{Cz} \frac{\rho_C}{\rho_L} = \nabla_{xy} \cdot \left[\frac{\zeta^3}{12\eta} \nabla_{xy} p - \mathbf{u}_{Cxy} \frac{\zeta}{2} \right] - \partial_t \zeta}. \quad (2.27)$$

Recalling that ρ_L is constant and $\mathbf{u}_S = 0$, this equation reduces to the Reynolds equation Eq. (1.13) when there is no growth or dissolution, i.e. $v_{Cz} = 0$.

A similar procedure is applied to the concentration field. Assuming $c \sim \mathcal{O}(1)$ we obtain to leading order from Eqs. (2.6) and (2.7)

$$\partial_z [D(c) \partial_z c] = 0. \quad (2.28)$$

Integrating this relation, and using local conservation of mass at the boundaries Eqs. (2.8) and (2.9), we obtain

$$\partial_z c = 0 \quad (2.29)$$

showing that the concentration does not depend on z . We may now write Eq. (2.19) in the lubrication limit using Eq. (2.7) and Eq. (2.26) as

$$\boxed{\frac{v_{Cz}}{\Omega} + \partial_t [\zeta c] - \nabla_{xy} \cdot \left[\frac{\zeta^3}{12\eta} c \nabla_{xy} p \right] + \frac{\mathbf{u}_{Cxy}}{2} \cdot \nabla_{xy} [c \zeta] = \nabla_{xy} \cdot [\zeta D(c) \nabla_{xy} c]}. \quad (2.30)$$

Slow surface kinetics

Another consequence of the lubrication expansion is that the left-hand side of Eq. (2.10) is equal to the local growth-dissolution rate (along z)

$$v_{Cz} \approx \Omega\nu(c - c_{eq}), \quad (2.31)$$

where from Eq. (2.18) the local growth rate is

$$v_{Cz} = -\partial_t \zeta - u_{Cz} + u_{Cxy} \cdot \nabla_{xy} h, \quad (2.32)$$

up to terms of order $\mathcal{O}(\epsilon^2)$. When the kinetic constant is small, $\nu = \mathcal{O}(\epsilon)$, from Eq. (2.31), the concentration is given by

$$\boxed{c = c_{eq} + \frac{v_{Cz}}{\Omega\nu}}. \quad (2.33)$$

Fast surface kinetics

The assumption of a finite attachment-detachment kinetic constant $\nu \sim \mathcal{O}(1)$, corresponds to the limit where surface kinetics is fast as compared to transport by diffusion. Indeed, in the lubrication limit since $v_{Cz} \sim \mathcal{O}(\epsilon)$ and $c \sim \mathcal{O}(1)$ in Eq. (2.31), finite kinetics implies

$$\boxed{c = c_{eq}(x, y, t)}. \quad (2.34)$$

The same result can trivially be obtained letting $\nu \rightarrow \infty$ in Eq. (2.31). Hence for finite attachment-detachment kinetics, the concentration in the lubrication limit is equal to the local equilibrium concentration. This is the consequence of the slenderness of the liquid film which implies slow diffusion along the confined crystal surface, leaving ample time for local equilibration of the concentration via attachment and detachment at the LC interface.

Chemical potential

The chemical potential enters in the model via Eq. (2.11). Thus, the equilibrium concentration appearing in Eqs. (2.33) and (2.34) is

$$c_{eq} = c_0 e^{\Delta\mu/(k_B T)} \approx c_0 \left(1 + \frac{\Delta\mu}{k_B T} \right)$$

where the last equality holds when assuming linearized Gibbs-Thomson relation.

Let us compare the different contributions of the chemical potential. The lubrication expansion imposes $p \sim \mathcal{O}(\epsilon^{-1})$. For disjoining forces to be able to balance viscous forces, we choose $W'(x, y, h) \sim \mathcal{O}(\epsilon^{-1})$. As a consequence, the pressure term and the interaction term in Eq. (2.12) are of the same order of magnitude. In addition, since the curvature $\kappa \sim \partial_{xx} h \sim \partial_{yy} h \sim \epsilon^2$ is small, only large stiffnesses $\tilde{\gamma} \sim \mathcal{O}(\epsilon^{-3})$ can make the capillary term $\tilde{\gamma} : \kappa$ relevant. However even if surface stiffness is not so large, the capillary term can be relevant in two cases: (i) if the curvature locally blows up, and (ii) far from the substrate where the potential term W' can be neglected. We will see in the following that these conditions can be reached during the dynamics. In order to include all relevant cases in the following we keep the capillary term so that the chemical potential reads:

$$\boxed{\frac{\Delta\mu(x, y, t)}{\Omega} = \tilde{\gamma}_1 \partial_{x_1 x_1} \zeta + \tilde{\gamma}_2 \partial_{x_2 x_2} \zeta + W'(x, y, h) + \left(\frac{\rho_C}{\rho_L} - 1 \right) (p_0 - p)}, \quad (2.35)$$

where x_1 and x_2 are the directions of principal curvature, and $\tilde{\gamma}_1, \tilde{\gamma}_2$ are the related surface stiffnesses [1].

Force balance

Finally, since W' is of the same order as p in the lubrication limit, force balance Eq. (2.20) reads

$$F_{Cz} = \iint_{\text{contact}} dA (p - p^{ext} + W'(x, y, h)), \quad (2.36)$$

$$\mathbf{F}_{Cxy} = \iint_{\text{contact}} dA \left[\frac{\eta \mathbf{u}_{Cxy}}{\zeta} - (p - p^{ext}) \nabla_{xy} \left(h_s - \frac{\zeta}{2} \right) \right], \quad (2.37)$$

where dS reduces to $dA = dx dy$ as a consequence of the lubrication expansion. To derive the last relation (see Appendix A.5.3), we have assumed that $p = p^{ext}$ is constant and ζ is large enough for W' to be negligible at the boundary of the contact zone.

As a summary, we have derived a thin film model for the contact region during dissolution and growth, which consists of two differential equations Eqs. (2.27) and (2.30) for the coupled two-dimensional space and time dependent fields p and ζ , and an additional vectorial integral constraint Eqs. (2.36) and (2.37) which determines the time-dependent crystal velocity \mathbf{u}_C . This system of equations, which is a central result of this thesis, is not only nonlinear but also nonlocal due to the force balance equation. In the following, to reduce the complexity of the equations we make some simplifying assumptions.

2.4 Simplifications and geometries

We consider a single contact and assume:

- (i) equal and constant densities between the liquid and the crystal $\rho_C = \rho_L$;
- (ii) no lateral crystal motion $\mathbf{u}_{Cxy} = 0$ and no lateral force $F_{Cxy} = 0$;
- (iii) a diffusion constant independent of concentration $D(c) = D$;
- (iv) a flat substrate: h_s independent of x and y . We use the interaction potential U , defined by $U(\zeta) = W(x, y, h)$. It follows that $W'(h) = \partial_h W(h) = -\partial_\zeta U(\zeta) = -U'(\zeta)$.
- (v) small concentrations $\Omega c \ll 1$;

We also define the supersaturation as

$$\sigma = \frac{c - c_0}{c_0}. \quad (2.38)$$

In addition for the sake of simplicity, we will often assume (see Chapters 3 and 4) a linearized (local) thermodynamic relation, $\Delta\mu/(k_B T) \ll 1$ so that $c_{eq} \approx c_0(1 + \Delta\mu/(k_B T))$. The simplifications introduced above imply that the chemical potential reads (see Eq. (2.12))

$$\frac{\Delta\mu}{\Omega} = \tilde{\gamma}_1 \partial_{x_1 x_1} \zeta + \tilde{\gamma}_2 \partial_{x_2 x_2} \zeta - U'(\zeta). \quad (2.39)$$

Finally, we consider two simple geometries. The first one is a one-dimensional ridge (Fig. 2.2), which is invariant along y , and left-right symmetric with $h(x) = h(-x)$. The second geometry is an axisymmetric contact (Fig. 2.3), the shape of which depends only on the distance r from the origin in the x, y plane. In the following, we will often refer to the symmetric ridge as 1D, and the axisymmetric contact as 2D.

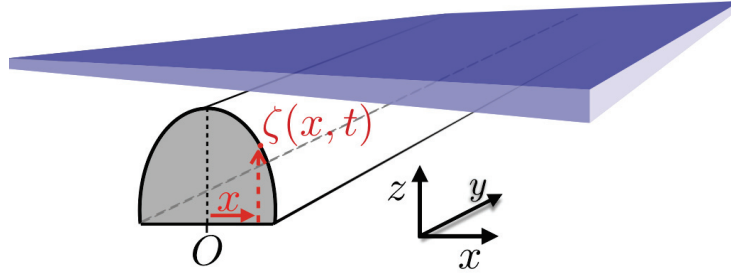


Figure 2.2: Sketch of a symmetric ridge. The crystal interface depends only on x . The substrate is represented by the plane in blue.

2.4.1 Symmetric ridge

Consider first the ridge case obeying the $x \rightarrow -x$ symmetry, with a system length $2L$. Assuming $\rho_C = \rho_L$, the integration of Eq. (2.27) leads to

$$p = p^{ext} + u_{Cz} \int_x^L dx \frac{12\eta x}{\zeta^3}. \quad (2.40)$$

Inserting this expression into Eq. (2.36) provides us with a nonlocal relation between the crystal velocity and the surface height:

$$2u_{Cz} \int_0^L dx \int_x^L dx' \frac{12\eta x'}{\zeta^3} = F_{Cz} + 2 \int_0^L dx U'(\zeta). \quad (2.41)$$

This equation relates the sum of the load and interaction forces between the crystal and the substrate on the right-hand side, to the forces caused by viscous dissipation in the film on the left-hand side. In the viscous term, the crystal velocity u_{Cz} is multiplied by the hydrodynamic mobility of the crystal which depends on the interface profile ζ . The expression of this mobility is well known and has been reported previously in the literature [42].

Using Eq. (2.27), assuming no lateral motion, constant diffusion and equal densities $\rho_L = \rho_C$, and in the limit of small concentrations $\Omega c \ll 1$, Eq. (2.30) takes a simple form¹

$$\partial_t \zeta = -D\Omega \partial_x \zeta (\partial_x c) - u_{Cz}. \quad (2.42)$$

It should be remarked that a final consequence of this geometry is that $\tilde{\gamma}_2$ in Eq. (2.39) is irrelevant since we are left with only a single principal direction of curvature.

2.4.2 Axisymmetric contact

Let us now consider an axisymmetric contact. Using cylindrical coordinates in a contact zone of radius R , we obtain equations that are similar to those of the symmetric ridge:

$$2u_{Cz} \pi \int_0^R dr r \int_r^R dr' \frac{6\eta r'}{\zeta(r')^3} = F_{Cz} + 2\pi \int_0^R dr r U'(\zeta), \quad (2.43)$$

$$\partial_t \zeta = -D\Omega \frac{1}{r} \partial_r [r \zeta (\partial_r c)] - u_{Cz}. \quad (2.44)$$

In the following chapters we will mainly make use of this formulation of the problem which has the advantage to still have the numerical cost of a 1D problem but describes a 2D surface. While the 1D ridge is important for understanding the consequences of geometry (as for instance found

¹ Note that even though in the lubrication limit the advection term in the concentration disappears, an effect of advection was still present in Eq. (2.30) due to the term depending on $\nabla_{xy} p$. Here, the assumption of dilute limit $\Omega c_{eq} \ll 1$, cancels also this term. It follows that hydrodynamics effects reduce solely to viscous dissipation in the force balance equation Eq. (2.36) (or Eqs. (2.41) and (2.43)).

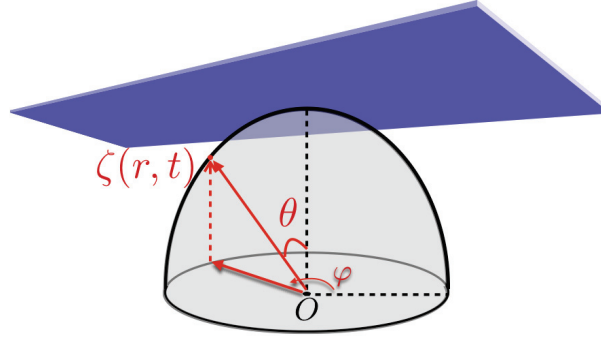


Figure 2.3: Sketch of an axisymmetric contact. The crystal profile is invariant with respect to the azimuthal angle ϕ and depends only on the radial distance r . The substrate is represented by the plane in blue.

in bearing problems – see Section 1.2.1), the 2D axisymmetric geometry is better suited for comparison to real systems. Finally, it should be noted that in the axisymmetric geometry the surface tension $\gamma(\theta, \phi)$ is isotropic with respect to the azimuthal angle ϕ , and anisotropic with respect to the polar angle θ . It follows that $\tilde{\gamma}_1 = \tilde{\gamma}_2$.

2.4.3 Chemical potential

In the two geometries considered above the chemical potential at the liquid-crystal interface Eq. (2.39), reduces to

$$\frac{\Delta\mu}{\Omega} = \tilde{\gamma}\kappa - U'(\zeta), \quad (2.45)$$

where the stiffness is, as a consequence of the lubrication limit, $\tilde{\gamma} = \gamma(0) + \gamma''(0)$ (see Appendix A.5). Finally, the curvature is given in the lubrication limit (small slopes) by

$$\kappa_{1D} = \partial_{xx}\zeta, \quad \text{or} \quad (2.46)$$

$$\kappa_{2D} = \partial_{rr}\zeta + \frac{\partial_r\zeta}{r}, \quad (2.47)$$

for a 1D contact and a 2D axisymmetric contact, respectively. The derivation of κ_{2D} is illustrated in Appendix A.6.

2.5 Summary of relations for slow surface kinetics

The evolution equation of the interface given by Eq. (2.42) or Eq. (2.44) can be expressed in a more convenient way considering it together with Eq. (2.33). This provides an implicit equation for the local growth rate given by

$$\mathbf{v}_{Cz} = \partial_x[\zeta\Omega D(\partial_x c_{eq})] + \partial_x\left[\frac{\zeta D}{\nu}(\partial_x \mathbf{v}_{Cz})\right], \quad (2.48a)$$

$$\mathbf{v}_{Cz} = \frac{1}{r}\partial_r[r\zeta\Omega D(\partial_r c_{eq})] + \frac{1}{r}\partial_r\left[r\frac{\zeta D}{\nu}(\partial_r \mathbf{v}_{Cz})\right], \quad (2.48b)$$

where the former applies to the 1D ridge and the latter to the axisymmetric contact. Using Eq. (2.32) the evolution of the profile is given by

$$\partial_t\zeta = -\mathbf{v}_{Cz} - u_{Cz} \quad (2.49)$$

where u_{Cz} is determined by the force balance expression Eq. (2.41) or Eq. (2.43). As discussed previously, the equilibrium concentration depends on the profile via the chemical potential. For instance in the linearized case we have from Eqs. (2.11) and (2.45)

$$c_{eq} = c_0 \left[1 + \frac{\Omega}{k_B T} \left(\tilde{\gamma}\partial_{rr}\zeta + \frac{\tilde{\gamma}}{r}\partial_r\zeta - U'(\zeta) \right) \right],$$

for the axisymmetric geometry and

$$c_{eq} = c_0 \left[1 + \frac{\Omega}{k_B T} (\tilde{\gamma} \partial_{xx} \zeta - U'(\zeta)) \right],$$

for the symmetric ridge.

2.6 Summary of relations for fast surface kinetics

The above equations suggest also a criterion to assess the typical lateral length scale above which diffusion should be the limiting mass transport process. Indeed, comparing the two terms containing v_{Cz} in Eq. (2.48), we obtain

$$l_0^2 \approx \frac{D\zeta}{\nu}. \quad (2.50)$$

This lengthscale can be for instance compared to the total length (1D) or radius (2D) of the contact. Above l_0 we can then combine Eq. (2.34) and Eqs. (2.42) and (2.44) to obtain the evolution equations in the fast surface kinetics regime:

$$\partial_t \zeta = -D\Omega \partial_x [\zeta (\partial_x c_{eq})] - u_{Cz}, \quad (2.51a)$$

$$\partial_t \zeta = -D \frac{1}{r} \partial_r \left[r \zeta (\partial_r c_{eq}) \right] - u_{Cz}. \quad (2.51b)$$

As in the slow surface kinetics limit discussed above, u_{Cz} is given from the force balance by Eq. (3.3) or Eq. (3.4), and the equilibrium concentration is expressed via Eq. (2.11) with Eq. (2.45).

2.7 Numerical scheme and boundary conditions

The two cases discussed above, namely fast precipitation or diffusion dominated kinetics and slow precipitation kinetics, are solved using an explicit second order Euler scheme in time. The details of the algorithms used are exposed in Appendices B.1 and B.2. Even though the fast precipitation kinetics case is in principle included in Eq. (2.48b) by choosing a large kinetic constant ν , for computational efficiency it is convenient to develop a specific code to solve Eq. (2.51a) or Eq. (2.51b).

In the following, we discuss the conditions adopted at the boundary of the integration domain. These are crucial for the numerical solution and physical interpretation of the results. We consider initially a fixed simulation box, i.e. a contact zone with a constant size. This assumption is valid if the typical time scales of the phenomena happening within the contact area are faster than the evolution of the contact size. This approximation will be referred to as the *quasi-static approximation* and will be discussed and questioned in different places in this thesis. We have also investigated the more complex case of a laterally expanding or shrinking contact. The technical details are given in Appendix B.3. This scheme will be used in practice in the last chapter of this thesis when addressing the problem of the crystallization force. The main programs developed for this work are uploaded on *github* at https://github.com/lucagl/codes_thesis. They are open source and can be downloaded and compiled on Linux.

Assuming a macroscopic constant concentration bath outside the contact zone, we choose at the boundary of the integration domain r_{bc} to fix the supersaturation σ_{bc} . A second boundary condition is given by imposing a constant film width $\zeta(r_{bc}) = \zeta_{bc}$. Since we assume the interaction potential $U(\zeta)$ to be constant outside the contact area, ζ_{bc} has to be chosen large enough to ensure that $U'(\zeta_{bc}) \approx 0$. In the case of a constant system size, we have $r_{bc} = R$ with R (or L in 1D) the size of the simulation box. For compactness, we will only present the axisymmetric case. The discussion can be trivially extended to the case of a 1D ridge.

2.7.1 Boundary conditions for a fixed simulation box

We start from the general case Eq. (2.48b). Using the definition of supersaturation and Eq. (2.33) we have

$$\sigma(r) = \frac{c(r) - c_0}{c_0} = \frac{c_{eq}(r)}{c_0} - 1 + \frac{v_{Cz}(r)}{c_0 \Omega \nu} \quad (2.52)$$

where c_0 is the concentration in equilibrium with a macroscopic (flat and isolated) crystal far from the substrate (solubility). Recalling the expression for the local velocity Eq. (2.32), the condition of fixed film width at the boundary implies that $\partial_t \zeta_{bc} = 0$ so that

$$v_{Cz}^{bc} = -\partial_t \zeta_{bc} - u_{Cz} = -u_{Cz}. \quad (2.53)$$

Combining the latter relation with Eqs. (2.11) and (2.52), we obtain a condition on the chemical potential at the boundary,

$$\exp[\Delta\mu_{bc}/(k_B T)] = (1 + \sigma_{bc} + \frac{u_{Cz}}{c_0 \Omega \nu}) \quad (2.54)$$

which, in the limit of a small supersaturation, simplifies to

$$\Delta\mu_{bc}/(k_B T) = (\sigma_{bc} + \frac{u_{Cz}}{c_0 \Omega \nu}). \quad (2.55)$$

where u_{Cz} depends on the profile via Eq. (2.43).

In the case of the diffusion limited regime (fast surface kinetics), using $c(r) \approx c_{eq}(r)$ or equivalently $\nu \rightarrow \infty$, Eq. (2.55) reduces to

$$\exp[\Delta\mu_{bc}/(k_B T)] = \sigma_{bc} + 1, \quad (2.56)$$

or in the limit of small supersaturations:

$$\Delta\mu_{bc}/(k_B T) = \sigma_{bc}. \quad (2.57)$$

At the center of the contact, $r = 0$ we impose $\partial_r \zeta = 0$ for symmetry reasons. In addition, since $\partial_r c_{eq} \sim \partial_r \Delta\mu$ and $\partial_r \Delta\mu$ is odd with respect to ζ , the concentration flux $-D\partial_r c$ vanishes.

Finally, assuming constant width and supersaturation at the boundary, to solve numerically the crystal evolution at slow surface kinetics one has to couple Eqs. (2.43), (2.48b) and (2.49) to the boundary conditions Eqs. (2.53) and (2.54) (or Eq. (2.55) when assuming linearized thermodynamic relation). In the case of fast surface kinetics Eqs. (2.43) and (2.51b) have to be solved imposing Eq. (2.56) (or Eq. (2.57)).

2.7.2 Boundary conditions for an expanding simulation box

The case of a crystal expanding laterally is technically more complex. While the conditions at the center of the crystal are identical to those discussed above, here an interpolation procedure is used to determine the height, the chemical potential and local growth rate at the boundary of the discretized integration domain. The boundary itself $r_{bc}(t)$ can take arbitrary positions and is not necessarily on the discretization grid. In general, $r_{bc}(t)$ is located between the last grid point and the penultimate point. Whenever $r_{bc}(t)$ crosses a grid point a new grid point is added or removed from the lattice to maintain r_{bc} between the last point and the penultimate point. Details on the numerical scheme are given in Appendix B.3.

The crystal moves laterally with velocity $\dot{r}_{bc} = v_l$. From the condition of fixed film width at the boundary $\zeta(r_{bc}) = \zeta_{bc}$, we have $\dot{\zeta}_{bc} = \partial_t \zeta_{bc} + v_l \partial_r \zeta_{bc} = 0$ and using Eq. (2.49)

$$-v_{Cz}^{bc} - u_{Cz} = -v_l \partial_r \zeta_{bc}. \quad (2.58)$$

We also have from Eq. (2.52)

$$v_{Cz}^{bc} = \Omega \nu c_0 (\sigma_{bc} + 1 - e^{\Delta\mu_{bc}/(k_B T)}). \quad (2.59)$$

As compared to the case of a simulation box of fixed size, we now have an additional unknown, which is the velocity v_l of the contact expansion. We therefore need to impose an additional physical condition.

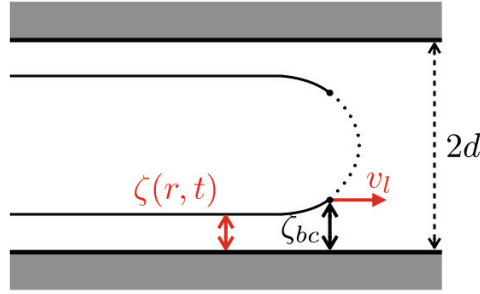


Figure 2.4: Sketch of the geometrical scheme used to derive Eq. (2.62) in the hypothesis that the crystal surface is an arc of circle outside the contact region. The crystal is observed laterally along r . The gray rectangles represent the two parallel walls.

Double contact

A possible choice of third constraint is to fix the curvature at the boundary, κ_{bc} . Given that $U'(\zeta_{bc})$ vanishes, this is equivalent to fixing the chemical potential (or equivalently the equilibrium concentration) at the boundary $\Delta\mu_{bc} = \Omega\tilde{\gamma}\kappa_{bc}$. We combine Eqs. (2.58) and (2.59) to express v_l as

$$v_l = \partial_r \zeta_{bc}^{-1} [u_{Cz} + \Omega\nu c_0 (1 + \sigma_{bc} - e^{\Delta\mu_{bc}/(k_B T)})]. \quad (2.60)$$

The problem can then be solved numerically combining Eqs. (2.43), (2.48b) and (2.49) with the interpolation scheme discussed above and the conditions at the boundary Eqs. (2.59) and (2.60). In general, κ_{bc} can depend on time and should be derived from an analysis of the matching of the fields outside the contact. However, the curvature at the boundary has a simple geometrical interpretation in the special case of a double parallel contact as the one represented in Fig. 2.4 when ν is small. Indeed in this limit, the growth rate outside the contact region is constant and thus the curvature is uniform. If the two walls are separated by a distance $2d$ a good approximation of the curvature is

$$\kappa_{bc}(t) = \left[\sqrt{1 + (\partial_r \zeta_{bc}(t))^2} (d - \zeta_{bc}) \right]^{-1} + \frac{1}{d + r_{bc}}. \quad (2.61)$$

Assuming that the surface profile outside the contact is an arc of circle (isotropy with respect to the polar angle), we can further simplify the previous expression:

$$\kappa_{bc}(t) = \left[\sqrt{1 + (\partial_r \zeta_{bc}(t))^2} (d - \zeta_{bc}) \right]^{-1}. \quad (2.62)$$

This approximation converges to the correct value when $r_{bc} \gg d$. The error is maximum when $r_{bc} \ll d$. In the latter case, if the shape of the crystal is a sphere, the approximation underestimates curvature by a factor two because it only considers one of the two principal curvatures². Assuming small slopes, and large contacts separation we have $\kappa_{bc} \approx 1/d$ independent of time.

The system of a crystal confined between two walls is particularly meaningful when addressing the problem of the force of crystallization in absence of an external load. In particular the geometry implies zero vertical rigid body velocity $u_{Cz} = 0$. Note that this simplifies both the evolution equation

$$\partial_t \zeta = -v_{Cz}, \quad (2.63)$$

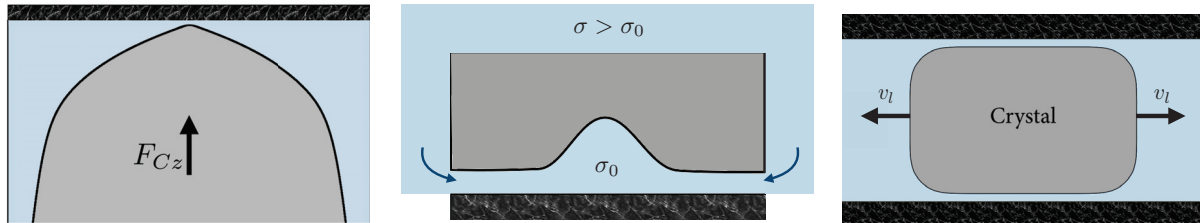
with v_{Cz} given by Eq. (2.48b), and the lateral expansion (or shrinking) velocity of the the simulation box

$$v_l = \partial_r \zeta_{bc}^{-1} [\Omega\nu c_0 (1 + \sigma_{bc} - e^{\frac{\Delta\mu_{bc}}{k_B T}})]. \quad (2.64)$$

In the limit of large kinetic constants $\nu \rightarrow \infty$ this formulation breaks down and v_l diverges. In this case a different boundary condition in addition to Eqs. (2.58) and (2.59) has to be imposed.

²Note that all the preceding relations were obtained in the small slope limit. In contrast, Eqs. (2.61) and (2.62) include finite angles to describe the interface between two substrates.

Figure 2.5: Sketches of the three main case studies discussed in the following chapters. In the axisymmetric geometry, the grey area is a section of the crystal projected along r . Black rectangle: substrate. Light blue: liquid solution.



(a) Dissolution of a single contact induced by an external load. The shape represented is the one observed for a finite exponential disjoining pressure.

(b) Formation of a cavity on the confined surface of a crystal growing on a substrate. Supersaturation outside the contact region: σ . Supersaturation in the center of the contact region: σ_0 .

(c) Crystal growing in a pore. A crystallization pressure normal to the substrate can be observed.

However, we cannot find a suitable condition without solving the evolution of the diffusion field outside the contact region which is beyond the scope of this work.

2.8 Summary

In this chapter, we introduced a general model of growth and dissolution of a confined rigid crystal. This model describes the non-equilibrium dynamics within the contact region using a continuum thin film equation and accounts self-consistently (in the lubrication regime) for surface tension effects, for the microscopic interaction potential between the crystal and the substrate, for surface kinetics and for non-equilibrium transport processes such as diffusion and liquid flow. A number of simplifying assumptions (such as considering an axisymmetric contact) were invoked in order to obtain a description that is simpler both for the interpretation of the results and for numerical efficiency.

Some variants of the model including or not the effect of surface precipitation/dissolution kinetics were discussed. We also introduced the quasi-static approximation which assumes a constant contact size (no lateral expansion or shrinking). We finally presented a method to include the lateral expansion of the contact.

In the following, as illustrated in Fig. 2.5, we will apply these model variants to different problems:

- (a) Pressure solution, Chapter 3: Fast surface kinetics, linearized thermodynamic relation between chemical potential and concentration in 1D ridge or 2D axisymmetric contacts of constant size. Results: effects of the functional form of the disjoining pressure on the morphology within the contact and on the dissolution rates.
- (b) Cavity formation in confined growth, Chapter 4: Fast or slow surface kinetics and linearized thermodynamic relation in an axisymmetric contact of constant size. Results: characterization of the conditions for the formation of a cavity.
- (c) Crystallization force, Chapter 5: Slow surface kinetics, full exponential relation between chemical potential and concentration and no rigid vertical displacement of the crystal ($u_{Cz} = 0$) in an expanding axisymmetric contact. Results: description of the non-equilibrium crystallization force.

The different approximations will be critically discussed throughout this thesis with respect to concrete case studies.

In this chapter, we explore the problem of dissolution under an external load, known as pressure solution. In particular, we focus on the effect of the functional form of substrate-crystal interactions. In steady state, diverging (power-law) repulsions are found to lead to flat contacts with a monotonic increase of the dissolution rate as a function of the load. Forces induced by viscous dissipation then surpass those due to disjoining pressure at large loads. In contrast, finite repulsions (exponential) lead to sharp pointy contacts with a dissolution rate independent of the load and the liquid viscosity. This sharp tip of the profile is regularized by the effect of surface tension. Ultimately, in steady state, the crystal never touches the substrate when pressed against it. This last result is independent of the nature of the crystal-surface interaction.

3.1 Introduction

We presented in the Introduction the phenomenon of stress-induced dissolution or pressure solution. We showed that this phenomenon is important in geological systems [61] and can lead to a complex phenomenology both regarding observed dissolution rates [68, 84, 90] and emerging morphologies [65, 68, 83].

Pressure solution usually takes place at surfaces separated by a thin film of solution from the confining wall (pore surface or other crystal). We also reported that interactions (disjoining pressures) are present between the solid surface and the confining substrate. The effect of such microscopic interactions is however in general ignored in existing continuum modeling approaches [63, 82, 124]. Nevertheless, these interactions should be important since they can combine with the spontaneous remodeling of the surface via dissolution and growth to determine the contact morphology and dynamics. The standard theory describing surface-surface interaction is the DLVO approach [43]. However, DLVO was found to be accurate at all separations only for smooth crystalline surfaces in dilute electrolyte solutions [46]. Indeed, for other surfaces and solutions, significant deviation, especially at short range (few nanometers), were reported in the literature, where different authors have revealed the existence of additional repulsive interactions at short distances (a few nanometers) referred to as hydration forces [46, 48, 49]. These interactions, the exact mathematical form of which is still a matter of debate, are often recognized to be exponentially decaying. Beyond hydration forces, other specific interactions include [43] oscillations at the molecular scale due to liquid ordering, solute-induced effects, depletion effects, etc (see Fig. 1.11b). Owing to this wide variety of behaviors, we here focus on two simple and generic classes of repulsive interaction potentials, with exponential or power-law dependence on

the distance. These two classes of interactions respectively exhibit the fundamental property of inducing finite or diverging forces when the distance vanishes.

Our first goal is to question the role of the form of the interaction potential on the dynamics of pressure solution. A second goal is to identify the consequences of hydrodynamic advection in the thin liquid film. Indeed, in the absence of dissolution or growth, the hydrodynamics of squeezed films (see Section 1.2.1) is known to lead to an evolution of the thickness of the film exhibiting a non-trivial dependence on the solid geometry and dimensionality [42]. The novelty here is that the geometry of the dissolving surface evolves in time, and emerges from a coupling between different forces and mass transport processes at play in the system.

In the framework of the model introduced in the previous chapter, we will focus on the investigation of steady-states surface profiles with a fixed contact area. The dissolution rate is found to increase indefinitely with increasing load in the case of diverging repulsions. Viscosity effects then become relevant for large enough loads. However, in the case of finite repulsions, the dissolution rate is independent both on the viscosity and on the load at large loads.

Moreover, as expected intuitively, the shape of the solid is flattened in the contact region for diverging repulsions. However, we find sharp and pointy contact shapes for finite repulsions. In the limit of large loads, surface tension is found to be irrelevant for diverging repulsions, while it is crucial in the case of finite repulsions to regularize the pointy shapes at small scales.

We have also investigated the effect of dimensionality via the comparison of one-dimensional ridge contacts, and two-dimensional axisymmetric contacts. Dimensionality does not induce any qualitative change in the behavior of pressure solution for diverging repulsions. However, for finite repulsions and when surface tension is neglected, the minimum distance between the dissolving solid and the substrate decreases exponentially with the load in the ridge geometry, while it reaches zero for a finite force in the axisymmetric case. Surface tension then comes into play at large enough loads, and forbids touching contact in the axisymmetric geometry.

3.2 Simulation details

We tackle the problem of pressure solution using the model presented in the previous chapter at constant contact size and in the fast precipitation regime. We expect indeed that given the reduced separation induced by the external load, diffusion should be slower than surface kinetics. This assumption is used in most pressure solution creep models [87]. Inspired by tribology studies [42], we also consider the effect of dimensionality.

For the symmetric ridge (1D), using Eq. (2.51a) with Eq. (2.11) and the linearized Gibbs-Thomson relation $\Delta\mu/(k_B T) \ll 1$, we have

$$\partial_t \zeta = -B \partial_x \left[\zeta \partial_x (\tilde{\gamma} \partial_{xx} \zeta - U'(\zeta)) \right] - u_{Cz}, \quad (3.1)$$

where by definition

$$B = \frac{D \Omega^2 c_0}{k_B T}. \quad (3.2)$$

is an effective mobility combining D the diffusion constant, Ω the volume of crystal type molecules, c_0 the solubility, k_B the Boltzmann constant and T the temperature. Let us recall the expression for the crystal velocity (dissolution rate) u_{Cz} given by

$$2u_{Cz} \int_0^L dx \int_x^L dx' \frac{12\eta x'}{\zeta^3} = F_{Cz}^{1D} + 2 \int_0^L dx U'(\zeta). \quad (3.3)$$

For the axisymmetric contact from Eq. (2.51b) we have to solve

$$2u_{Cz} \pi \int_0^R dr r \int_r^R dr' \frac{6\eta r'}{\zeta(r')^3} = F_{Cz}^{2D} + 2\pi \int_0^R dr r U'(\zeta), \quad (3.4)$$

$$\partial_t \zeta = -B \frac{1}{r} \partial_r \left[r \zeta \partial_r (\tilde{\gamma} \partial_{rr} \zeta + \frac{\tilde{\gamma}}{r} \partial_r \zeta - U'(\zeta)) \right] - u_{Cz}, \quad (3.5)$$

where the quantity proportional to the surface stiffness $\tilde{\gamma}$ is the mean curvature in axial symmetry (see Appendix A.6). As illustrated in the previous chapter, the surface stiffness is given by $\tilde{\gamma} = \gamma(0) + \gamma''(0)$ where $\gamma(\theta)$ is the anisotropic surface energy depending on the angle $\theta = \arctan \partial_r \zeta$ (or in 1D $\theta = \arctan \partial_x \zeta$). Finally, in the following we will assume the quasistatic limit. This approximation is discussed in more details in Section 3.4.4.

3.2.1 Interaction potentials

We chose to study two generic types of repulsive interaction potentials. The first one diverges when the film thickness ζ vanishes

$$U(\zeta) = \frac{A}{\zeta^n}, \quad (3.6)$$

where A is a constant. In practice, numerical results have been obtained with $n = 3$. However, we will keep an arbitrary exponent n in the discussions.

The second type of potential exhibits a finite repulsion when $\zeta \rightarrow 0$

$$U(\zeta) = Ae^{-\frac{\zeta}{\lambda}}, \quad (3.7)$$

where λ is a decay length representing for instance the Debye length in the case of electrostatic interactions [43].

The essential difference between these potentials is that Eq. (3.6) leads to an infinite repulsion force when $\zeta \rightarrow 0$, whereas this force is finite for Eq. (3.7).

3.2.2 Normalization

In order to perform simulations and to analyze the results of the model, we write the model equations in a dimensionless form and identify the relevant dimensionless parameters. A similar procedure, with slight variations in the choice of the normalization, will be adopted in all the following chapters.

For conciseness, we only show the scaled equations in 1D. All variables appearing in normalized units are labeled with a top bar. In the case of the power law repulsion, Eq. (3.6) with $n = 3$, we have

$$\partial_{\bar{t}} \bar{\zeta} = -\partial_{\bar{x}} \left[\bar{\zeta} \partial_{\bar{x}} \left(\partial_{\bar{x}\bar{x}} \bar{\zeta} + \frac{1}{\bar{\zeta}^4} \right) \right] - \bar{u}_{Cz}, \quad (3.8a)$$

$$\bar{u}_{Cz} \int_0^{\bar{L}} d\bar{x} \int_{\bar{x}}^{\bar{L}} d\bar{x}' \frac{24\bar{\eta}\bar{x}'}{\bar{\zeta}^3} = \bar{F}_{Cz} - 2 \int_0^{\bar{L}} d\bar{x} \frac{1}{\bar{\zeta}^4}, \quad (3.8b)$$

where \bar{u}_{Cz} , $\bar{\eta}$ and \bar{F} are the rescaled velocity, viscosity and external force, respectively. For the exponential repulsion Eq. (3.7), we have

$$\partial_{\bar{t}} \bar{\zeta} = -\partial_{\bar{x}} \left[\bar{\zeta} \partial_{\bar{x}} \left(\partial_{\bar{x}\bar{x}} \bar{\zeta} + e^{-\bar{\zeta}} \right) \right] - \bar{u}_{Cz}, \quad (3.9a)$$

$$\bar{u}_{Cz} \int_0^{\bar{L}} d\bar{x} \int_{\bar{x}}^{\bar{L}} d\bar{x}' \frac{24\bar{\eta}\bar{x}'}{\bar{\zeta}^3} = \bar{F}_{Cz} - 2 \int_0^{\bar{L}} d\bar{x} e^{-\bar{\zeta}}. \quad (3.9b)$$

We start by defining the dimensionless repulsion strength \bar{A} . For the exponential potential we set $\bar{A} = A/\tilde{\gamma}$, while for power-law repulsions with the case $n = 3$, we use $\bar{A} = A/(\tilde{\gamma}\lambda^3)$. The normalized film thickness is $\bar{\zeta} = \zeta/\lambda$, and the normalized coordinates are $\bar{x} = x\bar{A}^{1/2}/\lambda$, $\bar{y} = y\bar{A}^{1/2}/\lambda$. The normalized time is defined as $\bar{t} = tB\tilde{\gamma}\bar{A}^2/\lambda^3$. Notice that the scale λ is imposed by the expression of U in the case of an exponential repulsion, while it is an arbitrary lengthscale corresponding to the actual film width in the case of power-law repulsions.

The normalized repulsion strength \bar{A} comes into play in spatiotemporal scales but not as a parameter of the normalized equations. As a consequence, it cannot change the model behavior

qualitatively. The only parameters explicitly appearing in the normalized equations are the normalized viscosity $\bar{\eta}$, and external load \bar{F}_{Cz} . The normalized viscosity reads

$$\bar{\eta} = \frac{B}{\lambda^2} \eta = \frac{D\Omega^2 c_0}{\lambda^2 k_B T} \eta.$$

Since the loads have different dimensionality in 1D (force per unit length) and 2D (force), their normalization is different

$$\begin{aligned} \bar{F}_{Cz}^{1D} &= \frac{F_{Cz}^{1D}}{\bar{\gamma} \bar{A}^{1/2}}, \\ \bar{F}_{Cz}^{2D} &= \frac{F_{Cz}^{2D}}{\bar{\gamma} \lambda}. \end{aligned}$$

The boundary conditions introduce three additional dimensionless parameters. The normalized system size

$$\bar{L} = \frac{L \bar{A}^{1/2}}{\lambda}, \quad \text{or} \quad \bar{R} = \frac{R \bar{A}^{1/2}}{\lambda}, \quad (3.10)$$

the normalized film thickness at the boundary

$$\bar{\zeta}_{bc} = \frac{\zeta_{bc}}{\lambda}, \quad (3.11)$$

and the normalized supersaturation

$$\bar{\sigma}_{bc} = \frac{k_B T \lambda}{A \bar{\gamma} \Omega} \sigma_{bc}. \quad (3.12)$$

Below, all simulations are performed with normalized variables and coordinates. However, the analysis of the equations is performed in physical coordinates to make the physical interpretation more transparent.

3.2.3 Simulations parameters

Simulations are performed with $\bar{L}, \bar{R} = 100$, substrate position $\bar{h}_s = 2$, film thickness at the boundary $\bar{\zeta}_{bc} = 12$, and boundary supersaturation $\sigma_{bc} = 0$. The discretization bin size is $\Delta \bar{x} = 0.2$ for most simulations. However in some cases, to be able to resolve the contact shape at very high external forces (see Section 3.3.2 and Fig. 3.6), it was necessary to increase the spatial resolution up to 16 times. Details on the numerical scheme are given in Appendix B.1.

The simulations were always started with a flat profile (see top panel of Fig. 3.1). When applying a concentration higher than the equilibrium one at the boundary, we observe crystal growth: the crystal translates downward by addition of growth units at the surface, and $u_{Cz} < 0$. When applying an external load, F_{Cz} with the sign in the positive direction hence pushing the crystal towards the substrate, we observe dissolution, i.e. pressure solution and $u_{Cz} > 0$. The latter case is the main focus of this chapter.

3.3 Results

As an illustrative example, we show in Fig. 3.1 the numerical solution for the profile of a 1D ridge obeying Eqs. (3.1) and (3.3) when an external load pushes the crystal upwards against the substrate, and when the interaction is in the form of a singular repulsion Eq. (3.6). A similar shape is observed when solving Eqs. (3.4) and (3.5) for an axisymmetric contact looking at the section along the radius. The simulation shows that the interface profile reaches a steady state characterized by a constant crystal velocity (dissolution rate) and fixed interface position.

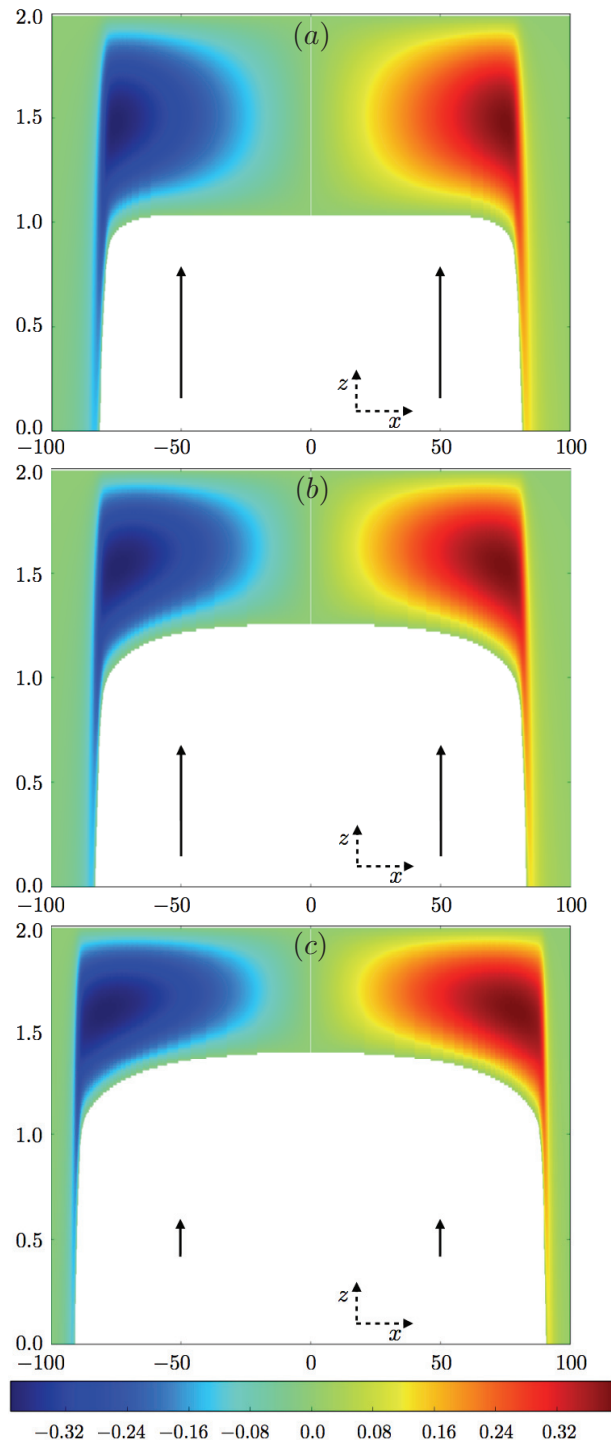


Figure 3.1: Snapshots of the numerical solution of Eq. (3.1) representing a dissolving contact ridge (1D). Size of the simulation box $\bar{L} = 100$ (physical size $L \approx 1\mu\text{m}$) under an external pressure $p = 26\text{MPa}$. The viscosity is $\bar{\eta} = 0.5$. The crystal-substrate interaction is diverging at contact and given by Eq. (3.6). The crystal is in white and the black arrows are proportional to the crystal velocity u_{Cz} . The time increases from the top panel to the bottom one. (a): initial condition. As an example using physical constants related to calcite (see Section 3.4.1), physical time frames are: (b) 10s, (c) 6.7min. The colormap (in arbitrary units) shows the amplitude of the x component of liquid velocity field \mathbf{u}_{Lxy} , as obtained from Eqs. (2.25) and (2.40). The vertical scale is in nanometers. The substrate is located at $h_s = 2\text{nm}$.

As discussed earlier in Section 2.3.1, in the contact region and in the absence of blow-up of the curvature, we expect the surface tension contribution to the interfacial chemical potential to be small in front of the disjoining pressure term. Since large loads imply large $U'(\zeta)$ from the force balance Eqs. (3.3) and (3.4), this further suggests that surface tension effects are negligible. Discarding this contribution, steady-state solutions with a constant profile i.e. $\partial_t \zeta = 0$, obey respectively in 1D or 2D

$$0 = u_{cz} - B\partial_x[\zeta\partial_x U'(\zeta)], \quad (3.13a)$$

$$0 = u_{cz} - \frac{B}{r}\partial_r[r\zeta\partial_r U'(\zeta)]. \quad (3.13b)$$

This equation is integrated as

$$\frac{x^2}{2B}u_{cz} = \tilde{U}(\zeta(r)) - \tilde{U}(\zeta_0), \quad (3.14a)$$

$$\frac{r^2}{4B}u_{cz} = \tilde{U}(\zeta(r)) - \tilde{U}(\zeta_0), \quad (3.14b)$$

where $\zeta_0 = \zeta(0)$, and $\tilde{U}(\zeta)$ is defined via the relation

$$\tilde{U}'(\zeta) = \zeta U''(\zeta), \quad (3.15)$$

which, up to an additive constant leads to $\tilde{U}(\zeta) = \zeta U'(\zeta) - U(\zeta)$. Since we expect physically that the interaction potential tends to a constant as $\zeta \rightarrow \infty$, i.e. that $U(\infty)$ is a constant, then $\tilde{U}(\infty)$ should also be a constant. Therefore, \tilde{U} cannot increase indefinitely when $\zeta \rightarrow \infty$ on the r.h.s. of Eqs. (3.14a) and (3.14b). As a consequence, there are finite x_m or r_m where $\zeta \rightarrow \infty$ and they obey

$$\frac{x_m^2}{2B}u_{cz} = \tilde{U}(\infty) - \tilde{U}(\zeta_0), \quad (3.16a)$$

$$\frac{r_m^2}{4B}u_{cz} = \tilde{U}(\infty) - \tilde{U}(\zeta_0). \quad (3.16b)$$

Since ζ diverges at some finite distance x_m or r_m from the center of the contact, the size of the contact in steady-state pressure solution is always finite.

In the limit of large forces, we expect ζ_0 to become small. The situation then turns out to be very different depending on how $\tilde{U}(\zeta_0)$ behaves when ζ_0 is small. The following sections discuss separately the cases of finite and diverging interaction potentials $U(\zeta)$, corresponding to finite or diverging $\tilde{U}(\zeta)$ as $\zeta \rightarrow 0$.

3.3.1 Singular repulsion: power law case

Let us start with the analysis of the results for a singular power-law repulsion between the crystal surface and the substrate. Combining Eq. (3.6) and Eq. (3.15) we find

$$\tilde{U}(\zeta) = \frac{-(n+1)A}{\zeta^n}. \quad (3.17)$$

Inserting this expression in Eqs. (3.14a) and (3.14b), provides us with the steady-state profile:

$$\zeta(x) = \left(\frac{\zeta_0^n}{1 - x^2/x_m^2} \right)^{1/n}, \quad (3.18a)$$

$$\zeta(r) = \left(\frac{\zeta_0^n}{1 - r^2/r_m^2} \right)^{1/n}. \quad (3.18b)$$

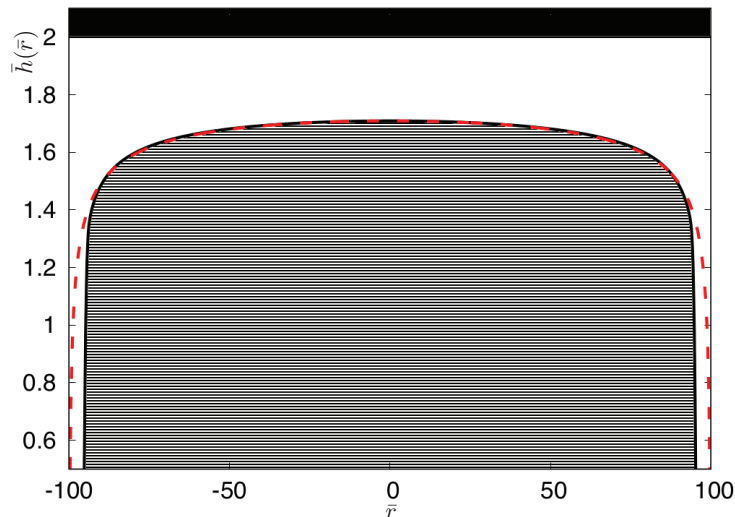


Figure 3.2: Flattened steady-state observed for a singular power-law crystal-substrate repulsion. Cross section of the steady state profile projected along \bar{r} (solid line) dissolving under an external load, $\bar{F}_{Cz} = 10^8$, at $\bar{\eta} = 1$ against a flat substrate ($\bar{h}_s = 2$). Geometry: axisymmetric contact in a simulation box of size $\bar{R} = 100$. The interaction with the substrate is a singular power law repulsion, Eq. (3.6) with $n = 3$. The red dashed line is the analytical prediction from Eq. (3.18) with $r_m = R$ and $\zeta_0 \approx 0.29$ as a fitting parameter.

These profiles diverge at $x = x_m$ or $r = r_m$, which is related to the minimum distance in the contact via Eqs. (3.16a) and (3.16b)

$$x_m^2 = \frac{2B(n+1)A}{\zeta_0^n u_{Cz}}, \quad (3.19a)$$

$$r_m^2 = \frac{4B(n+1)A}{\zeta_0^n u_{Cz}}. \quad (3.19b)$$

The distance x_m or r_m at which the profile diverges should a priori be distinguished from the size of the contact region. Indeed far away from the substrate, the influence of the potential vanishes, and as a consequence surface-tension effects should become dominant, so that Eq. (3.14) is not valid anymore. Let us define L_c as the half-width of the contact region in 1D, and R_c as the radius of the contact region in 2D. An intuitive definition of the contact region is the zone which is close enough to the substrate to be under the influence of the interaction potential U .

For large contacts, we expect that the distance separating x_m and L_c , or r_m and R_c should be negligible as compared to the size of the contact region. As a consequence, we assume $x_m \approx L_c$ or $r_m \approx R_c$. Furthermore, we perform simulations with a fixed ζ_{bc} , which is large as compared to ζ_0 but small as compared to the size L , or R of the simulation box. Thus, the contact region should fill most of the simulation box, and finally, we expect $x_m \approx L_c \approx L$ or $r_m \approx R_c \approx R$. In Fig. 3.2 we show the steady state cross section obtained from the simulation (solid line) at large times, which is in good agreement with Eq. (3.18) using $r_m = R$ (dashed line) and ζ_0 as a fitting parameter. Using Eq. (3.19) and the fitted value of ζ_0 we obtain a value for u_{Cz} . For instance in 2D with $\bar{F} = 10^8$ and $\bar{R} = 100$, this procedure leads to $\bar{\zeta}_0 = 0.290$ and $\bar{u}_{Cz} = 0.022$ to be compared with $\bar{\zeta}_0 = 0.291$ and $\bar{u}_{Cz} = 0.016$ measured directly in the numerical solution of the full model. The agreement with the numerical results improves as the external load is increased. A similar agreement is obtained in 1D. As a consequence, the profile is well predicted at large forces, and we can safely use it in the force balance equation.

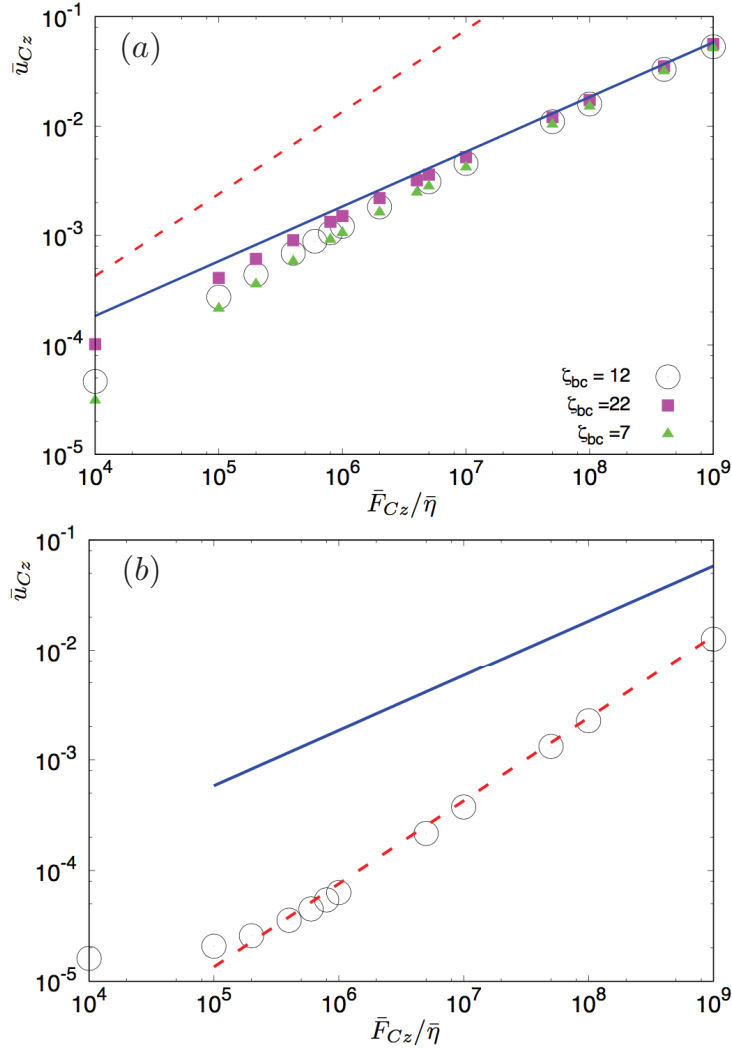


Figure 3.3: Dissolution rate observed for a (singular) power-law repulsion ($n = 3$) as a function of the applied load. Geometry: axisymmetric contact. Lines represent asymptotic analytical predictions with $\bar{R}_c = \bar{R} = 100$: solid blue line, hydrodynamic regime Eq. (3.22b); dashed red line, diffusion regime Eq. (3.23b). (a): $\bar{\eta} = 1$, the symbols show simulation results obtained using different boundary thickness ζ_{bc} . (b): $\bar{\eta} = 10^{-3}$. The results are shown in normalized units.

In 1D, using Eq. (3.18) with Eq. (3.19a) and $x_m = L_c$ we obtain from force balance Eq. (3.3)

$$\begin{aligned} \frac{F_{Cz}^{1D}}{L_c} &= 24\eta\phi\left(\frac{n+3}{n}\right)\frac{n\sqrt{\pi}}{(n+3)}\left(\frac{1}{BA(n+1)}\right)^{\frac{3}{n}}\left(\frac{L_c^2}{2}u_{Cz}\right)^{\frac{n+3}{n}} \\ &+ \phi\left(\frac{n+1}{n}\right)2n\sqrt{\pi}A^{-\frac{1}{n}}\left(\frac{1}{B(n+1)}\right)^{\frac{n+1}{n}}\left(\frac{L_c^2}{2}u_{Cz}\right)^{\frac{n+1}{n}}, \end{aligned} \quad (3.20)$$

where

$$\phi(z) = \frac{\Gamma(1+z)}{2\Gamma(\frac{3}{2}+z)},$$

with Γ the Euler-Gamma function.

Similarly, in 2D force balance Eq. (3.4) imposes

$$\begin{aligned} \frac{F_{Cz}^{2D}}{\pi R_c^2} &= 12\eta\frac{n^2}{(2n+3)(n+3)}\left(\frac{1}{BA(n+1)}\right)^{\frac{3}{n}}\left(\frac{R_c^2}{4}u_{Cz}\right)^{\frac{n+3}{n}} \\ &+ \frac{n^2}{2n+1}A^{-\frac{1}{n}}\left(\frac{1}{B(n+1)}\right)^{\frac{n+1}{n}}\left(\frac{R_c^2}{4}u_{Cz}\right)^{\frac{n+1}{n}}, \end{aligned} \quad (3.21)$$

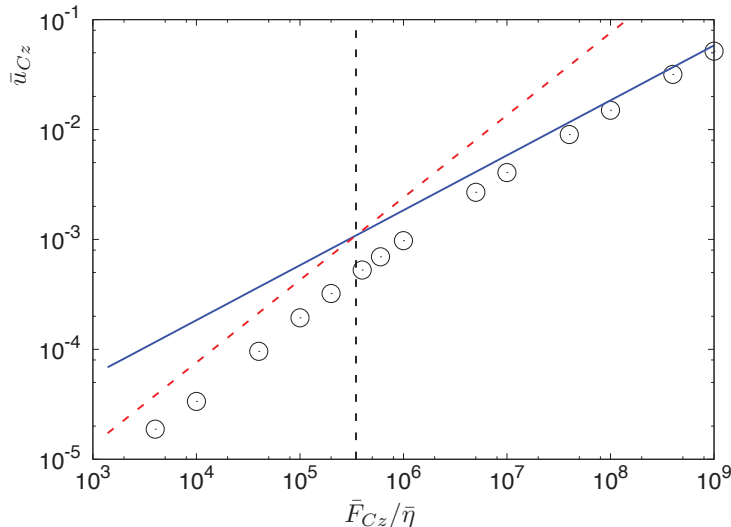


Figure 3.4: Dissolution rate as a function of the applied load for power law (singular) repulsion. Geometry: axisymmetric contact. The viscosity is $\bar{\eta} = 10^{-1}$. Lines represent analytical predictions with $\bar{R}_c = \bar{R} = 100$, circles indicate simulation results. Solid blue line, hydrodynamic regime Eq. (3.22b); dashed red line, diffusion regime Eq. (3.23b). The black dashed line represents the expected threshold between the two regimes according to Eq. (3.25). The results are shown in normalized units.

(some technical details about the derivation of this relation can be found in Appendix C.1.1). Using 3.21, we find two separate regimes depending on the value of η : For large viscosities we identify a *hydrodynamic regime*

$$u_{Cz}^{1D} = C_h^{1D} L_c^{-\frac{3n+6}{n+3}} \left(\frac{F_{Cz}^{1D}}{\eta} \right)^{\frac{n}{n+3}}, \quad (3.22a)$$

$$u_{Cz}^{2D} = C_h^{2D} R_c^{-\frac{4n+6}{n+3}} \left(\frac{F_{Cz}^{2D}}{\eta} \right)^{\frac{n}{n+3}}, \quad (3.22b)$$

while for small viscosities a *diffusion regime* is found, with

$$u_{Cz}^{1D} = C_d^{1D} L_c^{-\frac{3n+2}{n+1}} (F_{Cz}^{1D})^{\frac{n}{n+1}}, \quad (3.23a)$$

$$u_{Cz}^{2D} = C_d^{2D} R_c^{-\frac{4n+2}{n+1}} (F_{Cz}^{2D})^{\frac{n}{n+1}}. \quad (3.23b)$$

The expressions of the constants C_h^{1D} , C_h^{2D} , C_d^{1D} , C_d^{2D} are reported in Appendix C.1.1. In Fig. 3.3 we compare the prediction Eqs. (3.22b) and (3.23b) using $R_c = R$ (solid and dashed lines) and the results in 2D obtained from the complete numerical solution of the model (circles). The analytical prediction is in good agreement with the numerical solution for large external loads.

In order to probe the sensitivity of the results with respect to the value of the film thickness at the boundary $\bar{\zeta}_{bc}$, we monitored the consequences of the variation of $\bar{\zeta}_{bc}$. We found small quantitative effects but no influence on the qualitative behavior of the relevant observables. This is exemplified with the variations of the dissolution rates in the top panel of Fig. 3.3.

Using Eq. (3.19) to eliminate u_{Cz} in the expression of the force Eqs. (3.20) and (3.21), a relation between external load and the minimum thickness ζ_0 can be obtained, which is found to be in good agreement with the simulations. For the sake of concision, the expression of this relation in 2D and its comparison with the numerical solution of the full model are shown in Appendix C (Eq. (C.8), and Fig. C.1). As an additional remark Eqs. (3.20) and (3.21) show that there is no substantial difference between one and two dimensions except, as expected from dimensional analysis, a different scaling of F_{Cz} and u_{Cz} with the contact size.

Finally, it is interesting to assess what is the critical length and load separating the diffusive and hydrodynamic regimes. Equating the expressions of the velocity in the two regimes, for the

ridge case we find that the critical size above which the force is dominated by diffusion effects is given by

$$L_* = B_{1D} \eta^{\frac{n+1}{2}} F_{Cz}^{1D}, \quad (3.24)$$

while for the axisymmetric contact

$$R_* = B_{2D} \eta^{\frac{n+1}{4}} (F_{Cz}^{2D})^{1/2}, \quad (3.25)$$

where B_{1D} and B_{2D} are constants reported in Appendix C.1.1. Hence, at a fixed force, large contacts will be dominated by diffusion. Also, as the external load is increased at constant contact size the hydrodynamic term in the force balance become dominant. Once again, good agreement with the simulations is found as illustrated in Fig. 3.4. Here using Eq. (3.25), with $\bar{R}_* = 100$, $\bar{\eta} = 0.1$, $n = 3$ (since in simulations units $B = 1$ and $A = 1/3$, $B_{2D} \approx 5.4$) we expect the diffusion limited regime approximately for $\bar{F}_{Cz} < 3.5 \times 10^4$ and the hydrodynamic regime otherwise. The threshold indicated in the figure by the dashed vertical line corresponds to the observed trend.

3.3.2 Finite repulsion: exponential case

In the case of an exponential repulsion, $\tilde{U}(\zeta = 0)$ is finite. As a consequence, the behavior of steady-state solutions is different. First, the dissolution rate is asymptotically independent of the load. Second, the shape of the contact is sharp and pointy. Third, in the absence of surface tension, touching contact (i.e. $\zeta = 0$) would be observed in 2D for a finite loading force but not in 1D. Finally, as opposed to what observed so far, surface tension becomes relevant at large enough forces preventing contact in 2D.

Without surface tension

Neglecting surface tension we proceed in a similar way as in the power-law case. Recalling Eq. (3.15) and using the exponential interaction potential Eq. (3.7), we find

$$\tilde{U}(\zeta) = -\frac{A}{\lambda}(\lambda + \zeta)e^{-\frac{\zeta}{\lambda}}. \quad (3.26)$$

As opposed to the power-law repulsion case, the function $\tilde{U}(\zeta)$ cannot be inverted explicitly. Therefore, ζ cannot be explicitly obtained from Eq. (3.14). However, since \tilde{U} is a monotonic function of ζ , it is still possible to compute r as a function of ζ without ambiguity from Eq. (3.14).

In the large force limit since we expect $\zeta_0 \ll \lambda$ (this will be confirmed below using force balance) and since $\tilde{U}(0)$ is finite, we find that the dissolution rate reaches a constant value independent of the load and of the viscosity. Indeed, from Eq. (3.16):

$$u_{Cz}^{1D} \approx B \frac{2A}{L_c^2} \left(1 + \frac{\zeta_0}{\lambda}\right) e^{-\frac{\zeta_0}{\lambda}}, \quad (3.27a)$$

$$u_{Cz}^{2D} \approx B \frac{4A}{R_c^2} \left(1 + \frac{\zeta_0}{\lambda}\right) e^{-\frac{\zeta_0}{\lambda}}. \quad (3.27b)$$

Taking the limit $\zeta_0 \rightarrow 0$, we find

$$u_{Cz}^{1D} = B \frac{2A}{L_c^2}, \quad (3.28a)$$

$$u_{Cz}^{2D} = B \frac{4A}{R_c^2}. \quad (3.28b)$$

Again assuming that $L_c \approx L$, or $R_c \approx R$ at large forces, these results are confirmed in Fig. 3.5 from the comparison with the numerical solution of the full model. The different viscosities, indicated by circles ($\bar{\eta} = 1000$), triangles ($\bar{\eta} = 1$) and squares ($\bar{\eta} = 0.001$), affect the absolute value of the applied force needed to reach the plateau but not the plateau value itself.

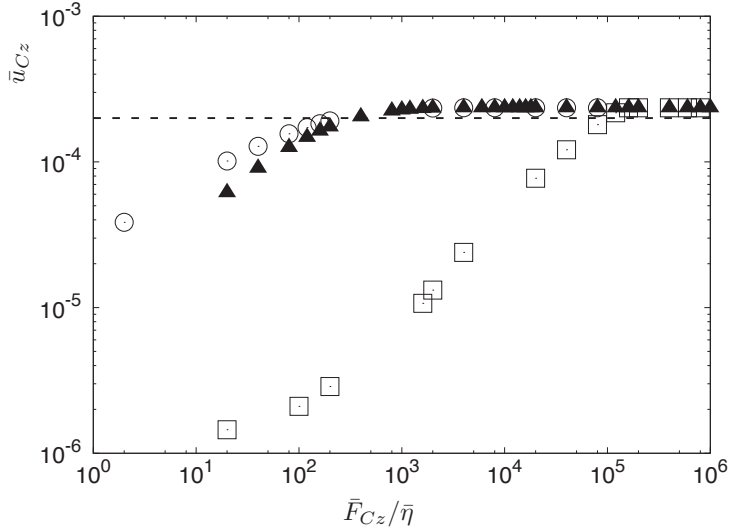


Figure 3.5: Dissolution rate as a function of the external load for an exponentially decaying crystal-substrate interaction which is finite at touching contact. Geometry: 1D ridge contact. Triangles $\bar{\eta} = 0.5$, squares $\bar{\eta} = 5 \times 10^{-4}$, circles $\bar{\eta} = 5 \times 10^2$. Dashed line: analytical prediction Eq. (3.28a) using $\bar{L}_c = \bar{L} = 100$ and $\zeta_0/\lambda = 0$. The results are in normalized units.

A second consequence arising from the finiteness of the exponential interaction is the sharp pointy shape of the steady-state profile showed in Fig. 3.6. Indeed, since $\tilde{U}'(\zeta = 0) = 0$ from Eq. (3.15), we have $\tilde{U}(\zeta) \approx \tilde{U}(0) + \tilde{U}''(0)\zeta^2/2$ for $\zeta \ll \lambda$. Using this expansion into Eq. (3.14) and letting $\zeta_0 \rightarrow 0$, we find that the profile ζ_{sing} in the center of the contact region is a singular wedge in 1D and a cone in 2D :

$$\zeta_{sing} \approx \left(\frac{u_{Cz}}{B\tilde{U}''(0)} \right)^{1/2} |x| = \left(\frac{u_{Cz}}{BA} \right)^{1/2} \lambda |x|, \quad (3.29a)$$

$$\zeta_{sing} \approx \left(\frac{u_{Cz}}{2B\tilde{U}''(0)} \right)^{1/2} |r| = \left(\frac{u_{Cz}}{2BA} \right)^{1/2} \lambda |r|. \quad (3.29b)$$

When $\zeta_0 \ll \lambda$, the complete profile for arbitrary ζ (i.e. smaller or larger than λ) can be obtained from Eqs. (3.14) and (3.26). Using the axisymmetric contact, with $R_c = R$ and u_{Cz} given by Eq. (3.28b) this expression (dotted blue line) is found to be in good agreement with the simulation in Fig. 3.6. Better agreement (red dashed line) can be reached using the numerical value of u_{Cz} obtained from the simulation (which is equivalent to assuming a slightly smaller effective size, $R_c < R$). Nevertheless as shown by the inner panel in Fig. 3.6, close to the tip the numerical solution is smooth and exhibits a parabolic shape. This regularization of the singular tip is discussed in the next section and is due to the contribution of the surface tension.

Using Eq. (3.3), force balance in 1D now reads:

$$\frac{F_{Cz}^{1D}}{L_c} = \left[12\eta B \frac{A}{\lambda^3} \psi_1\left(\frac{\zeta_0}{\lambda}\right) + \frac{A}{\lambda} \psi_2\left(\frac{\zeta_0}{\lambda}\right) \right] \left(\frac{e^{\frac{\zeta_0}{\lambda}}}{1 + \frac{\zeta_0}{\lambda}} \right)^{\frac{1}{2}}, \quad (3.30)$$

where the function ψ_1 and ψ_2 defined in Eqs. (C.14) and (C.15) exhibit the following limits

$$\lim_{z \rightarrow 0} \psi_1(z) = \sqrt{2} \ln \frac{1}{z} + C_1,$$

$$\lim_{z \rightarrow 0} \psi_2(z) = C_2,$$

with $C_1 \approx 1.645$ and $C_2 \approx 0.8398$. It follows that, when $\zeta_0 \ll \lambda$ and $\zeta_0 \ll \lambda \exp[-C_2/(12\sqrt{2}\bar{\eta})]$, we have

$$F_{Cz}^{1D} \approx 12\sqrt{2}\bar{\eta} \frac{L_c A}{\lambda} \ln\left(\frac{\lambda}{\zeta_0}\right). \quad (3.31)$$

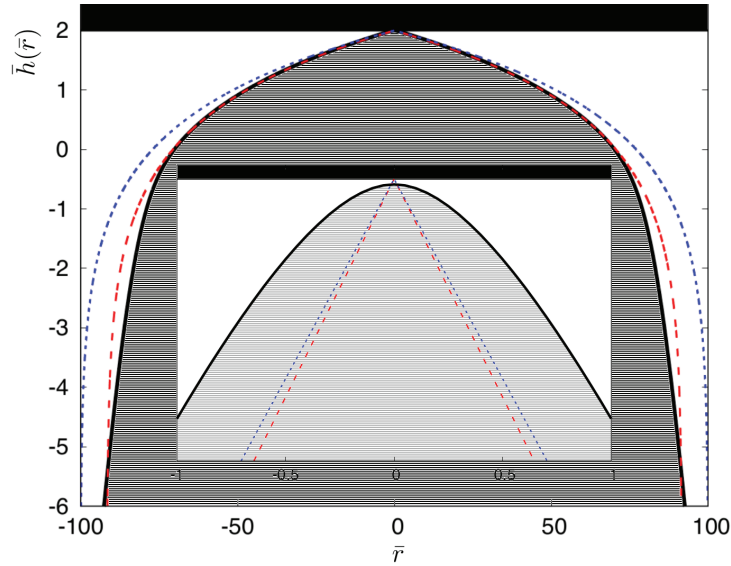


Figure 3.6: Pointy steady-state for a (finite) exponential repulsion. Cross section of the steady state profile projected along \bar{r} (solid line) dissolving under an external load $\bar{F}_{Cz} = 1.7 \times 10^5$, at $\bar{\eta} = 1$ against a flat substrate ($\bar{h}_s = 2$). Geometry: axisymmetric contact in a simulation box of size $\bar{R} = 100$. The interaction with the substrate is a finite exponential repulsion, Eq. (3.7). Blue dotted line: analytical prediction Eq. (3.5) assuming the contact area to be equal to the surface size R . Red dashed line: analytical prediction Eq. (3.5) with a smaller contact size R_c . The inner plot shows a zoom of the tip.

This relation indicates that the minimum distance in the contact region decreases exponentially with the applied load in 1D. The prediction Eq. (3.30) using $L_c = L$, which is represented in Fig. 3.7 by the red solid line, compares well with the numerical results (red circles) when ζ_0 is not too small. Note that this type of asymptotic logarithmic behavior of the force with respect to the minimum separation is reminiscent of the 1D inclined slider bearing discussed in Section 1.2.1 [42].

In addition, we obtain in 2D (some details of the derivation are reported in Appendix C.1.2)

$$\frac{F_{Cz}^{2D}}{\pi R_c^2} = \left[12\eta B \frac{A}{\lambda^3} \psi\left(\frac{\zeta_0}{\lambda}\right) \frac{e^{\frac{\zeta_0}{\lambda}}}{1 + \frac{\zeta_0}{\lambda}} + \frac{A}{4\lambda} \left(\frac{2\zeta_0}{\lambda} + 1\right) \frac{e^{-\frac{\zeta_0}{\lambda}}}{1 + \frac{\zeta_0}{\lambda}} \right], \quad (3.32)$$

where the function ψ obeys

$$\lim_{z \rightarrow 0} \psi(z) = (1 - \ln 2).$$

Hence, within this approximation, the LC interface touches the substrate (i.e. $\zeta_0 = 0$) for a finite force

$$F_c^{2D} = \left[12\eta B \frac{A}{\lambda^3} (1 - \ln(2)) + \frac{A}{4\lambda} \right] \pi R_c^2. \quad (3.33)$$

The external force is plotted as a function of ζ_0 in Fig. 3.7. Equation (3.32) with $R_c = R$ is represented by the blue solid line and has to be compared with the blue squares obtained by direct numerical integration. Once again, Eq. (3.32) agrees with the numerical results for external forces that are not too large: $F_{Cz}^{2D} < F_c^{2D}$.

With surface tension

An inspection of Fig. 3.7 reveals that the agreement between the predicted force-minimum distance relation and the full numerical solution of thin film equations is accurate only when the forces are not too large. However, as we keep increasing the external load, this prediction (solid lines) fails to reproduce the numerical results. As anticipated previously, the shape of the crystal close to the tip (see inner panel of Fig. 3.6) is not well described by Eq. (3.16). Indeed, as $\zeta_0 \rightarrow 0$,

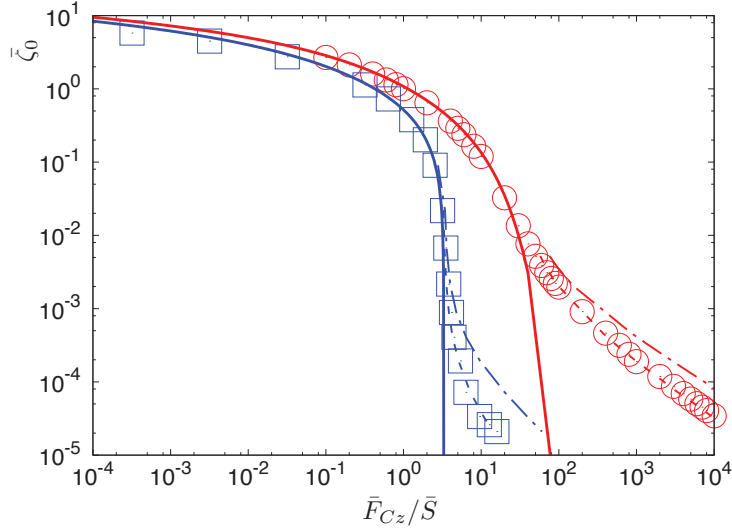


Figure 3.7: Minimum film thickness of the liquid film as a function of the applied load. The plot shows the minimum distance $\bar{\zeta}_0$ between the crystal and the substrate versus the external load normalized by surface area \bar{S} (scaled pressure). Red, ridge contact (1D); blue, axisymmetric contact (2D). Circles (1D) and squares (2D) show the numerical results; Solid lines report the analytical predictions neglecting surface tension Eqs. (3.30) and (3.32) blue and using $\bar{L}_c = \bar{L} = 100$, $\bar{R}_c = \bar{R} = 100$; Dashed lines: prediction adding the singular contribution of the surface tension term Eqs. (3.35a) and (3.35b) to the previous expression, and using the parameters u_{Cz} and $\partial_{xx}\zeta_0$ or $\partial_{rr}\zeta_0$ from the simulations. Dashed-dotted lines: full analytical prediction using Eqs. (3.37a) and (3.37b). 1D viscosity, $\bar{\eta} = 0.5$; 2D viscosity, $\bar{\eta} = 1$. The results are in normalized units. The critical force in 2D Eq. (3.33) provides the maximum value of $\bar{F}_{Cz}^{2D}/\bar{S}$ for the solid blue line and corresponds to $p \approx 3.3\text{MPa}$.

the curvature at the tip diverges, leading to the singular pointy shape reported in Eq. (3.29). Thus, surface tension effects proportional to the curvature become relevant.

We here resort to a simple matching procedure to account for the consequences of surface tension. First, in the tip region for $x < x_*$ or $r < r_*$, where x_* and r_* are the tip width in 1D and 2D respectively, a Taylor expansion of ζ leads to:

$$\zeta^{tip} = \zeta_0 + \frac{x^2}{2} \partial_{xx}\zeta_0, \quad (3.34a)$$

$$\zeta^{tip} = \zeta_0 + \frac{r^2}{2} \partial_{rr}\zeta_0, \quad (3.34b)$$

where $\partial_{rr}\zeta_0$ and $\partial_{xx}\zeta_0$ are the second derivatives of ζ calculated at $x = 0$ or $r = 0$.

Using this solution let us compute the contribution of the tip region to force balance Eqs. (3.3) and (3.4). We obtain

$$F_{\text{tip}}^{1D} = 2 \frac{Ax_*}{\lambda} \left(1 - \frac{\zeta_0}{\lambda} - \partial_{xx}\zeta_0 \frac{x_*^2}{6\lambda} \right) + \eta \frac{6\pi u_{Cz}}{\sqrt{2}(\partial_{xx}\zeta_0)^{3/2} \zeta_0^{3/2}}, \quad (3.35a)$$

$$F_{\text{tip}}^{2D} = \frac{\pi Ar_*^2}{\lambda} \left(1 - \frac{\zeta_0}{\lambda} - \partial_{rr}\zeta_0 \frac{r_*^2}{4\lambda} \right) + \eta \frac{6\pi u_{Cz}}{(\partial_{rr}\zeta_0)^2 \zeta_0}, \quad (3.35b)$$

where we used $\zeta/\lambda \ll 1$ in the tip region. From this expression, it appears that, if x_* or r_* is not increasing too fast when the load increases and $\zeta_0 \rightarrow 0$, the dominant term is the one proportional to the viscosity.

To confirm the validity of this statement, we checked that the increase of the force at small ζ_0 is well predicted by adding the singular contribution corresponding to the last term of Eqs. (3.35a) and (3.35b) to the previous expressions. The result reported in Fig. 3.7, agrees well with the deviations at small ζ_0 . However, this relation is still not fully predictive, since we used $\partial_{xx}\zeta_0$

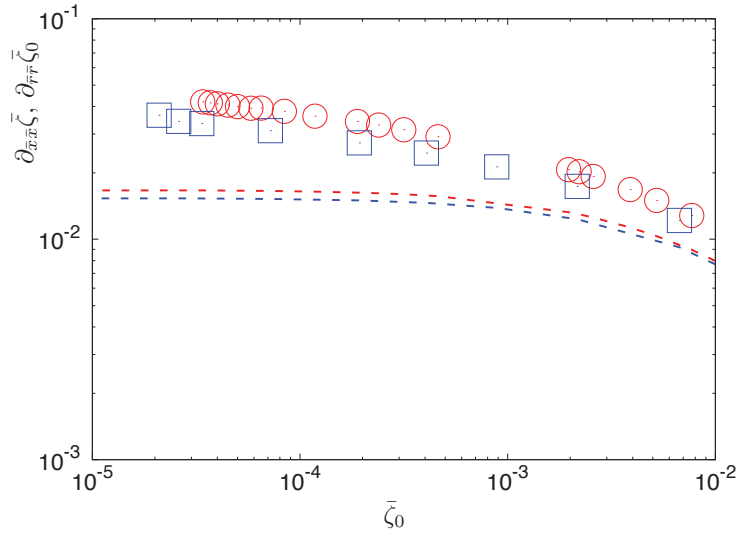


Figure 3.8: Curvature at the tip as a function of the tip-substrate gap $\bar{\zeta}_0$. Red circles: simulations result for the wedge contact (1D); Blue squares: simulations result for the axisymmetric conical contact (2D). Sizes of the simulation boxes are $\bar{L} = \bar{R} = 100$; dashed red and blue lines analytical prediction using the solution of Eq. (C.26), Eq. (C.20), respectively using the the assumption $L_c \approx L$, $R_c \approx R$. The results are in normalized units.

and $\partial_{rr}\zeta_0$ obtained from the numerical solution. In order to find an additional relation linking ζ_0 and $\partial_{xx}\zeta_0$ or $\partial_{rr}\zeta_0$, we match the solutions far from and close to the tip.

Far from the tip, we assume a small deviation $\delta\zeta$ from the singular solution Eq. (3.29), leading to $\zeta = \zeta_{sing} + \delta\zeta$. To find an expression for $\delta\zeta$ we insert the previous relation into the full steady-state differential equation in the presence of curvature terms

$$0 = u_{Cz} + B\partial_x \left[\zeta \left(\tilde{\gamma} \partial_{xx} \zeta - U'(\zeta) \right) \right], \quad (3.36a)$$

$$0 = u_{Cz} + B \frac{1}{r} \partial_r \left[r \zeta \left(\tilde{\gamma} \partial_{rr} \zeta + \frac{\tilde{\gamma}}{r} \partial_r \zeta - U'(\zeta) \right) \right], \quad (3.36b)$$

for the 1D and 2D respectively. Matching the height and the slope of the tip solution Eq. (3.34) with the perturbative solution outside the tip region $\zeta = \zeta_{sing} + \delta\zeta$ at some position x_* or r_* leads to two equations. These two equations are used to obtain x_* or r_* , and $\partial_{xx}\zeta_0$ or $\partial_{rr}\zeta_0$, as a function of ζ_0 . We, therefore, have a profile with two regions that is completely determined by ζ_0 . Since ζ is expected to be small, we perform calculations in the limit $\zeta \ll \lambda$. The details of the derivations are quite cumbersome, and is therefore reported in Appendix C.2.

Two important remarks are in order. First, due to the correction $\delta\zeta$, the profile becomes wider when approaching the tip region in agreement with the shape observed in the full numerical solution in Fig. 3.6.

As a second remark, the matching analysis suggests that $\partial_{xx}\zeta_0$ and $\partial_{rr}\zeta_0$ tend to a constant for $\zeta_0 \rightarrow 0$. Using these results in the expression of the force, we obtain asymptotically a power law dependence of the force on ζ_0

$$F_{tip}^{1D} = \frac{12\pi\eta\tilde{\gamma}^{3/2}B\lambda^{3/2}}{C_{1D}^{3/2}\sqrt{2}AL_c^2} \frac{1}{\zeta_0^{3/2}} + \text{non singular terms}, \quad (3.37a)$$

$$F_{tip}^{2D} = \frac{24\pi\eta\tilde{\gamma}^2B\lambda^2}{C_{2D}^2AR_c^2} \frac{1}{\zeta_0} + \text{non singular terms}, \quad (3.37b)$$

where the constants $C_{1D} = \partial_{xx}\bar{\zeta}_0(\bar{\zeta}_0 = 0)$ and $C_{2D} = \partial_{rr}\bar{\zeta}_0(\bar{\zeta}_0 = 0)$ are the values of the normalized second derivatives at the tip when $\bar{\zeta}_0 \rightarrow 0$. From simulations, we find $C_{1D} \approx 0.017$ and $C_{2D} \approx 0.015$ (see Fig. 3.8). Note that we used the approximated expression of the dissolution rates u_{Cz} given by Eq. (3.28).

Table 3.1: Summary of the asymptotic regimes at large loads following the notation of Eq. (3.38). For exponential potentials in the absence of surface tension effects, the dependence of u_{Cz} and ζ_0 on the load and system size is not a power-law. In 1D the dependence is logarithmic Eq. (3.31), and in 2D ζ_0 vanishes (i.e. the crystal touches the substrate) for a finite force F_c^{2D} Eq. (3.33).

Repulsion	Power-Law		Exponential			
Regime	Hydrodyn.	Diffusion	1D no surf. tens.	1D surf. tens.	2D no surf. tens.	2D surf. tens.
	$\bar{\eta} \geq 1$	$\bar{\eta} \ll 1$	$F_{Cz}^{1D} \ll F_c^{1D}$	$F_{Cz}^{1D} \gg F_c^{1D}$	$F_{Cz}^{2D} < F_c^{2D}$	$F_{Cz}^{2D} \gg F_c^{2D}$
α_u	$\frac{n}{n+3}$	$\frac{n}{n+1}$	0(constant)	0(constant)	0(constant)	0(constant)
β_u	$-\frac{4n+6}{n+3}$	$-\frac{4n+2}{n+1}$	-2	-2	-2	-2
α_ζ	$-\frac{1}{n+3}$	$\frac{-1}{n+1}$	exponential	-2/3	$\zeta_0 \rightarrow 0$ as $F_{Cz}^{2D} \rightarrow F_c^{2D}$	-1
β_ζ	$\frac{2}{n+3}$	$\frac{2}{n+1}$	exponential	-4/3		-2

The sum of the contribution without surface tension Eqs. (3.30) and (3.32) with the contribution of the tip Eqs. (3.37a) and (3.37b), are presented in Fig. 3.7 by the dashed-dotted lines. The agreement with the full numerical solution is not quantitative but is satisfactory considering the heuristic character of the matching procedure. Fitting the numerical results with power laws at large forces, we obtain for the wedge-like contact $F_{Cz} \sim \zeta_0^{-1.3}$ to be compared with the prediction $F_{Cz} \sim \zeta_0^{-3/2}$ from Eq. (3.37a), while for the conical contact $F_{Cz} \sim \zeta_0^{-1.1}$ to be compared with $F_{Cz} \sim \zeta_0^{-1}$ from Eq. (3.37b).

As a final comment, the critical force for which surface tension becomes relevant is given by Eq. (3.33) in 2D. In 1D, comparing Eqs. (3.31) and (3.37a) by

$$F_c^{1D} \approx 24\eta B \frac{A}{2\lambda^3} L_c,$$

up to logarithmic corrections.

3.4 Discussion

To summarize, we found that for large external loads the dissolution rate u_{Cz} and minimum distance ζ_0 between the dissolving crystal and the substrate obey scaling laws

$$u_{Cz} \sim F_{Cz}^{\alpha_u} L_c^{\beta_u} \quad \zeta_0 \sim F_{Cz}^{\alpha_\zeta} L_c^{\beta_\zeta} \quad (3.38a)$$

$$u_{Cz} \sim F_{Cz}^{\alpha_u} R_c^{\beta_u} \quad \zeta_0 \sim F_{Cz}^{\alpha_\zeta} R_c^{\beta_\zeta}, \quad (3.38b)$$

where F_{Cz} is the external load and L_c or R_c are the contact sizes for the ridge and the axisymmetric contact, respectively. The exponents α_u , β_u , α_ζ , β_ζ displayed in Table 3.1 are found to depend on dimensionality (ridge or axisymmetric), on viscosity, and on the type of interaction potential (diverging as a power-law or finite at contact).

3.4.1 Orders of Magnitude

Before discussing precise systems, we provide some orders of magnitude describing the energy scale of the interactions. Various experiments and standard textbooks [43] indicate that the order of magnitude of disjoining pressures is typically $U' \sim \text{MPa}$ when the distance between the surfaces is $\zeta \sim \text{nm}$. For exponential interactions with decay length $\lambda \sim \text{nm}$ (corresponding e.g. to the Debye length or to hydration scales), we obtain that $A \sim \lambda U' \sim \text{mJ} \cdot \text{m}^{-2}$. As a consequence, the dimensionless repulsion strength (see Section 3.2.2) is $\bar{A} = A/\gamma \sim 10^{-2}$. For power-law interactions, with a typical distance $\lambda \sim \text{nm}$, we have $A \sim U' \lambda^{n+1}$. As a consequence, we also find $\bar{A} = A/\gamma \lambda^n \sim 10^{-2}$.

We now consider two different crystals: calcite CaCO_3 , and sodium chlorate NaClO_3 . For calcite we use [144]: solubility at 25°C $c_0 \approx 10^{24} \text{m}^{-3}$ (solubility of calcite can in general span between 10^{23} and 10^{25}m^{-3}), molecular volume $\Omega \approx 100 \text{\AA}^3$, ionic diffusion constant [145] $D \approx$

$10^{-5}\text{cm}^2/\text{s}$, water-solution interfacial tension [146, 147] $\gamma \approx 100\text{mJ}$ and $T \approx 300\text{K}$. For each variable y in physical units, and the corresponding variable \bar{y} in normalized units, we define the rescaling factor s_y from the relation $y = s_y\bar{y}$. These rescaling factors have to be applied to the simulation results to recover physical units. In the case of Calcite, we have the following orders of magnitude:

$$\begin{aligned} s_\zeta &= \mathcal{O}(1 \text{ nm}) \\ s_x &= \mathcal{O}(10 \text{ nm}) \\ s_t &= \mathcal{O}(10^{-1} \text{ s}) \\ s_p &= \mathcal{O}(\text{MPa}) \\ s_\eta &= \mathcal{O}(10^2 \text{ Pa s}). \end{aligned}$$

Considering now NaClO_3 with [92, 148] $c_0 \approx 10^{28}/\text{m}^3$ (at 25°C), $\Omega \approx 100^3$, $D \approx 10^{-5}\text{cm}^2/\text{s}$, $\gamma \approx 10\text{mJ}$, and $T \approx 300\text{K}$, using the same assumption on the interaction range and strength, we have $\bar{A} = 10^{-1}$ and:

$$\begin{aligned} s_\zeta &= \mathcal{O}(1 \text{ nm}) \\ s_x &= \mathcal{O}(1 \text{ to } 10 \text{ nm}) \\ s_t &= \mathcal{O}(10^{-6} \text{ s}) \\ s_P &= \mathcal{O}(\text{MPa}) \\ s_\eta &= \mathcal{O}(10^{-2} \text{ Pa s}). \end{aligned}$$

As an illustrative example of the use of these rescaling factors, simulations were performed in a box of normalized width 100 with an initial distance equal to 1 between the dissolving crystal and the substrate. For both calcite and sodium chlorate, this corresponds to thicknesses of the order of the nanometer. In addition, contact widths are $\sim 1\mu\text{m}$ for calcite, and $\sim 100\text{nm}$ to $1\mu\text{m}$ for sodium chlorate.

Some remarks are in order. First, the order of magnitude of the relevant pressures does not depend much on the system. In contrast, the order of magnitude of the timescale and of the relevant viscosities depend strongly on the solubility c_0 , which can vary by many orders of magnitude from one material to another.

As discussed previously for dissolution with singular (power-law) repulsions, one could discriminate between diffusive and hydrodynamic regimes. The simulation results show that the high viscosity regime (hydrodynamic regime) is expected for $\bar{\eta} \geq 1$ (top panel of Fig. 3.3) for $F_{Cz}/S \sim 10^2\text{MPa}$ to 10GPa with $S = \pi R^2$, and micro-metric crystals ($\bar{R} = 100 \leftrightarrow R = 1\mu\text{m}$). For calcite this would be expected for $\eta \sim 10^2 \text{ Pa s}$ which is much larger of the value for water ($\approx \text{mPa s}$). As a consequence, for this system the observation of such a regime should be difficult in natural environments. However, for highly soluble salts such as NaClO_3 , we would need $\eta \sim 10\text{mPa}$ much closer to the value of water. Therefore the hydrodynamic dissolution regime should be easier to observe with salts.

However, physical parameters such as viscosity and diffusion can also depend on pressure, temperature, pH or be affected by phenomena inherent to confinement. For example, large pressure [149, 150] and nanoconfinement are known to lead to changes in the viscosity value. As discussed in Section 1.2.3, nanoconfinement when an electrical double layer is present on the surfaces could indeed promote higher effective viscosities (electro-viscosity) [51, 54].

3.4.2 Comparison with existing literature

Since it relates deformation strains, contact size and stress on single contacts dissolution (eventually connecting it to the overall grain compaction problem) in an axisymmetric geometry, Weyl's model [33] is a first natural candidate for comparison to our model. Weyl predicts that

$$u_{Cz} = 8D\lambda bF_{Cz}/R_c^2, \quad (3.39)$$

where D is the diffusion constant, λ is the film thickness, b a linear stress coefficient linking local solute concentration with the applied stress and R_c is the contact size.

As discussed in Section 1.4.3 of the introduction, other models consider the phenomena at the scale of the grain rather than the contact region [62, 63, 87, 89, 124]. Rutter [82] summarizes most of the previously cited models (for diffusion controlled kinetics) and also treats the global problem at the thin film contact area, as done by Weyl. In cylindrical symmetry and for small external stresses, Rutter [82] predicts

$$\dot{\epsilon} = 32C_0DwVF_{Cz}/(\mathcal{R}_gT\rho_Cd^3), \quad (3.40)$$

while for high external stresses (> 100 MPa) he finds

$$\dot{\epsilon} = 40c_0Dw \exp[F_{Cz}V/(2.3\mathcal{R}_gT)]/(d^3\rho_C), \quad (3.41)$$

where $\dot{\epsilon}$ is the strain rate, c_0 is the concentration at the interface, ρ_C is the crystal density, D is the diffusion at the grain boundary, w is an effective width, \mathcal{R}_g is the gas constant and d is the grain size (proportional to the contact size).

The relations predicted by Weyl and Rutter are in general not in agreement with our predictions both for power law repulsion and finite exponential repulsion Eqs. (3.22b), (3.23b) and (3.28b). However, in the case of finite exponential repulsion our model report similar scaling with the contact area, R_c^{-2} (assuming $\dot{\epsilon} \sim u_{Cz}/R_c$ and $d \sim R_c$ [84]). Globally, the absence of description of microscopic physical ingredients such as viscosity, interaction potential, and surface tension in these models lead to a very different and non-specific behavior.

Previous modeling attempts have also addressed the regime of slow interface kinetics [62, 124]. They suggest that the dissolution rate could then be independent of the contact area. In this regime, power-law relations between strain rate and applied stress are also proposed if the system is characterized by nonlinear surface rates [61, 62]. It is interesting to remark that in our framework power laws relations are obtained as a consequence of disjoining pressure effects in a purely diffusion driven model. However, given the comparable diffusivity of ions at small separations to that of bulk reported for some materials [46, 89], the investigation of the slow dissolution limit is an interesting perspective to be explored with our modeling approach.

A number of experimental observations have suggested power law relations between strain rates (crystal velocity) and applied stress and or grain size [61, 68, 85]. This is compatible with the results we obtained for the singular repulsive power-law potential in Eqs. (3.22a), (3.22b), (3.23a) and (3.23b) and Fig. 3.3. However, Croizé et al. [84] underline that though there exists a positive correlation between the strain rate and the applied stress, this dependence is weak. With the support of both original measurements on calcite pressure solution and data from the literature, they claim that other effects such as the grain size are likely to be dominant. These observations are consistent with the scenario predicted for exponential interaction in Eq. (3.28) and Fig. 3.5.

Using the pressure range 1 to 10^3 MPa, which is the one usually considered in pressure solution experiments, the velocities (dissolution rates) obtained by our simulations are 10^{-3} to 10^{-1} nm s $^{-1}$ for calcite and 10^{-1} to 10 μ m s $^{-1}$ for sodium chlorate. The observable usually reported in pressure solution experiments is the strain rate. Experimental values of the strain rates for calcite [61, 84] vary between 10^{-9} s $^{-1}$ and 10^{-4} s $^{-1}$. Using $\dot{\epsilon} = u_{Cz}/R_c$ as the definition of the strain rate [84], we obtain values between 10^{-6} s $^{-1}$ and 10^{-4} s $^{-1}$, compatible with the experimental ones. For NaClO $_3$, because of the faster timescales due to the much higher solubility, the dissolution rate and as a consequence the strain rate increases of a factor of about 10^5 . This is in disagreement with the literature [85], where similar orders of magnitude as those of calcite are found. Such discrepancy could be caused by the fact that in our system exhibits an under-saturated concentration bath at the boundaries of the contact. In multi-contact systems where the liquid reservoir per contact is finite, the global supersaturation of the bath should increase due to the release of crystal molecules in the liquid. This should lead to a decrease in dissolution rates. The study of such interactions between different contacts is, therefore, an important perspective for our modeling approach to address systems with multiple contacts.

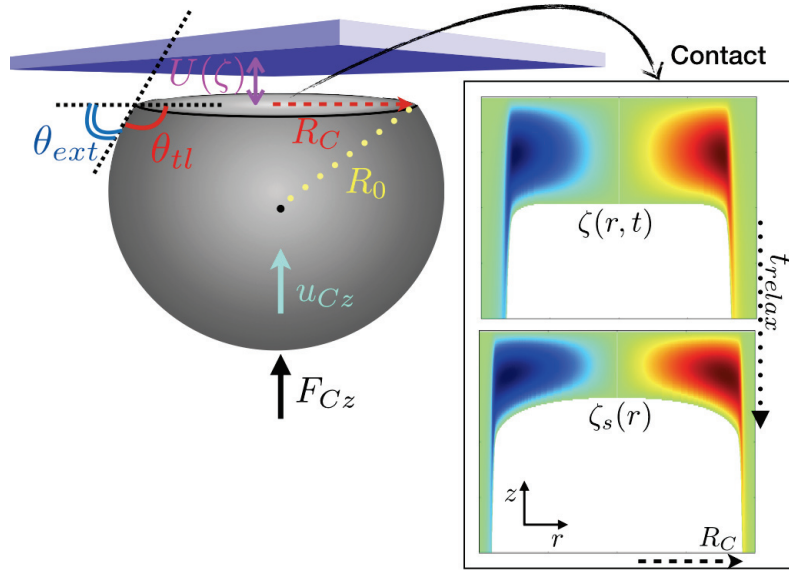


Figure 3.9: Sketch of a spherical crystal dissolving against a substrate by pressure solution. Right panel: the first and last frame of Fig. 3.1 representing the evolution to a steady state (for a diverging disjoining pressure). The time to reach the steady state is the relaxation time, t_{relax} . The notations are given in the text.

As far as the morphology of the contact is concerned, some experiments on quartz grains aggregates [83] showed that in addition to relative smooth interfaces, irregular ridge and plateau structures can develop at the grain contacts after undergoing pressure solution. The appearance of point-like and ridge-like singularities for exponential repulsions in our model could be a first step towards the understanding of these morphologies.

In general, further experimental investigation involving observations at the scale of a single microscopic contact would be useful to test our model predictions.

3.4.3 Quasi-static approximation

Finally, one major assumption of our study is the constant size of the contact region. While specific needle-like crystal shapes may indeed present a constant contact area during dissolution, it is clear that more general shapes, e.g. conical or spherical crystals would exhibit a growing contact area as dissolution proceeds. In addition redeposition of material outside the contact could also change the contact area during pressure solution. Our description could still hold if the change in the contact area was slower than the relaxation of the crystal profile within the contact. Such a separation of timescales, where a steady-state is reached within the contact as if the contact size was constant at all times, is a definition of the quasistatic approximation.

In the following, we discuss the validity of this approximation. Effects such as redeposition, growth, or dissolution outside the contact are assumed to be smaller than the dissolution in the contact region. The different variables appearing below are represented in Fig. 3.9.

From dimensional analysis of Eq. (3.5) neglecting the contribution of surface tension, the relaxation time t_{relax} towards a steady-state profile $\zeta_s(r)$ with a contact of size R_c is

$$t_{relax} \sim \frac{R_c^2}{B\tilde{U}'(\zeta_s)}. \quad (3.42)$$

In addition from force balance Eq. (3.4), we have

$$F_{Cz} \sim R_c^2 U'(\zeta_s). \quad (3.43)$$

Since $U'(\zeta_s) \sim \tilde{U}'(\zeta_s)$, we find

$$t_{relax} \sim \frac{R_c^4}{BF_{Cz}}. \quad (3.44)$$

Assuming a small angle at the edge of the contact (see Fig. 3.9) $\theta_{ext} = \pi - \theta_{tl}$, where θ_{tl} is the contact angle, dissolution induces a growth velocity for the contact radius

$$\dot{R}_c = \frac{u_{Cz}}{\theta_{ext}}. \quad (3.45)$$

We must therefore require that the relaxation time is smaller than the time associated with the growth of the contact radius:

$$t_{relax} \ll \frac{R_c}{\dot{R}_c}, \quad (3.46)$$

leading to

$$\frac{R_c^4}{BF_{Cz}} \ll \frac{R_c \theta_{ext}}{u_{Cz}}. \quad (3.47)$$

For example in the case of a power-law potential in the diffusion-dominated regime, u_{Cz} is given by Eq. (3.23b), and this condition leads to

$$F_{Cz} \gg \frac{A}{\theta_{ext}^{n+1} R_c^{n-1}}. \quad (3.48)$$

Using the relation stated above in this subsection $A \sim U' \lambda^{n+1}$, and the force balance $F_{Cz} \sim R_c^2 U'$, we finally obtain a simple condition

$$\theta_{ext} \gg \frac{\lambda}{R_c}. \quad (3.49)$$

With similar calculations, considering the case of an exponential repulsion one obtains exactly the same result as in Eq. (3.49). Since we assumed $\lambda/R_c \sim 10^{-5}$ above (with $\lambda \sim \text{nm}$ and $R_c \approx 100 \mu\text{m}$), this result suggests that for angles not too small $\theta_{ext} \gg 10^{-5}$, the quasistatic approximation should be valid.

Within this approximation, the dissolution rate and the contact radius will depend on the shape of the dissolving solid. For example for a cone of half angle θ_{cone} , assuming no redeposition outside the contact region, the radius of the contact area obeys

$$\dot{R}_c = u_{Cz} \tan \theta_{cone}. \quad (3.50)$$

Similarly, for a sphere of radius R_0 (see Fig. 3.9), we have

$$\dot{R}_c = u_{Cz} \left(\frac{R_0^2}{R_c^2 - 1} \right)^{1/2}. \quad (3.51)$$

At constant force, since $u_{Cz} \sim R_c^{\beta_u}$ from Eq. (3.38b), we find for the conical case that

$$R_c \sim t^{1/(1-\beta_u)}, \quad (3.52)$$

and

$$u_{Cz} \sim t^{\beta_u/(1-\beta_u)}. \quad (3.53)$$

For the spherical case when $R_c \ll R_0$ we have

$$R_c \sim t^{1/(2-\beta_u)} \quad (3.54)$$

and

$$u_{Cz} \sim t^{\beta_u/(2-\beta_u)}. \quad (3.55)$$

Choosing again the example of power-law repulsion in the diffusion limited regime where $\beta_u = -(4n + 2)/(n + 1)$, we find $u_{Cz} \sim t^{-(4n+2)/(5n+3)}$ and $u_{Cz} \sim t^{-(2n+1)/(3n+2)}$ for the conical and spherical cases respectively.

It is interesting to compare the relations above for the contact radius Eqs. (3.52) and (3.54), to the scaling law for contact island observed by Dysthe et al. [90], $R_c \sim t^{1/3}$. These authors interpret this exponent with the help of an analogy with the standard diffusion limited phase separation scaling of spinodal decomposition.

Assuming a power-law repulsion, thus $\beta_u = -(4n + 6)/(n + 3)$ (hydrodynamic regime) or $\beta_u = -(4n+2)/(n+1)$ (diffusion regime), it is not possible to obtain for a positive and finite n an exponent $1/3$, both in the spherical and conical cases. However, with an exponential repulsion, we have $\beta_u = -2$. This corresponds to $R_c \sim t^{1/4}$ in the spherical case and $R_c \sim t^{1/3}$ in the conical one. Thus, within the approximations discussed above, we obtain for a finite exponential repulsion in the conical case the same scaling law than in the experiments of Dysthe et al., and a scaling law for the spherical crystal which is not too far from their results too. This suggests, as an alternative interpretation based on a simplified single contact picture, that the observed power-law relations for the time evolution of the contact could depend on the underlying interactions.

3.4.4 Limitations of the model

One should keep in mind that there are limits in the application of our continuum model. For instance, when ζ_0 reaches the molecular scale, the continuum approach will break down and one should resort to different models based on molecular methods. An interesting step in this direction was recently proposed in the literature using Kinetic Monte Carlo simulations [121]. Atomistic simulations may also allow one to include atomic steps, which were shown to be relevant for pressure solution experiments [151].

Moreover, one of the approximations used in our study of pressure solution is the linearization of the Gibbs-Thomson relation. The full nonlinear expression of the Gibbs-Thomson relation must be kept when $U'(\zeta) \ll k_B T/\Omega$. At room temperature $k_B T/\Omega \sim 1\text{MPa}$ for molecular crystals, and $k_B T/\Omega \sim 1\text{GPa}$ for atomic crystals. As discussed at the beginning of this section, we may assume maximum disjoining pressures U' of the order of the MPa, and the assumption $U'(\zeta) \ll k_B T/\Omega$ although not systematically valid, should apply in many cases. As discussed in Appendix C.3, our analysis can be extended to the case where the full nonlinearity of the Gibbs-Thomson relation is kept. This leads to similar results as those discussed above in the presence of an exponential potential. The only important difference appears for power-law interactions where the functional form of the dissolution rate and minimum distance with the force are not power-law anymore. Instead, they exhibit an essential singularity as discussed in Appendix C.3.

Another limitation of our model is the absence of elastic or plastic displacements in the solid. However, our results show that even in the absence of elasticity or plasticity, significant shape changes can be observed in contact zones due to dissolution or growth kinetics in the presence of disjoining pressure effects. Hence, elasticity or plasticity are not the only pathways towards flat contact shapes in pressure solution, and dissolution alone is a sufficient mechanism. Beyond displacements, elasticity also gives rise to an additional contribution to the chemical potential [6] $\sim \Omega\sigma^2/2E$, where E is the Young modulus and σ is the elastic stress tensor. For this contribution to be dominant as compared to that coming from disjoining pressure $\Omega U'$, one should have stresses larger than $(2EU')^{1/2}$. Taking $U' \sim \text{MPa}$, and $E \sim 10\text{GPa}$, we obtain that stresses should typically exceed 10^2MPa for elastic effects to be relevant in the chemical potential. In addition, pointy morphologies such as those obtained in our model for finite repulsions should lead to a concentration of stresses which could result in significant elastic or plastic effects. Further studies in this direction are needed.

Another important assumption of the model is that of equal densities between the liquid and the solid, $\rho_L = \rho_C$. The general consequence of dropping this assumption would be that hydrodynamic effects should be stronger, since (see also Section 1.1.5) dissolution induced flow depends on liquid-solid density ratio. As far as steady-state are concerned, assuming that the

effect of the density difference is small on the chemical potential (see Eq. (2.35)), the asymptotic results given here should be qualitatively unaffected. Indeed, the remaining effect will be in the force balance equation via the pressure Eq. (2.27) so that it is sufficient to consider an effective viscosity given by $\eta_{eff} = \rho_C / \rho_L \eta$. As far as the dynamical picture is concerned, the effect of $\rho_L \neq \rho_C$ is difficult to assess without resorting to numerical approaches. This is a direction of research which needs further investigations.

3.5 Summary

We have applied the model exposed in Chapter 2 to study pressure solution against a flat wall in ridge-like (1D) and in axisymmetric (2D) contacts. We assumed the fast surface kinetics limit, with a fixed contact size and linearized Gibbs-Thomson relation.

We have considered two different types of repulsions between the substrate and the crystal. These led to specific behaviors. In the case of a power-law repulsion diverging at contact, the crystal interface flattens under load, and the dissolution rate exhibits a power-law dependence on the load and the contact size. A change in this power-law is found at large loads and viscosities when the forces induced by viscous dissipation surpass those due to disjoining pressure.

In contrast, a finite exponential repulsion produces pointy contacts and a dissolution rate asymptotically independent of the load and of the viscosity. For large loads, the sharp pointy shape of the tip is regularized by surface tension, and the force balance is dominated by viscous effects. Touching contact (i.e. $\zeta_0 = 0$) is never reached. Analytic results indicate that the tip could touch the substrate only in 2D in the absence of surface tension.

Confined Growth and cavity formation

We study the evolution of growing crystals after sedimentation or heterogeneous nucleation on a substrate. Our thin film model shows that a cavity forms on the surface confined by a flat wall. The cavity appears when growth cannot be maintained in the center of the contact region due to an insufficient supply of growth units through the liquid film between the crystal and the wall. A similar behavior is observed in an experiment on sodium chlorate crystals (NaClO_3) performed in the University of Oslo. We obtain a non-equilibrium morphology diagram specifying the conditions under which a cavity forms. This diagram is characterized by a linear critical curve separating a flat growth regime and a regime featuring a cavity. Simulations and experiments support this result. We then study the case where the thickness of the liquid film between the crystal and the wall is reduced down to the nanoscale. Two new observations are in order. First, in the presence of an attractive van der Waals contribution to the disjoining pressure, the formation of the cavity, which previously appeared continuous, becomes sub-critical (discontinuous). In addition, there is a minimum supersaturation required to form a cavity. Second viscosity becomes relevant and hinders the formation of the cavity. We demonstrate that there is a critical value of the viscosity above which no cavity forms. The critical viscosity increases as the square of the thickness of the liquid film. A quantitative discussion of model materials such as calcite, sodium chlorate, glucose, and sucrose is also provided. Finally, we find that the morphology diagram describing the transition can be reformulated to account for slow surface kinetics.

4.1 Introduction

Here, we wish to discuss the growth dynamics with the simplest type of contact, i.e. with a flat, rigid, and impermeable wall. We assume the seed crystal to be already present in the solution and to be stable and focus on the subsequent growth by the effect of a supersaturated solution. Crystals can be directly formed on substrate surfaces —such as during heterogeneous nucleation [152, 153, 154, 155, 156], or can be sedimented on substrates due to gravity. We show that confinement leads to the formation of a cavity in the growing crystal. The cavity forms due to insufficient material supply in the center of the contact. After their formation, cavities can expand up to the edge of the contact, leading to growth rims that have been observed in force of crystallization experiments since the beginning of the 20th century [33, 95, 96, 104]. We will discuss separately the case of “large” film thicknesses – between 10 and 100nm, and “small” film thicknesses – smaller than 10nm.

As discussed in Section 2.6 and Eq. (2.50), if the contact size is larger than a typical length scale l_0 , the system kinetics is limited by diffusion transport (fast surface kinetics). We initially assume the contact sizes to be larger than l_0 so that the limit of fast surface kinetics applies.

The first system we consider is designed to describe growth after sedimentation on a substrate and is inspired by experiments on sodium chlorate performed by Felix Kohler and Dag Kristian Dysthe in Oslo University. In these experiments, the crystal is weakly maintained against the substrate due to its own weight, and the liquid film thickness is in the range from 10 to 100nm due to the presence of nano-scale roughness or dust between the crystal and the substrate. Our thin film model provides qualitative agreement and in some aspects quantitative agreement with experiments on NaClO_3 . We also find a relatively simple description of the conditions under which cavities form. In particular, the main statement of this first part is that cavity formation can be described in terms of a morphology diagram.

We then focus on the consequences of reducing crystal-substrate separation down to the nanoscale, where novel ingredients come into play. The first ingredient is the functional form of the disjoining pressure. Indeed, at this scale we expect (see Sections 1.2.2 and 3.1) a van der Waals attraction to be present [43, 45]. This gives rise to a minimum in the interaction potential which corresponds to an equilibrium thickness for the liquid film. This distance is usually in the scale from 1 to 10 nm [43]. In the presence of such a minimum, heterogeneous nucleation can occur on the substrate because there is a gain of energy when a crystal grows with an interface in this minimum. Hence, this second scenario could describe growth along a flat substrate after heterogeneous nucleation. We will show that in this case a similar morphology diagram is obtained but the transition, becomes discontinuous. Furthermore, beyond a critical value of the viscosity cavities cannot appear. We here also extend the quantitative discussion to other materials such calcite and sugars.

In the last part, we consider the limit of slow surface kinetics. Surface kinetics becomes relevant when the contact size is small enough (at most microns for salts), and when the film thickness is large enough to allow for sufficiently fast transport by diffusion. Slow kinetics leads to a drop in the growth rate. Moreover, cavities can still form. Finally, a generalization of the morphology diagram, initially introduced for diffusion limited kinetics, is formulated.

4.1.1 Summary of model equations

In this chapter, all systems are modeled using a constant contact size. We also assume axisymmetric geometry and linearized Gibbs-Thomson relation. The evolution equations are:

$$\partial_t \zeta = -\frac{\Omega D}{r} \partial_r [r \zeta \partial_r c(r)] - u_{Cz}, \quad (4.1)$$

$$c(r) = \begin{cases} c_0 + \frac{c_0}{k_B T} \left[\Omega (\tilde{\gamma} \partial_{rr} \zeta + \frac{\tilde{\gamma}}{r} \partial_r \zeta - U'(\zeta)) \right] = c_{eq}(r) \\ \text{or} \\ \frac{v_{Cz}}{\Omega \nu} + c_0 + \frac{c_0}{k_B T} \left[\Omega (\tilde{\gamma} \partial_{rr} \zeta + \frac{\tilde{\gamma}}{r} \partial_r \zeta - U'(\zeta)) \right] \end{cases} \quad (4.2a)$$

$$u_{Cz} 2\pi \int_0^R dr r \int_r^R dr' \frac{6\eta r'}{\zeta(r')^3} = F_{Cz} + 2\pi \int_0^R dr r U'(\zeta). \quad (4.3)$$

where Eq. (4.2a) corresponds to the limit of fast attachment kinetics and Eq. (4.2b) includes the contribution of surface kinetics. The term in the square brackets of Eqs. (4.2a) and (4.2b) is the chemical potential at the interface

$$\frac{\Delta\mu}{\Omega} = \tilde{\gamma} \kappa - U'(\zeta)$$

with the curvature $\kappa = \partial_{rr} \zeta - \partial_r \zeta / r$.

The interaction potential $U(\zeta)$ and the external force F_{Cz} are chosen differently depending on the system considered. The interaction potential will determine the typical separation between the crystal and the substrate hereafter denoted by h .

In the first part, inspired by the Oslo experiments, the film thickness is controlled by the presence of nano-scale roughness or dust between the crystal and the substrate. This leads to film thicknesses between $h = 10\text{nm}$ and 100nm . We consider the crystal gravitational buoyancy force to maintain the confined surface in the vicinity of the substrate and a repulsive interaction potential which forbids thicknesses smaller than h .

In the second part, we consider separations of the order of the nanometer and include a van der Waals long-range attractive force combined to a short-range repulsion giving rise to a minimum in the interaction potential corresponding to h . In this case, we discard gravitational force which are negligible.

In the first two parts we will make use of Eqs. (4.1) and (4.3) with Eq. (4.2a), in the third part, to account for slow kinetics, Eq. (4.2b) will be used to express the concentration at the LC interface.

4.2 Morphology diagram and comparison to UiO experiment

Cavity formation is observed in experiments using optical microscopy with sodium chlorate crystals (NaClO_3) growing in the vicinity of a glass surface. Similar results are obtained using our continuum model. The comparison between simulations and experiments demonstrates that the appearance of the cavity is a robust phenomenon relying on a small number of ingredients.

In particular, we show that the birth of the cavity is characterized by a non-equilibrium morphology diagram describing the balance between growth rate and mass supply. This diagram is found to be robust with respect to variations in the system properties such as crystal anisotropy, disjoining pressure amplitude, and transport coefficients. Indeed, despite their differences, both experiments and simulations collapse on the same diagram.

4.2.1 Experimental setup and preliminary observations

The experimental setup developed in the University of Oslo (UiO) allows one to control the solution supersaturation while measuring the confined crystal surface topography. A NaClO_3 seed crystal with a volume of $\sim 1\text{mm}^3$ is placed in a $60\ \mu\text{l}$ chamber filled with a saturated NaClO_3 solution. The solubility $c_0(T)$ of NaClO_3 is strongly temperature dependent [157, 158]. The temperature of the sample chamber and oil immersion objective is controlled with a long-term precision of 1 mK. By adjusting the temperature T below or above the equilibrium temperature T_{eq} , to obtain growth or dissolution, the relative saturation $\sigma_b = (c_b - c_0(T))/c_0(T)$ can be controlled with an accuracy of 0.1%. The equilibrium point, $c_b = c_0(T_{eq})$, is identified when the crystal exhibits roundish edges and neither grows nor dissolves. The high nucleation barrier of NaClO_3 prevents the appearance of other seed crystals in the chamber that could affect the concentration of the bulk solution [159].

The confined crystal interface is observed from below using reflection interference contrast microscopy (RICM) based on the interference between reflections from the glass interface and the confined crystal interface (see fig.4.1). Using a specialized objective, a high power LED light source, and a 16bit camera this method allows for a measurement of the distance $\zeta(\mathbf{r})$ between the crystal and the glass with nm precision [160]. Due to the presence of dust grains on the substrate, the distance $\zeta(\mathbf{r})$ cannot be decreased below a minimum value which ranges from 10nm to 80nm. In all measurements, the lateral extent $2L$ of the crystal facet facing the substrate is determined by tracking the edges with a precision of 15nm.

During growth when the size $2L$ exceeds a critical value, which depends on the average film width h and on the supersaturation σ_b , a cavity forms within the contact region. Snapshots of the temporal evolution slightly above the threshold are shown in Fig. 4.1. The corresponding surface plots are shown in Fig. 4.2A. The appearance of the cavity can be interpreted as a consequence of a lower growth rate in the central part of the facet as compared to the parts closer to the

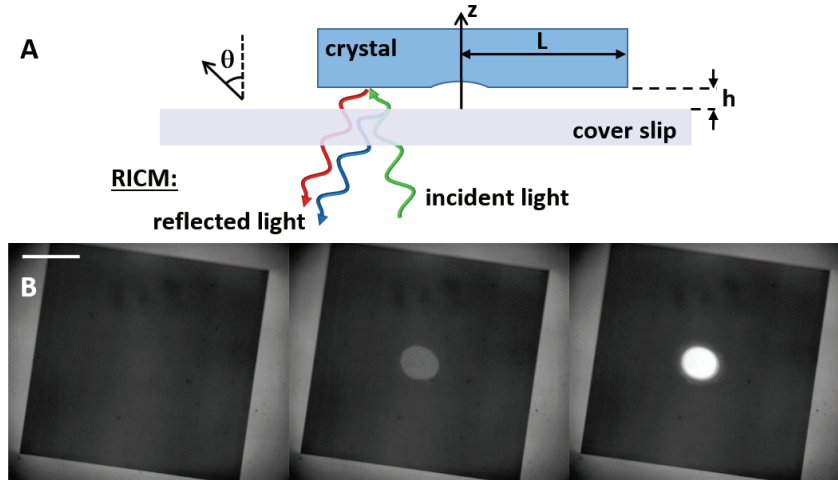


Figure 4.1: **A:** Experimental setup and observations performed in UiO. A growing crystal is placed against a glass substrate. The crystal surface profile is determined with nm accuracy by RICM using the interference between the light reflected by the crystal interface (shown in red) with the light reflected by the glass-solution interface (shown in blue). **B:** RICM images showing the formation of a cavity as growth proceeds. Snapshots just before the start of cavity formation, 15min later, and 35min later. Crystal size: $188\mu m \times 192\mu m$, supersaturation: $\sigma_b = 0.093$, distance to the glass substrate: $h = 51nm$.

facet edges. Intuitively, this lower growth rate is due to confinement limiting the diffusive mass supply from the bulk liquid.

4.2.2 Simulation details

In order to mimic the experimental conditions where thicknesses smaller than h are forbidden by dust grains, we consider the repulsive potential

$$U(\zeta) = \mathcal{A} f\left(\frac{\zeta - h}{\bar{\lambda}h}\right), \quad (4.4)$$

where \mathcal{A} and $\bar{\lambda}$ are constants, and $f(x) = e^{-x}/x$ is a Yukawa-like term. Even though in the model we neglect the hydrodynamic flow induced by the density difference between the crystal and the solution during growth, we keep the density difference as the origin of the gravitational force F_{Cz} maintaining the crystal on the substrate. In the following, we show the relevant dimensionless variables and parameters used to solve the evolution equations and relate them to their physical counterpart.

Let us explicitly separate the interaction amplitude \mathcal{A} into two contributions: one representing a dimensionless amplitude \bar{a} and one containing the physical units $A [J/m]$. We therefore rewrite the interaction potential as:

$$U(\zeta) = \bar{a}A \frac{e^{-\frac{\zeta-h}{h\bar{\lambda}}}}{\zeta - h}, \quad (4.5)$$

where $\bar{\lambda}$ is a dimensionless constant representing the interaction range. It follows that $\mathcal{A} = \bar{a}A/(h\bar{\lambda})$.

The evolution equations Eqs. (4.1), (4.2a) and (4.3) were solved in a dimensionless form. After rescaling, the only parameters appearing in the equation are the dimensionless repulsion

strength \bar{a} and range $\bar{\lambda}$, and the dimensionless external force \bar{F} and viscosity $\bar{\eta}$:

$$\partial_{\bar{t}}\bar{\zeta} = -\frac{1}{\bar{r}}\partial_{\bar{r}}\left\{\bar{r}\bar{\zeta}\partial_{\bar{r}}\left[\partial_{\bar{r}\bar{r}}\bar{\zeta} + \frac{\partial_{\bar{r}}\bar{\zeta}}{\bar{r}} - \bar{U}'(\bar{\zeta})\right]\right\} - \bar{u}_{Cz}, \quad (4.6a)$$

$$\bar{u}_{Cz} 2\pi \int_0^{\bar{R}} d\bar{r} \bar{r} \int_{\bar{r}}^{\bar{R}} d\bar{r}_1 \frac{6\bar{\eta}\bar{r}_1}{\bar{\zeta}^3} = \bar{F}_{Cz} + 2\pi \int_0^{\bar{R}} d\bar{r} \bar{r} \bar{U}'(\bar{\zeta}), \quad (4.6b)$$

where the superscript $'$ indicates a derivative taken with respect to $\bar{\zeta}$ and

$$\bar{U}(\bar{\zeta}) = \left(\bar{a} \frac{e^{-\frac{(\bar{\zeta}-1)}{\bar{\lambda}}}}{\bar{\zeta}-1}\right) \quad (4.7)$$

is the normalized interaction. Defining $\bar{A} = A/(\tilde{\gamma}h)$, the normalized film thickness and radial coordinate are $\bar{\zeta} = \zeta/h$ and $\bar{r} = r\bar{A}^{1/2}/h = r/l$ respectively. Where we defined the radial length scale $l = h/\bar{A}^{1/2}$. Recalling that $B = D\Omega^2 c_0/(k_B T)$, the normalized external force and time are $\bar{F}_{Cz} = F_{Cz}/(\tilde{\gamma}h)$ and $\bar{t} = B\tilde{\gamma}ht/l^4$, respectively. Other relevant dimensionless quantities are the normalized system size

$$\bar{R} = R/l, \quad (4.8)$$

the normalized viscosity

$$\bar{\eta} = \frac{D\Omega^2 c_0}{h^2 k_B T} \eta, \quad (4.9)$$

the normalized supersaturation

$$\bar{\sigma} = \frac{k_B T l^2}{\Omega \tilde{\gamma} h} \sigma, \quad (4.10)$$

and the dimensionless vertical crystal velocity

$$\bar{u}_{Cz} = \frac{l^4 k_B T}{h^2 \tilde{\gamma} D \Omega^2 c_0} u_{Cz}. \quad (4.11)$$

When not indicated differently, we choose $\bar{a} = 10^{-3}$ for definiteness. From simulations it appears that (see Fig. 4.6) the repulsion amplitude \bar{a} in Eq. (4.5) does not influence the results over a large span of conditions. The dimensionless range $\bar{\lambda}$ of the repulsion potential is kept small $\bar{\lambda} = 10^{-2}$ so that the liquid film thickness is approximately equal to h in all simulations. Inspired by the experimental observations we consider a separation of $h = 80\text{nm}$. Finally, we set $l = 1\mu\text{m}$. As a consequence, the size of a simulation box required to match experimental crystal sizes from 10 to $100\mu\text{m}$, ranges from $\bar{R} = 10$ to 100 in normalized units.

In experiments, the crystal surface facing the substrate is a facet. As discussed in Section 1.1.2 surface stiffness is expected to diverge for faceted orientations [1] leading to a singular crystal shape. Such singularities cannot be handled by our continuum model where the crystal shape always exhibits a smooth profile. However, we approach the behavior of a facet using $\tilde{\gamma} = 10^2\text{J/m}^2$, roughly 10^3 times larger than the expected surface tension $\gamma(0) \sim 0.1\text{J/m}^2$ [92]. This estimate of the effective stiffness was obtained by requiring that $\bar{\sigma}$ and \bar{u}_{Cz} (Eqs. (4.10) and (4.11)) are close to the experimental values. Using large but finite values of the stiffness at facets, as discussed in Section 1.1.2, is a standard strategy in continuum models which include anisotropy [16, 17].

From the experimental observation that the vertical size of the crystal is roughly equal to its lateral extent along the substrate, the gravitational buoyancy force maintaining the crystal on the substrate is assumed to be proportional to the cube of the diameter $F_{Cz} \approx \Delta\rho g(2R)^3$, where g is the gravitational acceleration and $\Delta\rho$ is the solid-liquid density difference. Note that we keep the density difference as the origin of the gravitational force but, as discussed in Chapter 2, we neglect its effect on the hydrodynamic flow and chemical potential. Assuming $T = 300\text{K}$, other relevant parameters for NaClO_3 are [148, 157, 161] $c_0 = 9.9\text{molL}^{-1}$, $\Delta\rho = 10^3\text{kgm}^{-3}$, and $\Omega = 4.17 \times 10^{-5}\text{m}^3\text{mol}^{-1}$. The viscosity of the saturated solution $\eta = 7\text{mPas}$ is obtained

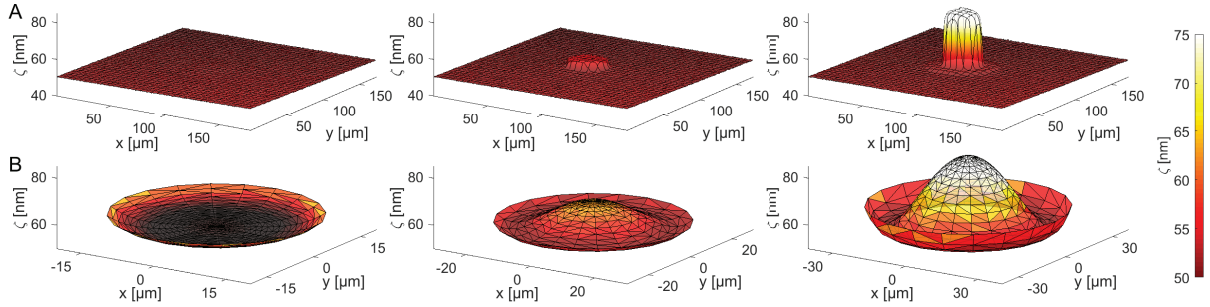


Figure 4.2: 3D view of cavity formation at the confined crystal interface. **A:** Surface plot of the distance $\zeta(\mathbf{r})$ between crystal interface and glass substrate from the RICM images reported in Fig. 4.1B. **B:** Simulation result showing axisymmetric steady states with film width $h = 50\text{nm}$, supersaturation $\sigma_{bc} \approx 0.004$ and thickness $\zeta_{bc} = 1040\text{nm}$ at the edge of the simulation box of radius R . The surface plots represent only the contact region of radius $L < R$ with supersaturation $\sigma_b = \sigma(L) < \sigma_{bc}$ at their edge. From left to right : $R = 60\mu\text{m}$, $L \approx 20\mu\text{m}$, and $\sigma_b \approx 0.0011$; $R = 65\mu\text{m}$, $L \approx 28\mu\text{m}$, and $\sigma_b \approx 0.0014$; $R = 70\mu\text{m}$, $L \approx 37\mu\text{m}$, and $\sigma_b \approx 0.0019$.

from an extrapolation from measurements at lower saturations [162]. A similar extrapolation of experimental data for diffusion [163] suggests D smaller than $0.4 \times 10^{-9}\text{m}^2\text{s}^{-1}$. We chose $D = 0.13 \times 10^{-9}\text{m}^2\text{s}^{-1}$ for definiteness.

We solved numerically Eq. (4.6) in a circular simulation box of fixed radius R , with fixed film width $\zeta(R) = \zeta_{bc}$ and supersaturation $\sigma(R) = \sigma_{bc}$ at the boundary of the integration domain. We chose $\zeta_{bc} = 1040\text{nm}$. However, as shown in the following (see Fig. 4.5), the value of the thickness at the boundary does not influence the results.

All simulations were started with a flat contact region. Steady-state profiles are reached at long simulation times. They are reported in Fig. 4.2B for increasing sizes R of the simulation box. As in the experiments, we find that a cavity forms when the size of the crystal exceeds a critical value. As shown in Fig. 4.2B, the effective extent of the contact is smaller than the total radius R of the simulation box. Hereafter, we indicate the effective contact radius with L . **This shall not be confused with the notation in the previous chapter which referred to the total size of a 1D ridge.**

Despite the absence of growth-induced expansion of the contact size in simulations, a good qualitative agreement is obtained with the experiments. This agreement suggests that the quasistatic assumption is valid, i.e. the evolution of the lateral crystal size is slow enough to have a negligible influence on the diffusion field in the contact region.

4.2.3 Non-equilibrium morphology diagram

Based on this hypothesis of quasistatic dynamics, the threshold for cavity formation can be deduced from mass conservation. Within the thin film approximation, the concentration does not depend on the z coordinate, and mass balance for a disc of radius r and constant thickness h of liquid film centered in the contact region reads

$$\pi r^2 J_k = -2\pi r h J_d(r), \quad (4.12)$$

where $J_k = |u_{Cz}|/\Omega$ is the mass flux entering the crystal per unit facet area, and $J_d(r) = -D(dc/dr)$ denotes the diffusion flux entering into the liquid volume. The modulus is introduced since growth velocities are negative with our conventions. The concentration is integrated as

$$c(r) = c_b - \frac{J_k}{4hD} (L^2 - r^2), \quad (4.13)$$

where $c(L) = c_b$ is the concentration at the edge of the contact region. It follows that the local supersaturation $\sigma(r) = c(r)/c_0 - 1$ decreases toward the center of the facet. In particular in the

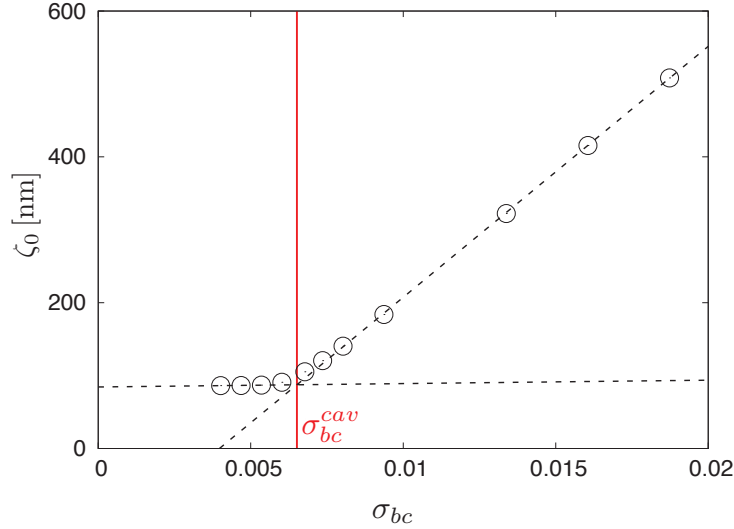


Figure 4.3: Interpolation procedure to determine critical supersaturation at a given size. The central width of the contact, ζ_0 , is plotted against the boundary supersaturation. The simulation box radius is $R = 50\mu\text{m}$.

center we have:

$$\sigma(0) = \sigma(L) - \frac{|u_{Cz}|L^2}{4hDc_0\Omega}. \quad (4.14)$$

We expect that when a cavity is present in the center of the contact, the chemical potential in $\zeta_0 = \zeta(r=0)$ is $\Delta\mu(0) < 0$. This follows from the observation that the presence of a cavity implies $U'(\zeta_0) \approx 0$ (assuming that it is deep enough for the interaction with the substrate to vanish in the center) and $\kappa(\zeta_0) < 0$. On the contrary, before the cavity forms the interface is approximately flat $\kappa(\zeta_0) \approx 0$ and $U'(\zeta_0) > 0$, leading to $\Delta\mu(0) > 0$. The formation of the cavity occurs between these two situations, thus the chemical potential should be close to zero at the transition. We therefore identify the transition with the condition $\Delta\mu^{cav}(0) \approx 0$, where the label *cav* indicates a critical value for cavity formation. Note that $\sigma = \exp[\Delta\mu/(k_B T)] - 1$ in the diffusion limited scenario considered here (see Eq. (2.56)). As a consequence, the criterion $\Delta\mu^{cav}(0) = 0$ is equivalent to the condition $\sigma^{cav}(0) = 0$. This corresponds intuitively to the fact that growth can be maintained in the central region only if the supersaturation is positive at $r = 0$. This is confirmed by the numerical solution of Eq. (4.6) showing that a cavity starts forming approximately when the supersaturation vanishes in the center of the contact.

We therefore obtain as condition for cavity formation that $\sigma(0) \leq 0$. From Eq. (4.14) this corresponds to

$$|u_{Cz}| \geq 4D\Omega c_0 \sigma_b \frac{h}{L^2} = \beta, \quad (4.15)$$

where $\beta = 4D\Omega c_0 \sigma_b h/L^2$, and $\sigma_b = \sigma(L) = c_b/c_0 - 1$. In the following, we show how the critical values of the parameters σ_b and L are in practice calculated in simulations.

4.2.4 Determination of transition line and contact size in simulations

As shown in Fig. 4.3, the transition appears continuously in simulations: we do not observe any discontinuity in the growth rate or in other properties at the transition.

To assess the value of the critical supersaturation we proceeded as follows. We performed a series of simulations at a given box radius R , usual conditions imposed at the edge of the simulation box σ_{bc} and ζ_{bc} . In all simulations, the initial condition is a flat profile in the contact region placed at $\bar{\zeta} = 1$. We then wait until the system attains a steady state, i.e. the growth rate u_{Cz} and interface position ζ reach time-independent values. As shown in Fig. 4.3 for a given box radius, we observe that the film thickness at the center of the contact $\zeta(r=0) = \zeta_0$, changes

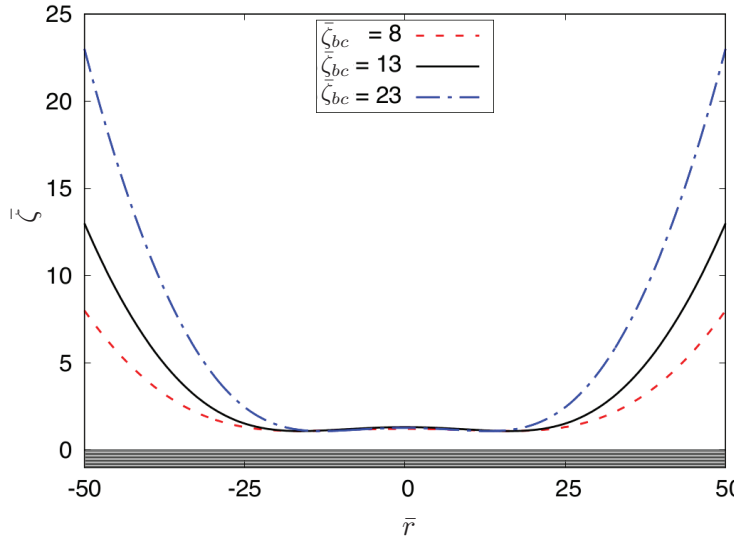


Figure 4.4: Crystal steady-state profiles in normalized units projected along \bar{r} and for different normalized film width $\bar{\zeta}_{bc}$ at the boundary of the integration box. The substrate is represented by a shaded rectangle. The crystals are at the transition: the boundary supersaturations are the critical ones. The simulation box radius is $\bar{R} = 50$. The normalized effective contact radius \bar{L} , boundary $\bar{\sigma}_{bc}$ and contact $\bar{\sigma}_b = \bar{\sigma}(\bar{L})$ supersaturations are: dashed red line $\bar{L} \approx 23$, $\bar{\sigma}_{bc} \approx 0.033$, $\bar{\sigma}_b \approx 0.011$; black line $\bar{L} \approx 21$, $\bar{\sigma}_{bc} \approx 0.051$, $\bar{\sigma}_b \approx 0.016$; blue dashed-dotted line $\bar{L} \approx 17$, $\bar{\sigma}_{bc} = 0.077$, $\bar{\sigma}_b = 0.022$.

as we increase σ_{bc} . First, at low supersaturations, we can identify an initial regime where ζ_0 is roughly constant: this corresponds to growth with a flat contact. At higher supersaturations, however, the central width ζ_0 starts to increase linearly to the applied boundary supersaturation. To estimate the critical boundary supersaturation σ_{bc}^{cav} , we consider the intersection of the linear fits of these two regimes. For illustrative purposes, this is represented by the dashed lines in Fig. 4.3. Once the critical boundary supersaturation σ_{bc}^{cav} is estimated (red vertical line), we perform a simulation at σ_{bc}^{cav} to evaluate the critical growth rate, u_{Cz}^{cav} .

As shown in Fig. 4.4, the typical profile obtained at the transition presents a contact radius L which is smaller than the total simulation box R . We determine L from the condition $\zeta(L) = h + 20\bar{\lambda}h$. Finally, using Eq. (4.2a) and the definition of σ we assess the corresponding supersaturation at the edge of the contact radius from

$$\sigma_b = \sigma(L) = \frac{\Delta\mu(L)}{k_B T} = \frac{\Omega}{k_B T} \left[\tilde{\gamma}\kappa(L) - U'(\zeta(L)) \right], \quad (4.16)$$

where $\kappa = \partial_r \zeta / r + \partial_{rr} \zeta$ is the mean curvature of the crystal interface. The procedure is then repeated for different sizes of the simulation box and the results can be used to obtain the three parameters L_{cav} , σ_b^{cav} and u_{Cz}^{cav} , which are used to build the morphology diagram.

Finally, we monitored the effect of the imposed film thickness ζ_{bc} at the edge of the integration domain on the observed critical size and supersaturation. Using the procedure described previously with different ζ_{bc} , we obtain good data collapse for the transition line in the (σ_b, L) plane. This is shown in Fig. 4.5 for $\zeta(L) = h + 20\bar{\lambda}h$. The collapse is less satisfactory for $\zeta(L) = h + 15\bar{\lambda}h$ and $\zeta(L) = h + 10\bar{\lambda}h$. As a consequence, we used $\zeta(L) = h + 20\bar{\lambda}h$ for determination of the morphology diagram.

4.2.5 Determination of the transition in experiments

In the experiments conducted in UiO, the transition was explored performing growth cycles. This procedure allows one to explore an entire range of supersaturations with a single sample. For each cycle, the surface profile $\zeta(\mathbf{r})$ was monitored during growth at fixed supersaturation. Then the critical size at which the cavity forms was recorded. As soon as the depth of the cavity exceeded 15nm, the temperature was increased to attain a saturation value at which the

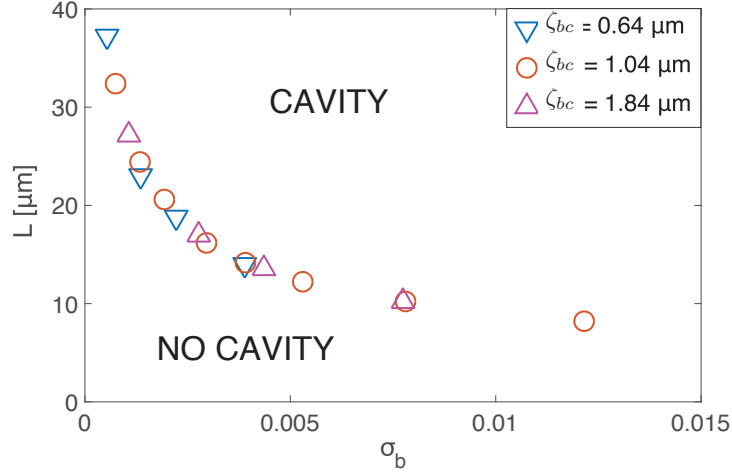


Figure 4.5: Collapse of the transition line in the (σ_b, L) plane using different fixed film width ζ_{bc} at the edge of the simulation box.

cavity closes again. Once the interface is flat, the entire procedure was automatically repeated with a different growth supersaturation. The vertical growth rate u_{Cz} could be obtained from the increase of the depth of the cavity just after its formation. This method assumes that the growth rate at the bottom of the cavity is negligible leading to a deepening which is only due to the growth rate u_{Cz} of the contact region outside the cavity. However, since the lateral growth rate u_{Cx} is easier to determine than u_{Cz} from the growth of the cavity, u_{Cz} was determined from a linear interpolation of the relation between the two velocities based on a large number of measurements. The ratio u_{Cx}/u_{Cz} was found to be roughly independent of L , h , and σ_b . In addition, geometrical corrections were used to evaluate β for elongated and inclined crystals. This is discussed in the supplemental material of [106] together with further technical details.

4.2.6 Results and comparison

Simulation results reported in Fig. 4.6B support the prediction of Eq. (4.15) since a transition line is observed in the $(u_{Cz}/D, \beta/D)$ plane separating a flat growth regime and growth featuring a cavity. However, the slope $\alpha \approx 0.61$ is slightly lower than the expected value $\alpha = 1$.

One striking property of the transition line is its robustness with respect to the variation of the physical parameters that do not enter into Eq. (4.15). Indeed, as shown in Fig. 4.6B, large variations in gravitational force F_{Cz} , and of the interaction amplitude \mathcal{A} , lead to negligible changes in the transition line position. Furthermore, increasing or decreasing one of the transport coefficients D or η by a factor of 10 also does not affect the transition line.

The experimental measurements reported in Fig. 4.6A, also agree with a linear behavior of the transition line in the $(u_z/D, \beta/D)$ plane. Diffusion constants $D = 0.093 \cdot 10^{-9} \text{m}^2 \text{s}^{-1}$ or $D = 0.057 \cdot 10^{-9} \text{m}^2 \text{s}^{-1}$ respectively provide quantitative agreement with the slopes predicted by Eq. (4.15) or by simulations in Fig. 4.6B. These constants are consistent with an extrapolation of the values of D reported in the literature [163]. Indeed, direct quantitative measurement of the diffusion constant at saturation is difficult due to crystal nucleation.

There are differences between experiments and simulations. Looking at Figs. 4.1 and 4.2 it can be seen that in the experiments the cavity emerges from a perfectly flat facet and is less smooth than in simulations. This is a consequence of our model non-singular anisotropy (finite stiffness) and small slope approximation forbidding abrupt discontinuities on the surface.

A second qualitative observation is the random opening and closure of the cavity observed in experiments. The results reported above correspond to the lower boundary of the stochastic transition regime. Such fluctuations could be attributed to a nucleation-like process associated

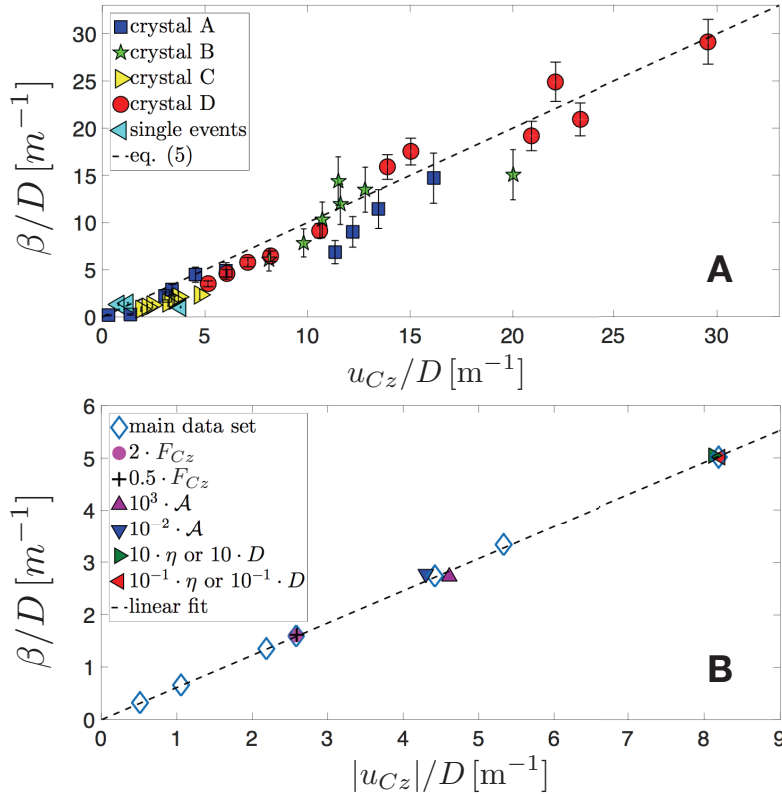


Figure 4.6: Non-equilibrium morphology diagram for cavity formation. **A** Transition line in experiments for different crystals. The results are plotted assuming $D = 0.0935 \times 10^{-9} \text{m}^2 \text{s}^{-1}$ which allows for a perfect correspondence with Eq. (4.15). **B** Transition line in simulations. Colored filled dots are obtained for repulsion strength \bar{a} , viscosity η or diffusion D , and external force F_{Cz} , different with respect to the main set of simulations.

with the competition between thermal fluctuations, and surface tension driven closure of the cavity. Since we have not modeled fluctuations, this cannot be captured in our simulations. As an additional difference, the value of the film thickness h affecting the growth rate in simulation results (since from Eq. (4.11) u_{Cz} is proportional to h), has no noticeable effect on the growth rate in experiments (see also supplemental material of [106]). This latter observation shows that our model does not catch the details of the kinetics as observed in experiments.

However, it is interesting to note that despite these differences, both experiments and simulations collapse on a linear transition line. The robustness of this linearity can be traced back to the fact that it depends only on two ingredients: mass conservation, and diffusion-limited mass transport, as discussed above in the derivation of Eq. (4.15). The results in the following sections, where we study systems that are different from the one considered here, show similar transition diagrams further supporting the robustness of the morphology diagram.

4.3 Nano-confinement: Restrictions to the transition and discontinuity

We here investigate the novel phenomenology arising when assuming a reduced separation, of the order of the nanometer, between the crystal and the substrate. As discussed in the introduction, to account for the physics of thin films with nano-scale thickness, the disjoining pressure $U(\zeta)$ should include an attractive van der Waals contribution. This is combined with a power law repulsion at short distances to account for short-range repulsions due to hydration forces observed at this scale [46, 48, 49].

We show that the presence of an attraction makes the transition discontinuous. Indeed,

various quantities, such as the depth of the cavity, exhibit a jump at the transition. In addition, there is a minimum supersaturation needed to induce cavity formation. However, the non-equilibrium morphology diagram describing the occurrence of the cavity remains unaffected as compared to the case where disjoining pressure is purely repulsive.

As a second ingredient which becomes relevant when the film thickness is decreased down to the nanoscale is viscosity. Indeed we observe that viscosity hinders the formation of the cavity. We also show the existence of a critical viscosity above which cavities cannot form. We determine the value of the critical viscosity and find it to be proportional to the square of the film thickness. This result can also be reformulated as the existence of a critical thickness below which the cavity will not form for a given viscosity.

In this section, we also make use of analytical derivations to gain better insight into the critical behavior of the viscosity and of the supersaturation. The possibility to handle the problem analytically is another consequence of the attractive well. Indeed the existence of a minimum in the interaction allows one to resort to a perturbative analysis with respect to a well-defined equilibrium position of the crystal interface.

We here accompany the presentation of model results with a broad semi-quantitative discussion of the nano-confined growth of various materials, viz., calcium carbonate, sodium chlorate, glucose, and sucrose. Although they belong to disparate classes of materials, with time-scales ranging from second to geological times and contact lengthscales from microns to centimeters, our modeling approach suggests that their behavior can be globally classified based on a small number of dimensionless physical parameters.

4.3.1 Simulation details

We consider a system with a confinement geometry similar to that of the experiments in Section 4.2: a growing crystal is separated from a flat, impermeable and inert substrate by a thin film of solution. However, here, the film thickness is assumed to be of the order of nanometers.

The system can also be visualized in Fig. 4.7. In this figure, the white area is the crystal projected along the radius separated from the substrate (dark-blue rectangle) by the liquid film. The hydrodynamic velocity of the liquid is represented by the color map as done in Fig. 3.1 of Chapter 3. We also assume as before a macroscopic solution reservoir at the boundary of the simulation box.

Since we focus on small distances ζ , we need to account for the van der Waals contribution to $U(\zeta)$, which is usually attractive for a liquid film between two solids [43]. We also included a short-range repulsive term to account for a generic effective repulsion preventing contact. The interaction potential then reads

$$U(\zeta) = \frac{A}{12\pi} \left(-\frac{1}{\zeta^2} + \frac{2h}{3\zeta^3} \right), \quad (4.17)$$

where A is the Hamaker constant and h the equilibrium thickness. It follows that the disjoining pressure appearing in Eq. (4.2a) is

$$U'(\zeta) = \mathcal{A} \left(\frac{1}{\zeta^3} - \frac{h}{\zeta^4} \right), \quad (4.18)$$

where $\mathcal{A} = A/6\pi$. Here we consider no external force since we expect gravity effects to be negligible as compared to Van der Waals attraction at this scales. Thus $F_{Cz} = 0$ in Eq. (4.3).

In practice, as done in the previous section, the dynamical equations were solved in normalized units:

$$\partial_{\bar{t}} \bar{\zeta} = -\frac{1}{\bar{r}} \partial_{\bar{r}} \left\{ \bar{r} \bar{\zeta} \partial_{\bar{r}} \left[\partial_{\bar{r}\bar{r}} \bar{\zeta} + \frac{\partial_{\bar{r}} \bar{\zeta}}{\bar{r}} - \left(\frac{1}{\bar{\zeta}^3} - \frac{1}{\bar{\zeta}^4} \right) \right] \right\} - \bar{u}_{Cz}, \quad (4.19a)$$

$$\bar{u}_{Cz} 2\pi \int_0^{\bar{R}} d\bar{r} \bar{r} \int_{\bar{r}}^{\bar{R}} d\bar{r}' \frac{6\bar{\eta}\bar{r}'}{\bar{\zeta}^3} = \bar{F}_{Cz} + 2\pi \int_0^{\bar{R}} d\bar{r} \bar{r} \left(\frac{1}{\bar{\zeta}^3} - \frac{1}{\bar{\zeta}^4} \right). \quad (4.19b)$$

Table 4.1: Constants used in the simulations of nano-confined growth. Other parameters intervening in the scalings are assumed to be independent of the system considered. These are the temperature $T = 300\text{K}$, the interaction strength $\mathcal{A} = 10^{-21}\text{J}$ and the typical separation $h = 1\text{nm}$. Surface stiffnesses at the crystal water interface are assumed equal to surface tensions and are rough estimations due to lack of data and/or to large variability of it found in the literature. The last two columns indicate the bulk diffusion and viscosity *at saturation*. These are often not known in the literature for concentrated solutions so that their saturation value needs to be extrapolated.

Material	c_0	$\Omega [\text{\AA}^3]$	$\tilde{\gamma} [\text{mJ/m}^2]$	$D [10^{-9}\text{m}^2/\text{s}]$	$\eta [\text{mPas}]$
CaCO_3 ^a	10^{25}	59	100	0.8	1
NaClO_3 ^b	$6 \cdot 10^{27}$	69	10	0.3	7
Glucose ^c	$3 \cdot 10^{27}$	194	100	0.2	10
Sucrose ^d	$3.5 \cdot 10^{27}$	355	100	0.2	100

^a References [145, 147] Calcium carbonate is in general characterised by a wide range of solubility due to its strong dependency on carbon dioxide presence. The value in absence of CO_2 at 25° is [144] $c_0 = 0.013\text{g/L} \approx 10^{23}$. However this value can increase of about two orders of magnitude when CO_2 is present as is the case in natural environments as sea water [164]. We assume the latter.

^b References [92, 157, 162, 165] Data for the diffusion coefficient at saturation was not found. We estimated this value by extrapolating at higher concentration from [163]. Similarly we extrapolated the data for the viscosity from [162].

^c References [166, 167] There is lack of data for surface tension of glucose-water interfaces. We assume $\tilde{\gamma} \approx 100\text{mJ/m}^2$ as suggested by some experiments on sucrose [168].

^d References [166, 168, 169]. Diffusion constant was assumed similar to that of Glucose.

Defining the dimensionless repulsion strength $\bar{A} = \mathcal{A}/\tilde{\gamma}h^2$, the normalization is identical to the previous case where now h represents the minimum of the interaction. The only parameter explicitly appearing in the normalized equation is the dimensionless viscosity

$$\bar{\eta} = \frac{B\eta}{h^2} = \frac{D\Omega^2 c_0}{k_B T h^2} \eta. \quad (4.20)$$

A large value of $\bar{\eta}$ indicates a strong influence of viscosity. Since $\bar{\eta} \sim h^{-2}$, viscosity effects are seen to be important when h is small.

Two sets of simulations with different dimensionless viscosities, $\bar{\eta} = 10^{-5}$ and $\bar{\eta} = 10^{-2}$, were performed. They respectively aim at modeling low solubility crystals such as calcium carbonate (CaCO_3), and highly soluble crystals like salts and sugars. For the latter class, we focused on sodium chlorate (NaClO_3), which was used in the previous section and glucose. The parameters used are given in Table 4.1. Given the system under study, we also assume a film thickness $h = 1\text{nm}$ for all materials considered.

The value of the dimensionless viscosity depends on the physical parameters as described by Eq. (4.20). The viscosities used for the simulations are rough estimations. For instance glucose normalized viscosity actually lies in an intermediate regime between $\bar{\eta} = 10^{-2}$ and $\bar{\eta} = 10^{-1}$. Some exploratory simulations were also performed at viscosities higher than 10^{-1} . Larger viscosities could be encountered in other natural materials as more complex sugars. In the case of sucrose for instance, we have $\eta \approx 100\text{mPa}$ so that $\bar{\eta} > 1$ at saturation [169].

Finally, the value of the normalized repulsion strength \bar{A} is not fixed by the radial scale l , as done in the previous section, but chosen following the same lines as in Section 3.4.1. For simplicity we assume $A \approx 10^{-20}\text{J}$ [43] to be the same for all materials considered. Assuming some specific values for $\tilde{\gamma}$ and h , we can then calculate $\bar{A} = \mathcal{A}/\tilde{\gamma}h^2 = A/6\pi\tilde{\gamma}h^2$. In any case, the qualitative behavior is not influenced by \bar{A} which does not appear explicitly in the normalized equations, and only contributes to the spatial and temporal scales on which phenomena can be observed.

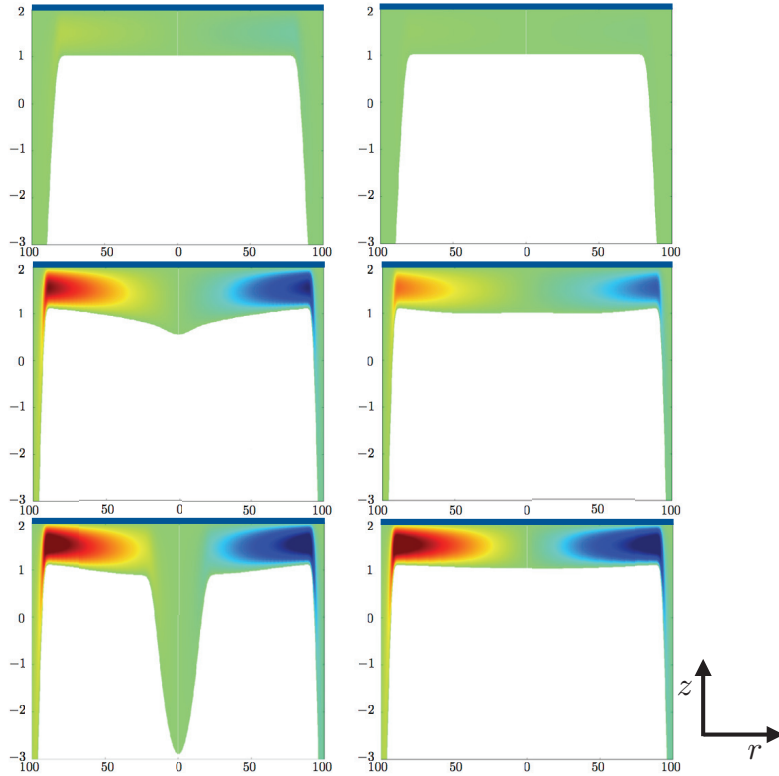


Figure 4.7: Simulation screenshots representing a section of an axisymmetric growing crystal (white). Time flows from top to bottom. The normalized supersaturation is for both panels $\bar{\sigma}_{bc} = 0.21$. Left column $\bar{\eta} = 10^{-2}$; right column $\bar{\eta} = 10^{-1}$, the cavity is not observed. The unit of the vertical scale is 1nm. The substrate is located at $h_s = 2\text{nm}$. The scale of the horizontal axis depends on the material. For instance for NaClO_3 the radial scale unit is 3.2nm. The color-map represents the liquid velocity in normalized units. Red color: positive velocities (flow from left to right); blue: negative velocities; green: vanishing velocity. The physical liquid velocity depends on the material, for instance in the left panel for NaClO_3 its maximum value (darker color) is $u_L \approx 66\mu\text{m/s}$.

4.3.2 Discontinuous transition

As in the previous section, we solved Eqs. (4.1), (4.2a) and (4.3) numerically in a circular simulation box of fixed radius R , fixed film width $\zeta(R) = \zeta_{bc}$, and fixed supersaturation $\sigma(R) = \sigma_{bc}$ at the boundary of the integration domain. In all simulations, we were able to reach a steady state characterized by a constant growth rate and crystal interface profile. We observe that for low enough viscosities $\bar{\eta}$, a cavity appears when increasing the simulation box radius R , or the boundary supersaturation σ_{bc} . In Fig. 4.7 we show two examples of simulations. The two simulations were realized using different normalized viscosities $\bar{\eta}$, and keeping the other parameters fixed. Simulations at higher viscosity, e.g. $\bar{\eta} = 0.1$, do not show the appearance of a cavity.

For the two set of simulations considered, namely $\bar{\eta} = 10^{-2}$ and $\bar{\eta} = 10^{-5}$, we studied the steady state profiles close to the transition. In Fig. 4.8 we show as an example the variation of the normalized width $\bar{\zeta}(0) = \bar{\zeta}_0$ of the film in the center of the contact as a function of the normalized supersaturation $\bar{\sigma}_{bc}$, and for fixed box size $\bar{R} = 40$. Each dot corresponds to a steady state reached in a single simulation. Considering a surface which is initially flat and in the minimum of the interaction potential ($\bar{\zeta}_0 = 1$), and gradually increasing the supersaturation $\bar{\sigma}_{bc}$, we observe a sharp jump in the value of $\bar{\zeta}_0$ at the transition (“forward” transition). This process corresponds to black circles and blue squares in Fig. 4.8. However, if we start with a system beyond the critical supersaturation, thus featuring a cavity, and slowly decrease the supersaturation $\bar{\sigma}_{bc}$, the transition is not observed at the same point, but at a lower supersaturation (“backward” transition). This is represented by red and yellow triangles in Fig. 4.8. Hence, the transition exhibits hysteresis.

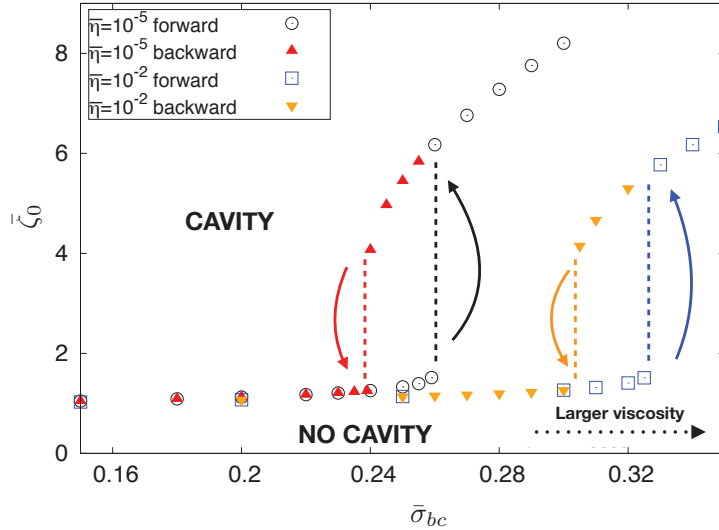


Figure 4.8: Film thickness at the center of the contact $\bar{\zeta}(r=0) = \bar{\zeta}_0$ versus supersaturation $\bar{\sigma}_{bc}$ at the boundary of the simulation box at different normalized viscosities $\bar{\eta}$. The size of the simulation box is $\bar{R} = 40$. The vertical axis is in nanometers. The size of the simulation box R and the supersaturation scale depend on the material. Calcium Carbonate, red triangles and black circles: $R = 400\text{nm}$, $\sigma_{bc} = 0.014 \times \bar{\sigma}_{bc}$; Sodium Chlorate, yellow triangles and blue squares: $R \approx 127\text{nm}$, $\sigma_{bc} = 0.017 \times \bar{\sigma}_{bc}$; Glucose, yellow triangles and blue squares: $R \approx 400\text{nm}$, $\sigma_{bc} = 0.05 \times \bar{\sigma}_{bc}$.

A similar discontinuity with hysteresis is observed when looking at the crystal growth rate $|u_{Cz}|$. However, as discussed in Appendix D.2 and shown in Fig. D.1, the discontinuity in $|u_{Cz}|$ is more apparent in the forward transition than in the backward transition.

For both the width at the center of the contact and the growth rate, no qualitative difference is observed between simulations at $\bar{\eta} = 10^{-2}$ and $\bar{\eta} = 10^{-5}$. The main difference lies in the shift of the transition towards larger supersaturations when the viscosity is increased.

4.3.3 Non-equilibrium morphology diagram

In analogy with Section 4.2, we represent the location of the transition¹ (when existing) in the plane with axis defined by the left hand side and right hand side of

$$\alpha |u_{Cz}^{cav}| = 4D\Omega c_0 \sigma_b^{cav} \frac{h}{L_{cav}^2}. \quad (4.21)$$

Following Section 4.2, here the heuristic multiplicative constant α is introduced in order to capture quantitatively the simulation results.

In order to build the non-equilibrium morphology diagram we need to evaluate the observables L_{cav} and σ_b^{cav} appearing in Eq. (4.21). The procedure is similar to the one adopted in the previous section. First, we determine the couple R and σ_{bc} at the transition from the $\sigma_{bc} - \zeta_0$ plot (Fig. 4.8). Then, we consider the contact radius L from the condition that $\zeta(L)$ exceeds the equilibrium position h by 1%. Finally, as before, we obtain σ_b^{cav} using the linearized thermodynamic relation in the fast attachment regime Eq. (4.16). The procedure is repeated for simulations at different box sizes and viscosities, and on the different branches of the hysteresis curve.

The results, shown in Fig. 4.9, confirm the prediction of a straight transition line passing through the origin in the $(|u_{Cz}|, 4D\Omega c_0 \sigma_b h / L^2)$ plane. Interestingly, the forward and the backward transitions roughly collapse on the same line. The differences in mass transport kinetics

¹Here there is a subtle difference in the arguments used in Section 4.2.3 to derive the transition line. In this case, due to the form of the interaction, the interface needs to be sufficiently far from the substrate in order to escape the attractive well in h . Thus there is a region where a cavity still does *not* form but with $U'(\zeta_0) < 0$ (see Fig. 4.10). It follows that here the threshold is expected in principle at a value $\Delta\mu^{cav}(0) < 0$. The results suggests however that this value is very small and the assumption $\Delta\mu^{cav}(0) \approx 0$ is still robust. This is related to the critical supersaturation of section Section 4.3.4 (which is also an effect quantitatively small).

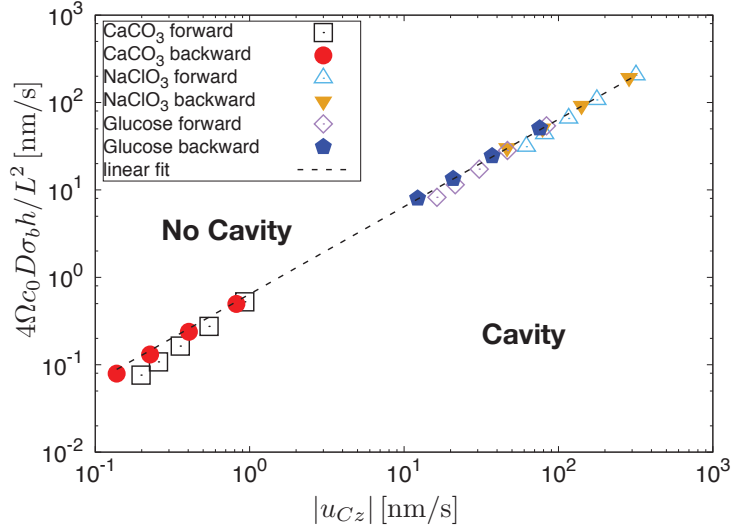


Figure 4.9: Non-equilibrium morphology diagram for different materials and transition pathways. The scaled viscosity $\bar{\eta}$ is assumed to be 10^{-5} for CaCO_3 , and 10^{-2} for NaClO_3 and Glucose.

between different materials however lead to differences in the orders of magnitude of the critical vertical growth velocity u_z^{cav} (from about 0.1 to 100nm). A linear fit for the slope of the transition line leads to $\alpha = 0.65 \pm 0.04$. This result is close to the value $\alpha \approx 0.61$ obtained in Section 4.2.6. However, the system studied in Section 4.2 was different, with a purely repulsive potential and a load to maintain the crystal close to the substrate. This result suggests that the constant α could be robust with respect to the details of the model potential.

4.3.4 Critical supersaturation and critical viscosity

To understand how viscosity can affect the transition we resort to a perturbative analysis of the steady-state solution. This is done assuming that, just before the transition, the profile deviates slightly from the equilibrium configuration $\zeta = \zeta_{eq} + \delta\zeta$, with $\zeta_{eq} \approx h$. The perturbation $\delta\zeta$, derived in Appendix D.1, exhibits a concave parabolic profile:

$$\delta\zeta = \frac{u_{Cz}}{4BhU''(h)} \left(r^2 - L^2 + \frac{4\tilde{\gamma}}{U''(h)} \right) - \frac{\Delta\mu_b - \Delta\mu_{eq}}{\Omega U''(h)}, \quad (4.22)$$

where $\Delta\mu_b = \Delta\mu(L)$, and $U''(h)$ is the second derivative of the substrate-crystal interaction potential with respect to ζ , calculated in the equilibrium position. The agreement between the perturbative solution and the full profile is good as illustrated in Fig. 4.10.

Hence, the thickness ζ_0 in the center of the contact increases as the supersaturation increases even in the absence of a cavity. This result suggests a simple mechanism for cavity formation. We use the standard result of the linear stability analysis of an infinite flat profile of thickness ζ , which indicates that the surface of the crystal should be stable when $U''(\zeta) > 0$, and unstable when $U''(\zeta) < 0$. This is similar to usual spinodal decomposition [170]. The initial profile with $\zeta = h$ is constant and in the minimum of the potential, with $U''(h) > 0$ corresponding to a stable configuration. Considering now a non-equilibrium profile with a concave parabolic $\zeta(r)$, an approximate criterion for the cavity to form is that the thickness $\zeta_0 = \zeta(r=0)$ at the center of the contact reaches the inflection point ζ^{cav} of the potential, where U'' changes sign, i.e., $U''(\zeta^{cav}) = 0$. This scenario is consistent with a discontinuous transition since upon destabilization the thickness ζ_0 in the center of the contact becomes larger than ζ^{cav} . Once the instability is initiated, the larger ζ_0 , the larger $U''(\zeta_0)$, and the stronger the destabilization, leading to a self-amplifying feedback². Note once again that this behavior is reminiscent of

²This is true at least in a finite range for ζ_0 . When ζ_0 becomes very large, $U''(\zeta_0)$ decreases allowing for steady state to be attained.

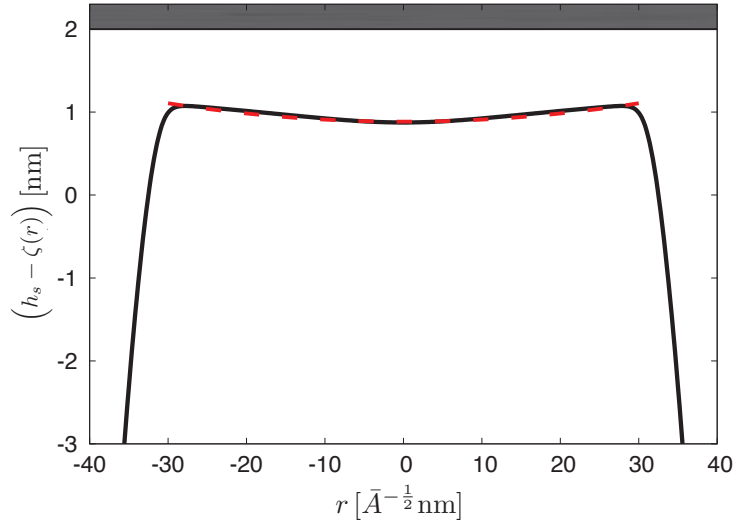


Figure 4.10: Section of the crystal profile close to the transition. The black zone at the top represents the substrate. The black line is the simulation result. The vertical axis is in physical units. The horizontal axis scaling depends on the material (via the constant \bar{A}). Simulation parameters: size of the box $\bar{R} = 40$, supersaturation at the boundary of the integration domain $\bar{\sigma}_{bc} = 0.2$. The dashed red line is obtained from Eq. (4.22) with L , u_{Cz} , $\Delta\mu_b$ measured in the simulation.

spinodal instabilities [171, 172, 173].

Using this simple argument, i.e. $\zeta_0 = \zeta^{cav}$, and in the limit of large contacts, we find an expression for the critical supersaturation:

$$\sigma_b^{cav} \approx \frac{\mathcal{A}\Omega}{3k_B T h^3} \left(\frac{1 + 12\bar{\eta}}{1 - 12\bar{\eta}} \right). \quad (4.23)$$

The details of the derivation are reported in Appendix D.1.

As a first consequence of Eq. (4.23), the critical supersaturation σ_b^{cav} is expected to reach a finite value σ_b^* , when the viscosity vanishes. This result differs from the behavior of purely repulsive potentials observed in Section 4.2, where vanishingly small supersaturations are able to destabilize large crystals. This difference is intuitively understood from the fact that the supersaturation here needs to be large enough to lead to an escape of the crystal surface from the potential well at $\zeta = h$. Thus the thermodynamic force related to supersaturation $\Delta\mu/\Omega$ must be larger than the disjoining force dragging the interface towards the minimum of the potential $U'(\zeta^{cav}) \approx (\zeta^{cav} - h)U''(h)$. Since $\sigma_b = \Delta\mu_b/k_B T$, we obtain that $\sigma_b^* = (\zeta^{cav} - h)U''(h)/(\Omega k_B T)$, which is identical to Eq. (4.23) when $\bar{\eta} = 0$ and U is given by Eq. (4.17). This result, which states that the critical supersaturation σ_b^{cav} is expected to reach a constant value when the viscosity vanishes and the size is large, is confirmed by simulations in Fig. 4.11 for small viscosities (blue and red triangles). However, the predicted value $\bar{\sigma}_b^* \approx 0.33$ is larger than the value observed in simulations $\bar{\sigma}_b^{cav}(L \rightarrow \infty) \approx 0.12$. Going back to physical variables $\sigma = \bar{\sigma}\mathcal{A}\Omega/(k_B T h^3)$, we find that the critical supersaturation at vanishing viscosities is small $\sigma_b^* \sim 10^{-2}$ to 10^{-3} for $h \sim 1$ nm. Since $\sigma_b^* \sim h^{-3}$, the critical supersaturation decreases quickly when the equilibrium thickness h increases, and $\sigma_b^* < 10^{-5}$ for $h = 10$ nm. Hence, this phenomenon could be difficult to observe in experiments where it is difficult to precisely control nanometric separations or have such a small resolution for the supersaturation³.

The expression Eq. (4.23) also provides information about the consequences of viscosity. For example, it agrees qualitatively with Fig. 4.8, where higher viscosities were shown to lead to a transition at higher supersaturations. In Fig. 4.11, we show the normalized critical (forward) supersaturation $\bar{\sigma}_b^{cav}$ at different normalized viscosities as obtained by simulations. This again

³We are only aware of the work of Désarnaud et al. [102] where they reach a similar resolution ($\approx 2 \times 10^{-5}$) for the supersaturation.

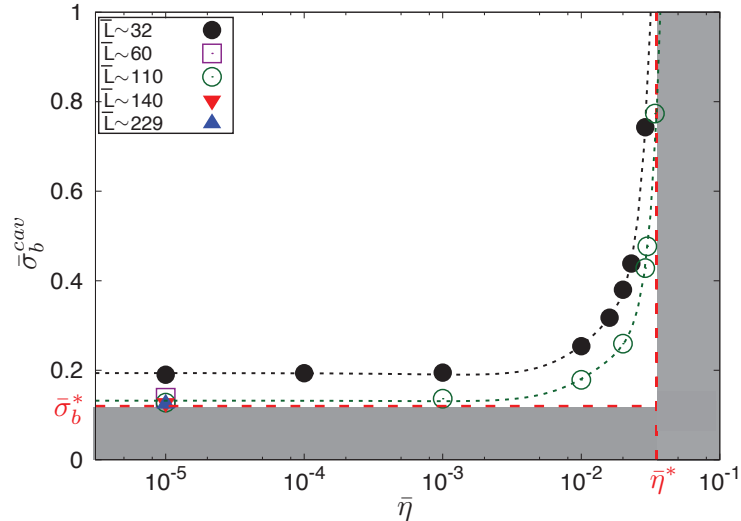


Figure 4.11: Critical supersaturation for the appearance of a cavity as a function of viscosity, as obtained by simulations for the forward transition (initially flat contact). The results are reported in normalized units. The critical supersaturation diverges at $\bar{\eta}^* \approx 0.34$. For larger normalized viscosities, cavities are not observed in simulations independently from the size of the contact (shaded area). The critical supersaturation converges to a fixed value when the contact size increase at fixed viscosity, as predicted by Eq. (D.16) and Eq. (4.23). At vanishing viscosity the critical supersaturation is $\bar{\sigma}_b^* \approx 0.12$ (red and blue triangles). Cavities cannot be observed independently from the size of the contact below this value (shaded area).

confirms good qualitative agreement with Eq. (4.23), since it agrees both with the increase of σ_b^{cav} with increasing $\bar{\eta}$, and with the divergence of σ_b^{cav} for a finite value of $\bar{\eta}$.

However, Eq. (4.23) is quantitatively inaccurate. For example, the observed threshold at $\bar{\eta}^* \approx 0.034$ is lower than the predicted value $\bar{\eta}^* = 1/12 \approx 0.08$. Despite the absence of a quantitatively accurate expression for the critical supersaturation as a function of viscosity, it is possible to obtain quantitative insights about the critical viscosity using the morphology diagram and a suitable expression for the growth rate u_{Cz} .

Indeed, inserting the parabolic profile $\zeta_{eq} + \delta\zeta$ of the film in the contact in the force balance equation Eq. (4.3), leads to a second relation valid below the transition

$$u_{Cz} = \frac{-4Bh(\Delta\mu_b - \Delta\mu_{eq})}{\left(\frac{6B}{h^2}\eta + \frac{1}{2} - \frac{4\tilde{\gamma}}{L^2U''(h)}\right)L^2\Omega}, \quad (4.24)$$

where $\Delta\mu_b$ is the interface chemical potential at the edge of the contact region, $\Delta\mu_b = \Delta\mu(L)$. This relation has to be combined with the expression for the equilibrium chemical potential, that for an attractive interaction reads

$$\Delta\mu_{eq} \approx \frac{2\Omega}{L} \sqrt{-2\tilde{\gamma}U(h)}, \quad (4.25)$$

The details of the derivation of Eqs. (4.24) and (4.25) are presented in Appendix D.1. Equation (4.24) exhibits quantitative agreement with simulation results as illustrated in Fig. 4.12.

Here, we wish to focus on steady-states close to the threshold of cavity formation. Since $\Delta\mu_{eq} \sim 1/L$ from Eq. (4.25), this term can be neglected far from equilibrium and for large system sizes where cavity formation occurs. For the same reason, we neglect the term of order $1/L^2$. Finally, assuming the supersaturation is small, we have $\Delta\mu_b = k_B T \sigma_b$, and we obtain

$$u_{Cz} \approx \frac{-4hD\Omega c_0 \sigma_b}{(6\bar{\eta} + 1/2)L^2}. \quad (4.26)$$

It follows from Eq. (4.26) that, as the viscosity increases, the growth rate u_{Cz} decreases. In addition, for low viscosities, the growth rate is independent of the viscosity.

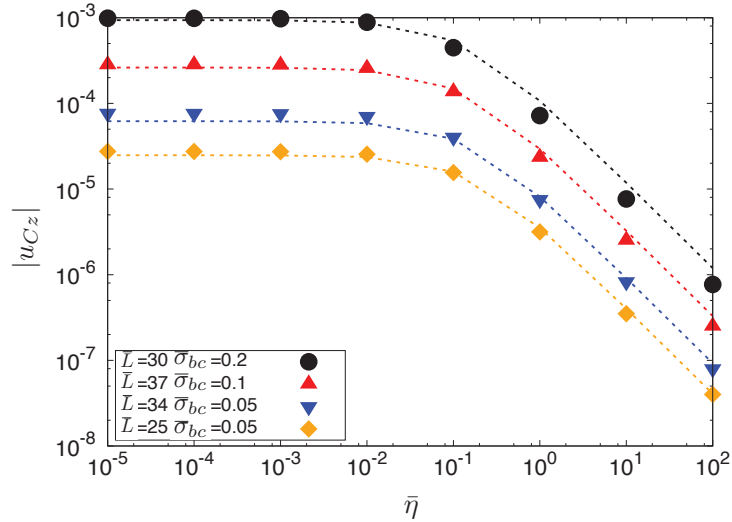


Figure 4.12: Growth rate $|u_{Cz}|$ as a function of the viscosity shown in normalized units before undergoing the transition (flat growth) for different sizes. The dots are simulation results, the dashed lines were computed using Eq. (4.24) with L and $\Delta\mu_b(\eta)$ (see Eq. (4.16)) measured in simulations and $\Delta\mu_{eq}$ given by Eq. (4.25). The value of the contact size L varies weakly when the viscosity is varied.

Inserting Eq. (4.26) in Eq. (4.21), we find the critical value of the viscosity above which the cavity cannot form

$$\frac{D\Omega^2 c_0}{k_B T h^2} \eta^* = \bar{\eta}^* = \frac{2\alpha - 1}{12} \approx 0.025 \pm 0.007. \quad (4.27)$$

Interestingly, if we assume the idealized case to hold ($\alpha = 1$), we would have obtained $\bar{\eta}^* = 1/12$ as in Eq. (4.23). Even though Eq. (4.26) and Eq. (4.27) rely on some approximations—based on our perturbative analysis and on the heuristic character of the parameter α —we find that Eq. (4.27) provides a reasonably accurate prediction close to the value $\bar{\eta}^* \approx 0.034$ from the full numerical solution of the model.

The experimental consequences of this result can be presented in two different ways. First, we may assume that disjoining pressure effects lead to a fixed film thickness, assumed for example to be $h \approx 1$ nm. Then, using Eq. (4.27) and considering the materials listed in Table 4.1, we find $\eta^* \approx 3.7 \times 10^3$ mPas for calcite, $\eta^* \approx 12$ mPas for sodium chlorate, $\eta^* \approx 4.6$ mPas for glucose and $\eta^* \approx 1.2$ mPas for sucrose. Cavity formation should be hindered or suppressed by viscosity effects when these values are equal to, or smaller than the values of viscosity at saturation reported in the last column of Table 4.1. These are 1, 7, 10 and 100 mPas, respectively. Thus, for example, we do not expect a cavity to appear for Sucrose while Calcite could feature a cavity. Conclusions on glucose or sodium chlorate are more difficult since the value of the critical viscosity is close to the viscosity at saturation.

The threshold can be reformulated in a different manner. Indeed, since the value of the critical viscosity increases as the square of h there is a critical thickness h^* above which a cavity can form for a given system. Using the bulk viscosity at saturation, we find $h^* \approx 0.016$ nm for CaCO_3 , $h^* \approx 0.76$ nm for NaClO_3 , $h^* \approx 1.5$ nm for glucose, and $h^* \approx 9.2$ nm for sucrose. These results once again state that cavity formation should be suppressed for Sucrose with nanoscale confinement. For other materials with smaller viscosities, the main effect of viscosity should be to shift the transition as shown in Fig. 4.8 and Fig. 4.9. In general, when the film thickness is larger than $h \approx 10$ nm as in Section 4.2, we expect cavities can form for most materials.

For different densities $\rho_C \neq \rho_L$, as also observed in the previous chapter, we expect viscosity effects to be enhanced. However, further analysis of the model would be necessary to reach quantitative conclusions.

4.4 Effect of surface kinetics

In both systems discussed above (with purely repulsive potentials, or potentials with a minimum) we assumed that mass transport via diffusion was slower than surface kinetics. We indeed expect, given the slenderness of the films considered, that in general transport in the contact region should be significantly reduced with respect to its bulk counterpart. In this section, we discuss the consequences of dropping this assumption.

First, we show that the morphology diagram describing the formation of the cavity can be generalized to include this scenario in a simple way. Second, we observe that one can still predict the velocity of the confined surface (before cavities form) in the presence of an attractive crystal-substrate interaction, as done with Eq. (4.26). As discussed in detail at the end of this section, this allows us to predict the shape of a crystal growing in the vicinity of a substrate where the free surfaces follow standard surface kinetics limited growth (see Frank construction in Section 1.1.4). These findings are supported by the numerical solution of the model equations in the slow surface kinetics limit (using Eq. (4.2b) instead of Eq. (4.2a) in Eq. (4.1)).

Let us initially determine when the effects of surface kinetics should be relevant. As discussed in Chapters 1 and 2 attachment-detachment kinetics at the crystal surface is described by the kinetic constant ν which accounts for the proportionality between the departure from equilibrium in the liquid close to the surface and the growth rate. The kinetic coefficient has the dimensions of a velocity. This process acts in series with diffusion in the liquid D . Between two parallel planes separated by the distance h , the mobility, defined as the ratio between total current in the xy -plane $\langle \mathbf{j}_{xy} \rangle$ (see also Chapter 2 and Appendix A.4) and the driving force $\nabla_{xy}c$, is equal to Dh as seen for instance in Eq. (4.1). The length scale emerging from the combination of these two processes is

$$l_0 = \sqrt{\frac{Dh}{\nu}}.$$

As discussed in Section 2.6, this length scale can also be obtained by simple comparison of the terms proportional to v_{Cz} in Eq. (2.48) (or identically Eq. (4.34a) later in this section). In the above relation, we have assumed, as in the previous sections, that the typical scale of the thickness is $\zeta \approx h$. For crystals larger than l_0 , the limiting mass transport process is diffusion, while for crystals smaller than l_0 , the limiting process is surface kinetics.

Unfortunately, kinetic constants are difficult to assess precisely in experiments, this is why the values reported in the literature can be very different for the same material. For salts, a large span of kinetic constant are reported ($\nu \sim 10^{-5}$ to 10^{-3}ms^{-1} [76]). Considering NaClO_3 , even if we assume a large diffusion constant (compare to e.g. Table 4.1) $D \sim 10^{-9}\text{m}^2\text{s}^{-1}$, a thickness $h \sim 100\text{nm}$, and the smallest kinetic constant $\nu \sim 10^{-5}\text{ms}^{-1}$, we find $l_0 \sim 3\mu\text{m}$. This number is small as compared to the experimentally relevant crystal sizes used in Section 4.2.1. Hence, we can safely assume that in the UiO experiments the formation of the cavity occurs within the diffusion-limited regime for NaClO_3 .

However if for instance we consider a material such as CaCO_3 characterized by much slower surface kinetics, the scenario could be different. Indeed, values of ν reported for CaCO_3 range between 10^{-7} to 10^{-4}ms^{-1} [174, 175]. Considering again $D \sim 10^{-9}\text{m}^2\text{s}^{-1}$, $h \sim 100\text{nm}$ and assuming the smallest kinetic constant, we find $l_0 \sim 30\mu\text{m}$.

This is why slow surface kinetics might be relevant also in confined growth for some materials. The general fact that even in confined geometries there exist cases in which surface kinetics combines with diffusion, as discussed in Section 3.4, is also suggested by experiments on pressure solution [46, 63].

4.4.1 Generalized morphology diagram

In Section 4.2.3, we discussed the conditions for cavity formation. The derivation was based on the observation that a cavity should appear when $\Delta\mu(r=0) \approx 0$, and on mass conservation, Eq. (4.14). These relations are unaffected by surface kinetics.

However, the relation between chemical potential and supersaturation σ is affected. In the case where we account for surface kinetics, the supersaturation at the interface is given by Eq. (2.52),

$$\sigma(r) = \frac{c_{eq}(r)}{c_0} - 1 + \frac{v_{Cz}}{c_0 \Omega \nu}.$$

From the thermodynamic relation $\Delta\mu(r) = k_B T \ln[c_{eq}(r)/c_0]$, we can thus express the interfacial chemical potential as

$$\Delta\mu(r) = k_B T \ln\left(-\frac{v_{Cz}(r)}{\nu \Omega c_0} + 1 + \sigma(r)\right). \quad (4.28)$$

When considering steady states we have from the definition of v_{Cz} (see Eq. (2.18)) that $v_{Cz} = -u_{Cz}$. This in particular allows to express the steady state interface chemical potential in the center of the contact as

$$\Delta\mu(0) = k_B T \ln\left(\frac{u_{Cz}}{\nu \Omega c_0} + 1 + \sigma(0)\right). \quad (4.29)$$

The relation above can be related to the condition for cavity appearance $\Delta\mu^{cav}(0) = 0$, giving a relation for the velocity at the transition

$$u_{Cz}^{cav} = -\sigma(0)\nu\Omega c_0. \quad (4.30)$$

Recalling the expression of the supersaturation in the center of the contact deduced from mass conservation Eq. (4.14) we also have:

$$\sigma(0) = \sigma_b - \frac{|u_{Cz}|L^2}{4hDc_0\Omega}.$$

Combining the latter relation with Eq. (4.30), we obtain the following generalized transition criterion:

$$|u_{Cz}^{cav}| = \frac{\Omega c_0 \sigma_b^{cav}}{\alpha L_{cav}^2 / (4hD) + \nu^{-1}}, \quad (4.31)$$

where we included the phenomenological constant α observed in simulations for fast surface kinetics ($\nu \rightarrow \infty$), such as the one measured from the slope of the transition line in Fig. 4.6 or in Fig. 4.9.

4.4.2 Growth rate before the transition

When the crystal-substrate interaction is attractive, following the same lines of Section 4.3 and Appendix D.1, it is possible to find an analytical expression for the steady-state crystal velocity below the transition in the limit of slow attachment kinetics. The derivation in Section 4.3.4 was based on a perturbative analysis of the steady-state solution $\zeta \approx \zeta_{eq} + \delta\zeta$ with $\zeta_{eq} \approx h$, where h is the minimum of the crystal-substrate interaction potential ($U'(h) = 0$), and $\delta\zeta$ is a small perturbation. Consider Eq. (4.1) with Eq. (4.2b). Since in steady-state ($\partial_t \zeta = 0$) $v_{Cz} = -u_{Cz}$, and u_{Cz} is a constant, we have $\partial_r u_{Cz} = 0$. As a consequence, steady-state equations for slow and fast surface kinetics are identical (Eq. (D.1)). Thus we obtain a parabolic steady state profile similar to that derived for the fast surface kinetics limit (Eq. (4.22)) and represented in Fig. 4.10. Since the crystal velocity depends on this profile via Eq. (4.3), one obtains an expression for the velocity before the formation of the cavity identical to Eq. (4.24),

$$u_{Cz} = \frac{-4Bh(\Delta\mu_b - \Delta\mu_{eq})}{\left(\frac{6B}{h^2}\eta + \frac{1}{2} - \frac{4\tilde{\gamma}}{L^2 U''(h)}\right) L^2 \Omega},$$

with the equilibrium chemical potential given by Eq. (4.25),

$$\Delta\mu_{eq} \approx \frac{2\Omega}{L} \sqrt{-2\tilde{\gamma}U(h)}.$$

Once again, the only difference is the link between $\Delta\mu_b$ and the supersaturation (Eq. (4.28)). Computing the linearized form of Eq. (4.28) in $r = L$ and using the steady-state condition $v_{Cz} = -u_{Cz}$, we have

$$\Delta\mu_b = k_B T (\sigma_b + \frac{u_{Cz}}{\Omega c_0 \nu}). \quad (4.32)$$

Using this expression in Eq. (4.24) we finally obtain in the limit of large contacts and large supersaturations ($\Delta\mu_{eq} \approx 0$)

$$u_{Cz} \approx \frac{-hD\Omega c_0 \sigma_b}{(3/2\bar{\eta} + 1/8)L^2 + hD\nu^{-1}}, \quad (4.33)$$

where h is the equilibrium position of the interaction, in the minimum of the attractive well (see Eq. (4.17)). This formula generalizes Eq. (4.26) including the effect of surface kinetics.

4.4.3 Simulations details and results

We here proceed to verify numerically the analytic conclusions of the previous sections, i.e.: i) cavity formation is described by the generalized transition line obeying Eq. (4.31), ii) Eq. (4.33) is a good estimate of the velocity before the transition.

Recalling Eq. (4.1), we now have to express the concentration by Eq. (4.2b). From the definition of v_{Cz} we rewrite these equations in a more compact way:

$$v_{Cz} = \frac{1}{r} \partial_r [r \zeta \Omega D (\partial_r c_{eq})] + \frac{1}{r} \partial_r [r \frac{\zeta D}{\nu} (\partial_r v_{Cz})], \quad (4.34a)$$

$$2u_{Cz} \pi \int_0^R dr r \int_r^R dr' \frac{6\eta r'}{\zeta(r')^3} = F_{Cz} + 2\pi \int_0^R dr r U'(\zeta), \quad (4.34b)$$

$$c_{eq} = c_0 + \frac{c_0}{k_B T} \left[\Omega \left(\tilde{\gamma} \partial_{rr} \zeta + \frac{\tilde{\gamma}}{r} \partial_r \zeta - U'(\zeta) \right) \right], \quad (4.34c)$$

$$\partial_t \zeta = -v_{Cz} - u_{Cz}. \quad (4.34d)$$

Note that we used the linearized thermodynamic relation, $c_{eq} \approx c_0(1 + \Delta\mu/(k_B T))$. As discussed in Section 4.4 and Appendix B.2, Eq. (4.34a) can be solved numerically by matrix inversion for v_{Cz} . This solution at each time step gives the evolution of the interface $\partial_t \zeta$ using Eq. (4.34d).

We consider the same set-ups as in Section 4.2 and in Section 4.3. The former is characterized by a purely repulsive disjoining pressure and represents, for instance, the evolution of a crystal after sedimentation on a substrate. The latter includes an attractive term in the disjoining pressure and could be associated with growth after heterogeneous nucleation. In the first case, U is given by Eq. (4.4) and F_{Cz} is the gravitational buoyancy force. In the second case U is given by Eq. (4.17) and $F_{Cz} = 0$. We also use a small normalized viscosity, $\bar{\eta} = 10^{-6}$, in order to focus on the dependence on the kinetic constant ν in Eq. (4.33).

Choosing the time scale associated to diffusion as a reference, the normalization of the equations is identical to that of Section 4.2.2 or Section 4.3.1 depending on the interaction considered, with an additional normalization for the kinetic constant given by

$$\bar{\nu} = \frac{l^2}{hD} \nu, \quad (4.35)$$

where l is the crystal size length scale defined previously. The boundary conditions are also identical to those used previously: fixed supersaturation σ_{bc} and width ζ_{bc} at the edge of the (constant) integration box, at $r = R$.

Morphology diagram

The constant α in Eq. (4.31) can be determined in the fast surface kinetics regime from the slope of the transition lines in the morphology diagrams discussed previously. In Fig. 4.6 we

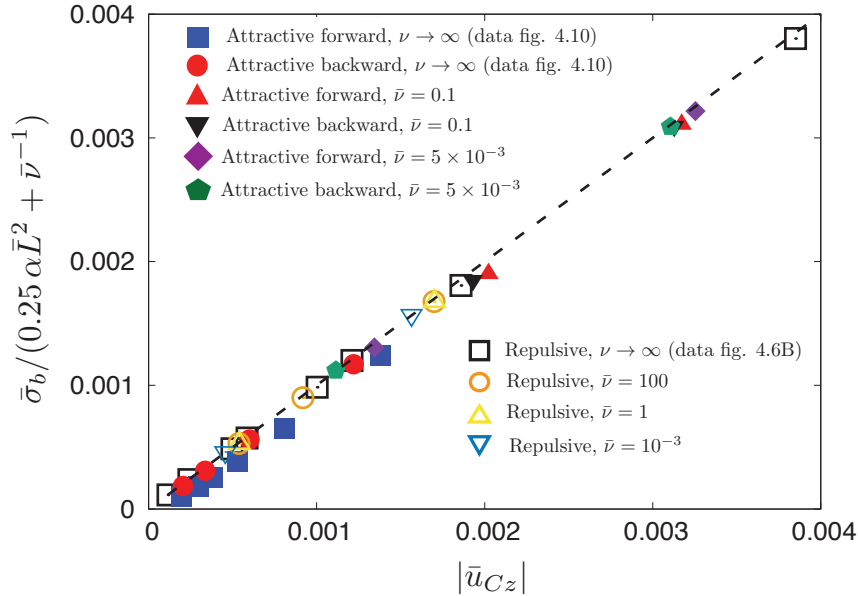


Figure 4.13: Generalized non-equilibrium morphology diagram for different normalized surface kinetics constants $\bar{\nu}$. The constant α appearing in the vertical axis is equal to 0.61. The dashed line is a reference line of slope one passing through the origin. The fact that the data for the attractive case does not exactly pass through the origin is a consequence of the non-vanishing σ_b for $L \rightarrow \infty$ (see Eq. (4.23)). Results are in normalized units.

had $\alpha \approx 0.61$. In Fig. 4.9, where we considered nano-confinement, the measured slope $\alpha \approx 0.65$ was a result of an average between simulations at $\bar{\eta} = 10^{-2}$, at $\bar{\eta} = 10^{-5}$, and the two branches (“forward” and “backward”) of the hysteresis curves. Here, we obtain α using the smallest viscosity, $\bar{\eta} = 10^{-5}$. Using the data obtained at this viscosity (black squares and red circles in Fig. 4.9) the fitted slope is again $\alpha \approx 0.61$. Therefore we use this value in Eq. (4.31).

We computed the generalized non-equilibrium morphology diagram using the same procedures as in the previous sections. Indeed, the transition appears in the same way as in the diffusion limited regime: We observe analogous continuous (repulsive interaction) or discontinuous transitions (attractive interaction) with hysteresis. The result are shown in Fig. 4.13. The data is reported in code units for a large span of values of the surface kinetic constant, from $\bar{\nu} = 10^{-3}$ to $\bar{\nu} = 100$, together with the results in the fast attachment limit (filled blue squares and red circles, and empty black squares) obtained in the previous sections. For the attractive case, we again considered the two different branches of the transition. All the data point collapse very well on the transition line given by Eq. (4.31) (slope equal to one).

As discussed in Appendix D.3 and shown in Fig. D.2, it is also interesting to plot the transition line without assuming the heuristic constant α (or equivalently fixing $\alpha = 1$). In this plot, we can observe that the slope of the transition line ranges from ≈ 0.6 for the fast kinetics case, to ≈ 1 when the effect of slow kinetics is dominant. In this representation, the slope of the morphology diagram is sensitive to the underlying kinetic mechanisms. This could be an interesting direction of research in experiments to probe the kinetic constant ν indirectly for a given material.⁴

Let us compare the values of the normalized kinetic constant, discussed so far, to physical quantities. This allows one to evaluate when deviations to the transition line obtained assuming dominant diffusion kinetics Eq. (4.15) should be observed. As a preamble, we note that in normalized units the generalized transition line Eq. (4.31) reduces to

$$|\bar{u}_{Cz}^{cav}| = \frac{\bar{\sigma}_b}{\alpha \frac{\bar{L}^2}{4} + \bar{\nu}^{-1}}. \quad (4.36)$$

⁴Additional important improvements on the interpretation of the morphology diagram have been achieved in Ref. [176].

The fast surface kinetics limit is simply given by the above with $\bar{\nu}^{-1} = 0$. Let us assume that the typical lateral scaling of the crystal is $l = \mu\text{m}$, that the film thickness h ranges from 10 to 100nm and that the smallest crystal contact considered is $L = 10\mu\text{m}$ (in the simulations we have explored contacts at most small as $\bar{L} \approx 8$). For salts as sodium chlorate let us take $\nu \approx 10^{-3}\text{ms}^{-1}$ [76, 148], and $D \sim 10^{-10}\text{m}^2\text{s}^{-1}$ (as suggested by the discussion in Section 4.2.6 and [163]). This corresponds to a normalized kinetic constant $\bar{\nu}$ (see Eq. (4.35)) from about 10^2 to 10^3 . From Eq. (4.36) with $\bar{L} = 10$, we find that the inclusion of the term $\bar{\nu}^{-1}$ would constitute a negligible correction to the denominator, smaller than 0.1%.

However, if we consider for instance CaCO_3 and use $\nu \approx 10^{-6}\text{ms}^{-1}$ [174, 175], we have $\bar{\nu}$ from about 10^{-1} to 10^{-2} . Confronting this value to Eq. (4.36) and assuming again $\bar{L} = 10$, it can be observed that now the exclusion of the term $\bar{\nu}^{-1}$ would imply an error from about 100% to 1000% in the denominator. Thus, this correction is necessary.

These observations are also confirmed by the numerical results showed in Appendix D.3 in Fig. D.2, where the data points at $\bar{\nu} = 10^2$ are not distinguishable from results obtained in the fast surface kinetics limit, whilst those computed using $\bar{\nu} = 10^{-1}$ or 10^{-2} are well separated from them.

Growth rate

Finally, we compare simulation results to the analytic expression for the velocity before the transition Eq. (4.33). This is shown in Fig. 4.14 for different values of the normalized kinetic constant $\bar{\nu}$. In the left panel, we consider the attractive case (with interaction given by Eq. (4.17)). The analytic expression (dashed red curve and open circles) compares very well to the simulation result (black filled circles). The value of L and σ_b appearing in Eq. (4.33) are extracted from the simulations. We also account for corrections coming from the equilibrium chemical potential⁵.

In the right panel, we consider the repulsive interaction case. When the term ν^{-1} dominates, the prediction (red empty triangles and dashed curve) is accurate with respect to simulations (black filled triangles). However, deviations are observed in the diffusion limited regime, i.e. for large $\bar{\nu}$ in Fig. 4.14b. Indeed, for a repulsive disjoining pressure there is no formal proof that Eq. (4.33) is correct. In particular, in this case, we cannot define an equilibrium position h to be used in the perturbative analysis.

4.5 Discussion

4.5.1 Comparison with existing literature

To the best of our knowledge the only modern works, before [106], precisely discussing the appearance of rims are those of Røyne and Dysthe [104] and Li et al. [105]. These authors mainly focused on measuring the rim width and also described in detail step dynamics and surface topography. In general, our results are not suited for a detailed comparison with their observations since we did not analyze rim width nor surface roughness.

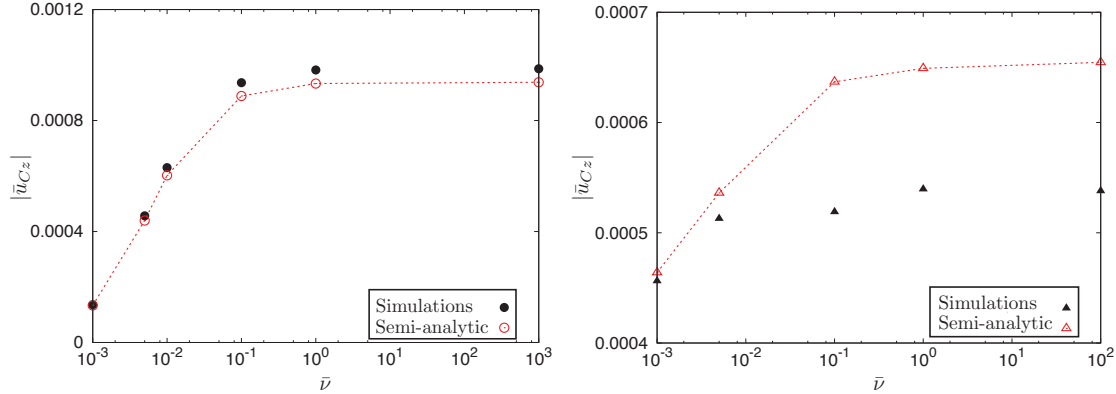
Note that Ref. [104] suggests that for large crystals the rim width is of order $l_0 = \sqrt{Dh/\nu}$ where D is the bulk diffusion, h the film thickness (assumed constant) and ν a kinetic constant for surface growth. Furthermore, for crystal sizes comparable to l_0 they also expect (but not observe directly) that rims should not form. Our findings do not agree with this conclusion since we demonstrated that, in the framework of our model, we can still find conditions for which rim can form for crystal sizes below l_0 .

⁵Since the contact considered are not very large ($\bar{L} \approx 25$). From Eq. (4.24), we have

$$u_{Cz} \approx \frac{-hD\Omega c_0 [\sigma_b + \Delta\mu_{eq}/(k_B T)]}{L^2/8 + hD\nu^{-1}}$$

where $\Delta\mu_{eq} \sim 1/L$ is given by Eq. (4.25) and the viscosity term has been neglected since small. In the repulsive case we assume $\Delta\mu_{eq} = 0$.

Figure 4.14: Normalized growth rate below the transition at different normalized kinetic constants compared to the predictions given by Eqs. (4.24) and (4.32) with Eq. (4.25). Terms of order $1/L^2$ in the denominator are neglected. Simulations are realized at small $\bar{\eta} = 10^{-6}$ hence in the vanishing viscosity regime (see Fig. 4.12). For the repulsive interaction we assumed $\Delta\mu_{eq} \approx 0$. The parameters L and σ_b are extracted from the simulations. This is why we refer to semi-analytic results. The simulation in box is for every simulation $\bar{R} = 40$.



(a) The interaction potential is given by Eq. (4.17). Filled black circles: simulation results. The same boundary supersaturation in R , $\bar{\sigma}_{bc} = 0.2$ is used for all simulations. The contact area increases with $\bar{\nu}$: first point on the left $\bar{L} = 24.6$, last points $\bar{L} = 30$. The supersaturation at the boundary of \bar{L} decrease from $\bar{\sigma}_b \approx 0.19$ to 0.15 . Open red circles: semi-analytic results.

(b) The interaction is given by Eq. (4.5). Filled black triangles: simulation results. Here supersaturations are chosen close to the transition ($\bar{\sigma}_{bc}$ changes for every point). This enforces for each simulation an average film width close to h . First point on the left $\bar{L} = 14.6$, $\sigma_b \approx 0.48$ last point $\bar{L} = 16.8$ $\sigma_b \approx 0.02$. Open red triangles: semi-analytic results.

4.5.2 Shape of a crystal growing on a substrate

We have developed a framework to describe the morphology and growth velocity of the confined surface. In particular, in the presence of an attractive interaction, we showed that Eq. (4.33) is an accurate prediction of the growth rate at the confined surface if no cavity is present or before a cavity forms. In order to obtain the global shape of a crystal growing on a substrate, we need in addition to determine the shape evolution outside the contact. In the case of diffusion-limited dynamics, this would require the full 3D solution of the diffusion equation which is beyond the scope of this thesis. However, for surface limited kinetics in the general anisotropic case the growth at the free faces is simply characterized by an orientation dependent velocity (see Section 1.1.4). A combination of the growth velocity outside and inside the contact leads to a generalization of the Frank construction [6] which allows one to determine the growth shape.

For instance, assuming for simplicity an isotropic crystal (see Fig. 4.15), in the hypothesis of surface driven growth outside the contact region, the free faces of the crystal move with velocity $u_0 = \nu\Omega c_0\sigma$ with σ the bulk supersaturation outside the contact area. This expression is obtained assuming a macroscopic crystal. Indeed, from Eq. (2.10) we expect for a large curvature radius and far from the substrate $c_{eq} \sim c_0$ (i.e. $\kappa \approx 0$ and $U' \approx 0$). Using Eq. (4.33), and the definition of critical diffusion length scale $l_0^2 = hD/\nu$, the velocity of the confined surface is given by

$$u_{Cz} = \frac{u_0}{\left(\frac{3}{2}\bar{\eta} + \frac{1}{8}\right)\frac{L^2}{l_0^2} + 1}, \quad (4.37)$$

where $\bar{\eta} = B/h^2\eta$ is the normalized viscosity defined in Eq. (4.9). As illustrated in Fig. 4.15 taking as reference frame the center of the crystal on the substrate, we define the radius of the island R , the contact size L , the contact angle θ_{tl} and the vertical width of the crystal h_0 . We then have $R = R_0 + u_0t$ with R_0 the initial size of the seed crystal, $L^2 = R^2 - h_0^2$, and $\theta_{tl} = \pi - \theta$ with $\tan\theta = L/h_0$. Equation (4.37) then can be combined to the above relations to describe the

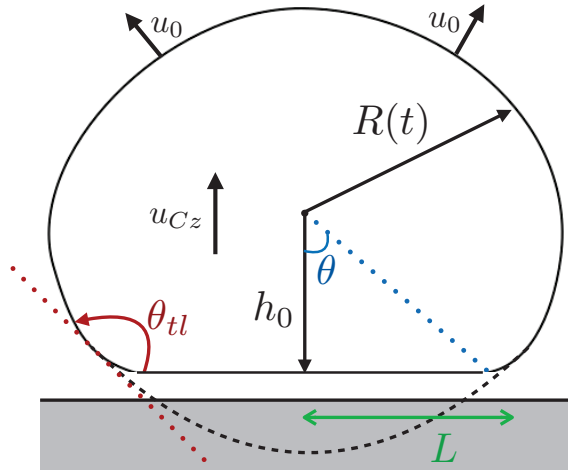


Figure 4.15: Sketch of a macroscopic crystal growing in the vicinity of a substrate, for instance, after heterogeneous nucleation. The evolution of the confined surface can be determined via Eq. (4.33) before a cavity appears. Notations are given in the text.

evolution of h_0 and θ_{tl} :

$$\dot{h}_0(t) = \frac{u_0 l_0^2}{(3/2\bar{\eta} + 1/8)(R(t)^2 - h_0(t)^2) + l_0^2} \quad (4.38a)$$

$$R(t) = R_0 + u_0 t \quad (4.38b)$$

$$\theta_{tl} = \pi - \arctan\left(\frac{R^2}{h_0^2} - 1\right)^{1/2}. \quad (4.38c)$$

The previous equations can be solved numerically. Since $\dot{h}_0 \sim R^{-2} \sim t^{-2}$, the height of the contact will reach a finite value h_∞ as $t \rightarrow \infty$. The fact that h_∞ is finite is the central result of this section. From the above observations it also follows that $\theta_{tl} \rightarrow \pi/2$.

This description will break down if a cavity appears under the contact since we do not know the expression of the velocity of the confined face with a cavity. The discussion of this section applies for example to the initial stages of growth after heterogeneous nucleation on a substrate. The evolution should follow Eq. (4.38) until cavity appears (at $L \geq L_{cav}$) or for cases in which cavity does not appear as such those discussed in Section 4.3 (highly soluble sugars and reduced separation with the substrate).

These results can be generalized for anisotropic growth outside the contact. Since h_∞ is finite, the asymptotic Frank shape will always be half of the free asymptotic shape, i.e. the Frank shape truncated by a plane passing through its center.

4.5.3 The heuristic constant alpha

The constant α , which accounts for the deviation from the expected slope of one in the morphology diagrams, seems to be robust with respect to details of the model as demonstrated by Figs. 4.6, 4.9 and 4.13. However, the physical reason for which this correction is observed is still not elucidated. Figure D.2 seems to suggest that the constant α might be an indication of an overall over-estimation of the surface area. Indeed, in Eq. (4.31) α appears at the denominator only in front of the term proportional to L^2 and theoretically predicted slope of one are indeed observed when $1/\nu \gg 1$. In the following, we argue that this interpretation is not satisfactory. This emerges when comparing how the estimation of the contact radius L performs with respect to different observables.

For instance, as illustrated in Fig. 4.5 the method used to compute L in Section 4.2 gave very good data collapse with respect to boundary conditions. This is not observed with alternative estimators.

Other inconsistencies with this interpretation emerge when considering the prediction of the growth rate below the transition. To illustrate this, let us consider the case of nano-confinement with an attractive interaction where u_{Cz} is given by the analytic formula Eq. (4.33). This prediction is compared with simulations in Figs. 4.12 and 4.14a (note that in the former figure also the y scale is logarithmic). A detailed inspection of the results reveals that perfect match between the analytic curve and the simulation points could be realized by increasing the contact radius of about 5%. However, if we now consider the morphology diagram in the diffusion limited scenario, α is ≈ 0.6 (we measured 0.61 in Fig. 4.6 or 0.65 in Fig. 4.9). This would correspond to a correction accounting for an over-estimation of the contact radius of about 20%. If we assume that even in Fig. 4.14b the discrepancy is partially due to erroneous contact radius estimation, then better agreement (though never as good as in the attractive case) could be achieved with corrections of the contact radius leading to an *under*-estimation of contact area of about 10% (corresponding to $\alpha \approx 1.2$). These observations demonstrate that the natural interpretation of α as a consequence of bad surface area estimation is not adequate.

Finally, α could also account for inaccurate estimations of the film width h . Indeed, it is not obvious that the average width under the contact area is h (before the cavity form). We assumed h to be enforced through the interaction potentials Eqs. (4.5) and (4.17), but its value in principle can depend on other parameters as for instance the supersaturation. However, from numerical results, looking for instance at Figs. 4.4 and 4.10 (where for the scaling adopted one has to compare to $\bar{h} = 1$), close to the transition we observe $\zeta(r) \approx h$ in the contact area. This does not support the hypothesis that α accounts for inaccurate evaluations of h .

4.5.4 Limitations of the model

Facets and effective stiffness

Some limitations of our approach are discussed in this section. The first one concerns the difficulty to analyze strongly anisotropic crystals which exhibit facets. Indeed, the stiffness $\tilde{\gamma}$ is expected to diverge at faceted orientations.

In Section 4.2, to obtain quantitative agreement with the experiments we had to assume a stiffness $\tilde{\gamma} = 10^2 \text{Jm}^{-2}$, whilst surface tension is $\gamma \approx 0.1 \text{Jm}^{-2}$ [92], leading to a ratio $\tilde{\gamma}/\gamma$ around 10^3 . As discussed in Section 1.1.2, it is common to find in the literature non-singular anisotropic continuum models to describe faceted surfaces. These models employ a regularization of the surface tension by means of a small parameter ϵ leading to $\tilde{\gamma}(0)/\gamma(0) \sim \epsilon^{-1}$ [16, 17]. For instance in [17] ϵ is taken between 10^{-2} and 6×10^{-4} leading to stiffnesses 10^2 to 1.6×10^3 larger than surface tension, in agreement with the factor used here.

Below, we provide a hand-waving discussion for the choice of the order of magnitude of the stiffness used in our simulations to match the experiments on NaClO_3 . Neglecting the interaction with the substrate, the chemical potential of the crystal interface $\Delta\mu$ is proportional to the product of the molecular volume Ω , surface stiffness $\tilde{\gamma}$, and surface mean curvature κ . In the presence of a facet –which is a singular flat and spatially extended part of the surface profile – the curvature κ of the crystal surface and the stiffness $\tilde{\gamma}$ are not well defined. However, within a non-singular continuum model such as that used in our simulations, we expect that κ is similar to the inverse of the radius R of the crystal. We therefore have $\Delta\mu \sim \Omega\tilde{\gamma}/R$.

As discussed in Chapter 2, within the diffusion-limited regime, fast attachment-detachment kinetics lead to fast relaxation towards local equilibrium and thus a small departure from equilibrium between the solid and the liquid at the crystal surface. From this observation, and assuming small supersaturations, we also derived the relation $\Delta\mu = k_B T \sigma$. We therefore obtain $\tilde{\gamma} \sim k_B T \sigma R / \Omega$. Assuming $R \sim 10^2 \mu\text{m}$, and using typical supersaturations for NaClO_3 in the UiO experiments $\sigma \sim 10^{-1}$, we find $\tilde{\gamma} \sim 6 \times 10^2 \text{Jm}^{-2}$. This order of magnitude is in agreement with the value $\sim 10^2 \text{Jm}^{-2}$ used in simulations.

In the regime of nano-confined crystals, we did not assume *ad hoc* values of the stiffness. If we apply a similar assumption, the results do not change qualitatively. Indeed, this will not change the measured slope α of the non-equilibrium phase diagram nor the value of the critical viscosity

since these quantities are independent of the stiffness. However, the numerical value of some physical observables would change. If we assume an effective stiffness about $10^3 - 10^4$ times the surface tension, crystal growth velocities (see Fig. 4.9) should be reduced by the same factor. In addition, due to our stiffness-dependent normalization of space variables, our simulations would correspond to larger crystal sizes (by a factor 10 - 100).

In order to reproduce the details of the anisotropy of the experimental shape, one promising strategy is to describe explicitly the dynamics of atomic steps, as suggested by previous studies of facet instabilities during free growth [29, 177].

Nano-confinement and transport

As discussed also in Sections 1.4 and 3.4, a second difficulty is to use continuum models to describe the consequences of nano-scale confinement on diffusion and hydrodynamics. It is known for example that diffusion constants in water can vary significantly with confinement [40]. In contrast, the hydrodynamic description of water with bulk viscosity is known to be quantitatively accurate for separations larger than ~ 1 nm [40]. At the nanoscale, liquids can also be structured in the vicinity of solid surfaces. For example, layering may lead to oscillations in the disjoining pressure [43]. Additional confinement effects specific to solutions appear when the liquid film thickness is decreased up to values that are comparable to the size of the solute molecules. Such confinement effects could be observed, e.g., for sucrose which exhibits a molecular size of the order of one nanometer. Globally, using continuum models to probe nanoscale hydrodynamic effects is a challenge. In order to reach quantitative accuracy, such methods must be based on effective models which are calibrated on molecular simulations to account for possible deviations from the bulk behavior. This strategy should allow one to describe some of the consequences of confinement by means of the thickness-dependence of physical parameters such as the diffusion constant and the viscosity. Achieving this goal would be an important step toward the quantitative modeling of crystal growth with nanoscale confinement. Indeed, modeling of the growth process in standard molecular dynamics simulations is difficult due to prohibitive computational time.

Thermal fluctuations and liquid flow

Another phenomenon which comes to the fore at the nanoscale is thermal fluctuations. While the model discussed here is purely deterministic, atomistic simulations such as Molecular Dynamics of Monte Carlo Simulations [121] can account for fluctuations. Thermal fluctuations could trigger the random opening and closure of the cavity observed in the experiment with NaClO_3 .

Larger-scale fluctuations or perturbations, such as those due to convection or stirring in the bulk fluid outside the crystal, should not be relevant here, since they influence mass transport at scales larger than the thickness of the diffusion boundary layer $\ell_{BL} = D/u_L$ at the free surface of the crystal, which is itself larger than the film thicknesses h considered here. Indeed, taking $D \sim 10^{-9} \text{m}^2/\text{s}$, we would need a very large hydrodynamic velocity $u_L \approx 1$ to 100cm/s outside the contact region for ℓ_{BL} to reach a scale comparable to that of the liquid film in the contact from $h \approx 1$ to 100nm .

4.6 Summary

We have shown in this chapter that when a growing crystal is placed in the vicinity of a flat wall, a cavity can form in the surface of the crystal facing the wall. The appearance of a cavity can be formulated in terms of a non-equilibrium morphology diagram characterized by a straight transition line passing through the origin. Despite differences with the model, e.g. with respect to crystal anisotropy, such a behavior is consistent with recent experiments on NaClO_3 .

The robustness of this description is confirmed when considering systems at reduced separations where the non-equilibrium morphology diagram is found to be unchanged (with a similar

value of the phenomenological constant α). In this case, other quantitative examples are discussed considering materials ranging from poorly soluble minerals (calcite) to high soluble sugars. However, some differences are observed at the nanoscale. First, we show that an attractive van der Waals interaction induces a discontinuous (subcritical) transition with hysteresis. Second, due to the nanoscale width of the liquid film separating the crystal and the confining wall, viscosity becomes relevant. The effect of viscosity is to shift the transition toward larger crystal sizes and larger supersaturations. Furthermore, the formation of the cavity can also be prevented by sufficiently large viscosities. We estimated the relevant critical viscosity above which no cavity should appear. In practice, such condition could be realized for instance for sucrose which exhibits a large viscosity at saturation.

In the last part, we showed that these phenomena should also be observed in systems where surface kinetics is slow. In particular, the transition line can be reformulated to account for small kinetic constants ν .⁶ Finally, we derived an analytic expression of the crystal interface velocity of a flat confined surface accounting for the combined effects of viscosity, diffusion, contact size, and surface kinetics. This expression could be used to predict crystal shapes in the vicinity of a substrate for example in the initial stages of growth after heterogeneous nucleation for surface limited kinetics. The results show that before a cavity forms the crystal can only be shifted up by a finite height due to growth at the confined surface.

⁶Additional important improvements on the interpretation of the morphology diagram have been achieved in Ref. [176].

Crystallization force: beyond the equilibrium thermodynamic picture

In this chapter, we study the crystallization force exerted by a growing crystal located between two parallel substrates. We first discuss equilibrium and show that our model accounts for the expected thermodynamic crystallization pressure. We then address the question of the out of equilibrium crystallization force by letting the crystal grow laterally. We find two out of equilibrium regimes: i) For small surface kinetic constants, the crystal exerts a crystallization pressure which is close to its equilibrium value. ii) For larger surface kinetic constants, a dramatic pressure drop is observed. We show that the latter is correlated to a transition characterized by the kinetic pinning of the triple line followed by the formation of a macroscopic film. Using both analytic arguments and simulations, we show the transition to depend only on the ratio between the diffusion constant and the product of the pore thickness (via the curvature of the growing surface outside the contact) times the surface kinetics constant.

5.1 Introduction

Crystallization force is the force that a crystal exerts on the surrounding medium when confined, for instance in a pore of a host material. Among the type of phenomena observed in confined growth, this is currently the one attracting the highest interest as demonstrated by the significant number of recent studies on the topic [76, 93, 100, 102, 178]. This interest is in particular driven by the crucial role of crystallization force in the weathering of buildings and historical heritage [75, 99].

However, as extensively discussed in Sections 1.3.2 and 1.4.3, there is still need of further insight from a theoretical perspective. Indeed, on the one hand, technical difficulties have limited the number of experiments able to measure such force directly. On the other hand, although significant understanding has been achieved for the equilibrium problem [35, 127], the existing theoretical approaches for out of equilibrium systems [76, 130, 132] do not account for microscopic ingredients at the contact (such as surface tension and disjoining pressures) and still strongly rely on equilibrium thermodynamics. Here, we study a simple “sandwich” geometry where an axisymmetric crystal grows between two flat and parallel walls (Hele-Shaw channel). Furthermore, we use a time-dependent simulation box to allow for lateral growth following the approach presented in Section 2.7.2.

In particular, we find that the interplay between diffusion and surface kinetics controls a *detachment transition*, consisting in the arrest of the triple line followed by the formation of a macroscopically thick liquid film between the expanding crystal and the substrate. The transition

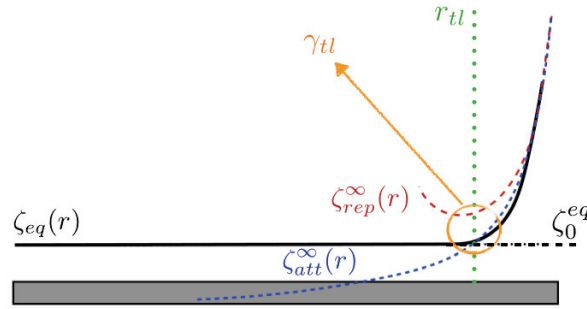


Figure 5.1: Sketch of the interpolation between the macroscopic crystal profile $\zeta_{eq}^\infty(r)$ (far from the substrate) and the actual equilibrium profile $\zeta_{eq}(r)$ (black line) for both repulsive $\zeta_{eq}^\infty = \zeta_{rep}^\infty$ (red dashed line), and attractive $\zeta_{eq}^\infty = \zeta_{att}^\infty$ (blue dashed line) crystal-substrate interaction potential. The black dashed line represents a flat equilibrium profile in the contact region, ζ_0^{eq} . The gray rectangle is the substrate. The area in the circle represents the region where contributions to the line tension γ_{tl} come from.

appears to depend on the ratio between a characteristic transport rate, depending on diffusion and pore size, and surface kinetics. After the transition, a dramatic drop in the crystallization pressure is observed although the crystal keeps growing laterally.

5.2 Thermodynamic Equilibrium

As discussed in the previous sections, the chemical potential is given by

$$\Delta\mu = \Omega [\tilde{\gamma}\kappa(\zeta) - U'(\zeta)] ,$$

with $\tilde{\gamma}$ the stiffness, $\kappa(\zeta)$ the curvature of the crystal profile and $U'(\zeta)$ the crystal-substrate disjoining force. At equilibrium we have $\Delta\mu(\zeta_{eq}) = \Delta\mu_{eq}$ where $\Delta\mu_{eq}$ is a constant. Let us consider the equilibrium profile of a macroscopic crystal¹ far from the substrate ζ_{eq}^∞ characterized by the property $U'(\zeta_{eq}^\infty) = 0$. The equilibrium chemical potential is then given by

$$\frac{\Delta\mu_{eq}}{\Omega} = \tilde{\gamma}\kappa(\zeta_{eq}^\infty) , \quad (5.1)$$

corresponding to the habitual Gibbs-Thomson relation (Laplace pressure) for a free crystal in the absence of a substrate. On the other hand, assuming the contact size to be large enough for the equilibrium profile to be flat in the center of the contact $\zeta_0^{eq} = \zeta_{eq}(0)$, we also have

$$\frac{\Delta\mu_{eq}}{\Omega} = -U'_0 , \quad (5.2)$$

where $U'_0 = U'(\zeta_0^{eq})$. Let us define with the name *triple line* the crossover between these two regions at a distance r_{tl} from the center of the contact. We consider an axisymmetric crystal and define the equilibrium force F_{eq} as the global force on the equilibrium crystal arising from the disjoining forces (see also the force balance Eq. (2.43) with $u_{Cz} = 0$)

$$F_{eq} = -2\pi \int_0^R dr [rU'(\zeta_{eq})] , \quad (5.3)$$

where $R \gg r_{tl}$. The equilibrium shape outside the contact is the solution of Eq. (5.1), and reads:

$$\zeta_{eq}^\infty(r) = \frac{\Delta\mu_{eq}}{4\Omega\tilde{\gamma}}(r^2 - r_{tl}^2) - \frac{F_{eq}}{2\pi\tilde{\gamma}} \ln \frac{r}{r_{tl}} + \zeta_{tl}^\infty . \quad (5.4)$$

¹The adjective ‘‘macroscopic’’ refers to a crystal which exhibits some part of its surface which is far enough from the substrate for the interaction to be negligible.

The details of the calculations are given in Appendix E.1. The precise definition of r_{tl} is to some extent arbitrary. In the following, we will use different conventions depending on the nature of the contact, e.g. adhesive (minimum in the interaction potential) or purely repulsive. These features are illustrated in Fig. 5.1. Using the fact that the chemical potential is constant (see above), we finally obtain two independent relations describing the system at equilibrium:

$$\frac{F_{eq}}{2\pi\tilde{\gamma}} \frac{1}{r_{tl}} = \frac{\Delta\mu_{eq}}{2\Omega\tilde{\gamma}} r_{tl} - \partial_r \zeta_{tl}^\infty, \quad (5.5a)$$

$$\frac{\tilde{\gamma}}{2} (\partial_r \zeta_{tl}^\infty)^2 = \Delta U + \frac{\Delta\mu_{eq}}{\Omega} (\zeta_{tl}^\infty - \zeta_0^{eq}) + \frac{\gamma_{tl}^0}{r_{tl}}, \quad (5.5b)$$

with $\Delta U = U_\infty - U_0$, $U_\infty = U(\zeta_{eq}(r \gg r_{tl})) \sim 0$, $U_0 = U(\zeta_0^{eq})$ and $\zeta_{tl}^\infty = \zeta_{eq}^\infty(r_{tl})$. The last term in the above equation γ_{tl}^0 is the line tension neglecting the excess volume (energetic cost associated to the difference in the number of particles between the real profile and the macroscopic one). The line tension represents the difference between the free-energy associated to a contact with a straight triple line (1D), and the one of the corresponding macroscopic configuration composed only of a macroscopic profile far from the substrate and a flat interface profile in the contact region (see Appendix E.1.1). Its expression together with the derivations of the above relations are given in Appendix E.1.

Equation (5.5a) characterizes the equilibrium force balance whilst Eq. (5.5b) is linked to the equilibrium shape of the profile at the triple line. Finally, one should note that the position of the triple line provides a definition of the contact radius L at equilibrium. The contact radius has a central role in assessing the crystallization pressure $P = F_{Cz}/(\pi L^2)$. This is why it is important to characterize the triple line at equilibrium. Indeed, as discussed in Section 5.4, r_{tl} can be used to benchmark the methods which estimate in practice the contact radius from simulations. In the following, this will allow us to realize reliable estimations of the contact radius to compute the pressure in out of equilibrium dynamics.

5.2.1 Equilibrium pressure with an attractive interaction

In the case of an attractive interaction, one has a perfect analogy with usual wetting concepts. First of all, as commented in Appendix E.1, if we consider the problem of a confined solid with zero external force we expect for a large crystal $\Delta\mu_{eq}/\Omega = 0$. Zero equilibrium chemical potential using Eq. (5.5b), implies in the small slope limit the usual Young relation plus a contribution from the line tension which vanishes for macroscopic crystals ($r_{tl} \rightarrow \infty$):

$$\frac{\tilde{\gamma}}{2} (\partial_r \zeta_{tl}^\infty)^2 \approx \tilde{\gamma}(1 - \cos \theta_{tl}) = \Delta U + \frac{\gamma_{tl}^0}{r_{tl}}, \quad (5.6)$$

with $\Delta U = U_\infty - U_0 = -U_0 > 0$ (using $U_\infty \approx 0$), and θ_{tl} the contact angle². In order to keep this well defined contact angle relation when $\Delta\mu_{eq} \neq 0$, we use the relation

$$\zeta_{tl}^\infty = \zeta_0^{eq}, \quad (5.7)$$

as a conventional definition of the triple line position r_{tl} .

Then, combining Eq. (5.5a) together with Eq. (5.5b) and the definition $\zeta_{tl}^\infty = \zeta_0^{eq}$ we obtain

$$\frac{\Delta\mu_{eq}}{\Omega} = \frac{F_{eq}}{\pi r_{tl}^2} + \frac{1}{r_{tl}} \left[8\tilde{\gamma} \left(\Delta U + \frac{\gamma_{tl}^0}{r_{tl}} \right) \right]^{1/2}, \quad (5.8)$$

where the sign in front of the square root is chosen from physical consideration. At equilibrium and in the dilute limit one has the standard thermodynamic relation $\Delta\mu_{eq} = k_B T \ln(1 + \sigma)$ [35],

²Note that in Eq. (5.6) $\gamma_{tl}^0 = \gamma_{tl}$ is not an approximation. Indeed, as shown in Appendix E.1, the limit of $\Delta\mu_{eq} = 0$ coincides with the limit of zero excess volume at the triple line.

where the equilibrium supersaturation σ is constant and uniform through the film and in particular equal to the one away from the contact region (the boundary supersaturation bath σ_{bc} in the numerical scheme). It follows that we can write

$$P_{eq} = \frac{k_B T}{\Omega} \ln(1 + \sigma) - \frac{1}{L} [8\tilde{\gamma}(\Delta U + \frac{\gamma_{tl}^0}{L})]^{1/2} \quad (5.9)$$

where $P_{eq} = F_{eq}/(\pi L^2)$ is the equilibrium pressure with $L = r_{tl}$ as the contact radius. Equation (5.9) is equivalent to the standard thermodynamic expression of Correns and Steinborn [98] for $L \rightarrow \infty$. Hence we can consider this expression as a generalization of Correns's expression which includes surface tension and wetting corrections for small crystals.

5.2.2 Equilibrium pressure with a repulsive interaction

As ΔU tends to zero, in Eq. (5.5b) the contact angle $\partial_r \zeta_{eq}^\infty(r_{tl})$, defined at $\zeta_{eq}^\infty(r_{tl}) = \zeta_0^{eq}$, will tend to zero as well. In particular, for a repulsive potential since $U_0 > 0$, there is no crossing of the macroscopic profile with the line $\zeta = \zeta_0^{eq}$ (see Fig. 5.1). This is why we need to assume a different definition of the triple line position. We choose to impose

$$\partial_r \zeta_{eq}^\infty(r_{tl}) = 0. \quad (5.10)$$

The first consequence of this convention is that the equilibrium contact angle relation Eq. (5.5b) gives a relation for the discontinuity ($\zeta_{tl}^\infty - \zeta_0^{eq}$) of the macroscopic profile at the triple line:

$$\frac{\Delta \mu_{eq}}{\Omega} (\zeta_{tl}^\infty - \zeta_0^{eq}) = -\Delta U + \frac{\gamma_{tl}}{r_{tl}}. \quad (5.11)$$

This relation has no practical use for the determination of the equilibrium force but can be used to predict the shape of the profile far from the substrate according to Eq. (5.4) if the other variables are known. From the definition of the triple line Eq. (5.10), the relation between equilibrium force and chemical potential is from Eq. (5.5a) simply given by

$$\frac{F_{eq}}{\pi r_{tl}^2} = \frac{\Delta \mu_{eq}}{\Omega}. \quad (5.12)$$

Finally, using again the link between equilibrium supersaturation and interface chemical potential in the dilute limit, we recover the expression of Correns [98]

$$P_{eq} = \frac{k_B T}{\Omega} \ln(1 + \sigma) \quad (5.13)$$

given that the contact size is $L = r_{tl}$ with r_{tl} defined through Eq. (5.10).

It is interesting to note that in this case, neither the functional form of the interaction nor effects linked to surface free energy play a role in the equilibrium pressure. In addition, the pressure P_{eq} is independent of the contact size.

5.3 Simulation details

Our goal now is to investigate how the crystallization pressure is affected by non-equilibrium growth conditions. As a preamble, we will verify that our model and numerical scheme can reproduce the equilibrium relations.

In order to do so, we consider the system illustrated in Fig. 2.5c, where a crystal is confined by a double contact separated by a distance $2d$ (pore size). For simplicity, as done in the previous chapter we consider an axisymmetric geometry. However, here we solve the system equations with an expanding simulation box as illustrated in Section 2.7.2. Also, in contrast to the previous chapters, we use the full nonlinear (exponential) relation between local interfacial

chemical potential and concentration but assume, given the geometry, zero vertical rigid body velocity, $u_{Cz} = 0$. Using Eqs. (2.11), (2.45), (2.48b) and (2.64) we have the following system of equations:

$$\partial_t \zeta = -\frac{1}{r} \partial_r [r \zeta \Omega D(\partial_r c_{eq})] - \frac{1}{r} \partial_r \left[r \frac{\zeta D}{\nu} (\partial_r (\partial_t \zeta)) \right], \quad (5.14a)$$

$$c_{eq} = c_0 e^{\Delta\mu/k_B T}, \quad (5.14b)$$

$$\Delta\mu = \Omega \left[\tilde{\gamma} \partial_{rr} \zeta + \frac{\tilde{\gamma}}{r} \partial_r \zeta - U'(\zeta) \right], \quad (5.14c)$$

$$v_l = -\frac{\partial_t \zeta_{bc}}{\partial_r \zeta_{bc}} = \partial_r \zeta_{bc}^{-1} [\Omega \nu c_0 (1 + \sigma_{bc} - e^{\frac{\Delta\mu_{bc}}{k_B T}})], \quad (5.14d)$$

where v_l is the velocity of the edge of the simulation box. Note that the terms multiplied by the stiffness in Eq. (5.14c) represent the axisymmetric curvature. The relation for the lateral contact velocity, Eq. (5.14d) depends on the boundary width ζ_{bc} , chemical potential $\Delta\mu_{bc}$, and supersaturation σ_{bc} . In particular, at the boundary we have from Eq. (5.14c)

$$\frac{\Delta\mu_{bc}}{\Omega} = (\tilde{\gamma} \kappa_{bc} - U'(\zeta_{bc})) \approx \tilde{\gamma} \kappa_{bc}, \quad (5.15)$$

where we assumed as usual that the film width at the boundary is large enough for the interaction with the substrate to vanish. The curvature at the boundary itself depends on the pore size and evolves during the integration according to³

$$\kappa_{bc} = \left[\left(1 + (\partial_r \zeta_{bc}(t))^2 \right)^{1/2} (d - \zeta_{bc}) \right]^{-1}. \quad (5.16)$$

We sometimes use an alternative boundary conditions where the curvature can be held fixed at the boundary. Globally, the quantities which are fixed in the integration are the film width at the boundary ζ_{bc} , the pore thickness d , and the bulk supersaturation outside the contact region σ_{bc} . The interaction potential appearing in Eq. (5.14c) is identical to that of Section 4.2,

$$U(\zeta) = \bar{a} A \frac{e^{-\frac{(\zeta-h)}{h\bar{\lambda}}}}{\zeta - h}, \quad (5.17)$$

where \bar{a} and $\bar{\lambda}$ are dimensionless constants representing respectively the repulsion amplitude and range, and the constant A [J/m] contains the physical units. Finally the force is calculated from the axisymmetric force balance equation Eq. (2.43) (with $u_{Cz} = 0$):

$$F = -2\pi \int_0^{r_{bc}(t)} dr r U'(\zeta), \quad (5.18)$$

with $r_{bc}(t)$ the boundary of the integration domain (here growing $v_l = \dot{r}_{bc}(t)$). The evolution equations are solved in normalized units following the numerical scheme illustrated in Appendix B.3. The normalized equations read

$$\partial_t \bar{\zeta} = \frac{1}{\bar{r}} \partial_{\bar{r}} \left[\bar{r} \bar{\zeta} \exp(\Delta\bar{\mu}) \partial_{\bar{r}} \Delta\bar{\mu} \right] - \frac{1}{\bar{r}} \partial_{\bar{r}} \left[\frac{\bar{\zeta}}{\bar{\nu}} \partial_{\bar{r}} (\partial_t \bar{\zeta}) \right] \quad (5.19a)$$

$$\Delta\bar{\mu} = \left[\partial_{\bar{r}\bar{r}} \bar{\zeta} + \frac{1}{\bar{r}} \partial_{\bar{r}} \bar{\zeta} - \bar{a} \left(\frac{e^{-\frac{(\bar{\zeta}-1)}{\bar{\lambda}}}}{\bar{\zeta} - 1} \right)' \right] \quad (5.19b)$$

$$\bar{v}_l = \partial_{\bar{r}} \bar{\zeta}_{bc}^{-1} [\bar{\nu} (1 + \sigma_{bc} - \exp(\Delta\bar{\mu}_{bc}))] \quad (5.19c)$$

$$(5.19d)$$

³Note that this expression is not exact since it approximates the constant-curvature surface outside the contact region by an arc of circle (thus assuming isotropy). For detailed discussion and schematics see Section 2.7.2.

where the superscript $'$ indicates derivative taken with respect to ζ and we directly inserted Eq. (5.14b) in Eq. (5.14a). Note that above we do not have a bar over the supersaturation σ . Indeed, we here choose a normalization which makes physical supersaturation correspond to the same quantity in code units ($\bar{\sigma} = \sigma$). Remark also that two alternative time scales can be used in the normalization of time, the diffusion one and the one linked to surface kinetics ν . We choose as previously the diffusive time scale. Then the dimensionless interaction amplitude is $\bar{a} = \Omega/(h^2 k_B T) A$, and dimensionless variables are the normalized width $\bar{\zeta} = \zeta/h$, radius $\bar{r} = r/l$ with $l^2 = \Omega \tilde{\gamma} h / (k_B T)$, and time $\bar{t} = k_B T c_0 D / (\tilde{\gamma} h) t$, where as in the previous section l is the rescaling factor to be applied to the radial distances. Beyond the constants $\bar{\lambda}$ and \bar{a} describing the potential, and the supersaturation σ_{bc} , another constant appearing in Eq. (5.19) is the normalized kinetic constant

$$\bar{\nu} = \frac{l^2}{Dh} \nu = \frac{\Omega \tilde{\gamma}}{D k_B T} \nu. \quad (5.20)$$

Equation (5.19)s have to be supplemented with a condition on the (normalized) curvature at the boundary of the integration domain Eq. (5.16). We then define the normalized pore half width

$$\bar{d} = \frac{h}{l^2} d. \quad (5.21)$$

The relation above is derived from the condition that $2d$ must have the same scaling as κ^{-1} . Finally, the profile obtained via Eq. (5.19) at each time step is used to compute the crystallization force via Eq. (5.18). This introduces the two last relevant normalized observables: the normalized crystallization force

$$\bar{F} = \frac{F}{h \tilde{\gamma}}, \quad (5.22)$$

and the normalized crystallization pressure

$$\bar{P} = \frac{\Omega}{k_B T} P, \quad (5.23)$$

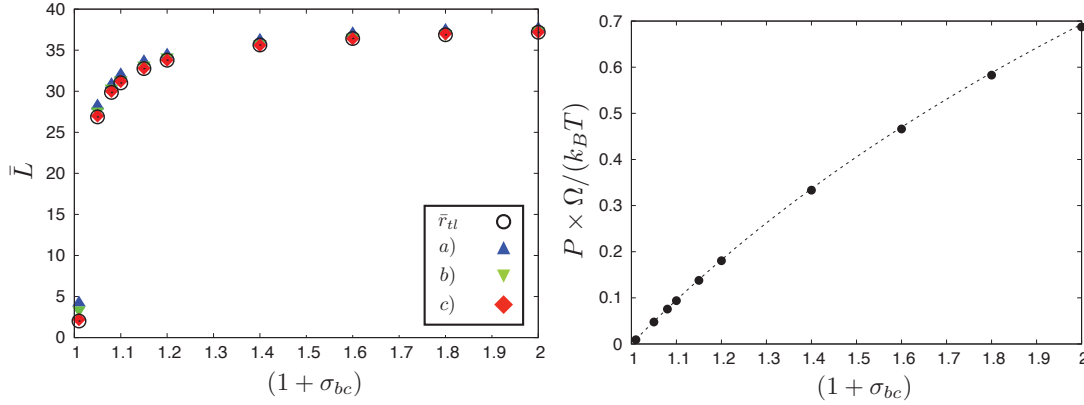
where $P = F/\pi L^2$ with $L = l \bar{L}$. We choose the normalized interaction amplitude to be $\bar{a} = \Omega/(h^2 k_B T) A = 10^{-3}$. This choice for example corresponds to a minimum separation enforced by the interaction $h \approx 10\text{nm}$, with $\Omega \sim 10^{-28}\text{m}^3$, $k_B T \sim 10^{-21}\text{J}$, and – to have a similar order of magnitude as in DLVO-type forces at nano-metric separation [43] – $\bar{A} \sim 10^{-12}\text{J/m}$. The interaction range is held fixed to $\bar{\lambda} = 10^{-2}$ in all simulations. In any case, as illustrated in Appendix E.2 at equilibrium, simulation results show that the choice of \bar{a} has no impact on steady-state results.

In the following, we will focus on qualitative discussions. Hence, results will be given in code units. However, some orders of magnitude for NaCl will be given. This choice is motivated by the recent experimental work of Désarnaud et al. [93] and Naillon et al. [76] where they use a similar configuration as the one adopted here. Parameters for NaCl are: [131, 179] $c_0 = 3.7 \cdot 10^{27}$, $\tilde{\gamma} = \gamma$ with $\gamma \approx 10^{-1}\text{Jm}^{-2}$, $\Omega = 45\text{\AA}$, $D = 10^{-9}\text{m}^2\text{s}^{-1}$. As discussed previously, kinetic constants of salts are reported to span a wide range of values: $\nu = 10^{-3}$ to 10^{-5}ms^{-1} [76]. Finally, in principle also here the question of the correct value of surface stiffness known to diverge for anisotropic faceted crystals arises (see discussion in Sections 1.1.2 and 4.5.4). Hence when physical units are given, we will also present results at a larger stiffness $\tilde{\gamma} = 10^2\text{Jm}^{-2}$ as that discussed in Section 4.2.

5.4 Equilibrium simulations and contact area determination

To validate the simulations and choose a method to estimate the contact radius L , we first performed equilibrium simulations. These are implemented imposing a fixed curvature κ_{bc} , supersaturation σ_{bc} and width ζ_{bc} at the boundary of the integration domain. The width at the

Figure 5.2: Left panel: Contact radius estimated in the different manners listed in the text compared to the target value r_{tl} . The simulation box is $\bar{R}_0 = 40.6$. At high supersaturations, all estimations converge to the correct value. Furthermore, this value is close to the total simulation box. Right panel: Equilibrium pressure, $P/(\pi L^2)$ versus boundary concentration using criterion c) to compute L , the dashed line is the analytic thermodynamic expression from Eq. (5.13).



boundary is chosen to be large enough for the interaction to be vanishing. Since $v_l = 0$ at equilibrium, equilibrium simulations correspond to

$$0 = \partial_r \zeta_{bc}^{-1} [\Omega \nu c_0 (1 + \sigma_{bc} - e^{\frac{\Delta \mu_{bc}}{k_B T}})], \quad (5.24)$$

so that, using Eq. (5.15), the curvature at the boundary is given by

$$\kappa_{bc}^0(\sigma_{bc}) = \frac{k_B T}{\tilde{\gamma} \Omega} \ln(1 + \sigma_{bc}). \quad (5.25)$$

The simulations were started with a flat contact of size R_0 . As expected the results are found to be independent of the initial conditions, as illustrated in Appendix E.2. The system reaches equilibrium after some equilibration time: the concentration is constant along all the profile and equal to the imposed value $c_0(1 + \sigma_{bc})$. The profile is stationary, zero mass flux is reached (see Appendix B.4) and a constant equilibrium force is observed. The time evolution of the crystallization force is illustrated in Fig. E.1 in Appendix E.2, where the force reaches a plateau corresponding to its equilibrium value. We also observe, as expected, that variations of the kinetic coefficient do not affect the simulation results but only influence the timescale needed to equilibrate the system.

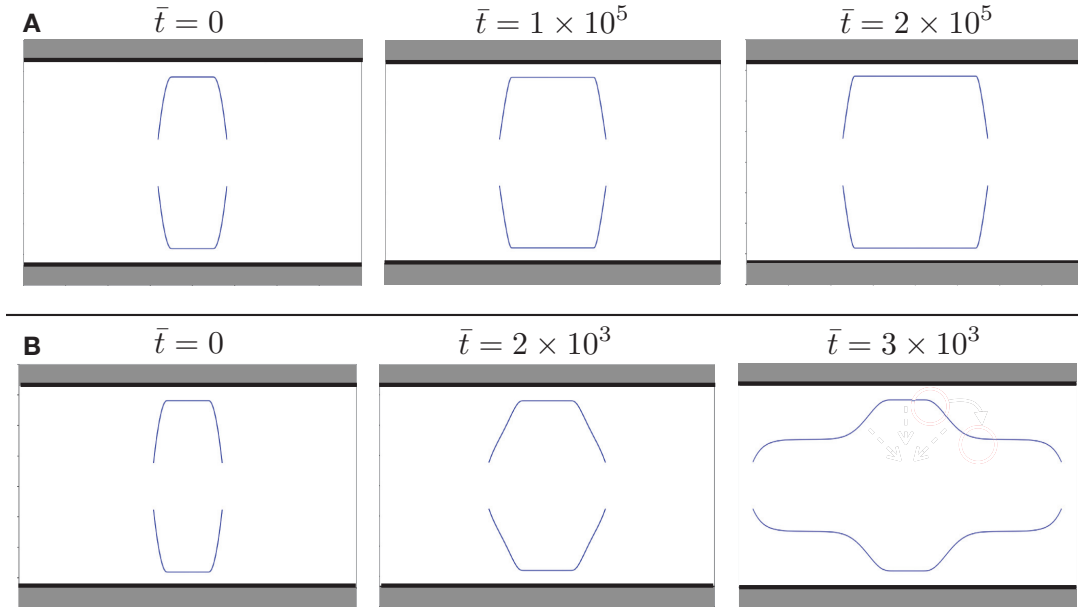
We then evaluated the equilibrium pressure. To do so, one has to estimate the contact radius L . In practical experiments, the determination of the contact area realizing a perfect match with the equilibrium prediction could be delicate. In our framework, a measure that would realize a perfect agreement with the usual thermodynamic relation Eq. (5.13) consists in identifying L with the triple line r_{tl} defined from $\partial_r \zeta_{eq}^\infty(r_{tl}) = 0$. However, this definition is not operationally accessible in out-of equilibrium simulations since it is valid only at equilibrium.

In the left panel of Section 5.4 we show different methods of estimation of the contact radius based on geometrical observations. These are:

- a) $L = \max_r [\zeta''(r)],$
- b) $L = \min_r [U'''(\zeta)],$
- c) $L = \max_r [U'''(\zeta)].$

We compare this estimations to the target value r_{tl} obtained from Eq. (5.12) given F_{eq} from numerical solution and $\Delta \mu_{eq} = k_B T \ln(1 + \sigma_{bc})$. Whilst collapse of the alternative estimations of L on the desired value r_{tl} is always obtained in the limit of large supersaturations and contacts, discrepancies are observed at lower supersaturations. This analysis suggests that the best

Figure 5.3: Blue curve: crystal profiles projected along r . Shaded area: pore walls. In both simulations $\sigma = 0.1$ and $\bar{d} = 100$. The vertical axis is downscaled and separation between the two profile is arbitrary and does not reflect the boundary curvature. The radial size is in code units. The box radius represented below (origin in the center of the figures) is $\bar{R}_\infty = 200$. Top panel $\bar{\nu} = 10^{-3}$. Bottom panel $\bar{\nu} = 4 \times 10^{-2}$. In physical units the total simulation box size is $2R_\infty = 1.2\mu\text{m}$ using $\bar{\gamma} = 100\text{mJ}$, or $2R_\infty = 40\mu\text{m}$ using a 10^3 times larger effective stiffness. The the time scale is $\approx 10^{-7}\text{s} \times \bar{t}$ or $\approx 10^{-4}\text{s} \times \bar{t}$ (effective stiffness).



estimate of the contact area is given by the position of the maximum second derivative of the interaction along the profile,

$$L = \max_r [U''(\zeta(r))]. \quad (5.26)$$

Using this criterion, we obtain very good agreement with the thermodynamic prediction as shown in the right panel of Section 5.4. Therefore in the following when calculating non-equilibrium crystallization pressure, we will use Eq. (5.26) to compute the contact area.

Note that this calculation is performed on points of the crystallization grid, hence they are affected by discretization. More refined interpolation schemes could be conceived but would result in a slower computation.

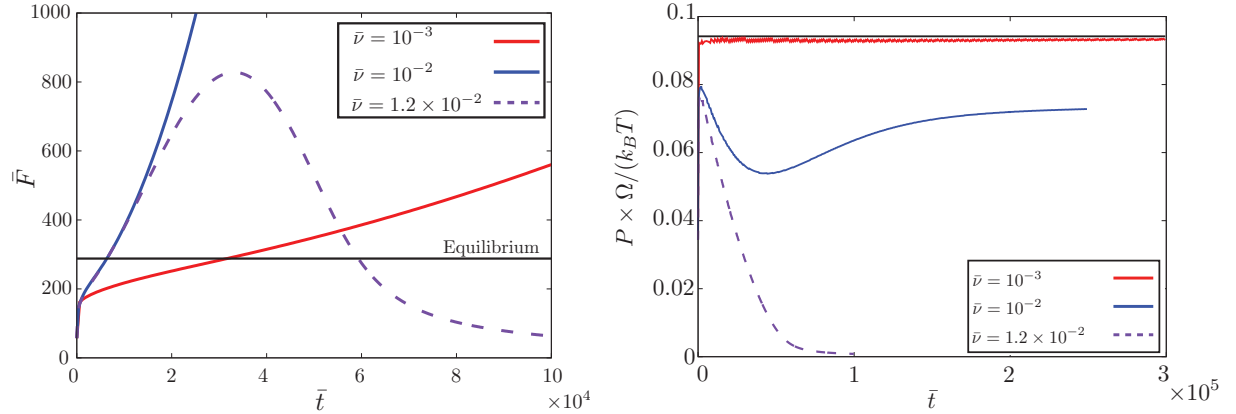
Finally, as illustrated in details in Appendix E.2, we tested the effect of variations of the potential amplitude \bar{a} on the equilibrium pressure and on the relaxation dynamics. We observe no variations of the equilibrium force and contact radius when varying \bar{a} by several orders of magnitude. Since the interaction is purely repulsive, this is in agreement with Eq. (5.13). This is a central result. On the contrary, according to Eq. (5.9), for sufficiently small contacts we would expect an effect of the interaction potential on the equilibrium pressure when the interaction is attractive. Exploratory simulations also reveal no effects of the choice of the thickness ζ_{bc} at the boundary of the integration domain on the equilibrium pressure.

5.5 Out of equilibrium results

Simulations are started using equilibrium profiles of size $\bar{R}_0 = 40.6$. Then lateral growth is allowed by letting the boundary curvature evolve according to Eq. (5.16) at a fixed pore size $2d$, and fixed supersaturation at the boundary σ_{bc} . We observe that the slope $\partial_r \zeta_{bc}$ tends to a constant value for large integration times. It follows from Eq. (5.16) that the curvature at the boundary, after a transient regime, is roughly constant.

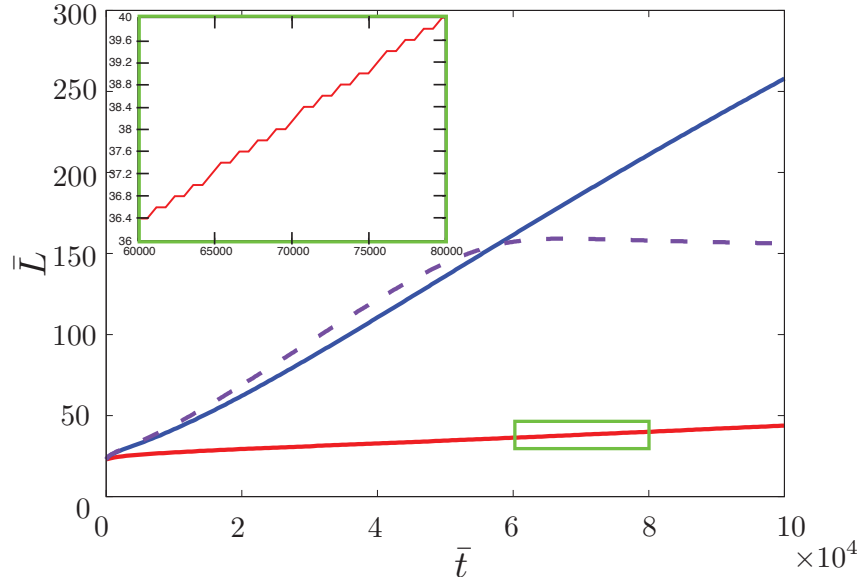
We initially compared simulations with different normalized kinetic constant $\bar{\nu}$. For small $\bar{\nu}$, the profile is flat in the contact region as illustrated by the top panel of Fig. 5.3. The

Figure 5.4: Out of equilibrium time evolution of crystallization force and pressure at different kinetic constants $\bar{\nu}$. Left panel, crystallization force. Right panel, corresponding pressure. The black curves are reference equilibrium values computed from equilibrium simulations. Bottom panel, corresponding time evolution of the contact area. Identical colors refer to the same simulation. For all simulations the boundary supersaturation is $\sigma_{bc} = 0.1$, the half box size is $\bar{d} = 100$, and the boundary width is $\zeta_{bc} = 8.1$. Results are reported in code units. For NaCl: physical time scale is $\approx 10^{-7}\text{s} \times \bar{t}$ or $\approx 10^{-4}\text{s} \times \bar{t}$ using larger effective stiffness; $\nu \approx 1\text{ms}^{-1} \times \bar{\nu}$ or $\nu \approx 10^{-3}\text{ms}^{-1} \times \bar{\nu}$ using larger effective stiffness. The pore size corresponds to $d = 100\text{nm}$ or $d = 100\mu\text{m}$ for the larger stiffness.



(a) The dashed line corresponds to a case of detachment of the crystal profile where the force decreases to zero. The corresponding contact area attains a quasi-stationary value. Therefore, only the drop of force can explain the observed drop of pressure. Black line: corresponding equilibrium force (at $\sigma_{bc} = 0.1$). For NaCl, physical force is given by $10^{-9}\text{N} \times \bar{F}$ or $10^{-6}\text{N} \times \bar{F}$ using the larger effective stiffness.

(b) Pressures corresponding to the forces in the left panel. The contact area area is calculated from the contact radius shown in the plot below. Oscillations are artifacts due to small readjustment of contact area on multiples of the bin size ($\Delta r = 0.2$). Black line: equilibrium pressure (at $\sigma_{bc} = 0.1$) for comparison. For NaCl, physical pressure is obtained multiplying by 92MPa.



(c) Contact radius calculated via Eq. (5.26). Inner panel, zoom on the area highlighted by the green rectangle showing oscillatory behavior. Dashed line, curve corresponding to the case of detachment. The quasi-stationary value can be used as a measure of the remaining contact patch after detachment. At long integration times the value slowly diminishes. We expect an eventual shrink ($L \rightarrow 0$) but this regime is numerically difficult to observe (very large total simulation domain, r_{bc} attained). Radial scale for NaCl is 3nm or $0.1\mu\text{m}$ assuming the larger effective surface stiffness.

width of this film is $\zeta(0) = \zeta_0 \approx h$, where h is the typical thickness scale enforced by the disjoining pressure (Eq. (5.17)). Looking at the relative (time-dependent) crystallization force, such dynamics corresponds to an increasing force with time (red curve in Fig. 5.4a). Interestingly, when considering the corresponding crystallization pressure (red line in Fig. 5.4b) $\bar{P} = \bar{F}/(\pi\bar{L}^2)$ with \bar{L} calculated via Eq. (5.26), after a short transient time \bar{P} reaches a plateau. The plateau oscillates around a stationary value very close to the *equilibrium* crystallization force that one would obtain at the same boundary supersaturation, $\bar{P}_{eq} = \ln(1 + \sigma_{bc})$. This reference value is represented by the black line in Fig. 5.4b. The oscillations are an artifact due to the fact that L is computed on discretized grid points. This discretization error can also be seen in the red curve in Fig. 5.4c representing the time evolution of the contact. Similar behaviors are observed at different supersaturations.

When one considers higher kinetic constants a new phenomenology emerges. As illustrated in the bottom panel of Fig. 5.3, we observe after a given integration time a sudden pinning of the triple line with a macroscopic film forming and a remaining contact patch in the center. Considering again the evolution of the normalized contact size \bar{L} (dashed violet curve), after an initial increase – corresponding for instance to the first two frames of Fig. 5.3 – \bar{L} reaches a quasi-stationary value (slowly decreasing) which represents the size of the remaining patch (as the one in the third frame of Fig. 5.3). However, the corresponding pressure (dashed violet line in Fig. 5.4b) vanishes. This is explained by the drop observed in the force (left panel). This drop corresponds to a progressive separation of the remaining contact from the substrate after the formation of the macroscopic film. This secondary progressive separation in the center is not large (not visible from Fig. 5.3) but is sufficient to cause a drop in the disjoining pressure. We also observe that after the transition and at large integration times, the contact size L of the patch reduces slowly. Even though direct numerical inspection is difficult due to the prohibitively large surface sizes reached, we expect that eventually the contact will disappear. Indeed, at the boundary of the patch, far from the concentration supply, the system gains energy dissolving at the positively curved interface and recrystallizing in the neighboring negatively curved area.

Finally, looking at the blue line in Fig. 5.4b we note a third intermediate regime. In this case, pressure appears to be finite but clearly lower than the equilibrium value. This type of regime is observed when ν is close but below the value for which the macroscopic film forms. This case can be observed comparing the blue and red curves in Figs. 5.4a and 5.4c. By direct inspection of the profiles, it appears that the contact corresponding to the curve right below the transition (blue) is slightly more distant from the substrate than the one corresponding to slower lateral growth (red). This explains the lower plateau in the pressure. The plateau value of these type of intermediate regimes seems also to depend on the boundary condition ζ_{bc} . Furthermore, the convergence to the plateau is extremely slow. This makes computational integrations difficult because of the very large system sizes needed to converge. In particular simulation with large ζ_{bc} converge much slower. It turns out that simulations which are stable with respect to the boundary conditions (see following) are those characterized by such large ζ_{bc} . This is why we are not in the position to draw any quantitative conclusion on these intermediate regimes. We thus discard these cases in the following discussion and focus on the origin of the detachment transition.

In the following, we derive a criterion for the onset of the kinetic pinning of the triple line and systematically analyze the dependence of this threshold on the simulation parameters.

5.5.1 Criterion for detachment

Here we provide an heuristic derivation that suggests a criterion for detachment. Let us consider the evolution equation,

$$\partial_t \zeta = \frac{1}{r} \partial_r [r \zeta \Omega D(\partial_r c_{eq})] + \frac{1}{r} \partial_r \left[r \frac{\zeta D}{\nu} (\partial_r \partial_t \zeta) \right]. \quad (5.27)$$

If we assume steady state at large integration times, $\partial_t \zeta - v_l \partial_r \zeta = 0$, we have $\partial_t \zeta = v_l \partial_r \zeta$. Since v_l depends only on the boundary condition via Eq. (5.14d), it is a constant with respect

to variations of r and we can write

$$v_l \partial_r \zeta = \frac{1}{r} \partial_r [r \zeta \Omega D (\partial_r c_{eq})] + \frac{1}{r} \partial_r \left[r \frac{\zeta D}{\nu} v_l (\partial_{rr} \zeta) \right]. \quad (5.28)$$

Using the relation $c_{eq} = c_0 \exp(\Delta\mu/k_B T)$, the definition of $\Delta\mu$ Eq. (5.14c), and integrating between r_0 and r we obtain

$$v_l \left(r \zeta - r_0 \zeta_{mf} - \int_{r_0}^r dr \zeta \right) = \frac{r \zeta \Omega^2 D c_{eq}}{k_B T} \partial_r (\tilde{\gamma} \partial_{rr} \zeta + \frac{\tilde{\gamma}}{r} \partial_r \zeta - U'(\zeta)) + v_l \frac{r \zeta D}{\nu} \partial_{rr} \zeta, \quad (5.29)$$

where r_0 is a point within the detached film of stationary (macroscopic) thickness ζ_{mf} . Terms at $r = r_0$ on the right hand side vanish. We now let $r \rightarrow r_{bc}$, where $r_{bc}(t)$ is the system size, then, assuming as usual $U'(\zeta(r_{bc}) = \zeta_{bc}) \approx 0$, the term into parenthesis in the right hand side of Eq. (5.29) is the curvature at the edge of the integration domain κ_{bc} . Since the curvature is expected to be constant far from the substrate, we assume that the derivative of the curvature vanishes at the boundary. Rearranging the previous terms and using the definition of κ_{bc} we have

$$\left(-\frac{r_0 \zeta_{mf}}{r_{bc} \zeta_{bc}} - \frac{1}{r_{bc} \zeta_{bc}} \int_{r_0}^{r_{bc}} dr \zeta \right) = \frac{D}{\nu} (\kappa_{bc} - \frac{1}{r_{bc}} \partial_r \zeta_{bc}), \quad (5.30)$$

leading to

$$\left(1 - \frac{\zeta_{mf}}{\zeta_{bc}} + \mathcal{O}\left(\frac{1}{r_{bc}}\right) \right) = \frac{D}{\nu} (\kappa_{bc} - \frac{1}{r_{bc}} \partial_r \zeta_{bc}). \quad (5.31)$$

In the second line we assumed that the region interpolating between ζ_{mf} and ζ_{bc} is small as compared to r_{bc} . Assuming that for $t \rightarrow \infty$ $r_{bc}(t)$ is large and $\partial_r \zeta_{bc} \ll r_{bc}$, we have

$$\left(1 - \frac{\zeta_{mf}}{\zeta_{bc}} \right) = \frac{D}{\nu} \kappa_{bc}. \quad (5.32)$$

For a stationary macroscopic film to exist, ζ_{mf} must be finite (and positive) leading to the criterion:

$$\frac{D}{\nu} \kappa_{bc} < 1. \quad (5.33)$$

Let us compare in detail this expected threshold with simulation results. First one has to assess a criterion to determine the transition event systematically. Inspired by the shape of the profile after the appearance of the macroscopic film, we define the observable *film thickening*, ζ_f given by

$$\zeta_f = \min_r [\partial_{rr} \zeta(r)]. \quad (5.34)$$

This quantity, after the transition corresponds to the location of the triple line pinning (right after the remaining contact patch). Before the transition, since the central area is flat and no concavity is present in $\zeta(r)$, ζ_f gives the width of the film under the contact.

In Fig. 5.5 we show ζ_f as a function of $\nu/(\kappa_{bc} D)$ for different normalized pore half widths \bar{d} and boundary thicknesses ζ_{bc} at large integration times. First of all, we observe that ζ_f is constant for low values of $\nu/(\kappa_{bc} D)$ and close to 1 (h in physical units, the typical crystal-substrate separation) representing the growth of a compact crystal. Then for $\nu/(\kappa_{bc} D) \geq 1$ we observe an abrupt increase of ζ_f representing the detachment. Provided that the integration time is large enough, the values after the transition can be identified with the stationary macroscopic film thickness, $\zeta_f(t \rightarrow \infty) = \zeta_{mf}$. For large d and ζ_{bc} , and when $d \gg \zeta_{bc}$, the transition point saturates at the expected threshold $\bar{\nu}/\bar{\kappa}_{bc} = 1$ (indicated by the black dashed vertical line) in agreement with Eq. (5.33). Furthermore, in this case the transition can be reformulated in terms of pore thickness (walls separation). Indeed, for $d \gg 1$ the curvature from Eq. (5.16) is $\kappa_{bc} \approx d^{-1}$. It follows that we can rewrite the condition for detachment as

$$\nu^* \approx \frac{D}{d}, \quad (5.35)$$

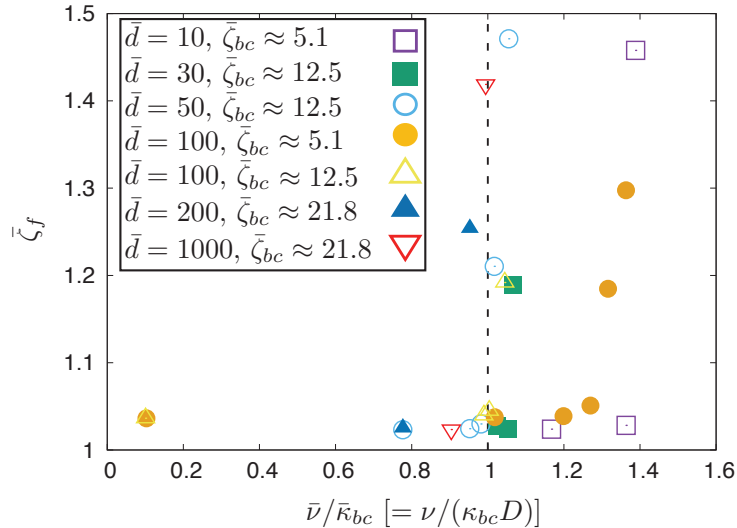


Figure 5.5: Film thickening in the detachment zone with respect to kinetic constant and curvature ratio. Results are obtained measured at large integration times for simulations at different normalized half film thickness \bar{d} and boundary width $\bar{\zeta}_{bc}$. All simulations use a supersaturation at the boundary of the contact zone $\sigma_{bc} = 1$. The vertical dashed line represents the position of the transition as expected from Eq. (5.33). Results are in code units.

with ν^* the critical kinetic coefficient and d the half pore thickness. Since it relates quantities which should be more accessible in experiments, this expression is more convenient for experimental investigations. Remark that in code units this condition reduces simply to

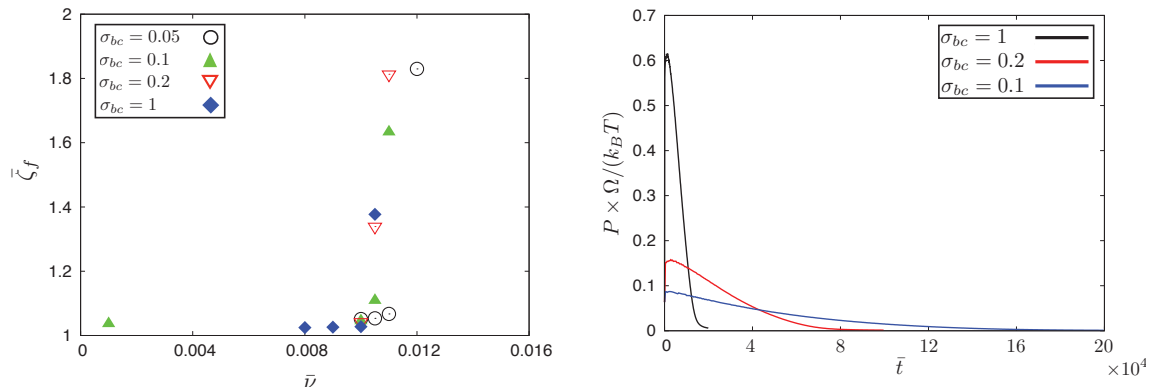
$$\bar{\nu}^* \approx \frac{1}{\bar{d}}. \quad (5.36)$$

Finally, we study the influence of the supersaturation on the detachment. This is shown in Fig. 5.6 for a fixed normalized pore size $2\bar{d} = 200$. As illustrated in the left panel, the effect of supersaturation on the location of the transition is small. In addition, this effect seems to vanish for large supersaturations. In the right panel of the same figure, we show the effect of the supersaturation on the time evolution of the crystallization pressure slightly above the transition (characterized by an asymptotic drop). The supersaturation affects significantly the relaxation time: for small σ_{bc} the decrease of P is slower. Due to very long relaxation times, for small σ_{bc} the simulation times required to reach the asymptotic state can be prohibitive.

To summarize, we have observed three asymptotic non-equilibrium regimes for the pressure at a given bulk supersaturation outside the contact region. These regimes seem to depend exclusively on how the kinetic constant compares to the boundary curvature (or pore width). These regimes are:

- i) The crystallization pressure is indistinguishable from the equilibrium one; no detachment of the interface.
- ii) An intermediate regime where the crystallization pressure reaches an asymptotic value below the equilibrium value but finite; no detachment of the interface.
- iii) The crystallization pressure and force asymptotically vanish: detachment of the interface, kinetic pinning of the triple line and formation of a macroscopic film.

Figure 5.6: Effect of supersaturation on (left panel) or after (right panel) the transition. All simulations at normalized half pore size $\bar{d} = 100$ and normalized boundary width $\bar{\zeta}_{bc} = 22.1$. Left panel, (small) effects on critical surface kinetics constant ν^* . Right panel, effects on time scales for pressure decrease after the transition. Physical units for NaCl are given in Fig. 5.4.



(a) Normalized film thickness in the detachment zone $\bar{\zeta}_f$ versus normalized surface kinetics constant $\bar{\nu}$ for different boundary supersaturations σ_{bc} at large integration times. Collapse at same ν^* observed for high supersaturations.

(b) Normalized pressure versus time at $\bar{\nu} = 1.05 \times 10^{-2}$ for different supersaturations. The critical kinetic constant is $\bar{\nu}^* \approx 10^{-2}$.

5.6 Discussion

5.6.1 Limitations and perspectives

Elasticity and facets

A limitation of our model, as also discussed in the case of pressure solution, is the absence of elastic strain in the crystal and the substrate. This might become important when large crystallization pressures are generated or when considering the possibility of non-hydrostatic stresses [35, 92].

A second limitation discussed in the previous chapter, is to account for strongly anisotropic crystals presenting facets. To obtain quantitative agreement with experiments on faceted crystals, we have used a ratio $\tilde{\gamma}/\gamma \sim 10^3$. However, the value of the stiffness $\tilde{\gamma}$ does not change the results qualitatively. Finally, our main result, i.e. the criterion for detachment Eq. (5.33), is independent of $\tilde{\gamma}$.

The macroscopic film

The detachment transition corresponds to the point where diffusion and surface kinetics are comparable. However by construction, our model for the motion of the interface outside the contact is valid only in the limit where surface kinetics is the slowest process. Hence, we are reaching the limits of validity of our model, and we need to have a critical view of the simulation results above the threshold. For instance, Eq. (5.32) suggests a relation for the macroscopic thickness above the transition:

$$\zeta_{mf} \approx \zeta_{bc} \left(1 - \frac{D}{\nu} \kappa_{bc}\right). \quad (5.37)$$

As shown in Appendix E.3 this relation compares well to numerical results. However, the film thickness in Eq. (5.37) depends on the imposed thickness at the boundary ζ_{bc} which is non-physical. Hence, if on the one hand the detachment transition is found to be robust with respect to boundary conditions, on the other hand Eq. (5.37) confirms that our modeling approach is not adapted to describe the evolution of the interface beyond the detachment transition.

Improvements of the model could be achieved including the full solution of the diffusion transport problem in the bulk outside the contact as done in Refs. [126, 130, 131]. However, these types of models can have also difficulties to converge when large kinetic constants are used [131].

A full exploration of the parameter space would be important to investigate some analogies. Indeed, on the one hand, we think that at the transition the observed phenomenology presents a striking similarity with the Landau-Levich transition [180, 181]. The Landau-Levich transition is a dynamical transition that occurs when drawing a solid out of a liquid bath. Above a threshold velocity, a film is entrained at the surface of the solid. Furthermore, after the detachment transition, the morphology observed in the simulations is similar to that observed in viscous fingering (Saffman-Taylor fingers) [182], or solidification and dendrites in a channel [183]. In addition, as surface kinetics becomes faster, morphological instabilities similar to the Mullins & Sekerka instability discussed in the introduction are expected to take place. A future perspective of our work is to try to formalize these analogies. This goes together with the development of a consistent formulation of the model able to describe the dynamics after the transition.

5.6.2 Comparison with existing literature

At equilibrium, we showed with Eq. (5.9) that for attractive interactions and small crystals, we expect a correction to the crystallization pressure from the interaction potential and the line tension. This is different to usual equilibrium crystallization pressure expressions accounting for surface tension effects in small crystals. For instance using the standard formula as found in Scherer [35] or Steiger [128] one would have in dilute limit and for isotropic surface free energy:

$$P_{eq} = \frac{k_B T}{\Omega} \ln(1 + \sigma) - \bar{\gamma} \kappa, \quad (5.38)$$

with $\bar{\gamma}$ an isotropic surface tension or an effective mean surface tension and κ the curvature of the crystal. Let us compare this expression with our findings for an attractive interaction. Using Eqs. (5.5b) and (5.7) in the small slope limit, Eq. (5.9) can be rewritten as:

$$P_{eq} = \frac{k_B T}{\Omega} \ln(1 + \sigma) - \frac{2}{r_{tl}} \tilde{\gamma} \theta_{tl}^*, \quad (5.39)$$

where r_{tl} is the radius of the triple line, and $\theta_{tl}^* = \pi - \theta_{tl}$, with θ_{tl} the equilibrium contact angle. The above expression is similar to Eq. (5.38). However, the curvature κ is given by the term $2\theta_{tl}^*/r_{tl}$. The angle θ_{tl}^* accounts for the interaction with the substrate and the line energy via Eq. (5.6). Finally, our formula contains the stiffness $\tilde{\gamma}$ instead of the surface tension γ due to the anisotropy of the crystal. Beyond the fact that anisotropy, line tension, and interactions are not explicitly considered in standard formulations, we have shown the crucial role of the choice of definition of the contact area. In our view, existing approaches are ambiguous on this point. For instance, we showed (Eq. (5.13)) that there are definitions of contact area for which the (repulsive) interaction with the substrate and surface tension effects are irrelevant independently from the crystal size.

As discussed in the introduction, out of equilibrium models of crystallization force are seldom found in the literature. To the best of our knowledge, the existing approaches have followed strategies which focus on solving the transport problem around the crystal and deduce the crystallization force via the Correns's equilibrium formula Eq. (5.13) or improved formulations (accounting for instance for the ionic number and non-ideal behavior) [35, 127, 128]. Some of these models are very sophisticated and are able to couple many phenomena including elasticity and crack generation and evolution, via coupled finite element, finite volume, and phase fields methods [130]. However, the resolution of these models is at the scale of the pore, with a poor description of the crystal interface and no inclusion of microscopic interactions between crystal and substrate nor surface tension effects. Furthermore, the systematic use of the equilibrium formulation of the crystallization force is in our view unsatisfactory.

Despite the general differences with current approaches, some analogies can be found with the work of Naillon et al. [76]. These authors claim that a sufficient condition to generate a large crystallization pressure is $Da^2 \ll 1$. This argument is based on the observation that $Da^2 \ll 1$ implies a large supersaturation in the contact region and on the assumption that the crystallization pressure is given by the equilibrium expression Eq. (5.13).

The dimensionless constant Da is known as Damköhler number [184] and represents the competition between precipitation rate (chemical reaction rate) and transport phenomena rate. In [76] the authors define $Da = \sqrt{d\rho_C\nu}/(\Delta cD)$ with Δc a typical concentration for the onset of crystallization with respect to a reference equilibrium one. Within our model, we can reformulate the condition of detachment in terms of a dimensionless Damköhler number. The natural definition of Da is for us

$$Da = \frac{d\nu}{D}. \quad (5.40)$$

With this definition, the detachment corresponds to $Da = 1$. Therefore at a given supersaturation, $Da < 1$ would imply a finite crystallization pressure close to the equilibrium prediction. This is similar to the conclusion of Naillon et al. However, our criterion is different since we obtained a sharp transition ($Da = 1$) for the drop of the crystallization pressure based on the non-equilibrium dynamics of the crystal interface within the contact (detachment transition) maintaining a constant supersaturation bath at the edges of the contact. In contrast, the interpretation of Naillon et al. relies on the concentration field outside the contact and assumes an equilibrium pressure within the contact.

As far as experiments are concerned, we showed that for repulsive interactions and small pore sizes we agree with the usual thermodynamic equilibrium description. Hence our results compare well to the experimental results of Désarnaud et al. [93] which are compatible with equilibrium predictions. However, better quantitative performance from our model could be achieved including the effect of chemical activities or accounting for the presence of more than one ionic species in the solute. For instance, the latter effect implies that the pressure obtained by Correns formula should be multiplied by a factor $n = 2$ when considering 1-1 salts as NaCl. We could account for corrections due to the number of ions using $n\Delta\mu/\Omega = \tilde{\gamma}\kappa - U'(\zeta)$ as the definition of chemical potential.

Finally, it is interesting to assess the critical kinetic constant ν^* for some specific materials. Choosing a pore size of order $10\mu\text{m}$ (similar to the order of magnitude used in [76, 93]), and using the diffusion constants reported in Table 4.1, we would have for instance $\nu^* \approx 10^{-4}\text{m/s}$ for Calcite and $\nu^* \approx 10^{-5}\text{m/s}$ for Sodium Chlorate. In crystallization force experiments NaCl is often considered. Using [179, 185] $D \sim 10^{-9}\text{m}^2\text{s}^{-1}$ we expect again $\nu^* \approx 10^{-4}\text{m/s}$. A similar value can be found using sodium sulfate [186] considered one of the most damaging agents during crystallization pressure [75, 100]. Precise evaluation of surface kinetics constants are difficult and few data are available in the literature. In general, as commented in the previous chapter, the range of values of surface kinetic constants of salts is 10^{-5} to 10^{-3}ms^{-1} [76]. It follows that according to our results, significant crystallization forces should not build up for pores larger than $100\mu\text{m}$.

If we assume precipitation rate of $\nu \approx 10^{-3}\text{ms}^{-1}$ for NaCl as Naillon et al. [76], our analysis suggests that vanishing crystallization force should be observed asymptotically. In particular, in [76] the authors report that, despite an initial bulk supersaturation of $\sigma = 0.7$, in less than 1s they observe a pressure corresponding to the equilibrium pressure at $\sigma = 0.005$. Using Eq. (5.13) this value corresponds to $\bar{P} \approx 5 \times 10^{-3}$. We assume the same parameters as in [76]: $d = 10\mu\text{m}$, $\nu = 10^{-3}\text{ms}^{-1}$, and $\sigma_{bc} = 0.7$. The rest of the parameters are those given in Section 5.3. From the simulation, we extracted the time needed to observe a drop of the crystallization pressure to $\bar{P} \approx 5 \times 10^{-3}$. In physical units, this corresponds to $t_{relax} \approx 0.02\text{s}$, a much shorter time than the one declared in [76]. Eventually, at longer times the pressure keeps decreasing and tends to zero. The observation of a shorter transient time could be due to the fact that the supersaturation is artificially held fixed outside the contact zone in our simulations. This continuum supply of mass can accelerate the process. Another hypothesis is that this difference in time scale is due again to the fact that in the experiments the crystal is faceted. Thus we should account for strong

anisotropy via the effective stiffness. Simulation using the effective stiffness $\tilde{\gamma} = 10^2 \text{Jm}^{-1}$ lead to $t_{relax} \approx 0.4\text{s}$. This is compatible with the transient time observed in [76].

5.7 Summary

We showed in this chapter that using a Hale-Shaw geometry formed by two parallel flat substrates, our model is able to describe the force of crystallization. The approach was validated by demonstrating in details that we can reproduce analytical predictions on the equilibrium crystallization pressure. We pointed out the crucial role of the definition of the contact area on the finite size corrections of the crystallization pressure.

Using a purely repulsive interaction, we found that high crystallization pressures, close to the ones expected at equilibrium, should be obtained for materials characterized by a slower surface kinetics.

In particular, we found a transition at a critical kinetic coefficient which depends on the ratio between pore size and diffusion. After the transition, we observe a kinetic pinning of the triple line leaving a central contact patch and giving birth to a macroscopic film. Simultaneously with the transition, we also observe a drop in the crystallization force and pressure. This transition is only weakly dependent on other parameters such as the supersaturation. The model, however, is not able to describe consistently the phenomenology after the transition because we did not include the description of diffusion transport away from the contact region. The investigation of such a regime would be interesting in order to compare with the film thickness selection of the Saffman-Taylor fingers problem. The coupling of the crystal shape and the diffusion field outside the contact region is thus an important future development of this model.

Another direction of investigation would be to fill the gap between growth with a vertical growth rate $u_{Cz} \neq 0$ and negligible load, which gives rise to rims, as discussed in Chapter 4, and growth without vertical growth rate $u_{Cz} = 0$, which gives rise to a force, as discussed here. The intermediate case with a vertical growth rate decreased by a load indeed corresponds to the seminal experiment of Becker and Day [95].

In this thesis, we presented a continuum model to describe crystals growing or dissolving in confinement. We assumed that the confinement is caused by one or more walls separated from the crystal by a thin liquid film (lubricated contacts), and we focused on the dynamics within a single contact. The model considers the coupled effect of hydrodynamics, surface tension, crystal-substrate interactions, diffusion in the liquid, and surface kinetics.

The first case study we addressed was dissolution against a substrate due to an external load (pressure solution). We showed that the morphology of the contact and the dissolution rates can behave very differently depending on the functional form of the interaction with the wall. In particular, a diverging (power-law) interaction leads to a flattened contact and power-law relations between the dissolution rate, applied load and contact size. The exponents of these laws depend on the viscosity of the liquid in the film. Indeed, the value of viscosity determines two regimes: one dominated by hydrodynamic dissipation and one by disjoining forces. However, when the interaction is finite (exponential) the surface profile becomes pointy and the dissolution rate exhibits an asymptotic value independent of the applied load. Moreover, although the disjoining pressure is finite, no touching contact (zero film thickness) is achievable due to the coupled effect of viscous dissipation and regularization of the tip shape by surface tension. We also considered the effect of dimensionality by comparing results for a 1D ridge and a 2D axisymmetric contact. We found that touching contacts in 2D could be observed for a finite load only in the absence of surface tension.

The second system we considered is an axisymmetric crystal growing on a substrate, e.g., after sedimentation or heterogeneous nucleation. In particular, we focused on the phenomenon of cavity formation on the confined crystal surface facing the substrate. In collaboration with Felix Kohler and Dag Kristian Dysthe (UiO) who performed experiments on NaClO_3 , we showed that cavity formation can be described by a non-equilibrium morphology (“phase”) diagram characterized by a straight transition line passing through the origin. The model also suggests a more general formulation of the transition line accounting for slow surface kinetics. Globally, the results indicated that the morphology diagram should be robust with respect to system details like the form of the disjoining pressure or the type of material. The functional form of the disjoining pressure influences the continuity of the transition. While a purely repulsive interaction leads to a continuous transition, an attractive well in the interaction provokes discontinuity with hysteresis at the transition. We also studied the effect of viscosity and found that beyond a critical viscosity, or better a critical film thickness, the cavity cannot form. This phenomenon is expected in experiments only at nanometric separations and for some highly soluble materials (e.g. sugars). Finally, we proposed a framework to describe the time evolution of the global shape of a growing crystal on a substrate which accounts for viscosity, diffusion, surface kinetics constant, and bulk supersaturation. This applies only for materials where growth at the unconstrained surfaces is driven by surface kinetics and before a cavity forms in the contact region.

We finally discussed the force of crystallization in a Hale-Shaw geometry, i.e. the (axisymmet-

ric) crystal is confined between two parallel walls. First, we discussed the equilibrium pressure and showed that the definition of the contact area is crucial. According to our definition of contact area, we expect corrections to the usual equilibrium pressure formula *only* in the presence of an attractive crystal-substrate interaction. Furthermore, we showed that equilibrium expressions found in the literature including the contribution of (isotropic) surface tension in small crystals should be modified. We then considered growth focusing on the non-equilibrium force and pressure of crystallization. We found two main regimes. A low surface kinetic constant regime, in which the crystallization pressure is roughly equal to the equilibrium pressure at the same bulk supersaturation. A higher surface kinetic constant regime, where the crystallization force vanishes asymptotically. This regime is characterized by a kinetic pinning of the triple line leading to the formation of a macroscopic film with a remaining contact patch in the center (detachment transition). This process is controlled by the ratio between the diffusion constant and the distance between the walls. The detachment transition presents a striking qualitative resemblance to the Landau-Levich transition. Furthermore, above the transition, the selection of the film width exhibits strong similarities with the viscous fingering problem (Saffman-Taylor fingers). The selection mechanism for the macroscopic film thickness remains an open question. Solving this problem would require to include the full solution of the diffusion problem outside the contact region. This is an important perspective of our work.

Other future developments of this work can be envisioned. Some of them are relatively simple and can be addressed within the current model or with minor modifications. The first one would be, due to the relevance in the current scientific debate [187], to address the effect of slow surface kinetics in pressure solution. Other natural developments include for instance to consider the effect of different shapes of the substrate on the growth or dissolution dynamics, or to simulate indentation problems where the crystal and the substrate are brought together by a time-dependent external force. Another short-term direction of research would also be to evaluate the effect of a laterally expanding contact on the problem of cavity appearance and pressure solution (dropping the quasi-static assumption).

Some perspectives are more complex and can require major modifications in the model equations. These consist in withdrawing some of the simplifying assumptions of the model. The most relevant ones are, in our opinion, crystal rigidity and equal densities between the crystal and the liquid. The inclusion of elastic effect would, for instance, improve the description of pressure solution. This would allow one to make link with the well known Asaro-Tiller type instabilities (arising from elastic effects) [67, 92].

In general, the difference of density between the crystal and the liquid should enhance hydrodynamic effects (see in the introduction Section 1.1.5). However, the density difference also affects the chemical potential. The consequences of this effect would require further investigations. Finally, another important perspective would be to include atomic steps in the model. This would provide a better description of faceted crystals.

To conclude, we hope that this work will foster new directions in the study of confined crystal growth and dissolution. In particular, the thin film model could become a systematic tool to investigate these type of problems. Indeed, the model is relatively simple given the complexity of the ingredients involved. The simplicity and the consequent transparency in the interpretation, we think, is the essential added value of our contribution. This allows to recognize the relative importance of the mechanisms at play in confined growth and dissolution problems.

Funding acknowledgment

This project has received funding from the European Union's Horizon 2020 research and innovation programme under grant agreement No 642976.



List of publications

- L. Gagliardi and O. Pierre-Louis. *Thin film modeling of crystal dissolution and growth in confinement*. *Physical Review E* 97, 012802 (01/2018)
- L. Gagliardi and O. Pierre-Louis. *Growth in nano confined crystals: Subcritical cavity formation and viscosity effects*. *New Journal of Physics* 20, 073050 (07/2018)
- F. Kohler, L. Gagliardi, O. Pierre-Louis, and D. K. Dysthe. *Cavity Formation in Confined Growing Crystals*. *Physical Review Letters* 121, 096101 (08/2018)
- L. Gagliardi and O. Pierre-Louis. *Confined Growth with slow surface kinetics: a Thin Film Model approach*. *Submitted* arXiv:1901.07347 (01/2019)
- L. Gagliardi and O. Pierre-Louis. *The Nonequilibrium Crystallization Force Elucidated via a Thin Film Model* (provisional title). *In preparation* (2019)

In this appendix, more details on the mathematical relations used to derive the model presented in Chapter 2 are given. We use the following conventions and definitions:

- h is the position of the liquid-crystal interface LC and h_s the position of the liquid-substrate interface LS .
- Subscript xy indicate two-dimensional vectors in the xy plane.
- Similarly $\nabla_{xy} \cdot \mathbf{a} = \partial_x a_x + \partial_y a_y$.
- $d\mathbf{r} = dx dy dz$ is the infinitesimal volume element and $dS = dx dy \sqrt{1 + (\nabla_{xy} h)^2}$ is the infinitesimal surface element.
- The normal to the LC interface (oriented towards the liquid) is given by

$$\hat{\mathbf{n}} = \frac{(-\nabla_{xy} h, 1)}{[1 + (\nabla_{xy} h)^2]^{1/2}}.$$

- The interface normal velocity (oriented towards the liquid) is given by

$$v_n = \frac{\partial_t h}{[1 + (\nabla_{xy} h)^2]^{1/2}}.$$

To derive the relations below we assume zero surface excess for total and crystal molecule type densities. In the following we will often assume for generality a time dependent liquid velocity $\rho_L(x, y, z, t)$ (even though keeping the incompressibility condition $\nabla \cdot \mathbf{u}_L = 0$). Indeed, most of the relations hold even with this general formulation. This could account for instance for spatial inhomogeneities. However, for simplicity from Appendix A.4 we will use (as declared from the beginning in the main text) constant liquid density ρ_L .

A.1 Global mass conservation

The total mass is the sum of the total mass of the solid units and the total mass of the liquid (neglecting surface mass excess):

$$\mathcal{M} = \iiint_{(L)} d\mathbf{r} \rho_L + \iiint_{(C)} d\mathbf{r} \rho_C. \quad (\text{A.1})$$

This quantity must be conserved, that is $\partial_t \mathcal{M} = 0$ up to terms at the boundaries of the system that are discarded here. The evolution of the total mass is then given by

$$\begin{aligned} \partial_t \iiint_{(L)} d\mathbf{r} \rho_L &= \iiint_{(L)} d\mathbf{r} \partial_t \rho_L - \oint_{(LC)} dS \rho_L v_n, \\ \partial_t \iiint_{(C)} d\mathbf{r} \rho_C &= \oint_{(LC)} dS \rho_C v_n, \end{aligned} \quad (\text{A.2})$$

where we used for convention that the interface velocity v_n is positive towards the liquid and that the crystal density is constant $\partial_t \rho_C = 0$. Also, we have used that $\partial_t h_s = 0$ to have no contribution from the LS interface. Using the continuity equation

$$\begin{aligned} \partial_t \rho_L &= -\nabla \cdot (\rho_L \mathbf{u}_L), \\ \partial_t \rho_C &= -\nabla \cdot (\rho_C \mathbf{u}_C), \end{aligned} \quad (\text{A.3})$$

and the divergence theorem we find

$$\partial_t \mathcal{M} = \oint_{(LC)} dS (\rho_L \mathbf{u}_L \cdot \hat{\mathbf{n}} - \rho_L v_n - \rho_C \mathbf{u}_C \cdot \hat{\mathbf{n}} + \rho_C v_n), \quad (\text{A.4})$$

where we used that since at the LS interface, since the substrate is immobile and impermeable, we have (Eq. (2.4)),

$$\mathbf{u}_L(z = h_S, t) \cdot \hat{\mathbf{n}}_S = 0. \quad (\text{A.5})$$

From the condition that conservation must be local, we have at the interface the usual relation [30], Eq. (2.3) in the main text

$$\rho_L (\mathbf{u}_L \cdot \hat{\mathbf{n}} - v_n) = \rho_C (\mathbf{u}_C \cdot \hat{\mathbf{n}} - v_n). \quad (\text{A.6})$$

A.2 Crystal mass conservation

The total number of crystal-type molecules (or atoms) reads:

$$\mathcal{N}_C = \iiint_{(C)} d\mathbf{r} \Omega^{-1} + \iiint_{(L)} d\mathbf{r} c. \quad (\text{A.7})$$

Here we assume that the solid is rigid, i.e. elastic deformations are small leading to negligible changes in the solid molecular volume Ω .

We then impose local conservation of the total number of atoms/molecules of the crystal-type in the volume and at the (LC) interface, $\partial_t \mathcal{N}_C = 0$. The contribution of the bulk concentration reads

$$\partial_t \iiint_{(L)} d\mathbf{r} c = \iiint_{(L)} d\mathbf{r} \partial_t c - \oint_{(LC)} dS c v_n. \quad (\text{A.8})$$

Then using mass conservation for the concentration:

$$\partial_t c + \mathbf{u}_L \cdot \nabla c = -\nabla \cdot \mathbf{j}, \quad (\text{A.9})$$

where \mathbf{j} is the diffusion flux, we obtain

$$\begin{aligned} \partial_t \iiint_{(L)} d\mathbf{r} c &= \iiint_{(L)} d\mathbf{r} (-\mathbf{u}_L \cdot \nabla c - \nabla \cdot \mathbf{j}) - \oint_{(LC)} dS c v_n, \\ &= \iiint_{(L)} d\mathbf{r} (-\nabla \cdot (\mathbf{u}_L c) - \nabla \cdot \mathbf{j}) - \oint_{(LC)} dS c v_n, \\ &= \oint_{(LC+LS)} dS (\hat{\mathbf{n}} \cdot \mathbf{u}_L c + \hat{\mathbf{n}} \cdot \mathbf{j} - c v_n). \end{aligned} \quad (\text{A.10})$$

In the second line, we have used the incompressibility of the fluid

$$\nabla \cdot \mathbf{u}_L(\mathbf{r}, t) = 0, \quad (\text{A.11})$$

and in the third one the divergence theorem. Since the substrate is immobile and impermeable, from Eq. (A.5), we have at the LS interface

$$\mathbf{j} \cdot \hat{\mathbf{n}}_S = 0. \quad (\text{A.12})$$

It follows that, as done previously we can drop the subscript (LS) in Eq. (A.10). Similarly, assuming no diffusion mass flux within the bulk of the crystal, we have for the crystal contribution

$$\partial_t \iiint_{(C)} d\mathbf{r} \Omega^{-1} = \oint_{(LC)} dS (v_n - \hat{\mathbf{n}} \cdot \mathbf{u}_C) \Omega^{-1}. \quad (\text{A.13})$$

Note that we used that the normal to the LC interface and the interface velocity are oriented towards the liquid. Finally, neglecting the excess density contribution we have

$$0 = \iiint_{(L)} dS [(\hat{\mathbf{n}} \cdot \mathbf{u}_L - v_n)c + \hat{\mathbf{n}} \cdot \mathbf{j} + (v_n - \hat{\mathbf{n}} \cdot \mathbf{u}_C)\Omega^{-1}], \quad (\text{A.14})$$

leading to Eq. (2.8) in the main text,

$$(v_n - \hat{\mathbf{n}} \cdot \mathbf{u}_C)\Omega^{-1} = (v_n - \hat{\mathbf{n}} \cdot \mathbf{u}_L)c - \hat{\mathbf{n}} \cdot \mathbf{j}. \quad (\text{A.15})$$

A.3 Energy changes

We here derive the expression of the time variation of the energy in the system. This allows obtaining the conditions of mechanical equilibrium. Assuming no heat transfer, the total energy variation is given by

$$\partial_t \mathcal{F}_{LC} + \partial_t \mathcal{E}_{kin} + \partial_t \mathcal{F}_{bulk}, \quad (\text{A.16})$$

where we label with \mathcal{F} the free energy and separated its bulk contribution from the liquid-crystal interface contribution and with \mathcal{E}_{kin} the kinetic energy due to liquid motion and dissipation and crystal motion. We proceed in evaluating each term of the previous expression.

Bulk free energy

Defining as $f_L(c)$ the bulk free energy density and as f_C the crystal free energy density the total bulk free energy reads

$$\mathcal{F}_{bulk} = \iiint_{(C)} d\mathbf{r} f_C + \iiint_{(L)} d\mathbf{r} f_L(c), \quad (\text{A.17})$$

and considering the movement of the crystallization front its time derivative reads

$$\begin{aligned} \partial_t \mathcal{F}_{bulk} &= \iiint_{(C)} d\mathbf{r} \partial_t f_C + \iiint_{(L)} d\mathbf{r} \partial_t f_L(c) \\ &+ \oint_{(LC)} dS (f_C - f_L(c)) v_n. \end{aligned} \quad (\text{A.18})$$

Using local mass conservation Eq. (A.9) and incompressibility Eq. (A.11), we have

$$\begin{aligned} \partial_t f_L(c) &= f'_L(c)(-\mathbf{u}_L \nabla c - \nabla \cdot \mathbf{j}) \\ &= -\nabla \cdot (\mathbf{u}_L f_L(c) + f'_L(c) \mathbf{j}) + \mathbf{j} \cdot \nabla f'_L(c) \end{aligned} \quad (\text{A.19})$$

The crystal has a similar contribution, but with no diffusion mass flux \mathbf{j} . As a consequence,

$$\begin{aligned} \partial_t \mathcal{F}_{bulk} &= \iiint_{(L)} d\mathbf{r} \mathbf{j} \cdot \nabla f'_L(c) \\ &+ \iint_{(LC)} dS [(\hat{\mathbf{n}} \cdot \mathbf{u}_L - v_n) f_L(c) + f'_L(c) \hat{\mathbf{n}} \cdot \mathbf{j}] \\ &- \iint_{(LC)} dS (\hat{\mathbf{n}} \cdot \mathbf{u}_C - v_n) f_C, \end{aligned} \quad (\text{A.20})$$

where, as done previously, we used that there is no contribution from the LS interface $\mathbf{u}_L \cdot \hat{\mathbf{n}} = 0$.

Interface free energy

At the interface, we have to consider two different contributions. One comes from the surface free energy, γ , and the other from the interaction per unit area with the substrate (disjoining pressure, see Section 1.2.2) W . We therefore write

$$\mathcal{F}_{LC} = \iint_{(LC)} dS \gamma + \iint_{(LC)} dx dy W[h(x, y); x, y]. \quad (\text{A.21})$$

where $h = h_s - \zeta$ is the position of the interface. The derivative reads [15]

$$\partial_t \mathcal{F}_{LC} = \iint_{(LC)} dS v_n \tilde{\gamma} \cdot \kappa + \iint_{(LC)} dx dy \partial_t h W', \quad (\text{A.22})$$

with κ the curvature tensor and $\tilde{\gamma}$ the stiffness tensor given in 1D by $\tilde{\gamma} = \gamma(\theta) + \gamma''(\theta)$, and $W' = \partial_z W(x, y, z)$. From the expression of the normal velocity and of dS , we can write

$$\partial_t \mathcal{F}_{LC} = \iint_{(LC)} dS v_n (\tilde{\gamma} \cdot \kappa + W'). \quad (\text{A.23})$$

Kinetic energy

Let us now consider the kinetic energy term. From [141] (p. 143, eq. 5.19) we have that the local variation of free-energy in the liquid is given by

$$\partial_t \left(\frac{\rho_L u_L^2}{2} \right) = \nabla \cdot \left[-\mathbf{u}_L \left(\frac{\rho_L u_L^2}{2} + p \right) + \varepsilon' \cdot \mathbf{u}_L \right] - \varepsilon' : (\nabla \otimes \mathbf{u}_L) + \mathbf{u}_L \cdot \mathbf{f}_L, \quad (\text{A.24})$$

where $\varepsilon'_{ij} = \eta(\partial_j u_{Li} + \partial_i u_{Lj})$ with i, j representing the Cartesian components x, y, z , is the viscous stress tensor, \mathbf{f}_L is an external body force acting on the liquid and \otimes is the tensor product. Assuming that the solid density is constant $\partial_t \rho_C = 0$ and using that $\rho_C \partial_t \mathbf{u}_C = \mathbf{f}_C$ where \mathbf{f}_C is an external force density on the crystal,

$$\partial_t \left(\frac{\rho_C u_C^2}{2} \right) = \mathbf{u}_C \cdot \mathbf{f}_C. \quad (\text{A.25})$$

In the spirit of the Stokes limit ($Re \ll 1$), we neglect inertial terms $\rho u_{L,C}^2$. Integrating the two equations and using the divergence theorem we then have an expression for the total variation of kinetic energy in the system given by

$$\begin{aligned} \partial_t \mathcal{E}_{kin} &= \iint_{(LC+LS)} dS [-\hat{\mathbf{n}} \cdot \varepsilon \cdot \mathbf{u}_L] \\ &+ \iiint_{(L)} d\mathbf{r} [-\varepsilon' : (\nabla \otimes \mathbf{u}_L) + \mathbf{u}_L \cdot \mathbf{f}_L] + \iiint_{(C)} d\mathbf{r} \mathbf{u}_C \cdot \mathbf{f}_C, \end{aligned} \quad (\text{A.26})$$

where we defined $\varepsilon_{ij} = \varepsilon'_{ij} - p\delta_{ij}$.

Let us separate the term $\hat{\mathbf{n}} \cdot \varepsilon \cdot \mathbf{u}_L$ in components normal and parallel to the interface :

$$\hat{\mathbf{n}} \cdot \varepsilon_L \cdot \mathbf{u}_L = \varepsilon_{Lnn}(\hat{\mathbf{n}} \cdot \mathbf{u}_L - \hat{\mathbf{n}} \cdot \mathbf{u}_C) + (\hat{\mathbf{n}} \cdot \varepsilon)_{\parallel} \cdot (\mathbf{u}_L - \mathbf{u}_C)_{\parallel} + \hat{\mathbf{n}} \cdot \varepsilon_L \cdot \mathbf{u}_C, \quad (\text{A.27})$$

where using local mass conservation Eq. (A.6), we rewrite

$$(\hat{\mathbf{n}} \cdot \mathbf{u}_L - \hat{\mathbf{n}} \cdot \mathbf{u}_C) = \left(1 - \frac{\rho_C}{\rho_L}\right)(v_n - \hat{\mathbf{n}} \cdot \mathbf{u}_C), \quad (\text{A.28})$$

and from the no slip hypothesis at LC and LS

$$(\mathbf{u}_L - \mathbf{u}_C)_{\parallel} = 0. \quad (\text{A.29})$$

Using that $\hat{\mathbf{n}}_S \mathbf{u}_L = 0$, we are then left with

$$\begin{aligned} \partial_t \mathcal{E}_{kin} &= - \oint\!\!\!\oint_{(LC)} dS \varepsilon_{Lnn} \left(1 - \frac{\rho_C}{\rho_L}\right) (v_n - \hat{\mathbf{n}} \cdot \mathbf{u}_C) \\ &+ \oint\!\!\!\oint_{(LC)} dS \hat{\mathbf{n}} \cdot \varepsilon_L \cdot \mathbf{u}_C \\ &- \iiint_{(L)} d\mathbf{r} \varepsilon' : [(\nabla \otimes \mathbf{u}_L) + (\nabla \otimes \mathbf{u}_L)^T] \\ &+ \iiint_{(L)} d\mathbf{r} \mathbf{u}_L \cdot \mathbf{f}_L + \iiint_{(C)} d\mathbf{r} \mathbf{u}_C \cdot \mathbf{f}_C. \end{aligned} \quad (\text{A.30})$$

A.3.1 Global force balance

We can now combine the three energetic contribution calculated:

$$\begin{aligned} &\partial_t \mathcal{F}_{LC} + \partial_t \mathcal{E}_{kin} + \partial_t \mathcal{F}_{bulk} \\ &= \oint\!\!\!\oint_{(LC)} dS [(\hat{\mathbf{n}} \cdot \mathbf{u}_L - v_n) f_L(c) + f'_L(c) \hat{\mathbf{n}} \cdot \mathbf{j}] \\ &+ \oint\!\!\!\oint_{(LC)} dS [-(\hat{\mathbf{n}} \cdot \mathbf{u}_C - v_n) f_C + v_n (\tilde{\gamma} \cdot \boldsymbol{\kappa} + W')] \\ &- \oint\!\!\!\oint_{(LC)} dS \left[\varepsilon_{Lnn} \left(1 - \frac{\rho_C}{\rho_L}\right) (v_n - \hat{\mathbf{n}} \cdot \mathbf{u}_C) + \hat{\mathbf{n}} \cdot \boldsymbol{\sigma}_L \cdot \mathbf{u}_C \right] \\ &- \iiint_{(L)} d\mathbf{r} \varepsilon' : [(\nabla \otimes \mathbf{u}_L) + (\nabla \otimes \mathbf{u}_L)^T] \\ &- \iiint_{(L)} d\mathbf{r} M [\nabla f'_L(c)]^2 \\ &+ \iiint_{(L)} d\mathbf{r} \mathbf{u}_L \cdot \mathbf{f}_L + \mathbf{u}_C \cdot \mathbf{F}_C. \end{aligned} \quad (\text{A.31})$$

In the previous expression we introduced the the total force acting on the crystal

$$\mathbf{F}_C = \int_{(C)} d\mathbf{r} \mathbf{f}_C = \mathbf{F}_C^{int} + \mathbf{F}_C^{ext}, \quad (\text{A.32})$$

where \mathbf{F}_C^{int} is the internal contribution coming from the liquid and the interface and \mathbf{F}_C^{ext} is an external contribution or *load*.

Considering only the LC contribution and using from local mass conservation Eqs. (A.6) and (A.15) to rewrite the second term of Eq. (A.20), we have

$$\begin{aligned}
 & \partial_t(\mathcal{F}_{LC} + \mathcal{E}_{kin} + \mathcal{F}_{bulk})_{LC} \\
 &= \oint\!\!\!\oint_{(LC)} dS \left[-\frac{\rho_C}{\rho_L} f_L(c) + f'_L(c)(\Omega^{-1} - \frac{\rho_C}{\rho_L} c) \right] (v_n - \hat{\mathbf{n}} \cdot \mathbf{u}_C) \\
 &+ \oint\!\!\!\oint_{(LC)} dS [f_C + \tilde{\gamma} \cdot \boldsymbol{\kappa} + W] (v_n - \hat{\mathbf{n}} \cdot \mathbf{u}_C) \\
 &- \oint\!\!\!\oint_{(LC)} dS \left[\varepsilon_{Lmn} (1 - \frac{\rho_C}{\rho_L}) \right] (v_n - \hat{\mathbf{n}} \cdot \mathbf{u}_C) \\
 &+ \oint\!\!\!\oint_{(LC)} dS [-\hat{\mathbf{n}} \cdot \boldsymbol{\sigma}_L + \hat{\mathbf{n}}(\tilde{\gamma} \cdot \boldsymbol{\kappa} + W')] \cdot \mathbf{u}_C.
 \end{aligned} \tag{A.33}$$

We recognize two type of contributions:

- i) Crystal motion terms, proportional to \mathbf{u}_C .
- ii) Crystal growth/dissolution terms, proportional to $v_n - \hat{\mathbf{n}} \cdot \mathbf{u}_C$.

The first term represents internal forces acting on the crystal. These terms must balance with the total internal force \mathbf{F}_C^{int} introduced in Eq. (A.32):

$$\mathbf{0} = \mathbf{F}_C^{int} + \oint\!\!\!\oint_{(LC)} dS [-\mathbf{n} \cdot \boldsymbol{\sigma}_L + \mathbf{n}(\tilde{\gamma} \cdot \boldsymbol{\kappa} + W')]. \tag{A.34}$$

Assuming no dissipation in the solid bulk, we have $\mathbf{F}_C^{int} = -\mathbf{F}_C^{ext}$ leading to the final relation (Eq. (2.13) in the main text):

$$\mathbf{F}_C^{ext} = \oint\!\!\!\oint_{(LC)} dS [-\mathbf{n} \cdot \boldsymbol{\sigma}_L + \mathbf{n}(\tilde{\gamma} \cdot \boldsymbol{\kappa} + W')]. \tag{A.35}$$

A.4 Planar currents

We now consider flow rate and mass conservation in the film integrating liquid velocity and concentration flux over the channel height, z . From now on we assume for simplicity the liquid density to be constant, ρ_L .

A.4.1 Total flow

Let us now define the (x, y) planar current:

$$\langle \mathbf{u}_{Lxy} \rangle(x, y) = \int_{h(x,y)}^{h_S(x,y)} dz \mathbf{u}_{Lxy}(x, y, z). \tag{A.36}$$

The divergence of the current reads

$$\begin{aligned}
 \nabla_{xy} \cdot \langle \mathbf{u}_{Lxy} \rangle(x, y) &= \partial_x \int_{h(x,y)}^{h_S(x,y)} dz u_{Lx}(x, y, z) + \partial_y \int_{h(x,y)}^{h_S(x,y)} dz u_{Ly}(x, y, z) \\
 &= \mathbf{u}_{Lxy}(x, y, h_S(x, y)) \cdot \nabla_{xy} h_S(x, y) - \mathbf{u}_{Lxy}(x, y, h(x, y)) \cdot \nabla_{xy} h(x, y) + \int_{h(x,y)}^{h_S(x,y)} dz \nabla_{xy} \cdot \mathbf{u}_{Lxy}(x, y, z) \\
 &= \mathbf{u}_{Lxy}(x, y, h_S(x, y)) \cdot \nabla_{xy} h_S(x, y) - \mathbf{u}_{Lxy}(x, y, h(x, y)) \cdot \nabla_{xy} h(x, y) - \int_{h(x,y)}^{h_S(x,y)} dz \partial_z u_{Lz}(x, y, z) \\
 &= -[u_{Lz}(x, y, z) - \mathbf{u}_{Lxy}(x, y, z) \cdot \nabla_{xy} z]_{z=h(x,y)}^{z=h_S(x,y)},
 \end{aligned} \tag{A.37}$$

where the last term of the third line is obtained from the incompressibility condition Eq. (A.11). Since the substrate is immobile (with or without slip), one has $\mathbf{u}_L(z = h_S) \cdot \hat{\mathbf{n}} = 0$, leading to

$$u_{Lz}(x, y, h_S(x, y)) - \mathbf{u}_{Lxy}(x, y, h_S(x, y)) \cdot \nabla_{xy} h_S(x, y) = 0. \quad (\text{A.38})$$

In addition, at $z = h(x, y)$, we have from Eq.(A.6)

$$v_n = \mathbf{u}_L \cdot \mathbf{n} + \frac{\rho_C}{\rho_L} (v_n - \mathbf{u}_C \cdot \mathbf{n}). \quad (\text{A.39})$$

Finally from the definition of v_n and $\hat{\mathbf{n}}$, using the previous relations in Eq. (A.37) we have

$$\partial_t h(x, y) = \nabla_{xy} \cdot \langle \mathbf{u}_{Lxy} \rangle(x, y) + \frac{\rho_C}{\rho_L} [\partial_t h(x, y) - u_{Cz} + \mathbf{u}_{Cxy} \cdot \nabla_{xy} h(x, y)]. \quad (\text{A.40})$$

From this relation together with the definition of the local growth rate v_{Cz} (Eq. (2.18)) we obtain Eq. (2.15) in the main text. This relation indicates that the width $h_s - h$ changes locally either because of a flow $\langle \mathbf{u}_{Lxy} \rangle$ in the xy plane, or because of a crystallization-dissolution process, which corresponds to the second line. This relation can be written in a different way

$$u_{Cz} - \mathbf{u}_{Cxy} \cdot \nabla_{xy} h = \nabla_{xy} \cdot \langle \mathbf{u}_{Lxy} \rangle(x, y) + \left(\frac{\rho_C}{\rho_L} - 1 \right) [\partial_t h(x, y) - u_{Cz} + \mathbf{u}_{Cxy} \cdot \nabla_{xy} h(x, y)]. \quad (\text{A.41})$$

Here, we observe that when $\rho_L = \rho_C$, as it will always be assumed in this work, the source term of the 2D flow $\langle \mathbf{u}_{Lxy} \rangle$ is controlled only by the crystal velocity \mathbf{u}_C .

A.4.2 Concentration current

Let us repeat a similar derivation for the diffusion flux associated with the solid units in the liquid. We define

$$\langle \mathbf{j} \rangle_{xy} = \int_{h(x,y)}^{h_S(x,y)} dz \mathbf{j}_{xy}, \quad (\text{A.42})$$

then

$$\nabla_{xy} \langle \mathbf{j} \rangle_{xy} = [\mathbf{j}_{xy} \cdot \nabla z]_{z=h}^{z=h_S} + \int_{h(x,y)}^{h_S(x,y)} dz \nabla_{xy} \cdot \mathbf{j}_{xy}. \quad (\text{A.43})$$

Using mass conservation of the concentration c in the liquid bulk Eq. (2.6), we find

$$\begin{aligned} \nabla_{xy} \langle \mathbf{j} \rangle_{xy} &= [\mathbf{j}_{xy} \cdot \nabla_{xy} z]_{z=h}^{z=h_S} - \int_{h(x,y)}^{h_S(x,y)} dz \partial_z \mathbf{j}_z - \int_{h(x,y)}^{h_S(x,y)} dz \partial_t c \\ &\quad - \int_{h(x,y)}^{h_S(x,y)} dz \mathbf{u}_{Lxy} \cdot \nabla_{xy} c - \int_{h(x,y)}^{h_S(x,y)} dz u_{Lz} \partial_z c. \end{aligned} \quad (\text{A.44})$$

From incompressibility Eq. (2.1),

$$\begin{aligned} \nabla_{xy} \langle \mathbf{j}_{xy} \rangle &= [\mathbf{j}_{xy} \cdot \nabla_{xy} z - j_z + c \partial_t h]_{z=h}^{z=h_S} \\ &\quad - \partial_t \int_{h(x,y)}^{h_S(x,y)} dz c - \int_{h(x,y)}^{h_S(x,y)} dz \nabla_{xy} \cdot (\mathbf{u}_{Lxy} c) - \int_{h(x,y)}^{h_S(x,y)} dz \partial_z (u_{Lz} c) \\ &= [\mathbf{j}_{xy} \cdot \nabla_{xy} z - j_z + c (\partial_t h + \nabla_{xy} z \cdot \mathbf{u}_{Lxy} - u_{Lz})]_{z=h}^{z=h_S} \\ &\quad - \partial_t \int_{h(x,y)}^{h_S(x,y)} dz c - \nabla_{xy} \cdot \int_{h(x,y)}^{h_S(x,y)} dz \mathbf{u}_{Lxy} c. \end{aligned} \quad (\text{A.45})$$

Using mass conservation at the LS and LC interfaces Eq. (2.6), we then obtain

$$\nabla_{xy} \langle \mathbf{j} \rangle_{xy} = -\Omega^{-1} (\partial_t h + \nabla_{xy} h \cdot \mathbf{u}_{Cxy} - u_{Cz}) - \partial_t \int_{h(x,y)}^{h_S(x,y)} dz c - \nabla_{xy} \cdot \int_{h(x,y)}^{h_S(x,y)} dz \mathbf{u}_{Lxy} c, \quad (\text{A.46})$$

which is finally written in a compact form as

$$\Omega^{-1}(\partial_t h + \nabla_{xy} h \cdot \mathbf{u}_{Cxy} - u_{Cz}) + \partial_t \langle c \rangle + \nabla_{xy} \cdot \langle \mathbf{u} \rangle_{Lxy} c = -\nabla_{xy} \langle \mathbf{j} \rangle_{xy}. \quad (\text{A.47})$$

This corresponds to 2D mass conservation. Using the definition of the local growth rate Eq. (2.18), the previous equation can be rewritten as reported in the main text, Eq. (2.19).

A.5 Lubrication expansion

We here show the standard rescaling adopted when applying the so-called lubrication expansion or small slope limit. We define a small parameter $\epsilon = h_0/\ell \ll 1$ where ℓ is the typical extent of the adhesion patches in the plane $x y$. We may then define normalized order one coordinates:

$$X = \frac{\epsilon x}{h_0}, \quad (\text{A.48a})$$

$$Y = \frac{\epsilon y}{h_0}, \quad (\text{A.48b})$$

$$Z = \frac{z}{h_0}. \quad (\text{A.48c})$$

Following the usual procedure for the lubrication expansion [41], defining a characteristic velocity U_O , we also use normalized velocities:

$$\mathbf{U}_{LXY} = \frac{\mathbf{u}_{Lxy}}{U_0}, \quad (\text{A.49a})$$

$$U_{LZ} = \frac{u_{Lz}}{\epsilon U_0}, \quad (\text{A.49b})$$

where the last equation is a consequence of incompressibility $\nabla_{xy} \mathbf{u}_{Lxy} + \partial_z u_{Lz} = 0$. Assuming parallel flow in the film (Poiseuille flow) $\nabla_{xy} p \sim \eta \partial_z^2 \mathbf{u}_{Lxy}$ and that the characteristic time is given by ℓ/U_0 we have:

$$P = \frac{\epsilon h_0 p}{\eta U_0}, \quad (\text{A.50a})$$

$$T = \frac{\epsilon U_0 t}{h_0}. \quad (\text{A.50b})$$

It is useful in the following to consider the effect of lubrication expansion on the LC normal $\hat{\mathbf{n}}$, and the velocity of the interface v_n are

$$\hat{\mathbf{N}} = \frac{(-\epsilon \nabla_{XY} H, 1)}{[1 + \epsilon^2 (\nabla_{XY} H)^2]^{1/2}}, \quad (\text{A.51a})$$

$$V_n = \frac{\epsilon U_0 \partial_T H}{[1 + \epsilon^2 (\nabla_{XY} H)^2]^{1/2}}. \quad (\text{A.51b})$$

Global mass conservation Eq. (A.6) (Eq. (2.3) in the main text) implies that also u_{Cz} scales as ϵ if the liquid crystal density ratio is finite:

$$U_{CZ} = \frac{\rho_L}{\rho_C} \epsilon U_0. \quad (\text{A.52})$$

Lubrication expansion also implies the curvature tensor of the interface to be simply given by the laplacian, $\kappa \approx \nabla^2 \zeta(x, y, t)$. Finally, given that in the geometries considered $\theta_x = \arctan \partial_x \zeta$ in 1D and $\theta_r = \arctan \partial_r \zeta$ in 2D with $r^2 = x^2 + y^2$, lubrication implies that the stiffness tensor is at the dominant order

$$\tilde{\gamma} = \gamma(\theta) + \gamma''(\theta) \sim \gamma(0) + \gamma''(0). \quad (\text{A.53})$$

A.5.1 Liquid velocity

The liquid velocity obeys to Navier-Stokes equation. This equation in absence of body force and for an incompressible fluid read

$$\rho_L \partial_t(\mathbf{u}_L) + \rho_L \nabla \cdot (\mathbf{u}_L \otimes \mathbf{u}_L) = -\nabla p + \nabla \cdot \boldsymbol{\varepsilon}' . \quad (\text{A.54})$$

We can write

$$\epsilon \text{Re}(\partial_T \mathbf{U}_{LXY} + (\mathbf{U}_L \cdot \nabla) \mathbf{U}_{LXY}) = -\partial_{XY} P + \partial_Z^2 \mathbf{U}_{LXY} + \epsilon^2 \nabla_{XY}^2 U_{LXY} , \quad (\text{A.55a})$$

$$\epsilon^3 \text{Re}(\partial_T U_{LZ} + (\mathbf{U}_L \cdot \nabla) U_{LZ}) = -\partial_Z P + \epsilon^2 (\partial_Z^2 U_{LZ} + \epsilon^2 \nabla_{XY} U_{LZ}) . \quad (\text{A.55b})$$

Assuming Reynolds number $\text{Re} = \rho U_0 h_0 / \eta$ at most of order one, in the lubrication approximation $\epsilon \rightarrow 0$ we obtain to leading order

$$-\nabla_{XY} P + \partial_Z^2 \mathbf{U}_{XY} = 0 , \quad (\text{A.56})$$

$$-\partial_Z P = 0 . \quad (\text{A.57})$$

Note that Eq. (A.55) implies that it is sufficient to assume Stokes equation Eq. (2.2) for the fluid ($\text{Re} \ll 1$). As a consequence P depends only on X, Y , and \mathbf{U}_{XY} exhibits a simple quadratic form

$$\mathbf{U}_{XY} = \frac{Z^2}{2} \nabla_{XY} P + \mathbf{A}Z + \mathbf{B} , \quad (\text{A.58})$$

where P , \mathbf{A} and \mathbf{B} are 3 unknown functions of X, Y which do not depend on Z . These functions are determined by the no-slip boundary conditions, and we find

$$\mathbf{U}_{LXY} = -\frac{(H_s - Z)(Z - H)}{2} \nabla_{XY} P + \mathbf{U}_{CXY} \frac{H_s - Z}{H_s - H} . \quad (\text{A.59})$$

Then, from Eq.(A.36)

$$\langle \mathbf{U}_{LXY} \rangle = \int_H^{H_s} dZ \mathbf{U}_{LXY} = -\frac{(H_s - H)^3}{12} \nabla_{XY} P + \frac{H_s - H}{2} \mathbf{U}_{CXY} . \quad (\text{A.60})$$

In physical coordinates

$$\langle \mathbf{u}_{Lxy} \rangle = -\frac{(h_s - h)^3}{12\eta} \nabla_{xy} p + \frac{h_s - h}{2} \mathbf{u}_{Cxy} , \quad (\text{A.61})$$

which corresponds to Eq. (2.26) with $\zeta = h_s - h$.

A.5.2 Concentration field

Assuming a finite concentration $c \sim O(1) \sim \epsilon^0$, and Fick's law for the diffusion flux $\mathbf{j} = -D(c) \nabla c$, Eq. (2.6) can be written in normalized quantities as

$$\epsilon U_0 (\partial_T c + U_{LXY} c + U_{LZ} c) = \frac{\epsilon^2}{h_0} [D(c) \nabla_{XY} c] + \frac{1}{h_0} \partial_z [D(c) \partial_z c] . \quad (\text{A.62})$$

To leading order, we obtain:

$$\partial_Z [D(c(X, Y, Z)) \partial_Z c(X, Y, Z)] = 0 . \quad (\text{A.63})$$

Similarly the boundary conditions Eqs. (2.8) to (2.10) reduce to leading order to

$$J_Z(H) = D(c) \partial_Z c(X, Y, H) = 0 , \quad (\text{A.64})$$

$$\partial_Z c(X, Y, H_s) = 0 , \quad (\text{A.65})$$

$$\epsilon U_0 \nabla_{Cz} = \nu (c(X, Y, H) - c_{eq}(X, Y)) , \quad (\text{A.66})$$

where $H = h/h_0$ and $H_s = h_s/h_0$ are the dimensionless LC interface and substrate position in lubrication expansion, respectively. In the last relation we assumed ν to be comparable to ϵ in general. This corresponds to the limit of slow attachment. A first integration of Eq. (A.63) leads to

$$J_Z = -D(c(X, Y, Z))\partial_Z c(X, Y, Z), \quad (\text{A.67})$$

where J_Z depends on X, Y but does not depend on Z . From Eq. (A.64), we have $J_Z = 0$, so that $\partial_Z c(X, Y, Z) = 0$, and $c(X, Y, Z)$ is independent of Z .

Fast attachment

The case of fast attachment kinetics follows from Eq. (A.66) when assuming $\nu \sim O(1) \sim \epsilon^0$. Indeed this gives to leading order

$$(c - c_{eq}) = 0. \quad (\text{A.68})$$

implying $c(X, Y, H) = c_{eq}(X, Y)$.

A.5.3 Force balance

In the following, the subscript *ext* is used to indicate quantities fixed by external constraints.

Since the surface energy exhibits translational invariance with respect to the displacement of the whole crystal, the surface stiffness contribution of the force balance vanishes (see Appendix A.5.4):

$$0 = \oint\!\!\!\oint_{(LC)} dS \hat{\mathbf{n}} (\tilde{\gamma} \cdot \boldsymbol{\kappa}). \quad (\text{A.69})$$

In addition, the integral of the normal vector vanishes (see Appendix A.5.4), so that

$$0 = \oint\!\!\!\oint_{(LC)} dS \hat{\mathbf{n}} p_{ext}. \quad (\text{A.70})$$

As a consequence, the global force balance from Eq. (2.13) reads

$$\mathbf{F}_C^{ext} = \oint\!\!\!\oint_{(LC)} dS [-\hat{\mathbf{n}} \cdot \boldsymbol{\varepsilon}' + \hat{\mathbf{n}}(p - p_{ext} + W')], \quad (\text{A.71})$$

where $\boldsymbol{\varepsilon}'$ is the viscous stress tensor $\varepsilon'_{ij} = \eta(\partial_j u_{Li} + \partial_i u_{Lj})$.

Now, assuming that both viscous dissipation and the deviation from the external pressure are small outside the contact, the non-vanishing contribution of the integral are in the contact only, leading to

$$\mathbf{F}_C^{ext} = \int dx \int dy (1 + (\nabla h)^2)^{1/2} [-\hat{\mathbf{n}} \cdot \boldsymbol{\varepsilon}' + \hat{\mathbf{n}}(p - p_{ext} + W')]. \quad (\text{A.72})$$

Projecting this relation on $\hat{\mathbf{z}}$:

$$\mathbf{F}_{Cz}^{ext} = \int dx \int dy (1 + (\nabla h)^2)^{1/2} [-\hat{\mathbf{n}} \cdot \boldsymbol{\varepsilon}' \cdot \hat{\mathbf{z}} + \hat{\mathbf{n}} \cdot \hat{\mathbf{z}}(p - p_{ext} + W')]. \quad (\text{A.73})$$

To leading order in the lubrication expansion $p \sim \epsilon^{-1}$, $\nabla_{xy} h \sim \epsilon$, $\mathbf{u}_{Lz} \sim \epsilon$, $\mathbf{u}_{Lxy} \sim 1$, $h \sim 1$. It follows that also $\varepsilon'_{ij} = \eta(\partial_i u_{Lj} + \partial_j u_{Li})/2 \sim \epsilon$, so that we are left with (Eq. (2.36) in the main text)

$$\mathbf{F}_{Cz}^{ext} = \int dx \int dy [p - p_{ext} + W']. \quad (\text{A.74})$$

In addition, the tangential force balance reads

$$\mathbf{F}_{Cxy}^{ext} = \mathbf{F}_C^{ext} - \hat{\mathbf{z}} (\mathbf{F}_C^{ext} \cdot \hat{\mathbf{z}}) = \int dx \int dy (1 + (\nabla h)^2)^{1/2} [-(\hat{\mathbf{n}} \cdot \boldsymbol{\varepsilon}')_{xy} + \hat{\mathbf{n}}_{xy}(p - p_{ext} + W')]. \quad (\text{A.75})$$

To leading order in the lubrication limit

$$\mathbf{F}_{Cxy}^{ext} = \int dx \int dy [-\eta \partial_z \mathbf{u}_{Lxy}|_{z=h} - \nabla h (p - p_{ext} + W')]. \quad (\text{A.76})$$

Using Eq.(A.59) we have

$$\eta \partial_z \mathbf{u}_{Lxy}|_{z=h} = -\frac{h_s - h}{2} \nabla p - \frac{\eta u_{Cxy}}{h_s - h}. \quad (\text{A.77})$$

Integrating by parts and using the gradient theorem for the W term

$$\mathbf{F}_{Cxy}^{ext} = \int dx \int dy \left[\frac{\eta u_{Cxy}}{h_s - h} - (p - p_{ext}) \nabla \frac{h_s + h}{2} \right] + \oint_{ext} dl_{ext} \hat{\mathbf{n}}_{extxy} \left[W(h) + (p - p_{ext}) \frac{h_s - h}{2} \right]. \quad (\text{A.78})$$

From the B.C. $p = p_{ext}$ outside the contact, the second term in the integral over the boundary of the domain vanishes. If we also assume a constant height $h = h_{bc}$ at the boundary, or if h_{bc} is large as compared to the range of the potential, then $W(h_{bc})$ should be constant, and $\oint_{ext} dl_{ext} \hat{\mathbf{n}}_{extxy} = \mathbf{0}$ (the integral of the normal vector on a closed line vanishes, see Appendix A.5.4).

Finally,

$$\mathbf{F}_{Cxy}^{ext} = \int dx \int dy \left[\frac{\eta u_{Cxy}}{h_s - h} - (p - p_{ext}) \nabla \frac{h_s + h}{2} \right]. \quad (\text{A.79})$$

corresponding to Eq. (2.37) in the main text.

A.5.4 Identities resulting from translational invariance of the free energy

Here we derive some integral identities that are used in the main text. These identities express the fact that the total force resulting from a translational invariant energy must vanish.

Consider a generic free energy functional $\mathcal{F}_{\mathcal{D}}$ acting over a domain \mathcal{D} in d dimensions and with boundary $\partial\mathcal{D}$ in $(d - 1)$ dimensions. Let us assume that its variation can be written as a surface integral

$$\delta\mathcal{F} = \oint_{\partial\mathcal{D}} dS (\delta\mathbf{r} \cdot \hat{\mathbf{n}}) \frac{\delta\mathcal{F}_{\mathcal{D}}}{\delta\mathbf{r}}, \quad (\text{A.80})$$

where $\delta\mathbf{r}$ is a d -dimensional infinitesimal variation of the domain boundary.

Let us now assume that $\mathcal{F}_{\mathcal{D}}$ is invariant under translations. Then, $\delta\mathcal{F}$ must vanish under infinitesimal translations, *i.e.* when $\delta\mathbf{r} = d\mathbf{r}$ is an arbitrary constant (independent on space coordinates). As a consequence

$$0 = d\mathbf{r} \cdot \oint_{\partial\mathcal{D}} dS \hat{\mathbf{n}} \frac{\delta\mathcal{F}_{\mathcal{D}}}{\delta\mathbf{r}}. \quad (\text{A.81})$$

Since this is true for any $d\mathbf{r}$, we find that the force acting on the domain surface vanishes:

$$0 = \oint_{\partial\mathcal{D}} dS \hat{\mathbf{n}} \frac{\delta\mathcal{F}_{\mathcal{D}}}{\delta\mathbf{r}}. \quad (\text{A.82})$$

This relation is valid for arbitrary shapes of the domain \mathcal{D} .

In particular, consider the surface energy

$$\mathcal{F}_S = \oint_{\partial\mathcal{D}} dS \gamma(\hat{\mathbf{n}}), \quad (\text{A.83})$$

whose variation is given by

$$\oint_{\partial\mathcal{D}} dS \hat{\mathbf{n}} (\kappa : \tilde{\gamma}) = 0, \quad (\text{A.84})$$

where γ is a general surface tension (function of the orientation), $\tilde{\gamma}$ is the stiffness tensor and κ is the curvature tensor. In the special case where the surface tension is isotropic, *i.e.* γ does not

depend on $\hat{\mathbf{n}}$, we obtain a known equality: the integral of the mean curvature times the normal vector of an arbitrary (sufficiently regular) surface vanishes[188]

$$\oint_{\partial\mathcal{D}} dS \hat{\mathbf{n}} H = 0, \quad (\text{A.85})$$

where H is the mean curvature.

Finally, another useful relation is obtained when choosing an energy proportional to the volume of the domain \mathcal{D} :

$$\oint_{\partial\mathcal{D}} dS \hat{\mathbf{n}} = 0. \quad (\text{A.86})$$

We find that the integral of the normal vector vanishes on any closed regular surface.

A.6 Mean curvature in axysymmetric contact

Here, some useful definitions for the 2D axysymmetric system are given. In cylindrical coordinates the gradient and divergence operators read:

$$\nabla f(r, \theta, z) = \partial_r f \hat{\mathbf{r}} + \frac{1}{r} \partial_\theta f \hat{\boldsymbol{\theta}} + \partial_z f \hat{\mathbf{z}} \quad (\text{A.87})$$

$$\nabla \cdot \mathbf{F} = \frac{1}{r} \partial_r (r F_r) + \frac{1}{r} \partial_\theta F_\theta + \partial_z F_z \quad (\text{A.88})$$

The mean curvature can be derived using the definition in [189, 190]. As showed from Weatherburn [189] in cylindrical coordinates the surface can be defined by an implicit function $f(r, \theta) = (r \cos \theta, r \sin \theta, h(r, \theta)) = 0$, where $h(r, \theta)$ is the height of the crystal surface. This reduces to $(r \cos \theta, r \sin \theta, h(r)) = 0$ in the axial-symmetry case. The mean curvature is given by

$$\kappa = \frac{1}{H^2} (EN - 2FM + GL) \quad (\text{A.89})$$

The different terms appearing in the previous equation are

$$\begin{aligned} E &= |\hat{\mathbf{t}}_1|^2 \\ G &= |\hat{\mathbf{t}}_2|^2 \\ F &= \hat{\mathbf{t}}_1 \cdot \hat{\mathbf{t}}_2 \\ H^2 &= EG - F^2 \end{aligned}$$

where $\mathbf{t}_1 = \partial_r f$ and $\mathbf{t}_2 = \partial_\theta f$ are the tangent to the curves $r = \text{constant}$ and $\theta = \text{constant}$, respectively. Defining the norm to the surface as

$$\hat{\mathbf{n}} = \frac{\hat{\mathbf{t}}_1 \times \hat{\mathbf{t}}_2}{H}$$

in axial-symmetry we have

$$\begin{aligned} \hat{\mathbf{t}}_1 &= (\cos \theta, \sin \theta, \partial_r) \\ \hat{\mathbf{t}}_2 &= (r \sin \theta, -r \cos \theta, 0) \\ \hat{\mathbf{n}} &= \frac{(r \partial_r h \cos \theta, r \partial_r h \sin \theta, -r)}{[1 + (\partial_r h)^2]^{1/2} r} \end{aligned}$$

The other terms appearing in Eq. (A.89) are defined as

$$\begin{aligned} N &= \hat{\mathbf{n}} \cdot (\partial_{\theta\theta} f) \\ L &= \hat{\mathbf{n}} \cdot (\partial_{rr} f) \\ M &= \hat{\mathbf{n}} \cdot (\partial_{r\theta} f) \end{aligned}$$

Using these definition we obtain the following result for the mean curvature

$$\kappa = -\frac{\partial_{rr}h}{[1 + (\partial_r h)^2]^{\frac{3}{2}}} - \frac{\partial_r h/r}{[1 + (\partial_r h)^2]^{\frac{1}{2}}}, \quad (\text{A.90})$$

reducing in the lubrication limit to Eq. (2.47) of the main text.

This appendix shows some technical details of the numerical integration procedure adopted to solve the model equations in the different regime considered. For compactness, only the axisymmetric contact is here shown. The symmetric ridge case (1D) is completely analogous.

Space-time is discretized on a lattice of $M = R/\Delta r$ bins and $N = T/\Delta t$ time steps. Functions on the lattice are labeled as $y(r, t) = y_j^k$ where the subscript $j = 1 \dots, M$ represents the lattice position and the superscript $k = 1, \dots, N$ represents time. We use a forward Euler scheme for the numerical solution of the evolution equations [191]. The scheme is second order in space and first order in time. This proves to be stable if the time increment is sufficiently small. Indeed, since the model's partial differential equations are of order four (see for instance Eq. (3.5)), using as hand-waving argument a simple von Neumann stability analysis, we expect that for a fourth-order PDEs in a forward scheme the time increment goes as $\Delta t \sim \Delta r^4$ [191]. In most of the simulations we performed $\Delta \bar{r} = 0.2$ (in code units). Only for some specific calculations presented in Chapter 3 it was necessary to reduce this number.

Except for time evolution constraints, the major source of numerical cost is the system size. This is relevant, as it will be shown in section B.2, when solving the equation accounting for slow surface kinetics, Eq. (2.48b). Indeed, in this case, an $M \times M$ matrix has to be inverted. This matrix can become particularly large when considering expanding simulation boxes as done to study the problem of the crystallization force (see Chapter 5).

In the following, we will express the evolution equation in terms of absolute interface position $h = h_s - \zeta$. We will also use normalized variables so that only $\bar{\eta}$ and $\bar{\nu}$ appear explicitly in the equations whilst the other constant ($D, \Omega, c_0, k_B T$) are taken equal to one. In the following sections, we will drop the bar on the rescaled variables for economy of notation.

Finally, an important technical point is the correct implementation of the conditions at the boundary. As illustrated in Section 2.7, these are: fixed boundary height $h_M^k = h_{bc} \forall k$ and fixed boundary supersaturation. A third condition on the curvature at the boundary is introduced only in the specific case of a laterally expanding simulation box (Chapter 5).

B.1 Numerical scheme for fast surface kinetics

Let us recall the evolution equation for the axisymmetric contact in the fast surface kinetics regime and in code units ($D = \Omega = c_0 = 1$)

$$\partial_t h = \frac{1}{r} \partial_r [r \zeta (\partial_r c_{eq})] + u_{Cz},$$

where u_{Cz} is the rigid body crystal velocity given by Eq. (2.43).

We introduce the concentration flux defined as

$$J = \zeta \partial_r c_{eq}, \quad (\text{B.1})$$

where $\zeta = h_s - h$. Given this definition the evolution equation can be rewritten as

$$\partial_t h = \frac{1}{r} \partial_r (rJ) = \frac{J}{r} + \partial_r J. \quad (\text{B.2})$$

Let us recall the relation between the equilibrium concentration and the chemical potential (Eq. (2.11) in the main text)

$$c_{eq} = c_0 e^{\mu/k_B T} \sim c_0 \left(1 + \frac{\mu}{k_B T}\right),$$

where the last relation is valid when assuming small concentrations (linearized Gibbs-Thomson relation). Note that we dropped the Δ symbol in front of the chemical potential to avoid confusion with the discretization increment. Given the initial profile at time zero h_j^0 , for $j = 1, \dots, (M-1)$ we can then determine the time derivative $\partial_t h^k$ by computing the following. First by definition we have

$$J_j^k = \exp(\mu_j^k) \frac{\zeta_j^k}{2\Delta r} (\mu_{j+1}^k - \mu_{j-1}^k), \quad (\text{B.3})$$

or when assuming linerized thermodynamic relation as in Chapters 3 and 4

$$J_j^k = \frac{\zeta_j^k}{2\Delta r} (\mu_{j+1}^k - \mu_{j-1}^k). \quad (\text{B.4})$$

The chemical potential itself is linked to the profile by Eq. (2.45) and the curvature Eq. (2.47):

$$\mu_j^k = -\frac{1}{\Delta r^2} (h_{j+1}^k - h_{j-1}^k - 2h_j^k) - \frac{1}{2(j\Delta r)\Delta r} (h_{j+1}^k - h_{j-1}^k) + U'(\zeta_j^k). \quad (\text{B.5})$$

Finally the derivative of J is simple given by

$$\partial_r J_j^k = \frac{1}{2\Delta r} (J_{j+1}^k - J_{j-1}^k). \quad (\text{B.6})$$

At the boundaries, namely $j = 0$ ($r = 0$) and $j = M$ ($r = R$) we cannot use symmetric derivatives as done above. For the center, we exploit that by symmetry consideration we have $\partial_r h_0^k = 0$. Using de l'Hopital relation we have

$$\partial_t h_0^k = 2\partial_r J_0^k = \frac{1}{3\Delta r} (8J_1^k - J_2^k), \quad (\text{B.7})$$

where the last equality is obtained using that from the parity of h $J_0^k = 0$ and $\partial_{rr} J_0^k = 0$. From similar considerations it follows also that

$$\mu_0^k = \frac{2}{\Delta r^2} \left(\frac{h_2^k}{6} + \frac{5h_0^k}{2} - \frac{8h_1^k}{3} \right). \quad (\text{B.8})$$

On the boundary $r = R$, we have that $h_M^k = h_{bc}$ and $\mu_M^k = \mu_{bc} = \log(\sigma_{bc} + 1)$. In the case we assume small supersaturations (Chapters 3 and 4), this reduces to $\mu_{bc} = \sigma_{bc}$. We can then compute J_M^k by a backward scheme:

$$J_M^k = \frac{\zeta_{bc}}{2\Delta r} (3\mu_{bc} - 4\mu_{M-1}^k + \mu_{M-2}^k), \quad (\text{B.9})$$

where $\zeta_{bc} = h_s - h_{bc}$. Finally the time evolution h_j^{k+1} can be determined by Euler forward integration:

$$h_j^{k+1} = h_j^k + \partial_t h_j^k + u_{Cz}^k, \quad (\text{B.10})$$

where u_{Cz} is obtained from simple numerical integration of Eq. (2.43) considering the profile at time k .

B.2 Numerical scheme for slow surface kinetics

Let us recall the evolution equation for the axysymmetric contact when surface kinetics is slow:

$$v_{Cz} = \frac{1}{r} \partial_r [r \zeta (\partial_r c_{eq})] + \frac{1}{r} \partial_r \left[r \frac{\zeta}{\nu} (\partial_r v_{Cz}) \right],$$

where $v_{Cz} = \partial_t h - u_{Cz}$ is the local interface velocity. Note that in the limit $\nu \rightarrow \infty$ we recover Eq. (2.51b). We introduce similarly to what done in the previous section with the concentration flux J defined in Eq. (B.1), the local growth flux Q :

$$Q = \frac{1}{\nu} \zeta \partial_r v_{Cz}. \quad (\text{B.11})$$

Thus, following the same lines of Appendix B.1 we rewrite the interface evolution equation as

$$v = \frac{1}{r} \partial_r (rJ) + \frac{1}{r} \partial_r (rQ) = \frac{J}{r} + \partial_r J + \frac{Q}{r} + \partial_r Q, \quad (\text{B.12})$$

where we dropped the label Cz from v . For the term Q we have similarly to J that

$$Q_j^k = \frac{\zeta_j}{2\nu \Delta r} (v_{j+1}^k - v_{j-1}^k). \quad (\text{B.13})$$

Since v appears also in the left hand side of Eq. (B.12) we explicitly use $\partial_r Q = \partial_r \zeta \partial_r v + \zeta \partial_{rr} v$ in order to solve for v :

$$\partial_r Q_j^k = \frac{1}{\nu} \left(\frac{\zeta_{j+1}^k - \zeta_{j-1}^k}{2\Delta r} \right) \left(\frac{v_{j+1}^k - v_{j-1}^k}{2\Delta r} \right) + \zeta_j^k \left(\frac{v_{j+1}^k - v_{j-1}^k - 2v_j^k}{\Delta r^2} \right). \quad (\text{B.14})$$

It follows that Eq. (B.12) together with Eqs. (B.3), (B.6), (B.13) and (B.14) defines a linear system

$$\mathbf{v}^k = (\mathbf{A}^k)^{-1} \cdot \mathbf{b}^k. \quad (\text{B.15})$$

Above we define the vector \mathbf{b}^k as

$$b_j^k = \partial_r J_j^k + \frac{J_j^k}{r_j^k}, \quad (\text{B.16})$$

for $j = 1 \dots M-1$, and the matrix \mathbf{A}^k as

$$A_{i,j}^k = \delta_{i,j} \left(2 \frac{\zeta_i^k}{\Delta r^2 \nu} + 1 \right) - \delta_{i,j+1} \left(\frac{\zeta_i^k}{\Delta r^2 \nu} + \frac{\partial_r \zeta_i^k}{2\Delta r \nu} + \frac{\partial_r \zeta_i^k}{2\Delta r r_i^k \nu} \right) + \delta_{i,j-1} \left(\frac{\zeta_i^k}{\Delta r^2 \nu} - \frac{\partial_r \zeta_i^k}{2\Delta r \nu} - \frac{\partial_r \zeta_i^k}{2\Delta r r_i^k \nu} \right), \quad (\text{B.17})$$

for $i = 1 \dots M-1$ and $j = 1 \dots M-1$. The derivative $\partial_r \zeta_i^k$ is computed using the same symmetric second order scheme as the first parenthesis in Eq. (B.14), and $r_i = i\Delta r$ represents the distance from the center and the i -th position. Finally, at the center of the crystal surface we have

$$\begin{aligned} b_0^k &= 2\partial_r J_0^k = \frac{1}{3\Delta r} (8J_1^k - J_2^k), \\ A_{0,0}^k &= \frac{5\zeta_0^k}{\nu \Delta r^2} + 1, \\ A_{0,1}^k &= -\frac{16\zeta_0^k}{2\nu \Delta r^2}, \\ A_{0,2}^k &= \frac{\zeta_0^k}{3\nu \Delta r^2}, \\ A_{0,j>2}^k &= 0. \end{aligned} \quad (\text{B.18})$$

In the first equation we used de L'Hopital relation and that $J_0^k = 0$. Similarly the last three relations follow from observing that $2\partial_r M_0^k$ reduces to $2\zeta_0^k \partial_{rr} v_0^k$. The conditions at the boundaries follow from Section 2.7:

$$\begin{aligned} b_M^k &= v_{bc}^k = -u_{Cz}^k, \\ A_{M,M}^k &= 1, \\ A_{M,j \neq M}^k &= 0. \end{aligned} \tag{B.19}$$

Finally we determine the evolution of h by explicit Euler integration

$$h_j^{k+1} = h_j^k + \Delta t (\partial_t h)_j^k = h_j^k + \Delta t (v_j^k + u_{Cz}^k) \tag{B.20}$$

where v_j^k is computed by matrix inversion through Eq. (B.15) and u_{Cz}^k is computed from the numerical integration of Eq. (2.43) at the time step k .

B.3 Numerical scheme for lateral growth

Whilst the evolution equations do not vary with respect to the previous case, new boundary conditions have to be introduced to account for lateral expansion of the contact.

We define r_{bc} as the continuum out of lattice position of the boundary of fixed height $h(r_{bc}) = h_{bc}$. The point r_{bc} can be viewed as a virtual coordinate not belonging to the lattice. Let us label with R the penultimate point on the grid. The lattice itself will grow or shrink of one bin if $r_{bc} > R + \Delta r$ or $r_{bc} < R - \Delta r$, respectively. The value of r_{bc} , from an initial condition $r_{bc}^0 > R$, will evolve in time according to

$$r_{bc}^{k+1} = r_{bc}^k + v_l^k \Delta t, \tag{B.21}$$

where v_l is the lateral velocity of the contact defined in Eq. (5.14d). We then have to impose a relation linking h_{bc} to the last point of the crystal profile on the lattice position h_M :

$$h_M^k = h_{bc} - \Delta_{bc} (\partial_r h)_M^k, \tag{B.22}$$

where $\Delta_{bc} = r_{bc}^{k+1} - R^k$ and $(\partial_r h)_M^k$ can be calculated using the backward derivative. Equation (B.22) is used to deduce the new point when the box is expanded. It follows that h_{M+1} is given by

$$h_{M+1}^k = \left(1 + \frac{3\Delta_{bc}}{2\Delta r}\right)^{-1} \left[h_{bc} - \frac{\Delta_{bc}}{2\Delta r} \left(h_{M-1}^k - 4h_M^k \right) \right], \tag{B.23}$$

where we used the second order backward calculation of $(\partial_r h)_M^k$. The case of shrinking ($\Delta_{bc} < 0$) is given by the above equation with $M = M - 2$. Similarly, we interpolate the boundary chemical potential and local growth rate using

$$\mu_M^k = \left(1 + \frac{3\Delta_{bc}}{2\Delta r}\right)^{-1} \left[\mu_{bc} - \frac{\Delta_{bc}}{2\Delta r} \left(\mu_{M-2}^k - 4\mu_{M-1}^k \right) \right]. \tag{B.24}$$

Using the same interpolation for the boundary value of v_{Cz} we redefine the boundary condition of the matrix \mathbf{A}^k given in Eq. (B.17). The non zero terms of the last line are now

$$\begin{aligned} \tilde{A}_{M,M} &= 1 + \frac{3\Delta_{bc}}{2\Delta r}, \\ \tilde{A}_{M,M-1} &= -\frac{2\Delta_{bc}}{\Delta r}, \\ \tilde{A}_{M,M-2} &= -\frac{\Delta_{bc}}{2\Delta r}. \end{aligned} \tag{B.25}$$

The lateral velocity, as reported in the main text, is given by

$$v_l^k = (\partial_r h_{bc}^{-1})^k \left[u_{Cz}^k + \Omega \nu c_0 \left(1 + \sigma_{bc} - \exp(\mu_{bc}^k / (k_B T)) \right) \right] \tag{B.26}$$

where $\sigma_{bc} = \sigma(r_{bc})$ and $\mu_{bc}^k = \mu(r_{bc})^k$ are the supersaturation and chemical potential outside the contact zone, respectively. Remark that the former is a constant parameter, the latter depends on time via the curvature at the boundary defined in Eq. (2.62),

$$\kappa_{bc}(t) = \left[\sqrt{1 + ((\partial_r h_{bc})^k)^2} (d - \zeta_{bc}) \right]^{-1}, \quad (\text{B.27})$$

width d the half walls separation in the geometry considered in the main text, Section 2.7.2. Using the definition of the axisymmetric curvature we have $(\partial_{rr} h_{bc})^k = -\kappa_{bc} - (\partial_r h_{bc})^k / r_{bc}^k$ so that the derivative at the boundary appearing in the above equations can be expressed as

$$(\partial_r h_{bc})^k = \frac{h_M^k - h_{M-1}^k - (\frac{\Delta r^2}{2} + \Delta_{bc} \Delta r) \kappa_{bc}^{k-1}}{\Delta r + (\frac{\Delta r^2}{2} + \Delta_{bc} \Delta r) / (r_{bc}^k)} \quad (\text{B.28})$$

where κ_{bc}^{k-1} is Eq. (B.27) computed at the previous time step. To use this second order scheme for Eq. (B.28) proves to be more stable than a first order scheme (simply using h_M^k and h_{M-1}^k).

Finally, the last element of the vector \mathbf{b}^k defined in Eq. (B.16) is

$$b_M^k = v_{bc} = \Omega \nu c_0 [1 + \sigma_{bc} - \exp(\mu_{bc}^k)]. \quad (\text{B.29})$$

To conclude, during the integration the system evolves as for the fixed simulation box case according to Eq. (B.15) with the boundary conditions above Eqs. (B.24), (B.25) and (B.29). Then Eq. (B.23) is called when a bin is added or removed in the lattice.

B.4 Conserved quantities during numerical integration

An observable which is computed during the numerical integration is the variation of mass. This can be used not only to check if the numerical scheme is consistent (mass is conserved) but also to monitor if a steady-state has been reached. The total mass in 2D and for an axisymmetric system is defined as

$$\mathcal{M}(t) = 2\pi \int_0^{r_{bc}} dr r h(r, y), \quad (\text{B.30})$$

with r_{bc} the total radius of the integration domain. For a fixed contacts $r_{bc} = R$, with R the simulation box radius on the lattice.

Assuming the general case of a small surface kinetics, the time derivative of the mass is

$$\begin{aligned} \dot{\mathcal{M}} &= 2\pi \int_0^R dr r \partial_t (h_s - h(r, y)) = -2\pi \int_0^R dr r \left[\frac{1}{r} \partial_r (rJ) + \frac{1}{r} \partial_r (rQ) + u_{Cz} \right] \\ &= -(2\pi R J(R) + 2\pi R Q(R) + \pi R^2 u_{Cz}), \end{aligned} \quad (\text{B.31})$$

where we used the flux introduced in Eqs. (B.3) and (B.11) and that for symmetry $J(0) = Q(0) = 0$. It follows that during numerical integration a consistency check is to compare the evolution of the total mass, from $\mathcal{M}(t + \Delta t) = \mathcal{M}(0) + \Delta t \dot{\mathcal{M}}(t)$, using the last line of Eq. (B.31) and the direct calculation in Eq. (B.30).

Furthermore, it should be noted that steady state $\dot{\mathcal{M}} = 0$ corresponds to

$$\tilde{J} = J(R) + Q(R) + \frac{R}{2} u_{Cz} = 0. \quad (\text{B.32})$$

In the case of fast surface kinetics where we make use of Appendix B.1 and Eq. (2.43), we have the same expressions as above but with $Q = 0$.

B.4.1 Expanding (shrinking) box

In this case, the evolution of the total mass reads:

$$\begin{aligned}
 \dot{\mathcal{M}} &= 2\pi\partial_t \left[\int_0^{r_{bc}} dr r (h_s - h(r, y)) \right] \\
 &= -2\pi \int_0^{r_{bc}} dr r \left[\frac{1}{r} \partial_r (rJ) + \frac{1}{r} \partial_r (rQ) + u_{Cz} \right] + \partial_t r_{bc} r_{bc} (h_s - h(r_{bc})) \\
 &= -(2\pi r_{bc} J(r_{bc}) + 2\pi r_{bc} Q(r_{bc}) + \pi r_{bc}^2 u_{Cz}) + 2\pi r_{bc} v_l \zeta_{bc},
 \end{aligned} \tag{B.33}$$

where v_l is defined in Eq. (5.14d) and $\zeta_{bc} = h_s - h_{bc}$ is the boundary width fixed by the integration scheme. Note that in practice we limit our analysis for the case of a crystal growing in a Hele-Shaw channel, thus $u_{Cz} = 0$ in the equation above. The quantities $Q(r_{bc})$ and $J(r_{bc})$ can be computed using a first order scheme:

$$\begin{aligned}
 J(r_{bc}) &= \frac{\zeta_{bc}}{\Delta r} (\mu_M^k - \mu_{M-1}^k), \\
 Q(r_{bc}) &= \frac{1}{\nu \Delta r} \zeta_{bc} (v_M^k - v_{M-1}^k).
 \end{aligned} \tag{B.34}$$

In the case explored in this work, namely $u_{Cz} = 0$, the steady state condition is $\dot{\zeta} = 0$

$$v_l \zeta_{bc} = J(r_{bc}) + Q(r_{bc}), \tag{B.35}$$

Note that equilibrium (zero fluxes) then implies $v_l = 0$.

Derivations of analytical relations in pressure solution

C.1 Steady state in the absence of surface tension

Using the axisymmetric system (2D), we here illustrate how to derive some relations of Sections 3.3.1 and 3.3.2. In 1D an analogous procedure is applied. In 2D, a single integration of Eq. (3.13) leads to

$$\frac{r}{2}u_{Cz} = B\zeta\partial_r\zeta U''(\zeta). \quad (\text{C.1})$$

Using the previous relation to express the differential rdr as a function of $d\zeta$ and considering only the contribution of the contact area, we can rewrite Eq. (3.4) in a more convenient form:

$$F_{Cz} = 2\pi \int_0^{R_c} r12\eta B dr \int_{\zeta(r)}^{\zeta(R_c)} d\zeta \frac{U''(\zeta)}{\zeta^2} - 2\pi \int_0^{R_c} dr rU'(\zeta(r)). \quad (\text{C.2})$$

C.1.1 Singular power law repulsion

Using Eq. (3.18) together with Eq. (3.6) in Eq. (C.2), we find

$$F_{Cz}^{2D} = 12\eta C_1(r_m, R_c) (R_c^2 u_{Cz})^{\frac{n+3}{n}} + C_2(r_m, R_c) (R_c^2 u_{Cz})^{\frac{n+1}{n}}, \quad (\text{C.3})$$

where

$$C_1 = B \frac{n(n+1)\pi A}{n+3} \left\{ \frac{-R_c^2}{\zeta^{n+3}(R_c)} + \frac{nr_m^2}{(2n+3)\zeta_0^{n+3}} \left[\left(\frac{R_c^2}{r_m^2} - 1 \right)^{\frac{n+3}{n}} + 1 \right] \left(\frac{r_m^2/R_c^2}{4B(n+1)A} \right)^{\frac{n+3}{n}} \right\}$$

$$C_2 = \frac{\pi n^2 A r_m^2}{(2n+1)} \left[\left(\frac{R_c^2}{r_m^2} - 1 \right)^{\frac{2n+1}{n}} + 1 \right] \left(\frac{r_m^2/R_c^2}{4B(n+1)A} \right)^{\frac{n+1}{n}}.$$

For large external loads, we have $r_m \sim R_c$ and $\zeta(r = R_c) \gg \zeta_0$, leading to Eq. (3.21).

The constants used in the main text in Eqs. (3.22a), (3.22b), (3.23a) and (3.23b) were obtained considering that one of the two terms in Eq. (C.3) dominates in the force balance depend-

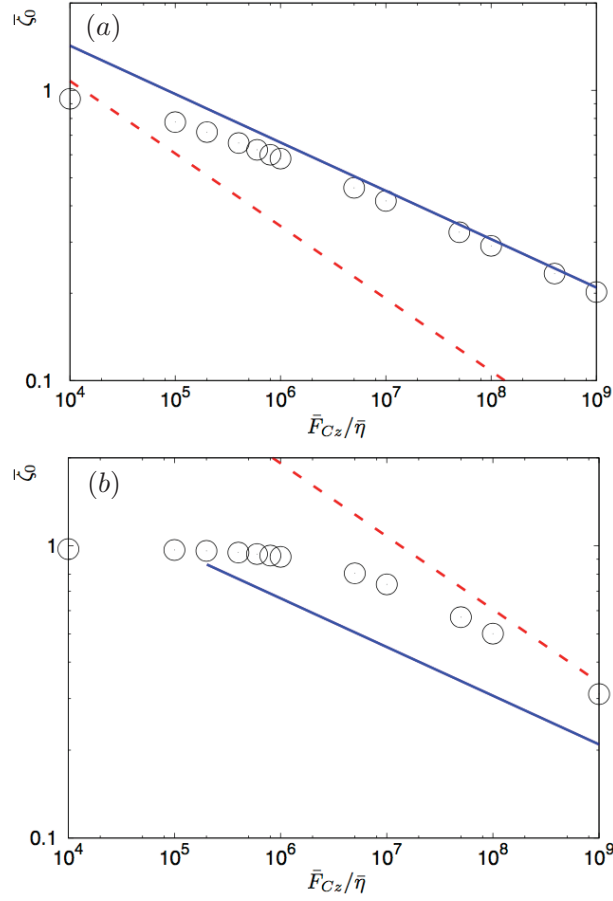


Figure C.1: Minimum film thickness ζ_0 as a function of the applied load for a (singular) power law repulsion. Geometry: axisymmetric contact. Lines represent analytical predictions extracted from Eq. (C.8) with $\bar{R}_c = \bar{R} = 100$, circles indicate simulation results. Solid blue line, hydrodynamic regime; dashed red line, diffusion regime. (a) $\bar{\eta} = 1$; (b) $\bar{\eta} = 10^{-3}$. The results are given in normalized units.

ing on the value of the viscosity. Their expressions are

$$C_h^{1D} = \frac{2(BA(n+1))^{\frac{3}{n+3}}}{\left(\frac{24n\sqrt{\pi}}{n+3}\phi\left(\frac{n+3}{n}\right)\right)^{\frac{n}{n+3}}} \quad (\text{C.4})$$

$$C_h^{2D} = \frac{4(BA(n+1))^{\frac{3}{n+3}}}{\left(\frac{12\pi n^2}{(2n+3)(n+3)}\right)^{\frac{n}{n+3}}} \quad (\text{C.5})$$

$$C_d^{1D} = \frac{2BA^{\frac{1}{n+1}}(n+1)}{\left(2n\sqrt{\pi}\phi\left(\frac{n+1}{n}\right)\right)^{\frac{n}{n+1}}} \quad (\text{C.6})$$

$$C_d^{2D} = \frac{4BA^{\frac{1}{n+1}}(n+1)}{\left(\frac{\pi n^2}{2n+1}\right)^{\frac{n}{n+1}}}. \quad (\text{C.7})$$

As discussed in the main text, the force can also be written as a function of the distance ζ_0 between the substrate and the crystal surface at the center of the contact:

$$\frac{F_{Cz}^{2D}}{\pi R_c^2} = 12\eta B \frac{n^2(n+1)A}{(2n+3)(n+3)} \left(\frac{1}{\zeta_0}\right)^{n+3} + \frac{n^2 A}{(2n+1)} \left(\frac{1}{\zeta_0}\right)^{n+1}, \quad (\text{C.8})$$

leading to the asymptotic scaling reported in Section 3.5. These results are confirmed by the numerical solution as showed in Fig. C.1.

Finally, as shown in Fig. 3.4, we have explored the transition between the diffusion and hydrodynamic scaling laws. This was done using an intermediate viscosity, $\bar{\eta} = 0.1$, and looking at the dissolution rates in a 2D contact of size $\bar{R}_c \approx \bar{R} = 100$. The constants appearing in Eqs. (3.24) and (3.25) are:

$$B_{1D} = \left[\frac{24B(n+1)\phi\left(\frac{n+3}{n}\right)}{(n+3)\left[2\phi\left(\frac{n+1}{n}\right)\right]^{\frac{n+3}{n+1}}} \right]^{\frac{n+1}{2}} \frac{1}{nA\sqrt{\pi}} \quad (\text{C.9})$$

$$B_{2D} = \left[\frac{12B(n+1)(2n+1)^{\frac{n+3}{n+1}}}{(2n+3)(n+3)} \right]^{\frac{n+1}{4}} \frac{1}{n\sqrt{A\pi}}. \quad (\text{C.10})$$

C.1.2 Finite exponential repulsion

In the case of a finite exponential repulsion, manipulations similar to those presented in the previous section lead to the following form of the force balance relation

$$F_{Cz}^{2D} = 48\eta \frac{\pi B^2 A^2}{\lambda^3 u_{Cz}} \psi\left(\frac{\zeta_0}{\lambda}\right) + \frac{\pi B A^2}{\lambda} \left(\frac{2\zeta_0}{\lambda} + 1\right) \frac{e^{-\frac{2\zeta_0}{\lambda}}}{u_{Cz}}, \quad (\text{C.11})$$

with

$$\psi(z_0) = \lambda \int_{z_0}^{\infty} dz e^{-z} \left(e^{-z} + z Ei(-z) \right), \quad (\text{C.12})$$

where Ei is the exponential integral defined as

$$Ei(x) = - \int_{-x}^{\infty} \frac{e^{-s}}{s} ds. \quad (\text{C.13})$$

Inserting the expression of u_{Cz} from Eq. (3.28b) into Eq. (C.11) we obtain Eq. (3.32).

C.1.3 1D case

In 1D, the derivations are similar to the 2D case. We obtain Eq. (3.30) where the two functions $\tilde{\psi}_1$ and $\tilde{\psi}_2$ are defined as:

$$\tilde{\psi}_1(z_0) = \int_{z_0}^{\infty} \frac{e^{-z}(e^{-z} + zE_i(-z))}{[(1+z_0)e^{-z_0} - (1+z)e^{-z}]^{\frac{1}{2}}} dz, \quad (\text{C.14})$$

$$\tilde{\psi}_2(z_0) = \int_{z_0}^{\infty} \frac{ze^{-2z}}{[(1+z_0)e^{-z_0} - (1+z)e^{-z}]^{\frac{1}{2}}} dz. \quad (\text{C.15})$$

C.2 Surface tension contribution in finite repulsion

We here report a derivation of the relation between the second derivative of the interface $\partial_{xx}\zeta_0$ or $\partial_{rr}\zeta_0$ and the minimum film width ζ_0 . This relation is obtained through a procedure where we match the two approximate solutions at the tip ζ_{tip} in Eq. (3.34), and far from the tip ζ_{sing} in Eq. (3.29).

C.2.1 1D case

In 1D we proceed as follows. Integrating two times Eq. (3.36a) we have

$$0 = \frac{x^2}{2B}u_{Cz} - \frac{A}{2\lambda}(\zeta^2 - \zeta_0^2) + \tilde{\gamma}\left(\zeta\partial_{xx}\zeta - \zeta_0\partial_{xx}\zeta_0 - \frac{1}{2}(\partial_x\zeta)^2\right), \quad (\text{C.16})$$

where we used the parity condition $\partial_x\zeta_0 = 0$ and the expansion of \tilde{U} , (given for the exponential repulsion by Eq. (3.26)), up to second order in ζ : $\tilde{U} \approx A(-1 + \zeta^2/(2\lambda^2))$.

Adding a perturbation $\delta\zeta$ to $\zeta_{sing} = \omega|x|$ given by Eq. (3.29a) we have

$$\zeta_{far} = \zeta_{sing} + \delta\zeta, \quad (\text{C.17})$$

with

$$\omega = \left(\frac{u_{Cz}}{BA}\right)^{\frac{1}{2}}\lambda. \quad (\text{C.18})$$

We then insert this relation in Eq. (C.16) to determine $\delta\zeta$ far from the tip. Neglecting the terms of smaller than $\delta\zeta$ for large x we find

$$\delta\zeta = \tilde{\gamma} \frac{-\frac{1}{2}\omega^2 - \zeta_0\partial_{xx}\zeta_0}{\frac{A}{\lambda^2}\omega x}. \quad (\text{C.19})$$

We define x_* as the value of x at which we match the solutions ζ_{sing} and ζ_{tip} . We obtain two independent relations. The first one accounts for the matching of the surface profiles at $x = x_*$, leading to $\omega x_* + \delta\zeta(x_*) = \zeta_0 + \partial_{xx}\zeta_0 x_*^2/2$. The second relation comes from the matching of the slopes $\omega + \partial_x\delta\zeta(x)|_{x_*} = \partial_{xx}\zeta_0 x_*$. Combining the two relations we obtain the following system of equations

$$\begin{aligned} \frac{3}{2}\partial_{xx}\zeta_0 x_*^2 - 2\omega x_* + \zeta_0 &= 0, \\ \omega x_* - \tilde{\gamma}\left(\frac{\omega^2}{2}\zeta_0\partial_{xx}\zeta_0\right)\frac{\lambda^2}{A\omega x_*} &= \zeta_0 + \frac{\partial_{xx}\zeta_0}{2}x_*^2. \end{aligned} \quad (\text{C.20})$$

C.2.2 2D case

In the axisymmetric system (2D) we follow a similar procedure. However, extra terms connected to the different expression of the curvature appear. Following the same steps as for the derivation

of Eq. (C.16), we Eq. (3.36b) two times. Then, given the parity condition and the expansion of \tilde{U} for small ζ , we obtain

$$0 = \frac{r^2}{4B} u_{Cz} - \frac{A}{2\lambda} (\zeta^2 - \zeta_0^2) + \tilde{\gamma} \left(\zeta \partial_{rr} \zeta - 2\zeta_0 \partial_{rr} \zeta_0 - \frac{1}{2} (\partial_r \zeta)^2 + \frac{\zeta \partial_r \zeta}{r} - \int_0^r dr' \frac{(\partial_{r'} \zeta)^2}{r'} \right). \quad (\text{C.21})$$

To derive an explicit expression for the correction to ζ_{sing} , we insert its expression Eq. (3.29b) plus a perturbation $\delta\zeta$ in Eq. (C.21). Thus Eq. (C.21) becomes

$$0 = -\frac{A}{\lambda^2} \omega r \delta\zeta - \tilde{\gamma} \left((\partial_{rr} \zeta_0)^2 \frac{r_*^2}{2} + 2\zeta_0 \partial_{rr} \zeta_0 \right) + \tilde{\gamma} \left(\frac{1}{2} \omega^2 - \omega^2 \ln\left(\frac{r}{r_*}\right) + \omega \frac{\delta\zeta}{r} + 2\omega \int_{r_*}^r dr \frac{\partial_r \delta\zeta}{r} + \omega r \partial_{rr} \delta\zeta \right). \quad (\text{C.22})$$

where now in 2D

$$\omega = \left(\frac{u_{Cz}}{2BA} \right)^{\frac{1}{2}} \lambda. \quad (\text{C.23})$$

Note that the integral term of Eq. (C.21) was rewritten as follows

$$\begin{aligned} \int_0^r dr \frac{(\partial_r \zeta)^2}{r} &= \int_0^{r_*} dr \frac{(\partial_r \zeta_{tip})^2}{r} + \int_{r_*}^r dr \frac{(\partial_r \zeta_{sing})^2}{r} \\ &= (\partial_{rr} \zeta_0)^2 \frac{r_*^2}{2} + \omega^2 \ln\left(\frac{r}{r_*}\right) + 2\nu \int_{r_*}^r dr \frac{\partial_r \delta\zeta}{r}. \end{aligned} \quad (\text{C.24})$$

If in the matching procedure, for $r \gg r_*$, we keep only dominant terms, as done above for the 1D case, we would obtain $\delta\zeta \approx 1/r$. Since this does not behave properly we make a crude approximation and keep only one higher order term $\omega \delta\zeta/r$ to account for higher order contributions in Eq. (C.22) (indeed, as $r \rightarrow r_*$ the integral term vanishes and we expect the other relevant term $r \partial_{rr} \delta\zeta$ to be of the same order as $\omega \delta\zeta/r$). With these assumptions we find

$$\delta\zeta = \tilde{\gamma} \frac{\frac{1}{2} \omega^2 - 2\zeta_0 \partial_{rr} \zeta_0 - \omega^2 \ln \frac{r}{r_*} - \frac{1}{2} (\partial_{rr} \zeta_0)^2 r_*^2}{\frac{A}{\lambda^2} \omega r - \gamma \omega \frac{1}{r}}. \quad (\text{C.25})$$

As before to obtain the matching between the two solutions ζ_{tip} and ζ_{sing} we use two conditions. First, we consider the matching of the thicknesses $\omega r_* + \delta\zeta(r_*) = \zeta_0 + \partial_{rr} \zeta_0 r_*^2/2$. A second relation accounts for the matching of the slopes $\omega + \partial_r \delta\zeta(r)|_{r_*} = \partial_{rr} \zeta_0 r_*$. Since in this case $\partial_r \delta\zeta(r)$ does not diverge for $r \rightarrow 0$, and since r_* is assumed to be small, we neglect the contribution $\partial_r \zeta|_{r_*}$ in the slope. This lead to the following system of equations:

$$\begin{aligned} \omega r_* + \tilde{\gamma} \left(\frac{\omega^2}{2} - 2\zeta_0 \partial_{rr} \zeta_0 - \frac{(\partial_{rr} \zeta_0)^2}{2} r_*^2 \right) \left(\frac{A}{\lambda^2} \omega r_* - \tilde{\gamma} \eta \frac{1}{r_*} \right)^{-1} &= \zeta_0 + \partial_{rr} \zeta_0 \frac{r_*^2}{2}, \\ \partial_{rr} \zeta_0 r_* &= \omega. \end{aligned} \quad (\text{C.26})$$

C.2.3 Numerical solution

Inserting the asymptotic analytical expression of the dissolution rate u_{Cz} , Eq. (3.28), in the definition of ω Eqs. (C.18) and (C.23), we solved numerically the linear systems of Eqs. (C.20) and (C.26) using MINPACK routine [192]. We obtain values of x_* (r_*) and of $\partial_{xx} \zeta_0$ ($\partial_{rr} \zeta_0$) for a given minimum distance ζ_0 . The results, displayed in Fig. 3.8, are represented by the dashed lines and compared with the simulation results. In particular we find (in normalized units) for $\zeta_0 = 0$, $\partial_{\bar{x}\bar{x}} \bar{\zeta}_0 \approx 0.0167$ and $\partial_{\bar{r}\bar{r}} \bar{\zeta}_0 \approx 0.0153$.

C.3 Beyond the linearization of the Gibbs-Thomson relation

A simple substitution allows one to include the effect of the exponential term in the analysis of the contact profile in the absence of surface tension:

$$U'(\zeta) \rightarrow k_B T \exp\left[\frac{U'(\zeta)}{k_B T}\right]. \quad (\text{C.27})$$

This leads to a different definition of \tilde{U} from the relation

$$\tilde{U}'(\zeta) = \zeta U''(\zeta) \exp\left[\frac{U'(\zeta)}{k_B T}\right]. \quad (\text{C.28})$$

The same procedure as that discussed in Section 3.3 can then be applied with this new expression for \tilde{U} .

For power-law potentials, this leads to an essential singularity in \tilde{U} when $\zeta \rightarrow 0$:

$$\tilde{U}(\zeta) = \zeta k_B T \left(e^{-\frac{An\zeta^{-n-1}}{k_B T}} - \frac{E_{1+\frac{1}{n+1}}\left(\frac{An\zeta^{-n-1}}{k_B T}\right)}{n+1} \right), \quad (\text{C.29})$$

where

$$E_m(z) = \int_1^\infty dt \frac{e^{-zt}}{t^m}. \quad (\text{C.30})$$

This essential singularity appears in the relation between u_{Cz} and the minimum thickness ζ_0 when $\zeta_0 \rightarrow 0$:

$$u_{Cz} = 4B[\tilde{U}(\zeta_0) - \tilde{U}(\infty)]. \quad (\text{C.31})$$

In contrast, there is no significant change in the case of an exponential potential. Indeed, the central property of being finite when $\zeta_0 \rightarrow 0$ is not affected by Eq. (C.27). Thus, the exponential potential again leads to a pointy shape, and constant dissolution rate obeying Eq. (3.28). Moreover, the details of the regularization of the tip due to surface tension can be affected but we do not expect major changes.

Analytic relation for cavity appearance and supplementary material

D.1 Perturbation analysis in presence of an attractive interaction

Using a perturbative approach from the equilibrium solution of Eqs. (4.1), (4.2a) and (4.3), we here derive approximate expressions for the growth rate and the critical supersaturation.

As a preamble, we characterize the equilibrium solution itself. Steady-state solution of Eq. (4.1) with Eq. (4.2a) obey

$$0 = B \frac{1}{r} \partial_r [r \zeta \partial_r (\tilde{\gamma} \partial_{rr} \zeta + \frac{\tilde{\gamma}}{r} \partial_r \zeta - U'(\zeta))] + u_{Cz}. \quad (\text{D.1})$$

The equilibrium solution is a particular steady-state equation obeying $u_{Cz} = 0$ and

$$\tilde{\gamma} \partial_{rr} \zeta_{eq} + \frac{\tilde{\gamma}}{r} \partial_r \zeta_{eq} - U'(\zeta_{eq}) = \frac{\Delta \mu_{eq}}{\Omega}, \quad (\text{D.2})$$

where $\Delta \mu_{eq}/\Omega$ is a constant which corresponds to the equilibrium chemical potential. The radius of the contact region is denoted as L . Multiplying Eq. (D.2) by $2\pi r$, and integrating between the center of the contact at $r = 0$ and a radius $r = R > L$, we find a relation between the equilibrium chemical potential and the slope at the boundary of the integration domain

$$\frac{\Delta \mu_{eq}}{\Omega} = \frac{2\tilde{\gamma}}{R} \partial_r \zeta_{eq}(R), \quad (\text{D.3})$$

where we have used the relation $2\pi \int_0^R r dr U'(\zeta) = 0$, corresponding to the equilibrium force balance Eq. (4.3). A second relation can be found when multiplying Eq. (D.2) by $\partial_r \zeta_{eq}$ and integrating with respect to r :

$$\frac{\tilde{\gamma}}{2} (\partial_r \zeta_{eq}(R))^2 - \Delta U = \frac{\Delta \mu_{eq}}{\Omega} (\zeta_{eq}(R) - \zeta_{eq}(0)) - \tilde{\gamma} \int_0^R \frac{(\partial_r \zeta)^2}{r} dr, \quad (\text{D.4})$$

where $\Delta U = U(\zeta_{eq}(R)) - U(\zeta_{eq}(0))$. Equation (D.4) relating the surface slope $\partial_r \zeta_{eq}(R)$ outside the contact to the depth of the potential well ΔU , is equivalent to a generalized form of the Young contact angle condition. The integral term in the second equation is related to the effect of line tension. In the following, we will neglect this term.

We now assume that the equilibrium profile is flat $\zeta_{eq}(r) \approx h$ with $U'(h) = 0$ for $r \leq L$. Then, we expect $\zeta_{eq}(L) \approx \zeta_{eq}(0) \approx h$, and combining Eq. (D.4) and Eq. (D.3) we find

$$\Delta \mu_{eq} \approx \frac{2\Omega}{L} \sqrt{-2\tilde{\gamma}U(h)}, \quad (\text{D.5})$$

where we assumed that the interaction potential vanishes far from the contact region $U(\zeta(r > L)) \approx 0$. Note that under these approximations the right hand side of Eq. (D.4) vanishes, and this equation is the small slope limit of the Young contact angle condition.

Consider now a system below the transition, so that no cavity is present. The crystal surface profile is then expected to be close to the equilibrium profile. We therefore consider the difference $\delta\zeta(r) = \zeta(r) - \zeta_{eq}(r)$ between the steady-state solution and the equilibrium solution to be small. Expanding Eq. (D.1) to linear order in $\delta\zeta(r)$, and integrating two times, we find

$$\tilde{\gamma}\partial_{rr}\delta\zeta + \frac{\tilde{\gamma}}{r}\partial_r\delta\zeta - \delta\zeta U''(\zeta_{eq}) - \frac{u_{Cz}}{2B} \int_r^L \frac{r'}{\zeta_{eq}(r')} dr' = \frac{\Delta\mu_b - \Delta\mu_{eq}}{\Omega}, \quad (D.6)$$

where we have used the parity of $\zeta(r)$ and Eq. (D.2), and we have defined the chemical potential at the edge of the contact zone $\Delta\mu_b = \Delta\mu(L)$ with $\Delta\mu(L)$ given by Eq. (2.45). Assuming again that in the contact area $r < L$ the equilibrium profile is flat $\zeta_{eq} \approx h$, Eq. (D.6) can be rewritten as:

$$\tilde{\gamma}\partial_{rr}\delta\zeta + \frac{\tilde{\gamma}}{r}\partial_r\delta\zeta - \delta\zeta U''(h) - \frac{u_{Cz}}{4Bh}(L^2 - r^2) = \frac{\Delta\mu_b - \Delta\mu_{eq}}{\Omega}. \quad (D.7)$$

A particular solution of this equation is a parabola:

$$\delta\zeta = \frac{u_{Cz}}{4BhU''(h)} \left(r^2 - L^2 + \frac{4\tilde{\gamma}}{U''(h)} \right) - \frac{\Delta\mu_b - \Delta\mu_{eq}}{\Omega U''(h)}. \quad (D.8)$$

A comparison between this solution and the profile obtained from numerical integration is shown in the main text in Fig. 4.10 for crystal close to the transition. The agreement is very satisfactory.

D.1.1 Viscosity effect on the growth rate

Applying a similar procedure to the force balance expression in Eq. (4.3) we have to leading order

$$u_{Cz} 2\pi \int_0^L dr r \int_r^L dr' \frac{6\eta r'}{\zeta_{eq}^3(r')} = 2\pi \int_0^L dr r \delta\zeta U''(\zeta_{eq}). \quad (D.9)$$

Using Eq. (D.6) to express the right hand side, we are left with

$$u_{Cz} 2\pi \int_0^L dr r \int_r^L dr' r' \left(\frac{6\eta}{\zeta_{eq}^3(r')} + \frac{1}{2B\zeta_{eq}(r')} \right) = -\pi L^2 \frac{\Delta\mu_b - \Delta\mu_{eq}}{\Omega} + 2\pi \tilde{\gamma} L \partial_r \delta\zeta(L). \quad (D.10)$$

As done previously we assume that in the contact area $r < L$, the equilibrium profile is $\zeta_{eq} \approx h$. With this assumption the previous relation reduces to

$$u_{Cz} \left(\frac{6\eta}{h^3} + \frac{1}{2Bh} \right) \frac{L^4}{4} = -L^2 \frac{\Delta\mu_b - \Delta\mu_{eq}}{\Omega} + 2L\tilde{\gamma}\partial_r\delta\zeta(L). \quad (D.11)$$

Using Eq. (D.8) to express the last term in the right hand size we have

$$\frac{L^4}{4} \left[\left(\frac{6\eta}{h^3} + \frac{1}{2Bh} \right) - \frac{4\tilde{\gamma}}{L^2 B h U''(h)} \right] u_{Cz} = -L^2 \frac{\Delta\mu_b - \Delta\mu_{eq}}{\Omega}. \quad (D.12)$$

We then obtain (Eq. (4.24) in the main text):

$$u_{Cz} = \frac{-4Bh(\Delta\mu_b - \Delta\mu_{eq})}{\left(\frac{6B}{h^2}\eta + \frac{1}{2} - \frac{4\tilde{\gamma}}{L^2 U''(h)} \right) L^2 \Omega}. \quad (D.13)$$

As showed in the main text in Fig. 4.12 the comparison between this relation and the direct numerical solution of u_{Cz} proves to be satisfactory.

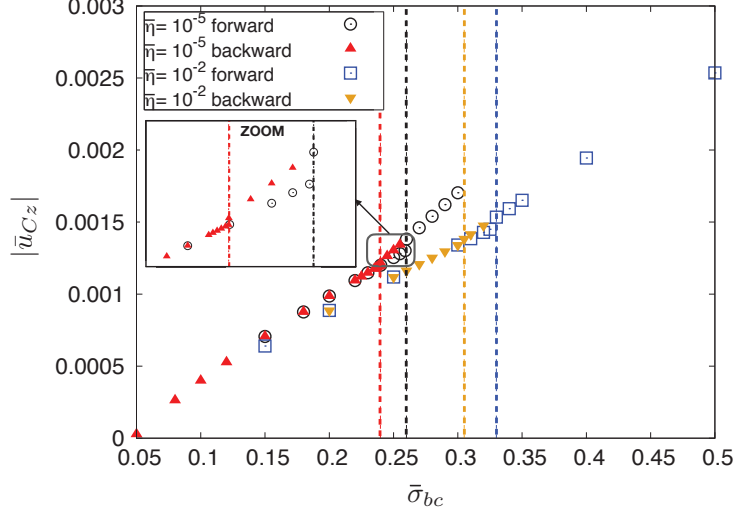


Figure D.1: Normalized growth rate $|\bar{u}_{Cz}|$ versus supersaturation $\bar{\sigma}_{bc}$ at the boundary of the simulation box for different normalized viscosities $\bar{\eta}$. The size of the simulation box is $\bar{R} = 40$. The system size and scales of the axes depend on the material. Calcium Carbonate, red triangles and black circles: $R = 400\text{nm}$, $\sigma_{bc} \approx 0.014 \times \bar{\sigma}_{bc}$, $u_{Cz} \approx 6.7 \times 10^5 \text{nm/s} \times \bar{u}_{Cz}$; Sodium Chlorate, yellow triangles and blue squares: $R \approx 127\text{nm}$, $\sigma_{bc} \approx 0.017 \times \bar{\sigma}_{bc}$, $u_{Cz} \approx 2.1 \times 10^5 \text{nm/s} \times \bar{u}_{Cz}$; Glucose, yellow triangles and blue squares: $R \approx 400\text{nm}$, $\sigma_{bc} \approx 0.05 \cdot \bar{\sigma}_{bc}$, $u_{Cz} \approx 5.5 \times 10^4 \text{nm/s} \times \bar{u}_{Cz}$. Vertical dashed lines indicate the critical supersaturation at the boundary of the simulation box for forward and backward transitions. Their color is the same as that of the corresponding symbols.

D.1.2 Viscosity effect on the critical supersaturation

As discussed in the main text, we expect the cavity to appear when $\zeta_0 > \zeta^{cav}$, where ζ_0 is the width at the center of the contact, and ζ^{cav} is defined by the relation $U''(\zeta^{cav}) = 0$. Given Eq. (4.18) and assuming again $\zeta_{eq} \approx h$, we find $\zeta^{cav} = 4/3 h$ and $\delta\zeta^{cav} = \zeta^{cav} - h = h/3$. Let us recall Eq. (D.8) and consider the correction to ζ_0 :

$$\delta\zeta(0) = \frac{u_{Cz}}{4BhU''(h)} \left(\frac{4\tilde{\gamma}}{U''(h)} - L^2 \right) - \frac{\Delta\mu_b - \Delta\mu_{eq}}{\Omega U''(h)}. \quad (\text{D.14})$$

Now we use the condition $\delta\zeta(0) = \delta\zeta^{cav}$ for the appearance of the cavity, and deduce the corresponding critical value of the chemical potential at the boundary:

$$\frac{\Delta\mu_b^{cav} - \Delta\mu_{eq}}{\Omega} = \frac{u_{Cz}}{4Bh} \left(\frac{4\tilde{\gamma}}{U''(h)} - L^2 \right) - \delta\zeta^{cav} U''(h). \quad (\text{D.15})$$

Using Eq. (4.24) we have

$$\frac{\Delta\mu_b^{cav} - \Delta\mu_{eq}}{\Omega} \approx \frac{\delta\zeta^{cav} U''(h) \left(\frac{6B}{h^2} \eta + \frac{1}{2} - \frac{4\tilde{\gamma}}{L^2 U''(h)} \right)}{\frac{1}{2} - \frac{6B}{h^2} \eta}. \quad (\text{D.16})$$

Using again the identity $\Delta\mu = k_B T \sigma$, neglecting the last term in the denominator ($\sim 1/L^2$) and the equilibrium chemical potential ($\sim 1/L$), we obtain Eq. (4.23).

D.2 Growth rate hysteresis in nano-confinement

In Fig. D.1 we show the normalized growth rate \bar{u}_{Cz} as a function of the normalized supersaturation at the boundary of the simulation box as obtained from the numerical solution of Eq. (4.19). The growth rate responds roughly linearly to changes in the supersaturation, and a small jump

followed by a change of slope is observed at the transition. Hysteresis is also found here but the discontinuity is more apparent when increasing the supersaturation from an initially flat surface (forward transition).

D.3 Probe the kinetic constant via the morphology diagram?

As discussed in the main text, when considering slow surface kinetics one has to use a generalized formulation of the transition line, Eq. (4.31). In that relation, benefiting from what observed in the fast surface kinetics limit (Figs. 4.6 and 4.9), we included the phenomenological slope α in front of the term proportional to the contact area. However, it is also interesting to consider the idealized limit (what would be expected without any input from simulation results) $\alpha = 1$. This leads to the transition line given by

$$|u_{Cz}^{cav}| = \frac{\Omega c_0 \sigma_b^{cav}}{L_{cav}^2 / (4hD) + \nu^{-1}} = \tilde{\beta}_{\alpha=1}. \quad (\text{D.17})$$

Representing the same data used for producing Fig. 4.13 in the plane $(u_{Cz}, \tilde{\beta}_{\alpha=1})$ leads to Fig. D.2. In this figure it can be observed that the data is bounded between two lines, one of slope ≈ 0.6 and one of slope ≈ 1 . The first corresponds to the limit of fast surface kinetics ($\nu \rightarrow \infty$) the latter to the limit of slow surface kinetics ($\nu \rightarrow 0$). Intermediate values are mixed regimes.

This explicitly shows that the morphology diagram is sensitive to the surface kinetic constant. Therefore – assuming the observed slopes are not an artifact of our simulations (see the discussion in Section 4.5.3) – this type of plots (or Fig. 4.13 in the main text) could be used in practice to probe the kinetic constant ν of a crystal if the other parameters are known. This kind of observations implies to fully explore the morphology phase diagram (thus one needs to observe cavities). Nothing indicates this should be simple in general, as also suggested by the great care taken to perform the experimental observations in Section 4.2 [106]. However, in experiments surface kinetic constants are difficult to assess and their value is still debated [174, 193]. In front of such technical difficulties, this approach might become reasonable.

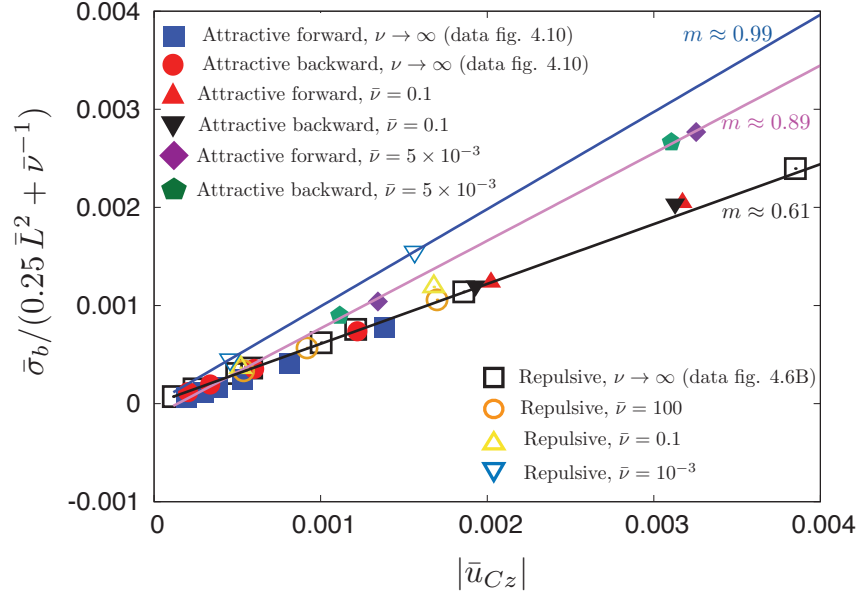


Figure D.2: Non-equilibrium morphology diagram where the y-axis is given by Eq. (D.17) (which does not include the heuristic constant α). Slopes, m , range from ≈ 0.61 in the diffusion driven limit (black empty squares), to ≈ 1 (blue empty triangles) in the slow surface kinetics limit. The former coincides with the value of the heuristic constant α . Results are in code units.

E.1 Thermodynamic equilibrium

Let us recall the equilibrium relations illustrated in Appendix D.1. At equilibrium null fluxes and rigid body velocity imply constant and uniform chemical potential $\Delta\mu(r) = \Delta\mu_{eq}$. Using Eq. (2.45), we express the equilibrium chemical potential as a function of the equilibrium profile and the interaction with the substrate:

$$\frac{\Delta\mu_{eq}}{\Omega} = \tilde{\gamma}(\partial_{rr}\zeta_{eq} + \frac{\partial_r\zeta_{eq}}{r}) - U'(\zeta_{eq}) \quad (\text{E.1})$$

where $\tilde{\gamma}$ is the stiffness of the crystal surface. From this relation, we can derive two further equations valid at equilibrium. The first one is exact and valid in all the domain. This is obtained by multiplying Eq. (E.1) by $\partial_r\zeta_{eq}dr$ and integrating:

$$\begin{aligned} \frac{\tilde{\gamma}}{2}(\partial_r\zeta_{eq})^2 &= U(\zeta_{eq}(r)) - U(\zeta_{eq}(0)) + \frac{\Delta\mu_{eq}}{\Omega}(\zeta_{eq}(r) - \zeta_{eq}(0)) \\ &\quad - \tilde{\gamma} \int_0^r \frac{(\partial_{r'}\zeta_{eq})^2}{r'} dr' \end{aligned} \quad (\text{E.2})$$

Let us introduce an equilibrium profile far from the substrate ζ_{eq}^∞ where the label ∞ indicates that this expression should approach the profile of a free crystal infinitely far from the substrate and hence in absence of interactions so that $U'(\zeta_{eq}^\infty) = 0 \forall r$. We expect this profile to be solution of the confined problem when $r \gg r_{tl}$ where the triple line position, r_{tl} , is the point after which $\zeta_{eq} \sim \zeta_{eq}^\infty$. Assuming the interaction to decay to zero far from the contact area, a second equilibrium relation is

$$- \int_0^{r^*} 2\pi r dr U'(\zeta_{eq}) = F_{eq} \quad (\text{E.3})$$

where $r^* \gg r_{tl}$. The integration of Eq. (E.1) on the increment $2\pi r dr$ between 0 and r for $r \geq r_{tl}$ leads to

$$\partial_r\zeta_{eq}^\infty(r) = \frac{\Delta\mu_{eq}}{2\Omega\tilde{\gamma}}r - \frac{F_{eq}}{2\pi\tilde{\gamma}}\frac{1}{r}, \quad (\text{E.4})$$

where we used that $\zeta_{eq} \rightarrow \zeta_{eq}^\infty$ for $r \gg r_{tl}$.

The previous relation can be integrated between r_{tl} and $r > r_{tl}$:

$$\zeta_{eq}^\infty(r) = \frac{\Delta\mu_{eq}}{4\Omega\tilde{\gamma}}(r^2 - r_{tl}^2) - \frac{F_{eq}}{2\pi\tilde{\gamma}} \ln \frac{r}{r_{tl}} + \zeta_{eq}^\infty(r_{tl}) \quad (\text{E.5})$$

Let us here rewrite the last integral term in Eq. (5.5b) as

$$\begin{aligned} \tilde{\gamma} \int_0^r dr \frac{(\partial_r \zeta_{eq})^2}{r} &= \tilde{\gamma} \int_{r_{tl}}^r dr \frac{(\partial_r \zeta_{eq}^\infty)^2}{r} + \\ &\tilde{\gamma} \int_0^r dr \left[\frac{(\partial_r \zeta_{eq})^2}{r} - \Theta(r - r_{tl}) \frac{(\partial_r \zeta_{eq}^\infty)^2}{r} \right] \end{aligned} \quad (\text{E.6})$$

The first term in the right hand side of the previous equation can be calculated from Eq. (E.5):

$$\begin{aligned} \tilde{\gamma} \int_{r_{tl}}^r dr \frac{(\partial_r \zeta_{eq}^\infty)^2}{r} &= \\ &\frac{\Delta \mu_{eq}^2}{8\Omega^2 \tilde{\gamma}} (r^2 - r_{tl}^2) - \frac{F_{eq}^2}{8\pi^2 \tilde{\gamma}} \left(\frac{1}{r^2} - \frac{1}{r_{tl}^2} \right) - \frac{\mu_{eq} F_{eq}}{2\pi \tilde{\gamma} \Omega} \ln \frac{r}{r_{tl}}. \end{aligned} \quad (\text{E.7})$$

When $r \gg r_{tl}$, using Eqs. (E.6) and (E.7) we can then rewrite Eq. (E.2) as

$$\begin{aligned} \frac{\Delta \mu_{eq}}{\Omega} (\zeta_{eq}^\infty(r) - \zeta_{eq}(0)) &= \frac{\tilde{\gamma}}{2} (\partial_r \zeta_{eq}^\infty(r))^2 - \Delta U + \\ &+ \frac{\Delta \mu_{eq}^2}{8\Omega^2 \tilde{\gamma}} (r^2 - r_{tl}^2) - \frac{F_{eq}^2}{8\pi^2 \tilde{\gamma}} \left(\frac{1}{r^2} - \frac{1}{r_{tl}^2} \right) - \frac{\mu_{eq} F_{eq}}{2\pi \tilde{\gamma} \Omega} \ln \frac{r}{r_{tl}} + \Gamma_{tl}, \end{aligned} \quad (\text{E.8})$$

where $\Delta U = U(\zeta_{eq}^\infty(r)) - U_0$ where $U_0 = U(\zeta_{eq}(0))$. We assume that $U(\zeta_{eq}^\infty(r)) = U_\infty$ for $r \gg r_{tl}$ where $U_\infty \sim 0$ is evaluated outside the contact area. The term Γ_{tl} is given by

$$\Gamma_{tl} = \tilde{\gamma} \int_0^r dr \left[\frac{(\partial_r \zeta_{eq})^2}{r} - \Theta(r - r_{tl}) \frac{(\partial_r \zeta_{eq}^\infty)^2}{r} \right]. \quad (\text{E.9})$$

We will show in the following that this term is related to the line tension.

E.1.1 1D line tension

Using a similar procedure for a one-dimension ridge contact we have in 1D the following relations:

$$\frac{\tilde{\gamma}}{2} (\partial_x \zeta_{eq})^2 = U(\zeta_{eq}(x)) - U(\zeta_{eq}(0)) + \frac{\Delta \mu_{eq}}{\Omega} (\zeta_{eq}(x) - \zeta_{eq}(0)) \quad (\text{E.10a})$$

$$\zeta_{eq}^\infty(x) = \frac{\Delta \mu_{eq}}{2\Omega \tilde{\gamma}} (x^2 - x_{tl}^2) - \frac{F_{eq}}{2\tilde{\gamma}} (x - x_{tl}) + \zeta_{eq}^\infty(x_{tl}). \quad (\text{E.10b})$$

Let us consider the equilibrium energy of a 1D crystal in the vicinity of a substrate. Defining the surface energy $\gamma(\theta)$ with $\theta = \arctan(\partial_x \zeta)$, it's energy will be given by

$$\begin{aligned} E_{tot} &= \int_{-\infty}^{\infty} dx \left[\gamma(\theta) [1 + (\partial_x \zeta_{eq}(x))^2]^{1/2} + U(\zeta_{eq}(x)) \right] \\ &\approx \int_{-\infty}^{\infty} dx \left[\gamma(0) + \tilde{\gamma} \frac{1}{2} (\partial_x \zeta_{eq}(x))^2 + U(\zeta_{eq}(x)) \right], \end{aligned} \quad (\text{E.11})$$

where the last relation is derived in the small slope limit ($\theta \approx 0$) and using the definition of stiffness, $\tilde{\gamma} = \gamma(\theta) + \gamma''(\theta)$. Let us consider a reference energy E_0 given by an infinitely large flat crystal in the vicinity of the substrate,

$$E_0 = \int_{-\infty}^{\infty} dx (\gamma(0) + U_0), \quad (\text{E.12})$$

and express energies with respect to this reference:

$$\xi_{tot} = E_{tot} - E_0 = \int_{-\infty}^{\infty} dx \left(\frac{\tilde{\gamma}}{2} (\partial_x \zeta_{eq}(x))^2 + U(\zeta_{eq}(x)) - U_0 \right), \quad (\text{E.13})$$

where $U_0 = U(\zeta_0^{eq})$ the energy of the flat equilibrium profile in the center $\zeta_0^{eq} = \zeta_{eq}(x=0)$. From Eq. (E.10a)

$$\Delta U(x) = \frac{\tilde{\gamma}}{2} (\partial_x \zeta_{eq}(x))^2 - (\zeta_{eq}(x) - \zeta_0^{eq}) \frac{\Delta \mu_{eq}}{\Omega}, \quad (\text{E.14})$$

width $\Delta U = U(\zeta(x)) - U_0$. We hence obtain

$$\xi_{tot} = \int_{-\infty}^{\infty} dx \left[\tilde{\gamma} (\partial_x \zeta_{eq}(x))^2 - (\zeta_{eq}(x) - \zeta_0^{eq}) \frac{\Delta \mu_{eq}}{\Omega} \right]. \quad (\text{E.15})$$

Let us now consider the energy of a crystal given by a flat crystal plus the contribution far from the substrate $x > x_{tl}$:

$$\begin{aligned} \xi_{macro} = E_{macro} - E_0 &= \int_{-\infty}^{x_{tl}} dx (\gamma(0) + U_0) + \int_{x_{tl}}^{\infty} dx \left[\gamma(0) + \frac{\tilde{\gamma}}{2} (\partial_x \zeta_{eq}^{\infty}(x))^2 + U(\zeta_{eq}^{\infty}(x)) \right] \\ &- \int_{-\infty}^{\infty} dx (\gamma(0) + U_0) = \int_{x_{tl}}^{\infty} dx \left[\frac{\tilde{\gamma}}{2} (\partial_x \zeta_{eq}^{\infty}(x))^2 + \Delta U \right]. \end{aligned} \quad (\text{E.16})$$

Since Eq. (E.14) is valid everywhere we have that

$$\xi_{macro} = \int_{x_{tl}}^{\infty} dx \left[\tilde{\gamma} (\partial_x \zeta_{eq}^{\infty}(x))^2 - (\zeta_{eq}^{\infty}(x) - \zeta_0^{eq}) \frac{\Delta \mu_{eq}}{\Omega} \right]. \quad (\text{E.17})$$

We define the line tension γ_{tl} as $\xi_{tot} - \xi_{macro}$. It follows that the 1D line tension is here given by

$$\begin{aligned} \gamma_{tl} &= \int_{-\infty}^{\infty} dx \left\{ \tilde{\gamma} (\partial_x \zeta_{eq}(x))^2 - \frac{\Delta \mu_{eq}}{\Omega} (\zeta_{eq}(x) - \zeta_0^{eq}) \right. \\ &\left. - \Theta(x - x_{tl}) \left[\tilde{\gamma} (\partial_x \zeta_{eq}^{\infty}(x))^2 - \frac{\Delta \mu_{eq}}{\Omega} (\zeta_{eq}^{\infty}(x) - \zeta_0^{eq}) \right] \right\}, \end{aligned} \quad (\text{E.18})$$

where Θ is the Heaviside function. This expression represents the difference between the free-energy associated to a contact with a straight triple line (1D) and the one of the corresponding macroscopic configuration composed only of a surface part (far from the substrate) and an interface part (in the contact region). The terms proportional to the surface tension $\tilde{\gamma}$ account for the energy of the triple line when expanding the contact, the second term proportional to the chemical potential is the excess volume per line unit and represent the energy associated to change the configuration from the macroscopic one to the real one $\zeta_{eq}(x)$.

Note that in the absence of an external force and when the disjoining pressure is attractive we have that $\zeta_0^{eq} = \zeta_{min}$ where ζ_{min} is the position of the minimum of the interaction and $\Delta \mu_{eq}/\Omega = U'(\zeta_{min}) = 0$. We can then define the line tension for $\Delta \mu_{eq} = 0$ as

$$\gamma_{tl}^0 = \tilde{\gamma} \int_{-\infty}^{\infty} dx \left[(\partial_x \zeta_{eq}(x))^2 - \Theta(x - x_{tl}) (\partial_x \zeta_{eq}^{\infty}(x))^2 \right], \quad (\text{E.19})$$

where $\gamma_{tl}(\Delta \mu_{eq} = 0) = \gamma_{tl}^0$. It should be observed also that a second consequence of considering an attractive interaction is that since $0 = \Delta \mu_{eq}/\Omega = \partial_{xx} \zeta^{\infty}$, it also follows that the slope of the the profile far from from the contact is constant, $\partial_x \zeta_{eq}^{\infty}(x) = \partial_x \zeta_{eq}^{\infty}(x_{tl})$.

Going back to the general case of arbitrary potentials, from the definition of γ_{tl}^0 , Eq. (E.18) can be written as

$$\gamma_{tl} = \gamma_{tl}^0 - \frac{\Delta \mu_{eq}}{\Omega} \left[\int_{-\infty}^{x_{tl}} dx (\zeta_{eq}(x) - \zeta_0^{eq}) + \int_{x_{tl}}^{\infty} dx (\zeta_{eq}(x) - \zeta_{eq}^{\infty}(x)) \right]. \quad (\text{E.20})$$

Using that $\Delta \mu_{eq}/\Omega = \kappa_{\infty} \sim 1/d$ with κ_{∞} the curvature at $x \gg 1$ and d as the half pore width, the excess volume term is at most of order $\mathcal{O}(1/d)$. Assuming that $d \gg 1$, we choose in the following to neglect the volume excess contribution, hence $\gamma_{tl} \sim \gamma_{tl}^0$.

The integral term Γ defined in Eq. (E.9), can be related to the 1D line tension assuming that $r_{tl} \gg 1$ and neglecting excess volume ($\gamma_{tl} \sim \gamma_{tl}^0$). Since we expect the integrand to be finite only in a neighborhood of the contact point r_{tl} , being $\partial_r \zeta_{eq} \sim 0$ for $r \ll r_{tl}$ and $\partial_r \zeta_{eq} \sim \partial_r \zeta_{eq}^\infty$, assuming $r \gg r_{tl}$ we can make the expansion $r \sim r_{tl} + \epsilon$. We hence have

$$\begin{aligned} \Gamma_{tl} &= \frac{\tilde{\gamma}}{r_{tl}} \int_0^\infty dr \frac{r_{tl}}{r} \left[(\partial_r \zeta_{eq})^2 - \Theta(r - r_{tl}) (\partial_r \zeta_{eq}^\infty(r))^2 \right] \\ &\sim \frac{1}{r_{tl}} (\gamma_{tl}^0 + \mathcal{O}(\frac{1}{r_{tl}})) \end{aligned} \quad (\text{E.21})$$

where we assumed that the 1D equilibrium profile is close to the 2D one for $r_{tl} \gg 1$.

E.1.2 General relations

Finally, the two equations describing the crystal at equilibrium are Eq. (E.4) and Eq. (E.8) evaluated in r_{tl} ,

$$\frac{F_{eq}}{2\pi\tilde{\gamma}} \frac{1}{r_{tl}} = \frac{\Delta\mu_{eq}}{2\Omega\tilde{\gamma}} r_{tl} - \partial_r \zeta_{tl}^\infty, \quad (\text{E.22a})$$

$$\frac{\tilde{\gamma}}{2} (\partial_r \zeta_{tl}^\infty)^2 = \Delta U + \frac{\Delta\mu_{eq}}{\Omega} (\zeta_{tl}^\infty - \zeta_0^{eq}) + \frac{\gamma_{tl}^0}{r_{tl}}, \quad (\text{E.22b})$$

respectively, with $\Delta U = U_\infty - U_0$, $U_\infty = U(\zeta_{eq}(r \gg r_{tl})) \sim 0$, $U_0 = U(\zeta_0^{eq})$, $\zeta_0^{eq} = \zeta_{eq}(0)$ and $\zeta_{tl}^\infty = \zeta_{eq}^\infty(r_{tl})$. As discussed in the main text a third equilibrium relation can be derived for the chemical potential. Considering the two asymptotic equilibrium solution, given by a flat profile in the contact, and a profile far from the interaction, outside the contact, we indeed have

$$\frac{\Delta\mu_{eq}}{\Omega} = -U'_0 = \tilde{\gamma}\kappa(\zeta_\infty). \quad (\text{E.23})$$

This relation also provides boundary conditions for the curvature. It shows for instance that in the case of an attractive interaction with a minimum and in the hypothesis of zero external force, $U'_0 = 0$ so that the macroscopic shape of the crystal far from the substrate is a line. However, if the interaction is purely repulsive $\kappa_\infty \neq 0$ and the macroscopic profile outside the contact is parabolic (see Eqs. (E.4) and (E.10b)).

We derive in the main text expressions of the equilibrium crystallization force distinguishing two separate cases:

- i) Attractive interaction. This will introduce a natural definition for the triple line, $\zeta_{tl}^\infty = \zeta_0^{eq}$ and lead to habitual contact angle relations.
- ii) Repulsive interaction. We choose the triple line as the point where $\partial_r \zeta_{tl}^\infty = 0$.

The two scenarios are illustrated in the main text in Fig. 5.1.

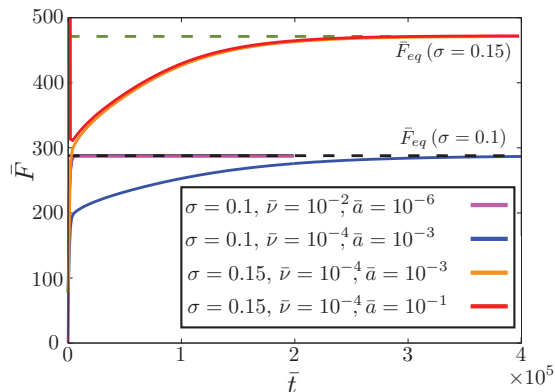
E.2 Equilibrium simulations: Relaxation dynamics

In the equilibrium case ($v_l = 0$), the force F , and contact area L , reach stationary values. These values are used to compute the equilibrium pressure, $P = F/(\pi L^2)$, shown in the main text (right panel of Section 5.4). From, the analytic equilibrium derivations (see above and Section 5.2), we expect that the stationary values of these observables are not affected by the value of the kinetic constant ν , and interaction amplitude \bar{a} . The former should only reflect on the kinetics of the process but cannot influence steady states (thus equilibrium). The latter because of the equilibrium relation Eq. (5.12), showing no effect of the disjoining pressure on the equilibrium pressure for a purely repulsive interaction (given our definition of contact radius).

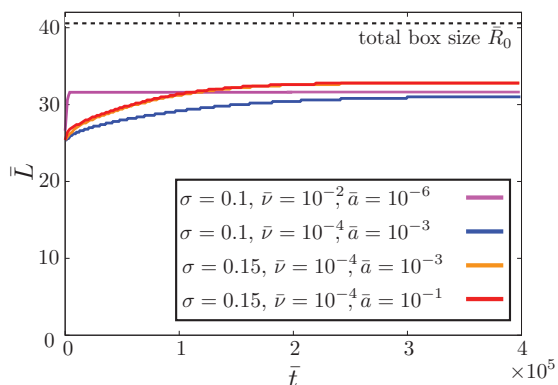
In Fig. E.1 we show the time evolution of the crystallization force and contact size of an arbitrary initial profile. Whatever is the choice of \bar{a} and ν the curves reach stationary values. This

Figure E.1: Time evolution of force and contact sizes in some exemplary equilibrium simulations. The total size of the simulation box is $\bar{R} = 40.6$. All curves reach a stationary value. The equilibration time depends on the kinetic constant ν . Two supersaturations at the boundary of the integration domain are considered: $\sigma = 0.1$ and $\sigma = 0.15$. Their effect is to shift the plateaus. Left panel: crystallization force. Right pane: contact size. Results are given in normalized quantities.

(a) The plot is cut on the top for better visualization. The highest point of the red curve would be $\bar{F} \approx 7800$. Dashed lines are the asymptotic equilibrium forces \bar{F}_{eq} at the given supersaturation.



(b) The contact size is computed using Eq. (5.26) in the main text. Oscillations are artifacts due to the discretization of the interface (see also bottom panel of Fig. 5.4). The orange curve is covered by the red one. The black dashed line is a reference length equal to the total size of the box $\bar{R}_0 = 40.6$.



stationary values as expected depend only on the supersaturation. Effects can be seen however on the relaxation dynamics. In particular, η reflects on relaxation times as seen comparing the fuchsia curves (higher ν) to the blue ones (smaller ν). In regard to the interaction amplitude \bar{a} , this has only a very short transient effect on the initial dynamics which is due to the choice of the initial condition. For instance, looking at the panel on the left, small \bar{a} provokes initial small forces since the initial position of the interface is too far to “feel” the interaction. On the contrary, larger forces are experienced when the interaction amplitude is large (red curve) due to the initial position of the interface. Finally, we performed exploratory simulations to test the effect of different boundary widths ζ_{bc} (not shown here). We found an effect on the contact size and equilibrium force. However, these are perfectly balanced in the equilibrium pressure which remains unaffected.

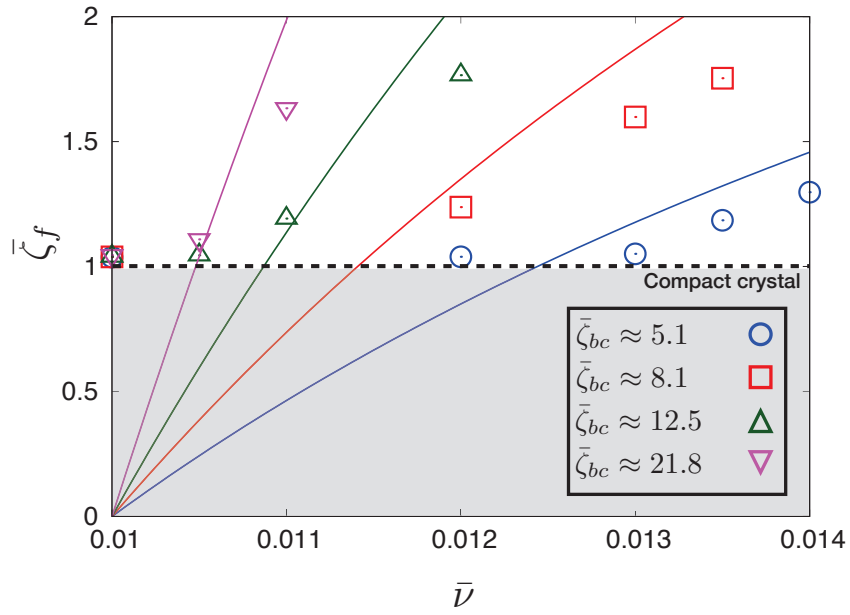
E.3 Macroscopic film width after the detachment

In this appendix we briefly illustrate that for a given width at the boundary ζ_{bc} , we can predict the width of the detached film ζ_{mf} via Eq. (5.37):

$$\zeta_{mf} \approx \zeta_{bc} \left(1 - \frac{D}{\nu} \kappa_{bc} \right).$$

Let us test this prediction assuming $\kappa_{bc} \approx d^{-1}$. In figure Fig. E.2 we show the film thickening ζ_f in the neighborhood of the transition as a function of the kinetic constant ν as computed from simulations for different values of the boundary film width ζ_{bc} . The results are compared to the analytic prediction above (solid line with the corresponding color) showing a reasonably good agreement. Higher discrepancies found for larger thickness ζ_{bc} at the boundary are probably due to the slower relaxation time characterizing this type of simulations, so that they have not yet converged to the asymptotic value $\zeta_f(t \rightarrow \infty) \approx \zeta_{mf}$.

Figure E.2: Pore half size $d = 100$ and boundary supersaturation $\sigma_{bc} = 0.1$. The x-axis starts from 0.01 for better visualization. The dashed black line is a reference line indicating the compact crystal (film thickening $\zeta_f \approx 1$). The area below is slightly opaque because not relevant.



- [1] Yukio Saito. *Statistical Physics Of Crystal Growth*. World Scientific Publishing, 1996. ISBN 981-02-2834-1.
- [2] W. K. Burton, N. Cabrera, and F. C. Frank. The Growth of Crystals and the Equilibrium Structure of their Surfaces. *Philosophical Transactions of the Royal Society A: Mathematical, Physical and Engineering Sciences*, 243(866):299–358, June 1951. ISSN 1364-503X, 1471-2962. doi: 10.1098/rsta.1951.0006.
- [3] Theodore L. Einstein. Equilibrium Shape of Crystals. *arXiv:1501.02213 [cond-mat]*, pages 215–264, 2015. doi: 10.1016/B978-0-444-56369-9.00005-8.
- [4] Chaouqi Misbah, Olivier Pierre-Louis, and Yukio Saito. Crystal surfaces in and out of equilibrium: A modern view. *Reviews of Modern Physics*, 82(1):981–1040, March 2010. ISSN 0034-6861, 1539-0756. doi: 10.1103/RevModPhys.82.981.
- [5] John D. Weeks. The Roughening Transition. In Tormod Riste, editor, *Ordering in Strongly Fluctuating Condensed Matter Systems*, pages 293–317. Springer US, Boston, MA, 1980. ISBN 978-1-4684-3628-0 978-1-4684-3626-6. doi: 10.1007/978-1-4684-3626-621.
- [6] Alberto Pimpinelli and Jacques Villain. *Physics of Crystal Growth*. Cambridge University Press, Cambridge, 1998. ISBN 978-0-511-62252-6. doi: 10.1017/CBO9780511622526.
- [7] Tormod Riste. *Ordering in Strongly Fluctuating Condensed Matter Systems*. Springer US, Boston, MA, 1980. ISBN 978-1-4684-3626-6 978-1-4684-3628-0. OCLC: 840288739.
- [8] P. Bennema, H. Meekes, and W.J.P. van Enckevort. Crystal Growth and Morphology: A Multi-Faceted Approach. In *Growth, Dissolution and Pattern Formation in Geosystems*, pages 21–64. Springer Netherlands, Dordrecht, 1999. ISBN 978-94-015-9179-9. OCLC: 851367967.
- [9] Sébastien Balibar, Harry Alles, and Alexander Ya Parshin. The surface of helium crystals. *Rev. Mod. Phys.*, 77(1):54, 2005.
- [10] J.C. Heyraud and J.J. Métois. Growth shapes of metallic crystals and roughening transition. *Journal of Crystal Growth*, 82(3):269–273, March 1987. ISSN 00220248. doi: 10.1016/0022-0248(87)90313-7.
- [11] G. Wulff. XXV. Zur Frage der Geschwindigkeit des Wachstums und der Auflösung der Krystallflächen. *Zeitschrift für Kristallographie - Crystalline Materials*, 34(1-6), January 1901. ISSN 2196-7105, 2194-4946. doi: 10.1524/zkri.1901.34.1.449.

- [12] Heinrich Liebmann. IX. Der Curie-Wulff'sche Satz über Combinationsformen von Krystallen. *Zeitschrift für Kristallographie - Crystalline Materials*, 53(1-6), January 1914. ISSN 2196-7105, 2194-4946. doi: 10.1524/zkri.1914.53.1.171.
- [13] Brian J. Spencer. Asymptotic solutions for the equilibrium crystal shape with small corner energy regularization. *Physical Review E*, 69(1), January 2004. ISSN 1539-3755, 1550-2376. doi: 10.1103/PhysRevE.69.011603.
- [14] S. Torabi, J. Lowengrub, A. Voigt, and S. Wise. A new phase-field model for strongly anisotropic systems. *Proceedings of the Royal Society A: Mathematical, Physical and Engineering Sciences*, 465(2105):1337–1359, May 2009. ISSN 1364-5021, 1471-2946. doi: 10.1098/rspa.2008.0385.
- [15] Olivier Pierre-Louis. Solid-state wetting at the nanoscale. *Progress in Crystal Growth and Characterization of Materials*, 62(2):177–202, June 2016. ISSN 09608974. doi: 10.1016/j.pcrysgrow.2016.04.009.
- [16] M. V. Ramana Murty. Morphological stability of nanostructures. *Physical Review B*, 62(24):17004–17011, December 2000. ISSN 0163-1829, 1095-3795. doi: 10.1103/PhysRevB.62.17004.
- [17] Jean-Noël Aqua, Adrien Gouyé, Antoine Ronda, Thomas Frisch, and Isabelle Berbezier. Interrupted Self-Organization of SiGe Pyramids. *Physical Review Letters*, 110(9), February 2013. ISSN 0031-9007, 1079-7114. doi: 10.1103/PhysRevLett.110.096101.
- [18] R Kern and P Müller. From Wulff KaisheW' theorem to nanodots. page 19, 2008.
- [19] R. K. P. Zia, J. E. Avron, and J. E. Taylor. The summertop construction: Crystals in a corner. *Journal of Statistical Physics*, 50(3-4):727–736, February 1988. ISSN 0022-4715, 1572-9613. doi: 10.1007/BF01026498.
- [20] D. Kashchiev and G. M. van Rosmalen. Review: Nucleation in solutions revisited. *Crystal Research and Technology*, 38(78):555–574, July 2003. ISSN 02321300, 15214079. doi: 10.1002/crat.200310070.
- [21] A. C. Lasaga. *Kinetic Theory in the Earth Sciences*. Princeton Series in Geochemistry. Princeton University Press, Princeton, N.J, 1998. ISBN 978-0-691-03748-6.
- [22] John W. Morse, Rolf S. Arvidson, and Andreas Lüttge. Calcium Carbonate Formation and Dissolution. *Chemical Reviews*, 107(2):342–381, February 2007. ISSN 0009-2665, 1520-6890. doi: 10.1021/cr050358j.
- [23] Ichiro Sunagawa. Growth and Morphology of Crystals. *Forma-Tokyo*, 14.1/2:147–166, 1999.
- [24] Takeshi Arakaki and Alfonso Mucci. A continuous and mechanistic representation of calcite reaction-controlled kinetics in dilute solutions at 25°C and 1 atm total pressure. *Aquatic Geochemistry*, 1(1):105–130, 1995. ISSN 1380-6165, 1573-1421. doi: 10.1007/BF01025233.
- [25] Jaroslav Nývlt. Nucleation and growth rate in mass crystallization. *Progress in Crystal Growth and Characterization*, 9(3-4):335–370, January 1984. ISSN 01463535. doi: 10.1016/0146-3535(84)90085-6.
- [26] F. C. Frank and M. B. Ives. Orientation-Dependent Dissolution of Germanium. *Journal of Applied Physics*, 31(11):1996–1999, November 1960. ISSN 0021-8979, 1089-7550. doi: 10.1063/1.1735485.
- [27] W. W. Mullins and R. F. Sekerka. Morphological Stability of a Particle Growing by Diffusion or Heat Flow. *Journal of Applied Physics*, 34(2):323–329, February 1963. ISSN 0021-8979, 1089-7550. doi: 10.1063/1.1702607.

-
- [28] J. S. Langer. Instabilities and pattern formation in crystal growth. *Reviews of Modern Physics*, 52(1):1–28, January 1980. ISSN 0034-6861. doi: 10.1103/RevModPhys.52.1.
- [29] A A Chernov. Stability of Facetted Shapes. *Journal of Crystal Growth*, 24/25:11–31, 1974.
- [30] William R. Wilcox. Crystallization flow. *Journal of Crystal Growth*, 12(2):93–96, February 1972. ISSN 00220248. doi: 10.1016/0022-0248(72)90036-X.
- [31] William R. Wilcox. Influence of convection on the growth of crystals from solution. *Journal of Crystal Growth*, 65(1-3):133–142, December 1983. ISSN 00220248. doi: 10.1016/0022-0248(83)90046-5.
- [32] A A Chernov. Step bunching and solution flow. *Journal of Optoelectronics and Advanced Materials*, 5(3):575, 2003.
- [33] Peter K. Weyl. Pressure solution and the force of crystallization: A phenomenological theory. *Journal of Geophysical Research*, 64(11):2001–2025, November 1959. ISSN 01480227. doi: 10.1029/JZ064i011p02001.
- [34] D. W. Durney. Solution-transfer, an Important Geological Deformation Mechanism. *Nature*, 235(5337):315–317, February 1972. ISSN 0028-0836, 1476-4687. doi: 10.1038/235315a0.
- [35] George W Scherer. Crystallization in pores. *Cement and Concrete Research*, 29(8):1347–1358, August 1999. ISSN 00088846. doi: 10.1016/S0008-8846(99)00002-2.
- [36] Robert J. Flatt, Michael Steiger, and George W. Scherer. A commented translation of the paper by C.W. Correns and W. Steinborn on crystallization pressure. *Environmental Geology*, 52(2):187–203, March 2007. ISSN 0943-0105, 1432-0495. doi: 10.1007/s00254-006-0509-5.
- [37] Ashwani K. Tripathi and Olivier Pierre-Louis. Triple-line kinetics for solid films. *Physical Review E*, 97(2), February 2018. ISSN 2470-0045, 2470-0053. doi: 10.1103/PhysRevE.97.022801.
- [38] A. Münch and B. Wagner. Contact-line instability of dewetting thin films. *Physica D: Nonlinear Phenomena*, 209(1-4):178–190, September 2005. ISSN 01672789. doi: 10.1016/j.physd.2005.06.027.
- [39] Pierre-Gilles de Gennes, Françoise Brochard-Wyart, and David Quéré. *Capillarity and Wetting Phenomena*. Springer New York, New York, NY, 2004. ISBN 978-1-4419-1833-8 978-0-387-21656-0. doi: 10.1007/978-0-387-21656-0.
- [40] Lydéric Bocquet and Elisabeth Charlaix. Nanofluidics, from bulk to interfaces. *Chem. Soc. Rev.*, 39(3):1073–1095, 2010. ISSN 0306-0012, 1460-4744. doi: 10.1039/B909366B.
- [41] Alexander Oron, Stephen H. Davis, and S. George Bankoff. Long-scale evolution of thin liquid films. *Reviews of Modern Physics*, 69(3):931–980, July 1997. ISSN 0034-6861, 1539-0756. doi: 10.1103/RevModPhys.69.931.
- [42] Bernard J. Hamrock. *Fundamentals of Fluid Film Lubrication*. Nasa scientific and technical information program edition, 1991.
- [43] Jacob Israelachvili. *Intermolecular and Surface Forces*. Elsevier, 2011. ISBN 978-0-12-375182-9. doi: 10.1016/C2009-0-21560-1.
- [44] E. J. W. Verwey, J. T. G. Overbeek, and K. van Nes. *Theory of the Stability of Lyophobic Colloids: The Interaction of Sol Particles Having an Electric Double Layer*. Elsevier Publishing Company, 1948.

- [45] E. J. W. Verwey. Theory of the Stability of Lyophobic Colloids. *The Journal of Physical and Colloid Chemistry*, 51(3):631–636, March 1947. ISSN 0092-7023, 1541-5740. doi: 10.1021/j150453a001.
- [46] Norma Alcantar, Jacob Israelachvili, and Jim Boles. Forces and ionic transport between mica surfaces: Implications for pressure solution. *Geochimica et Cosmochimica Acta*, 67(7):1289–1304, April 2003. ISSN 00167037. doi: 10.1016/S0016-7037(02)01270-X.
- [47] Patrick G. Hartley, Ian Larson, and Peter J. Scales. Electrokinetic and Direct Force Measurements between Silica and Mica Surfaces in Dilute Electrolyte Solutions. *Langmuir*, 13(8):2207–2214, April 1997. ISSN 0743-7463, 1520-5827. doi: 10.1021/la960997c.
- [48] J. J. Valle-Delgado, J. A. Molina-Bolívar, F. Galisteo-González, M. J. Gálvez-Ruiz, A. Feiler, and M. W. Rutland. Hydration forces between silica surfaces: Experimental data and predictions from different theories. *The Journal of Chemical Physics*, 123(3):034708, July 2005. ISSN 0021-9606, 1089-7690. doi: 10.1063/1.1954747.
- [49] Andrea Hamilton, Vasileios Koutsos, and Christopher Hall. Direct measurement of salt–mineral repulsion using atomic force microscopy. *Chemical Communications*, 46(29):5235, 2010. ISSN 1359-7345, 1364-548X. doi: 10.1039/b915709c.
- [50] William A Ducker and Tim J Senden. Measurement of Forces in Liquids Using a Force Microscope. *Langmuir*, 8:1831–1836, 1992.
- [51] Liqing Ren, Dongqing Li, and Weilin Qu. Electro-Viscous Effects on Liquid Flow in Microchannels. *Journal of Colloid and Interface Science*, 233(1):12–22, January 2001. ISSN 00219797. doi: 10.1006/jcis.2000.7262.
- [52] Liqing Ren, Weilin Qu, and Dongqing Li. Interfacial electrokinetic effects on liquid flow in microchannels. *International Journal of Heat and Mass Transfer*, page 10, 2001.
- [53] W. Sparreboom, A. van den Berg, and J. C. T. Eijkel. Principles and applications of nanofluidic transport. *Nature Nanotechnology*, 4(11):713–720, November 2009. ISSN 1748-3387, 1748-3395. doi: 10.1038/nnano.2009.332.
- [54] Moran Wang, Chi-Chang Chang, and Ruey-Jen Yang. Electroviscous effects in nanofluidic channels. *The Journal of Chemical Physics*, 132(2):024701, January 2010. ISSN 0021-9606, 1089-7690. doi: 10.1063/1.3290814.
- [55] Asger Bolet, Gaute Linga, and Joachim Mathiesen. Electrohydrodynamic channeling effects in narrow fractures and pores. *Physical Review E*, 97(4), April 2018. ISSN 2470-0045, 2470-0053. doi: 10.1103/PhysRevE.97.043114.
- [56] F. Liu, A. Klaassen, C. Zhao, F. Mugele, and D. van den Ende. Electroviscous Dissipation in Aqueous Electrolyte Films with Overlapping Electric Double Layers. *The Journal of Physical Chemistry B*, 122(2):933–946, January 2018. ISSN 1520-6106, 1520-5207. doi: 10.1021/acs.jpcc.7b07019.
- [57] J Lyklema and J.Th.G Overbeek. On the interpretation of electrokinetic potentials. *Journal of Colloid Science*, 16(5):501–512, October 1961. ISSN 00958522. doi: 10.1016/0095-8522(61)90029-0.
- [58] Nicolas F. Y. Durand, Arnaud Bertsch, Mina Todorova, and Philippe Renaud. Direct measurement of effective diffusion coefficients in nanochannels using steady-state dispersion effects. *Applied Physics Letters*, 91(20):203106, November 2007. ISSN 0003-6951, 1077-3118. doi: 10.1063/1.2801625.

-
- [59] Giacomo Bruno, Nicola Di Trani, R. Lyle Hood, Erika Zabre, Carly Sue Filgueira, Giancarlo Canavese, Priya Jain, Zachary Smith, Danilo Demarchi, Sharath Hosali, Alberto Pimpinelli, Mauro Ferrari, and Alessandro Grattoni. Unexpected behaviors in molecular transport through size-controlled nanochannels down to the ultra-nanoscale. *Nature Communications*, 9(1), December 2018. ISSN 2041-1723. doi: 10.1038/s41467-018-04133-8.
- [60] W. M. Deen. Hindered transport of large molecules in liquid-filled pores. *AIChE Journal*, 33(9):1409–1425, September 1987. ISSN 0001-1541, 1547-5905. doi: 10.1002/aic.690330902.
- [61] X. Zhang and C.J. Spiers. Compaction of granular calcite by pressure solution at room temperature and effects of pore fluid chemistry. *International Journal of Rock Mechanics and Mining Sciences*, 42(7-8):950–960, October 2005. ISSN 13651609. doi: 10.1016/j.ijrmms.2005.05.017.
- [62] Siese de Meer and Christopher J. Spiers. On Mechanisms and Kinetics of Creep by Intergranular Pressure Solution. In *Growth, Dissolution and Pattern Formation in Geosystems*, pages 345–366. Springer Netherlands, Dordrecht, 1999. ISBN 978-94-015-9179-9. OCLC: 851367967.
- [63] Rishi Raj. Creep in polycrystalline aggregates by matter transport through a liquid phase. *Journal of Geophysical Research: Solid Earth*, 87(B6):4731–4739, June 1982. ISSN 01480227. doi: 10.1029/JB087iB06p04731.
- [64] Won C Park and Erik H Schot. Stylolites: Their Nature and Origin. *Journal of Sedimentary Petrology*, 38(1):175–191, 1968.
- [65] Marcus Ebner, Daniel Koehn, Renaud Toussaint, François Renard, and Jean Schmittbuhl. Stress sensitivity of stylolite morphology. *Earth and Planetary Science Letters*, 277(3-4):394–398, January 2009. ISSN 0012821X. doi: 10.1016/j.epsl.2008.11.001.
- [66] D Koehn, F Renard, R Toussaint, and C Passchier. Growth of stylolite teeth patterns depending on normal stress and finite compaction. *Earth and Planetary Science Letters*, 257(3-4):582–595, May 2007. ISSN 0012821X. doi: 10.1016/j.epsl.2007.03.015.
- [67] Luiza Angheluta, Joachim Mathiesen, Chaouqi Misbah, and François Renard. Morphological instabilities of stressed and reactive geological interfaces. *Journal of Geophysical Research*, 115(B6), June 2010. ISSN 0148-0227. doi: 10.1029/2009JB006880.
- [68] Jean-Pierre Gratier, Dag K. Dysthe, and François Renard. The Role of Pressure Solution Creep in the Ductility of the Earth’s Upper Crust. In *Advances in Geophysics*, volume 54, pages 47–179. Elsevier, 2013. ISBN 978-0-12-380940-7. doi: 10.1016/B978-0-12-380940-7.00002-0.
- [69] Bram Cantaert, Elia Beniash, and Fiona C. Meldrum. Nanoscale Confinement Controls the Crystallization of Calcium Phosphate: Relevance to Bone Formation. *Chemistry - A European Journal*, 19(44):14918–14924, October 2013. ISSN 09476539. doi: 10.1002/chem.201302835.
- [70] Yun-Wei Wang, Hugo K. Christenson, and Fiona C. Meldrum. Confinement Increases the Lifetimes of Hydroxyapatite Precursors. *Chemistry of Materials*, 26(20):5830–5838, October 2014. ISSN 0897-4756, 1520-5002. doi: 10.1021/cm501770r.
- [71] Clara Anduix-Canto, Yi-Yeoun Kim, Yun-Wei Wang, Alexander Kulak, Fiona C. Meldrum, and Hugo K. Christenson. Effect of Nanoscale Confinement on the Crystallization of Potassium Ferrocyanide. *Crystal Growth & Design*, 16(9):5403–5411, September 2016. ISSN 1528-7483, 1528-7505. doi: 10.1021/acs.cgd.6b00894.

- [72] Masayoshi Tanaka, Eri Mazuyama, Atsushi Arakaki, and Tadashi Matsunaga. MMS6 Protein Regulates Crystal Morphology during Nano-sized Magnetite Biomineralization *in Vivo*. *Journal of Biological Chemistry*, 286(8):6386–6392, February 2011. ISSN 0021-9258, 1083-351X. doi: 10.1074/jbc.M110.183434.
- [73] Gregory A Pope, Thomas C Meierding, and Thomas R Paradise. Geomorphology’s role in the study of weathering of cultural stone. *Geomorphology*, 47(2-4):211–225, October 2002. ISSN 0169555X. doi: 10.1016/S0169-555X(02)00098-3.
- [74] L. A. Rijniens, H. P. Huinink, L. Pel, and K. Kopinga. Experimental Evidence of Crystallization Pressure inside Porous Media. *Physical Review Letters*, 94(7), February 2005. ISSN 0031-9007, 1079-7114. doi: 10.1103/PhysRevLett.94.075503.
- [75] Robert J. Flatt, Francesco Caruso, Asel Maria Aguilar Sanchez, and George W. Scherer. Chemo-mechanics of salt damage in stone. *Nature Communications*, 5(1), December 2014. ISSN 2041-1723. doi: 10.1038/ncomms5823.
- [76] A. Naillon, P. Joseph, and M. Prat. Ion Transport and Precipitation Kinetics as Key Aspects of Stress Generation on Pore Walls Induced by Salt Crystallization. *Physical Review Letters*, 120(3), January 2018. ISSN 0031-9007, 1079-7114. doi: 10.1103/PhysRevLett.120.034502.
- [77] David V. Wiltschko and John W. Morse. Crystallization pressure versus “crack seal” as the mechanism for banded veins. *Geology*, 29(1):79, 2001. ISSN 0091-7613. doi: 10.1130/0091-7613(2001)029<0079:CPVCSA>2.0.CO;2.
- [78] Jean-Pierre Gratier, Emanuelle Frery, Pierre Deschamps, Anja Røyne, François Renard, Dag Dysthe, Nadine Ellouz-Zimmerman, and Bruno Hamelin. How travertine veins grow from top to bottom and lift the rocks above them: The effect of crystallization force. *Geology*, 40(11):1015–1018, November 2012. ISSN 1943-2682, 0091-7613. doi: 10.1130/G33286.1.
- [79] L. A. Wilen and J. G. Dash. Frost Heave Dynamics at a Single Crystal Interface. *Physical Review Letters*, 74(25):5076–5079, June 1995. ISSN 0031-9007, 1079-7114. doi: 10.1103/PhysRevLett.74.5076.
- [80] A. W. Rempel, J. S. Wettlaufer, and M. G. Worster. Interfacial Premelting and the Thermomolecular Force: Thermodynamic Buoyancy. *Physical Review Letters*, 87(8), August 2001. ISSN 0031-9007, 1079-7114. doi: 10.1103/PhysRevLett.87.088501.
- [81] B. C. Regan, S. Aloni, K. Jensen, R. O. Ritchie, and A. Zettl. Nanocrystal-Powered Nanomotor. *Nano Letters*, 5(9):1730–1733, September 2005. ISSN 1530-6984, 1530-6992. doi: 10.1021/nl0510659.
- [82] E. H. Rutter and D. Elliott. The Kinetics of Rock Deformation by Pressure Solution [and Discussion]. *Philosophical Transactions of the Royal Society A: Mathematical, Physical and Engineering Sciences*, 283(1312):203–219, October 1976. ISSN 1364-503X, 1471-2962. doi: 10.1098/rsta.1976.0079.
- [83] S. F. Cox and M. S. Paterson. Experimental dissolution-precipitation creep in quartz aggregates at high temperatures. *Geophysical Research Letters*, 18(8):1401–1404, August 1991. ISSN 00948276. doi: 10.1029/91GL01802.
- [84] Delphine Croizé, François Renard, Knut Bjørlykke, and Dag Kristian Dysthe. Experimental calcite dissolution under stress: Evolution of grain contact microstructure during pressure solution creep. *Journal of Geophysical Research*, 115(B9), September 2010. ISSN 0148-0227. doi: 10.1029/2010JB000869.

-
- [85] Bas den Brok, Mohsine Zahid, and Cees W Passchier. Pressure solution compaction of sodium chlorate and implications for pressure solution in NaCl. *Tectonophysics*, 307(3-4): 297–312, June 1999. ISSN 00401951. doi: 10.1016/S0040-1951(99)00103-1.
- [86] Siese de Meer and Christopher J. Spiers. Creep of wet gypsum aggregates under hydrostatic loading conditions. *Tectonophysics*, 245(3-4):171–183, May 1995. ISSN 00401951. doi: 10.1016/0040-1951(94)00233-Y.
- [87] C.J. Spiers and Peter M. T. M Shutjens. Densification of crystalline aggregates by fluid-phase diffusional creep. In *Deformation Processes in Minerals, Ceramics and Rocks*, pages 334–353. Unwin Hyman, London, 1990. ISBN 978-94-011-6829-8.
- [88] Andrew M. Mullis. The role of silica precipitation kinetics in determining the rate of quartz pressure solution. *Journal of Geophysical Research*, 96(B6):10007, 1991. ISSN 0148-0227. doi: 10.1029/91JB00683.
- [89] A. Revil. Pervasive pressure solution transfer in a quartz sand. *Journal of Geophysical Research: Solid Earth*, 106(B5):8665–8686, May 2001. ISSN 01480227. doi: 10.1029/2000JB900465.
- [90] Dag Kristian Dysthe, Yuri Podladchikov, Francois Renard, Jens Feder, and Bjørn Jamtveit. Universal Scaling in Transient Creep. *Physical Review Letters*, 89(24), November 2002. ISSN 0031-9007, 1079-7114. doi: 10.1103/PhysRevLett.89.246102.
- [91] M. A. Grinfeld. The stress driven instability in elastic crystals: Mathematical models and physical manifestations. *Journal of Nonlinear Science*, 3(1):35–83, December 1993. ISSN 0938-8974, 1432-1467. doi: 10.1007/BF02429859.
- [92] Chaouqi Misbah, François Renard, Jean-Pierre Gratier, and Klaus Kassner. Dynamics of a dissolution front for solids under stress. *Geophysical Research Letters*, 31(6):n/a–n/a, March 2004. ISSN 00948276. doi: 10.1029/2003GL019136.
- [93] Julie Désarnaud, D. Bonn, and N. Shahidzadeh. The Pressure induced by salt crystallization in confinement. *Scientific Reports*, 6(1), November 2016. ISSN 2045-2322. doi: 10.1038/srep30856.
- [94] J. Lavalle. Recherche sur la formation des cristaux la temprature ordinaire. *Comptes Rendus de l'Academie des Sciences*, 36, 1853.
- [95] George F. Becker and Arthur L. Day. The Linear Force Of Growing Crystals. *Proceedings of the Washington Academy of Sciences*, 7:283–288, 1905. ISSN 03631095.
- [96] George F. Becker and Arthur L. Day. Note on the Linear Force of Growing Crystals. *The Journal of Geology*, 24(4):313–333, 1916.
- [97] S. Taber. The growth of crystals under external pressure. *American Journal of Science*, 41:532–556, 1916.
- [98] Carl W. Correns and W. Steinborn. Experimente zur Messung und Erklärung der sogenannten Kristallisationskraft. *Zeitschrift für Kristallographie - Crystalline Materials*, 101 (1-6), January 1939. ISSN 2196-7105, 2194-4946. doi: 10.1524/zkri.1939.101.1.117.
- [99] Rosa M. Espinosa-Marzal and George W. Scherer. Advances in Understanding Damage by Salt Crystallization. *Accounts of Chemical Research*, 43(6):897–905, June 2010. ISSN 0001-4842, 1520-4898. doi: 10.1021/ar9002224.
- [100] Mara Schiro, Encarnacion Ruiz-Agudo, and Carlos Rodriguez-Navarro. Damage Mechanisms of Porous Materials due to In-Pore Salt Crystallization. *Physical Review Letters*, 109 (26), December 2012. ISSN 0031-9007, 1079-7114. doi: 10.1103/PhysRevLett.109.265503.

- [101] A. Røyne, P. Meakin, A. Malthe-Sørenssen, B. Jamtveit, and D. K. Dysthe. Crack propagation driven by crystal growth. *EPL (Europhysics Letters)*, 96(2):24003, October 2011. ISSN 0295-5075, 1286-4854. doi: 10.1209/0295-5075/96/24003.
- [102] Julie Désarnaud, Olivier Grauby, Philippe Bromblet, Jean-Marc Vallet, and Alain Baronnet. Growth and Dissolution of Crystal under Load: New Experimental Results on KCl. *Crystal Growth & Design*, 13(3):1067–1074, March 2013. ISSN 1528-7483, 1528-7505. doi: 10.1021/cg3013359.
- [103] Anja Røyne. *Mechano-Chemical Interface Processes with Application to Rock Weathering*. PhD thesis, University of Oslo, Oslo, Norway, 2011.
- [104] Anja Røyne and Dag Kristian Dysthe. Rim formation on crystal faces growing in confinement. *Journal of Crystal Growth*, 346(1):89–100, May 2012. ISSN 00220248. doi: 10.1016/j.jcrysgro.2012.03.019.
- [105] Lei Li, Felix Kohler, Anja Røyne, and Dag Dysthe. Growth of Calcite in Confinement. *Crystals*, 7(12):361, December 2017. ISSN 2073-4352. doi: 10.3390/cryst7120361.
- [106] Felix Kohler, Luca Gagliardi, Olivier Pierre-Louis, and Dag Kristian Dysthe. Cavity Formation in Confined Growing Crystals. *Physical Review Letters*, 121(9), August 2018. ISSN 0031-9007, 1079-7114. doi: 10.1103/PhysRevLett.121.096101.
- [107] John A. Thomas and Alan J. H. McGaughey. Water Flow in Carbon Nanotubes: Transition to Subcontinuum Transport. *Physical Review Letters*, 102(18), May 2009. ISSN 0031-9007, 1079-7114. doi: 10.1103/PhysRevLett.102.184502.
- [108] R. M. Lynden-Bell and Jayendran C. Rasaiah. Mobility and solvation of ions in channels. *The Journal of Chemical Physics*, 105(20):9266–9280, November 1996. ISSN 0021-9606, 1089-7690. doi: 10.1063/1.472757.
- [109] Matej Kanduč, Alexander Schlaich, Emanuel Schneck, and Roland R. Netz. Water-Mediated Interactions between Hydrophilic and Hydrophobic Surfaces. *Langmuir*, 32(35):8767–8782, September 2016. ISSN 0743-7463, 1520-5827. doi: 10.1021/acs.langmuir.6b01727.
- [110] Matej Kanduč and Roland R. Netz. From hydration repulsion to dry adhesion between asymmetric hydrophilic and hydrophobic surfaces. *Proceedings of the National Academy of Sciences*, 112(40):12338–12343, October 2015. ISSN 0027-8424, 1091-6490. doi: 10.1073/pnas.1504919112.
- [111] Gøran Brekke-Svaland and Fernando Bresme. Interactions Between Hydrated Calcium Carbonate Surfaces at Nanoconfinement Conditions. *The Journal of Physical Chemistry C*, 122(13):7321–7330, April 2018. ISSN 1932-7447, 1932-7455. doi: 10.1021/acs.jpcc.8b01557.
- [112] Fernando Bresme and Luis G. Cámara. Computer simulation studies of Crystallization under confinement conditions. *Chemical Geology*, 230(3-4):197–206, June 2006. ISSN 00092541. doi: 10.1016/j.chemgeo.2006.02.025.
- [113] Luis G. Cámara and Fernando Bresme. Molecular dynamics simulations of crystallization under confinement at triple point conditions. *The Journal of Chemical Physics*, 119(5):2792–2800, August 2003. ISSN 0021-9606, 1089-7690. doi: 10.1063/1.1587127.
- [114] M. Kotrla. Numerical simulations in the theory of crystal growth. *Computer Physics Communications*, 97(1-2):82–100, August 1996. ISSN 00104655. doi: 10.1016/0010-4655(96)00023-9.

-
- [115] J. Villain. Continuum models of crystal growth from atomic beams with and without desorption. *Journal de Physique I*, 1(1):19–42, January 1991. ISSN 1155-4304, 1286-4862. doi: 10.1051/jp1:1991114.
- [116] O. Pierre-Louis, C. Misbah, Y. Saito, J. Krug, and P. Politi. New Nonlinear Evolution Equation for Steps during Molecular Beam Epitaxy on Vicinal Surfaces. *Physical Review Letters*, 80(19):4221–4224, May 1998. ISSN 0031-9007, 1079-7114. doi: 10.1103/PhysRevLett.80.4221.
- [117] Albert-László Barabási and H. Eugene Stanley. *Fractal Concepts in Surface Growth*. Press Syndicate of the University of Cambridge, New York, NY, USA, 1995. ISBN 978-0-521-48308-7 978-0-521-48318-6.
- [118] Inna Kurganskaya and Andreas Luttge. Kinetic Monte Carlo Simulations of Silicate Dissolution: Model Complexity and Parametrization. *The Journal of Physical Chemistry C*, 117(47):24894–24906, November 2013. ISSN 1932-7447, 1932-7455. doi: 10.1021/jp408845m.
- [119] Inna Kurganskaya and Andreas Luttge. Kinetic Monte Carlo Approach To Study Carbonate Dissolution. *The Journal of Physical Chemistry C*, 120(12):6482–6492, March 2016. ISSN 1932-7447, 1932-7455. doi: 10.1021/acs.jpcc.5b10995.
- [120] J. Whitehouse, R. A. Blythe, M. R. Evans, and D. Mukamel. Width Scaling of an Interface Constrained by a Membrane. *Physical Review Letters*, 121(5), August 2018. ISSN 0031-9007, 1079-7114. doi: 10.1103/PhysRevLett.121.058102.
- [121] Jørgen Høgberget, Anja Røyne, Dag K. Dysthe, and Espen Jettestuen. Microscopic modeling of confined crystal growth and dissolution. *Physical Review E*, 94(2), August 2016. ISSN 2470-0045, 2470-0053. doi: 10.1103/PhysRevE.94.023005.
- [122] Jørgen Høgberget. *Microscopic Modeling of Confined Crystal Surfaces: Growth, Dissolution and Equilibrium*. PhD thesis, University of Oslo, Oslo, Norway, 2016.
- [123] Andrew J. Gratz. Solution-transfer compaction of quartzites: Progress toward a rate law. *Geology*, 19(9):901, 1991. ISSN 0091-7613. doi: 10.1130/0091-7613(1991)019<0901:STCOQP>2.3.CO;2.
- [124] Vladislav Kruzhanov and Bernhard Stöckert. On the Kinetics of Elementary Processes of Pressure Solution. *Pure appl. geophys.*, 152:17, 1998.
- [125] Yutao Tao, Andrew Yeckel, and Jeffrey J. Derby. Analysis of particle engulfment during the growth of crystalline silicon. *Journal of Crystal Growth*, 452:1–5, October 2016. ISSN 00220248. doi: 10.1016/j.jcrysgro.2015.12.037.
- [126] Yutao Tao, Andrew Yeckel, and Jeffrey J. Derby. Steady-state and dynamic models for particle engulfment during solidification. *Journal of Computational Physics*, 315:238–263, June 2016. ISSN 00219991. doi: 10.1016/j.jcp.2016.03.050.
- [127] Michael Steiger. Crystal growth in porous materials—I: The crystallization pressure of large crystals. *Journal of Crystal Growth*, 282(3-4):455–469, September 2005. ISSN 00220248. doi: 10.1016/j.jcrysgro.2005.05.007.
- [128] Michael Steiger. Crystal growth in porous materials—II: Influence of crystal size on the crystallization pressure. *Journal of Crystal Growth*, 282(3-4):470–481, September 2005. ISSN 00220248. doi: 10.1016/j.jcrysgro.2005.05.008.
- [129] O Coussy. Deformation and stress from in-pore drying-induced crystallization of salt. *Journal of the Mechanics and Physics of Solids*, 54(8):1517–1547, August 2006. ISSN 00225096. doi: 10.1016/j.jmps.2006.03.002.

- [130] Jinhyun Choo and WaiChing Sun. Cracking and damage from crystallization in pores: Coupled chemo-hydro-mechanics and phase-field modeling. *Computer Methods in Applied Mechanics and Engineering*, 335:347–379, June 2018. ISSN 00457825. doi: 10.1016/j.cma.2018.01.044.
- [131] A. Naillon, P. Joseph, and M. Prat. Sodium chloride precipitation reaction coefficient from crystallization experiment in a microfluidic device. *Journal of Crystal Growth*, 463:201–210, April 2017. ISSN 00220248. doi: 10.1016/j.jcrysgro.2017.01.058.
- [132] Marcin Koniorczyk, Dariusz Gawin, Piotr Konca, and Dalia Bednarska. Modeling damage of building materials induced by sodium sulphate crystallization. *Bauphysik*, 38(6):366–371, December 2016. ISSN 01715445. doi: 10.1002/bapi.201610041.
- [133] W F Berg. Crystal growth from solutions. *Proceedings of the Royal Society A: Mathematical, Physical and Engineering Sciences*, 164(2):79–95, 1937.
- [134] A. Erdemir. Review of engineered tribological interfaces for improved boundary lubrication. *Tribology International*, 38(3):249–256, March 2005. ISSN 0301679X. doi: 10.1016/j.triboint.2004.08.008.
- [135] T. E. Karis, W. T. Kim, and M. S. Jhon. Spreading and dewetting in nanoscale lubrication. *Tribology Letters*, 18(1):27–41, January 2005. ISSN 1023-8883, 1573-2711. doi: 10.1007/s11249-004-1702-x.
- [136] Omar K. Matar, Vasileios Gkanis, and Satish Kumar. Nonlinear evolution of thin liquid films dewetting near soft elastomeric layers. *Journal of Colloid and Interface Science*, 286(1):319–332, June 2005. ISSN 00219797. doi: 10.1016/j.jcis.2004.12.034.
- [137] Jean-Noël Aqua, Thomas Frisch, and Alberto Verga. Nonlinear evolution of a morphological instability in a strained epitaxial film. *Physical Review B*, 76(16), October 2007. ISSN 1098-0121, 1550-235X. doi: 10.1103/PhysRevB.76.165319.
- [138] Maurice J. Blount, Michael J. Miksis, and Stephen H. Davis. Thin-film Flow Beneath a Vesicle During Adhesion Processes. *Procedia IUTAM*, 16:33–40, 2015. ISSN 22109838. doi: 10.1016/j.piutam.2015.03.005.
- [139] Thomas Le Goff, Paolo Politi, and Olivier Pierre-Louis. Frozen states and order-disorder transition in the dynamics of confined membranes. *Physical Review E*, 90(3), September 2014. ISSN 1539-3755, 1550-2376. doi: 10.1103/PhysRevE.90.032114.
- [140] Thomas Le Goff, Tung B. T. To, and Olivier Pierre-Louis. Thixotropy and shear thinning of lubricated contacts with confined membranes. *The European Physical Journal E*, 40(4), April 2017. ISSN 1292-8941, 1292-895X. doi: 10.1140/epje/i2017-11532-6.
- [141] Etienne Guyon, Jean-Pierre Hulin, Luc Petit, and Catalin D. Mitescu. *Physical Hydrodynamics, 2nd Edn.* Oxford University Press, January 2015. ISBN 978-0-19-870244-3. doi: 10.1093/acprof:oso/9780198702443.001.0001.
- [142] J.I Cahn and D.I Hoffman. A vector thermodynamics for anisotropic surfaces—II. Curved and faceted surfaces. *Acta Metallurgica*, 22(10):1205–1214, October 1974. ISSN 00016160. doi: 10.1016/0001-6160(74)90134-5.
- [143] Conyers Herring and Walter E. Kingston. *Physics of Powder Metallurgy.* McGraw-Hill, New York, NY, 1951.
- [144] F. Wolfgang Tegethoff, editor. *Calcium Carbonate.* Birkhäuser Basel, Basel, 2001. ISBN 978-3-0348-9490-6 978-3-0348-8245-3. doi: 10.1007/978-3-0348-8245-3.

- [145] Li Yuan-Hui and Sandra Gregory. Diffusion of ions in sea water and in deep-sea sediments. *Geochimica et Cosmochimica Acta*, 38(5):703–714, May 1974. ISSN 00167037. doi: 10.1016/0016-7037(74)90145-8.
- [146] Elly Van der Voort and P. Hartman. Calculated interfacial tensions for the calcite cleavage rhombohedron and water. *Journal of Crystal Growth*, 89(4):603–607, July 1988. ISSN 00220248. doi: 10.1016/0022-0248(88)90224-2.
- [147] Anja Røyne, Jan Bisschop, and Dag Kristian Dysthe. Experimental investigation of surface energy and subcritical crack growth in calcite. *Journal of Geophysical Research*, 116(B4), April 2011. ISSN 0148-0227. doi: 10.1029/2010JB008033.
- [148] W. Wang and W.R. Hu. Concentration distribution in crystallization from solution under microgravity. *Journal of Crystal Growth*, 160(3-4):398–405, March 1996. ISSN 00220248. doi: 10.1016/0022-0248(95)00929-9.
- [149] Jon Wonham. Effect of Pressure on the Viscosity of Water. *Nature*, 215(5105):1053–1054, September 1967. ISSN 0028-0836, 1476-4687. doi: 10.1038/2151053a0.
- [150] Jörn W. P. Schmelzer, Edgar D. Zanutto, and Vladimir M. Fokin. Pressure dependence of viscosity. *The Journal of Chemical Physics*, 122(7):074511, February 2005. ISSN 0021-9606, 1089-7690. doi: 10.1063/1.1851510.
- [151] Edgar Alejandro Pachon-Rodriguez, Agnès Piednoir, and Jean Colombani. Pressure Solution at the Molecular Scale. *Physical Review Letters*, 107(14), September 2011. ISSN 0031-9007, 1079-7114. doi: 10.1103/PhysRevLett.107.146102.
- [152] Ivan V. Markov. *Crystal Growth for Beginners: Fundamentals of Nucleation, Crystal Growth and Epitaxy*. World Scientific, New Jersey, 3rd edition edition, 2016. ISBN 978-981-314-342-5.
- [153] D. Turnbull. Kinetics of Heterogeneous Nucleation. *The Journal of Chemical Physics*, 18(2):198–203, February 1950. ISSN 0021-9606, 1089-7690. doi: 10.1063/1.1747588.
- [154] David Winter, Peter Virnau, and K. Binder. Monte Carlo Test of the Classical Theory for Heterogeneous Nucleation Barriers. *Physical Review Letters*, 103(22), November 2009. ISSN 0031-9007, 1079-7114. doi: 10.1103/PhysRevLett.103.225703.
- [155] Amanda J. Page and Richard P. Sear. Heterogeneous Nucleation in and out of Pores. *Physical Review Letters*, 97(6), 2006. ISSN 0031-9007, 1079-7114. doi: 10.1103/PhysRevLett.97.065701.
- [156] N. E. Chayen, E. Saridakis, and R. P. Sear. Experiment and theory for heterogeneous nucleation of protein crystals in a porous medium. *Proceedings of the National Academy of Sciences*, 103(3):597–601, January 2006. ISSN 0027-8424, 1091-6490. doi: 10.1073/pnas.0504860102.
- [157] Atherton Seidell. *Solubilities of Inorganic and Organic Compounds. A compilation of quantitative solubility data from the periodical literature, by Atherton Seidell, Ph. D., Washington. Supplement to the second edition containing data published during the years 1917-1926 i*, volume 266. D. VAN NOSTRAND COMPANY, New York, NY, USA, 2 edition, 1928.
- [158] Brian Crump, M. F. Hoq, Bhart Indu, and W. R. Ernst. Solubility and Density of Chloric Acid + Sodium Chlorate Solutions. *Journal of Chemical & Engineering Data*, 40(5): 1106–1110, September 1995. ISSN 0021-9568, 1520-5134. doi: 10.1021/jc00021a016.

- [159] Ru-Ying Qian and Gregory D. Botsaris. Nuclei breeding from a chiral crystal seed of NaClO₃. *Chemical Engineering Science*, 53(9):1745–1756, May 1998. ISSN 00092509. doi: 10.1016/S0009-2509(98)00040-2.
- [160] Laurent Limozin and Kheya Sengupta. Quantitative Reflection Interference Contrast Microscopy (RICM) in Soft Matter and Cell Adhesion. *ChemPhysChem*, 10(16):2752–2768, November 2009. ISSN 14394235, 14397641. doi: 10.1002/cphc.200900601.
- [161] Ajitha Sweetly. Crystallization and studies of an NLO material: NaClO₃ single crystal. *International Journal of Recent Scientific Research*, 3(qw):4, 2012.
- [162] A. N. Campbell, E. M. Kartzmark, and B. G. Oliver. The Electrolytic Conductances of Sodium Chlorate and of Lithium Chlorate in Water and in Water–Dioxane. *Canadian Journal of Chemistry*, 44(8):925–934, April 1966. ISSN 0008-4042, 1480-3291. doi: 10.1139/v66-135.
- [163] A. N. Campbell and B. G. Oliver. Diffusion coefficients of sodium and lithium chlorates in water, at 25°. *Canadian Journal of Chemistry*, 47(14):2681–2685, July 1969. ISSN 0008-4042, 1480-3291. doi: 10.1139/v69-440.
- [164] J. P. Miller. A portion of the system calcium carbonate-carbon dioxide-water, with geological implications. *American Journal of Science*, 250(3):161–203, March 1952. ISSN 0002-9599. doi: 10.2475/ajs.250.3.161.
- [165] Chemical Rubber Company and David R. Lide, editors. *CRC Handbook of Chemistry and Physics: A Ready-Reference Book of Chemical and Physical Data*. CRC Press, Boca Raton, 86. ed edition, 2005. ISBN 978-0-8493-0486-6. OCLC: 179976746.
- [166] J. K. Gladden and Malcolm Dole. Diffusion in Supersaturated Solutions. II. Glucose Solutions. *Journal of the American Chemical Society*, 75(16):3900–3904, August 1953. ISSN 0002-7863, 1520-5126. doi: 10.1021/ja01112a008.
- [167] A. Viet Bui and M.H. Nguyen. Prediction of viscosity of glucose and calcium chloride solutions. *Journal of Food Engineering*, 62(4):345–349, May 2004. ISSN 02608774. doi: 10.1016/S0260-8774(03)00249-8.
- [168] H. Hirschmüller. PHYSICAL PROPERTIES OF SUCROSE. In *Principles of Sugar Technology*, pages 18–74. Elsevier, 2013. ISBN 978-1-4832-3252-2. doi: 10.1016/B978-1-4832-3252-2.50007-6.
- [169] M. Mathlouthi and P. Reiser, editors. *Sucrose*. Springer US, Boston, MA, 1995. ISBN 978-1-4613-6150-3 978-1-4615-2676-6. doi: 10.1007/978-1-4615-2676-6.
- [170] John W Cahn. On spinodal decomposition. *Acta Metallurgica*, 9(9):795–801, September 1961. ISSN 00016160. doi: 10.1016/0001-6160(61)90182-1.
- [171] Vladimir S. Mitlin and Nikolai V. Petviashvili. Nonlinear dynamics of dewetting: Kinetically stable structures. *Physics Letters A*, 192(5-6):323–326, September 1994. ISSN 03759601. doi: 10.1016/0375-9601(94)90213-5.
- [172] S. Herminghaus. Spinodal Dewetting in Liquid Crystal and Liquid Metal Films. *Science*, 282(5390):916–919, October 1998. doi: 10.1126/science.282.5390.916.
- [173] R. Xie, A. Karim, J. F. Douglas, C. C. Han, and R. A. Weiss. Spinodal Dewetting of Thin Polymer Films. *Physical Review Letters*, 81(6):1251–1254, August 1998. ISSN 0031-9007, 1079-7114. doi: 10.1103/PhysRevLett.81.1251.
- [174] Jean Colombani. The Alkaline Dissolution Rate of Calcite. *The Journal of Physical Chemistry Letters*, 7(13):2376–2380, July 2016. ISSN 1948-7185. doi: 10.1021/acs.jpcllett.6b01055.

- [175] L.Niel Plummer and T.M.L Wigley. The dissolution of calcite in CO₂-saturated solutions at 25°C and 1 atmosphere total pressure. *Geochimica et Cosmochimica Acta*, 40(2):191–202, February 1976. ISSN 00167037. doi: 10.1016/0016-7037(76)90176-9.
- [176] Luca Gagliardi and O. Pierre-Louis. Confined Growth with slow surface kinetics: A Thin Film Model approach. *Submitted: arXiv:1901.07347*, 2019.
- [177] Hong Lin, Peter G. Vekilov, and Franz Rosenberger. Facet morphology response to nonuniformities in nutrient and impurity supply. II. Numerical simulations. *Journal of Crystal Growth*, 158(4):552–559, February 1996. ISSN 00220248. doi: 10.1016/0022-0248(95)00426-2.
- [178] Robert J. Flatt. Salt damage in porous materials: How high supersaturations are generated. *Journal of Crystal Growth*, 242(3-4):435–454, July 2002. ISSN 00220248. doi: 10.1016/S0022-0248(02)01429-X.
- [179] Y. C. Chang and A. S. Myerson. The diffusivity of potassium chloride and sodium chloride in concentrated, saturated, and supersaturated aqueous solutions. *AIChE Journal*, 31(6): 890–894, June 1985. ISSN 0001-1541, 1547-5905. doi: 10.1002/aic.690310603.
- [180] Maniya Maleki, Etienne Reyssat, David Quéré, and Ramin Golestanian. On the Landau-Levich Transition. *Langmuir*, 23(20):10116–10122, September 2007. ISSN 0743-7463, 1520-5827. doi: 10.1021/la700822y.
- [181] Giles Delon. *Nature de la transition de Landau-Levich*. PhD thesis, Université Paris 7 - Denis Diderot, 2007.
- [182] Thierry Dombre and Vincent Hakim. Saffman-Taylor fingers and directional solidification at low velocity. *Physical Review A*, 36(6):2811–2817, September 1987. ISSN 0556-2791. doi: 10.1103/PhysRevA.36.2811.
- [183] Pierre Pelcé, editor. *Dynamics of Curved Fronts*. Elsevier, 1988. ISBN 978-0-12-550355-6. doi: 10.1016/C2009-0-22180-5.
- [184] H. Scott Fogler. *Elements of Chemical Reaction Engineering*. Prentice Hall PTR International Series in the Physical and Chemical Engineering Sciences. Prentice Hall PTR, Upper Saddle River, NJ, 4th ed edition, 2006. ISBN 978-0-13-047394-3. OCLC: ocm56956313.
- [185] Christopher J. D. Fell and H. Peter. Hutchison. Diffusion coefficients for sodium and potassium chlorides in water at elevated temperatures. *Journal of Chemical & Engineering Data*, 16(4):427–429, October 1971. ISSN 0021-9568, 1520-5134. doi: 10.1021/jc60051a005.
- [186] H. Weingaertner, W. E. Price, A. V. J. Edge, and R. Mills. Transport measurements in aqueous sodium sulfate: Evidence for like-ion pairs in concentrated solutions. *The Journal of Physical Chemistry*, 97(23):6289–6291, June 1993. ISSN 0022-3654, 1541-5740. doi: 10.1021/j100125a031.
- [187] Delphine Croizé. *Mechanical and Chemical Compaction of Carbonates - An Experimental Study*. PhD thesis, University of Oslo, 2010.
- [188] Denis Blackmore and Lu Ting. Surface integral of Its Mean Curvature Vector. *SIAM Review*, 27(4):569–572, December 1985. ISSN 0036-1445, 1095-7200. doi: 10.1137/1027143.
- [189] Charles E Weatherburn. *Differential Geometry of Three Dimensions*. 2016. ISBN 978-1-316-60384-0. OCLC: 952634227.
- [190] Ron Goldman. Curvature formulas for implicit curves and surfaces. *Computer Aided Geometric Design*, 22(7):632–658, October 2005. ISSN 01678396. doi: 10.1016/j.cagd.2005.06.005.

- [191] Elizabeth Greenwell Yanik. Numerical Recipes in FORTRAN—The Art of Scientific Computing 2nd Ed. (W. H. Press, W. T. Vetterling, S. A. Teukolsky and B. P. Flannery). *SIAM Review*, 36(1):149–150, March 1994. ISSN 0036-1445, 1095-7200. doi: 10.1137/1036047.
- [192] Jorge J. Moré, Burton S. Garbow, and Kenneth E. Hillstom. User guide for MINPACK-1. Technical report, CM-P00068642, 1980.
- [193] Jean Colombani. Dissolution measurement free from mass transport. *Pure and Applied Chemistry*, 85(1):61–70, August 2012. ISSN 1365-3075, 0033-4545. doi: 10.1351/PAC-CON-12-03-07.

Abstract

This thesis discusses the modeling of growth and dissolution of confined crystals. We focus on the dynamics within lubricated (or hydrophilic) contacts and derive a continuum thin film model accounting for diffusion, surface kinetics, hydrodynamics, surface tension, and interactions with the substrate (disjoining pressure). The model is applied to different geological problems.

First, we study dissolution induced by an external load (pressure solution). We find the functional form of the disjoining pressure – finite or diverging at contact – crucial in determining steady-state dissolution rates and morphologies. These forms respectively lead to load-dependent or load-independent dissolution rates, and to flat or pointy surface profiles.

Second, we consider growth in the vicinity of a flat wall. We find that a cavity appears on the confined crystal surface. We obtain a non-equilibrium morphology diagram describing the formation of the cavity in agreement with experimental observations. When crossing the transition line, a cavity can appear continuously or discontinuously depending on the form of the disjoining pressure (repulsive or attractive). For nanometric film thicknesses, viscosity can hinder the formation of the cavity.

Finally, we address the question of the force of crystallization exerted by a crystal growing between two flat walls. We point out the importance of a precise definition of the contact area to define the equilibrium pressure. During growth, the triple-line undergoes a kinetic pinning transition depending solely on the ratio between the diffusion constant, and the product of the surface kinetic constant and the distance between the walls. After this transition, the crystallization force decreases to zero and a macroscopic film forms.

Résumé

Cette thèse traite de la modélisation de la croissance et de la dissolution de cristaux confinés. Nous nous concentrons sur la dynamique dans les contacts lubrifiés (ou hydrophiles) et dérivons un modèle continu de couche mince prenant en compte la diffusion, la cinétique de surface, l'hydrodynamique, la tension de surface et les interactions avec le substrat (pression de disjonction). Le modèle est appliqué à différents problèmes géologiques.

Premièrement, nous étudions la dissolution induite par une charge extérieure (dissolution sous contrainte). Nous trouvons que la forme fonctionnelle de la pression de disjonction – finie ou divergente au contact – est cruciale dans la détermination des taux de dissolution et des morphologies stationnaires. Ces formes conduisent respectivement à des taux de dissolution dépendant ou indépendants de la charge, et à des profils de surface plats ou pointus.

Deuxièmement, nous considérons la croissance à proximité d'un mur plat. Nous avons constaté qu'une cavité apparaît sur la surface confinée du cristal. Nous obtenons un diagramme de morphologie hors équilibre en accord avec les observations expérimentales. En traversant la ligne de transition, une cavité peut apparaître de manière continue ou discontinue en fonction de la forme de la pression de disjonction (répulsive ou attractive). Pour les épaisseurs de film nanométriques, la viscosité peut entraver la formation de la cavité.

Enfin, nous adressons la question de la force de cristallisation exercée par un cristal croissant entre deux parois planes. Nous soulignons l'importance d'une définition précise de l'aire de contact pour définir la pression d'équilibre. Pendant la croissance, la ligne triple subit une transition cinétique dépendant uniquement du rapport entre la constante de diffusion, et le produit de la constante cinétique de surface et de la distance entre les murs. Après cette transition, la force de cristallisation diminue jusqu'à s'annuler et un film macroscopique se forme.
